

DISS. ETH NO. 27064

**From the Po Valley to the Arctic:  
Field experiments to characterize the variability in  
physical and optical properties of atmospheric black  
carbon particles from polluted to clean environments**

A thesis submitted to attain the degree of  
DOCTOR OF SCIENCES of ETH ZURICH  
(Dr. sc. ETH Zurich)

presented by  
**Rosaria Erika Pileci**

M. Sc. Physics  
Università degli Studi di Milano

Born on 11.01.1991  
Citizen of Italy

Accepted on the recommendation of

Prof. Dr. Urs Baltensperger (examiner)  
Dr. Paola Formenti (co-examiner)  
Prof. Dr. Jing Wang (co-examiner)  
Dr. Martin Gysel-Beer (co-examiner)  
Dr. Rob L. Modini (co-examiner)

2020

DISS. ETH NO. 27064

**From the Po Valley to the Arctic:  
Field experiments to characterize the variability in  
physical and optical properties of atmospheric black  
carbon particles from polluted to clean environments**

A thesis submitted to attain the degree of  
DOCTOR OF SCIENCES of ETH ZURICH  
(Dr. sc. ETH Zurich)

presented by  
**Rosaria Erika Pileci**

M. Sc. Physics  
Università degli Studi di Milano

Born on 11.01.1991  
Citizen of Italy

Accepted on the recommendation of

Prof. Dr. Urs Baltensperger (examiner)  
Dr. Paola Formenti (co-examiner)  
Prof. Dr. Jing Wang (co-examiner)  
Dr. Martin Gysel-Beer (co-examiner)  
Dr. Rob L. Modini (co-examiner)

2020

"The real voyage of discovery consists not in seeking new landscapes, but in **having new eyes.**" Marcel Proust

# Table of contents

**Summary**

**Sommario**

## **Chapter 1:**

### **Introduction**

1.1 The Earth's climate

1.1.1 Human and natural drivers of climate change

1.1.2 The climate forcings from the preindustrial era

1.1.3 Impacts, vulnerability, adaptation and mitigation of climate change

1.2 Atmospheric aerosols: definition, properties and effects

1.2.1 Aerosol sources, formation and life cycle

1.2.2 Aerosol physical properties

1.2.3 Aerosol optical properties

1.2.4 Aerosol chemical properties

1.2.5 Aerosol impact on climate

1.2.6 Aerosol impact on human health

1.3 Black carbon aerosols

1.3.1 Nomenclature

1.3.2 Black carbon sources, formation and life cycle

1.3.3 Black carbon Impact on climate

1.3.4 Black carbon impact on human health

1.4 Aim of the work and thesis structure

## **Chapter 2:**

### **Methodologies**

2.1 Filter based absorption photometry

2.1.1 The Aethalometer

2.1.2 The multi-angle absorption photometer

2.2 The thermal optical technique

2.2.1 The sunset EC/OC analyzer

2.3 Laser induced incandescence

2.3.1 The Single-Particle Soot Photometer

2.3.2 The Single-Particle Soot Photometer Extended Range

2.4 comparison of BC measuring techniques

## **Chapter 3:**

### **Comparison of co-located rBC and EC mass concentration measurements during field campaigns at several European sites**

#### **Abstract**

##### 3.1 Introduction

##### 3.2 Methods

###### 3.2.1 Sampling campaign: measurements sites and experimental setup

###### 3.2.2 Thermal optical analysis

###### 3.2.2.1 Measurement principle, OC/EC split and involved artefacts

###### 3.2.2.2 EUSAAR-2 vs other existing protocols

###### 3.2.2.3 Variability of EC measurements with the EUSAAR-2 protocol

###### 3.2.3 The Single-Particle Soot Photometer (SP2)

###### 3.2.3.1 Principle of measurement

###### 3.2.3.2 rBC mass calibration

###### 3.2.3.3 Potential interferences and artefacts

###### 3.2.3.4 SP2 detection efficiency and detection range

###### 3.2.3.5 Methods to correct SP2 data or missing mass below LDL

###### 3.2.4 Auxiliary measurements

###### 3.2.4.1 Aerosol size distribution

###### 3.2.4.2 Absorption Ångström exponent (AAE) inferred from Aethalometer data

##### 3.3 Results and discussion

###### 3.3.1 rBC mass potentially missing below the LDL of the SP2

###### 3.3.1.1 Comparison of two approaches to correct for the truncated rBC mass

###### 3.3.1.2 Limits to rBC mass missed in small BC cores imposed by the BC particle number

###### 3.3.2 Comparison of observed EC and rBC mass concentrations

###### 3.3.3 Discussion of level of agreement between the rBC and EC mass concentration measurements

###### 3.3.3.1 Differences in upper cut-off diameters and in inlet losses

###### 3.3.3.2 Filter loading and EC/TC ratios

###### 3.3.3.3 Systematic EC and rBC bias due to the presence of particular types of particulate matter such as brown carbon or biomass burning BC

###### 3.3.4 Reconciliation of sources of discrepancy between rBC and EC mass

###### 3.3.5 Comparison with previous rBC and EC intercomparison studies

##### 3.4 Conclusions

### **Supplement of: Comparison of co-located rBC and EC mass concentration measurements during field campaigns at several European sites**

#### **Acknowledgment**

#### **Financial support**

**Author contributions**

**Data availability**

**Competing interests**

**Chapter 4:**

**Variability of physical and optical properties of freshly emitted and aged black carbon particles determined from stationary and mobile measurements in the Po Valley (Italy), during summertime**

Abstract

4.1 Introduction

4.2 Methods

4.2.1 Measurements period and sites

4.2.2 The mobile laboratory

4.2.3 Instruments used to measure aerosols optical properties

4.2.3.1 Absorption based instruments

4.2.3.2 The Single Particle Soot Photometer for BC particles

4.2.3.3 The thermal optical transmittance analysis for EC

4.2.4 The aerosol mass spectrometer for chemical composition

4.2.5 Gas monitors

4.3 Data treatment

4.3.1. Back carbon mass absorption cross-section

4.3.2 Positive matrix factorization

4.4 Results and discussion

4.4.1 Meteorological parameters

4.4.2 Aerosol chemical composition

4.4.3 Diurnal variability in BC mass concentrations and properties

4.4.4 Spatial variability of BC optical and physical properties

4.4.5 Mechanisms driving  $MAC_{BC}$  variability

4.4.6 Dependence of  $MAC_{BC}$  on using EC and rBC mass measurements

4.5 Conclusions

**Supplement of: Variability of physical and optical properties of freshly emitted and aged black carbon particles determined from stationary and mobile measurements in the Po Valley (Italy), during summertime**

**Acknowledgment**

**Financial support**

**Author contributions**

**Competing interests**

**Chapter 5:**

**Yearly physical characterization of the Arctic black carbon sampled at Zeppelin Observatory, Svalbard**

Abstract

5.1 Introduction

5.2 Methods

5.2.1 Measurement site

5.2.2 Inlets and instruments

5.2.2.1 Inlets

5.2.2.2 Single Particle Soot Photometer Extended Range (SP2-XR)

5.2.2.3 Multi-angle absorption photometer (MAAP)

5.2.2.4 Transmission electron microscopy (TEM)

5.2.2.5 Concentration weighted trajectory analysis (CWT)

5.3 Results and discussion

5.3.1 rBC mass concentration and size distribution

5.3.2 Presence of coarse BC particles in the TEM analysis

5.3.3 Determination of BC source regions

5.3.3.1 Seasonal rBC concentration weighted trajectories

5.3.3.2 Concentration weighted trajectories during large BC particles occurrence

5.3.4 Correlation between coarse mode BC particles and presence of clouds

5.3.5 Comparison between rBC and eBC mass concentrations

5.4 Conclusions

**Supplement of: Yearly physical characterization of the Arctic black carbon sampled at Zeppelin Observatory, Svalbard**

**Chapter 6:**

**Conclusions and perspectives**

**References**

**Curriculum Vitae**

**Acknowledgments**

# Summary

Black carbon (BC) is a very important aerosol component in the Earth system. First, because it induces a strong positive radiative forcing ( $RF_{BC} = +1.1 \text{ W m}^{-2} \pm 90 \%$ ), through two main pathways: aerosol-radiation interaction ( $RF_{ARI}$ ) and aerosol-cloud interaction ( $RF_{ACI}$ ). Second, because elevated concentrations of black carbon in ambient air are a public health concern, as they can cause allergies, pulmonary and cardiovascular diseases, and premature deaths. Both for correctly quantifying BC radiative forcing and for the implementation of air quality or human health regulations, a deep understanding of BC physical, optical and chemical properties, such as, mass concentration, mass size distribution and mixing state is required. Furthermore, BC emission abatement measures would have significant co-benefits for improving air quality and for counteracting climate warming on a short time scale.

BC properties change during the particles' life cycle. Freshly emitted BC particles are strongly light absorbing, hydrophobic and externally mixed fractal-like aggregates of primary carbon spherules. During atmospheric aging, the fractal aggregates become internally mixed with other aerosol species. The aging changes the size and composition of the coated BC particles, thus modifying their hygroscopicity and morphology. Moreover, aging is known to enhance the BC mass absorption cross-section ( $MAC_{BC}$ ) by a lensing effect. The  $MAC_{BC}$ , a key parameter for the BC radiative forcing calculation, is defined as the ratio of the light absorption coefficient caused by BC to the BC mass concentration. BC properties also depend on the emission source: particles from fossil fuel combustion generally have smaller volume equivalent diameters (70–140 nm) than particles produced by biomass burning (140–200 nm).

Black carbon particles are ubiquitous in the atmosphere even where no emission source is present, since they can be transported very far and reach very vulnerable places like the Arctic, triggering unforeseen effects. Due to their scarcity, BC properties measurements in such remote places are very precious in order to provide the information needed to develop global aerosol radiative forcing models.

Even if large progress in understanding the properties, life cycle and cloud-interaction mechanisms has been made in the past decades, there are still a lot of open questions concerning black carbon aerosols. During this PhD thesis, we had the ambition to address some of the most important ones through field campaigns from a polluted area i.e. the Po Valley, in Northern Italy, to a very clean and remote environment, at the Zeppelin Observatory, Svalbard, in the middle of the Arctic Sea.

The key instrument used in each campaign of this work was the Single Particle Soot Photometer (SP2) and its most recent version: the Single Particle Soot Photometer Extended Range (SP2-XR), an instrument based on the laser induced incandescence technique. The SP2 has become increasingly recognized as a valuable tool for quantifying aerosol refractory black carbon (rBC) properties because it provides simultaneously multiple information at single particle level. First, it unambiguously measures the mass of rBC in individual aerosol particles rather than inferring bulk BC loadings from measurements of aerosol optical/absorption properties. Second, it is able to give additional information such as the mass and number rBC size distributions and the rBC mixing state (both in a qualitative and in a quantitative way) of individual rBC-containing particles. Third, as the instrument detects individual aerosol particles, it is able to quantify rBC loadings even in very clean environments, such as the Arctic, where other techniques would require prohibitively long integration times.

The open research questions on black carbon science we addressed during this PhD work, were as follows:

## 1) **Black carbon mass concentration measurements**

The quantification of black carbon mass concentration is a very tricky business. There is neither an SI (International System of Units) traceable reference method nor a suitable standard reference material for quantifying it. Currently, BC mass is defined operationally through methodologies that use distinct physico-chemical and/or optical properties of BC in order to quantify its mass concentration in aerosols. The three most common applied techniques are the filter based thermal-optical evolved gas analysis; the laser induced



incandescence (LII) and the aerosol light absorption based methods. The specific terms used to refer to the mass of BC quantified by each of these three techniques are: elemental carbon (EC), refractory black carbon and equivalent black carbon (eBC), respectively. Aerosol optical absorption has long been used as a proxy for BC mass, but it can be influenced by both non-BC aerosol that absorbs at the same wavelength of the instrument used (e.g., dust or brown carbon), and by the enhancement of absorption by coatings. Moreover, eBC mass measurements rely on prior knowledge or assumed values of the  $MAC_{BC}$ . Such prior knowledge is not required for thermal optical measurements of EC mass or for LII measurements of rBC mass. Many BC technique intercomparisons are available in the literature but very few regard EC and rBC mass. This means that the debate on the comparability of these two quantities is still largely unresolved.

In the first paper work, we examined and quantified the level of agreement or disagreement between BC mass concentrations measured by the thermal-optical analysis and the LII technique. For this purpose, we compared co-located measurements of EC and rBC mass concentrations from field campaigns performed at several European sites (Bologna, Cabauw, Paris and Melpitz) in order to sample different aerosol types. This first multi-site intercomparison allowed us to more quantitatively assess the extent to which the EC and rBC concentration measurements agree or disagree with each other. Potential reasons for discrepancies such as different size cuts, calibration uncertainties and various interferences were discussed.

We found that the thermal-optical analysis and the LII technique provide an operationally defined measure of atmospheric BC mass in good overall agreement. However, systematic discrepancies up to  $\sim\pm 50\%$  were observed at some sites. The median of the observed rBC to EC mass ratios for the whole dataset was 0.92, with a GSD of 1.50. The median ratio varied from 0.53 to 1.29 from campaign to campaign. Potential reasons for the discrepancies were: source-specific SP2 response, the possible presence of an additional mode of small BC cores below the LDL of the SP2, differences in the upper cut-off of the SP2 and the inlet line for the EC sampling, or various uncertainties and interferences from co-emitted species in the EC mass measurement. The discrepancy between rBC and EC appears to be systematically related to the BC source, i.e. traffic versus wood and/or coal burning. However, it was not possible to identify causalities behind this trend due to potential cross-correlations between several aerosol and BC properties relevant for potential biases.

## 2) The relationship between $MAC_{BC}$ and BC properties

The scientific understanding of the factors that drive variability in the light absorption per BC mass remains inadequate and contributes to the large uncertainty in BC climate forcing quantification. Light absorption by externally mixed BC is reasonably well characterized, but internal mixing between BC and other aerosol components through processes such as gas condensation and coagulation can enhance the absorption by BC. The impact of internal mixing is not well understood, with disparities between laboratory observations and field studies. Laboratory studies typically show strong enhancement in BC light absorption, often by a factor of two or more for sufficiently large coating amounts. However, absorption enhancements by ambient BC vary among field studies, with several studies showing much weaker absorption enhancement for similar average coating amounts. This laboratory-ambient discrepancy translates into ambiguity in model representations of absorption by BC-containing particles and, thereby, uncertainty in model predictions of atmospheric warming by BC. Although the range of the literature  $MAC_{BC}$  values is consistent with more recent observations, the spread remains rather large. The  $MAC_{BC}$  variability can be primarily explained with the variability in BC physical and optical properties such as mixing state, BC core size, particle morphology and refractive index. However, it also depends on the measuring techniques used for the BC mass concentration and the absorption coefficient, which can have large uncertainties.

In the second paper work, we investigated the spatio-temporal variability of the  $MAC_{BC}$  value and its relation with the mixing state and BC core diameter in the Po Valley, Italy during summertime. Moreover, we provided an overall picture of the most relevant physical-optical black carbon properties, such as the refractory BC mass concentration, elemental carbon mass concentration, rBC mass size distribution, BC absorption coefficient, absorption Ångström exponent and single scattering albedo.

Our findings showed that the small variation of BC core diameters found during the campaign was not able to explain the much greater variability in the observed  $MAC_{BC}$  values, which was better explained with the variability of the BC mixing state. This result provides experimental confirmation that the lensing effect can substantially increase the MAC of black carbon by up to a factor of almost 2. However, while this study provides clear evidence of BC mixing state effects on  $MAC_{BC}$ , the observed  $MAC_{BC}$  values remain tainted with considerable uncertainty due to the lack of absolutely accurate mass measurement techniques. Indeed, in this study, the  $MAC_{BC}$  values based on rBC mass concentrations were 35 % higher than those based on EC mass concentrations. Moreover, the study of the relevant physical–optical black carbon properties in the Po Valley, gave evidence that the Po Valley, in summer, contains a 'pool' of aged BC particles into which fresh BC emissions are mixed on short temporal and spatial scales.

### 3) Long-term measurements of BC properties in the Arctic

The description of BC impacts on climate and air quality in the Arctic requires an accurate understanding of BC optical and microphysical properties, BC aerosol-cloud interaction, wet and dry deposition, and sources. In particular, the analysis of BC temporal variability can help understanding how changes in climate and anthropogenic activities affect BC. The BC atmospheric concentration in the Arctic region is controlled by BC emissions at high and middle latitudes, local meteorology and large-scale circulation, and BC removal efficiency through wet and dry deposition, which in turn are controlled by BC microphysical properties and meteorology. A better understanding of all the factors controlling BC atmospheric concentration is a key element to improve the model ability to describe the climate impact of BC and reduce the uncertainty of future climate scenarios. Moreover, increasing the time coverage of BC measurements, especially during winter on a global and regional scale would improve the knowledge of BC climate impact in the Arctic.

Long-term observations at Svalbard make use of optical filter-based techniques to infer the BC mass concentration, such as the multi-angle absorption photometer, the photo acoustic absorption photometer and the Aethalometer. However, the absorption coefficient calculated with these instruments can be prone to large uncertainties, due to multiple scattering and filter loading effects. Additional uncertainty results from the empirical conversion of the absorption coefficient to the equivalent black carbon mass concentration using an assumed  $MAC_{BC}$ . Thanks to the recent development of the Single Particle Soot Photometer, direct measurements of refractory black carbon have started also in the Arctic. However, the SP2 measurements in the Arctic are still scarce. Improving the comparability and accuracy of atmospheric BC measurements, by understanding the differences among different monitoring methods, is an urgent need in the Arctic.

To answer the need of a more complete characterization and longer time series of black carbon properties in the Arctic, we measured the rBC mass concentrations and the rBC size distributions at the Zeppelin Observatory in Svalbard, Norway, from April 2019 to March 2020. The measurements were performed with a Single Particle Soot Photometer Extended Range, the more compact version of the SP2. For the first time in this work, the SP2-XR was used for a long-term remote monitoring campaign. In addition, trajectory analyses were used to estimate the sources of BC. Finally, we compared the rBC mass concentrations with those derived from the MAAP to investigate their agreement or disagreement.

The study of the temporal variability of refractory black carbon mass concentration and rBC mass size distribution showed an annual average and median rBC mass concentrations were 8.0 and 3.8  $ng\ m^{-3}$ , respectively, while monthly averages ranged from a maximum of 24.7  $ng\ m^{-3}$  in February, to a minimum of 2.3  $ng\ m^{-3}$  in October. The annual average modal diameter,  $D_{rBC,mode}$  of the rBC size distribution was 197 nm with monthly values between  $D_{rBC,mode} = 161$  nm in August and  $D_{rBC,mode} = 233$  nm in December. Weighted BC concentration trajectory analyses showed that from October to March, BC concentrations at Zeppelin were mainly influenced by source regions in northern and central Russia. From April to July the BC mass came from extreme Northern areas: North Eurasia and Northern Canada, while in August and September the BC mass concentration originated mainly from North-East Europe. Unexpected but frequent occurrence of coarse BC particles with mass equivalent diameter bigger than 300 nm were found both in the SP2 mass size distribution and in the transmission electron microscopy analysis, prevalently in

June, September, October and November. The rBC mass concentration was compared with the equivalent black carbon (eBC) mass concentration measured with the MAAP. The monthly eBC/rBC mass ratio varied between 2.9 and 4.0. The principal reason of such large discrepancy was explained with the too low  $MAC_{BC}$  value applied to the absorption coefficients measured by the MAAP to calculate the equivalent black carbon mass concentration. Another cause of this discrepancy was found to be the limited detection range of the SP2-XR, which did not allow the total detection of coarse BC particles. Indeed, the frequent presence of coarse BC particles, was found to increase the eBC/rBC mass ratio by 33 %.

# Sommario

Il black carbon (BC) è un componente dell'aerosol atmosferico molto importante nel sistema terrestre. Primo perché induce una forte forzante radiativa positiva  $RF_{BC} = +1.1 \text{ W m}^{-2} \pm 90 \%$ , attraverso due percorsi principali: interazione aerosol-radiazione ( $RF_{ARI}$ ) e interazione aerosol-nube ( $RF_{ACI}$ ). In secondo luogo, perché elevate concentrazioni di black carbon nell'aria sono un problema per la salute pubblica, in quanto possono causare allergie, malattie polmonari, cardiovascolari e morti premature. Sia per quantificare correttamente la forzante radiativa del BC, sia per l'implementazione delle normative sulla qualità dell'aria e/o sulla salute umana, è necessaria una profonda comprensione delle proprietà fisiche, ottiche e chimiche del BC, come la sua concentrazione in massa, la distribuzione dimensionale e lo stato di miscelazione (noto come mixing state). Inoltre, le misure di abbattimento delle emissioni di BC avrebbero co-benefici significativi per il miglioramento della qualità dell'aria e per contrastare il riscaldamento climatico su scala temporale breve.

Le proprietà del BC cambiano durante il suo ciclo di vita. Le particelle di BC appena emesse sono aggregati frattali composti da sferette di carbonio, fortemente assorbenti, idrofobi e non mescolati con altre sostanze. Durante l'invecchiamento atmosferico, gli aggregati frattali si mescolano internamente con altre specie di aerosol. L'invecchiamento cambia la dimensione e la composizione chimica delle particelle di BC, modificandone l'igroscopicità e la morfologia. Inoltre, è noto che l'invecchiamento aumenta la sezione d'urto di assorbimento in massa del BC (BC mass absorption cross-section -  $MAC_{BC}$ ) mediante un effetto di lente (lensing effect).  $MAC_{BC}$  è un parametro chiave per il calcolo della forzante radiativa del BC ed è definito come rapporto tra il coefficiente di assorbimento della luce causato dal BC e la concentrazione in massa del black carbon. Le proprietà del BC dipendono anche dalla sorgente: le particelle derivanti da combustione di combustibili fossili hanno generalmente diametri equivalenti in volume inferiori (70-140 nm) rispetto alle particelle prodotte da combustione di biomassa (140-200 nm).

Le particelle di BC sono ubiquitarie nell'atmosfera anche dove non è presente alcuna fonte di emissione, poiché possono essere trasportate molto lontano e raggiungere luoghi molto vulnerabili come l'Artico, innescando effetti imprevedibili. A causa della loro scarsità, le misure delle proprietà del BC in luoghi così remoti sono molto preziose per fornire le informazioni necessarie per sviluppare modelli globali di forzante radiativa degli aerosol.

Anche se negli ultimi decenni sono stati compiuti grandi progressi nella comprensione delle proprietà, del ciclo di vita e dei meccanismi di interazione con le nubi, ci sono ancora molte questioni aperte riguardo al black carbon. Durante questa tesi di dottorato, abbiamo avuto l'ambizione di affrontare alcuni dei temi più importanti attraverso campagne di misura da un'area fortemente inquinata come la Pianura Padana, nel Nord Italia, a un ambiente molto pulito e remoto, come l'Osservatorio Zeppelin, Svalbard, nel mezzo del Mar Artico.

Lo strumento principale utilizzato in ogni campagna di misura è stato il Single Particle Soot Photometer (SP2) e la sua versione più recente: il Single Particle Soot Photometer Extended Range (SP2-XR), uno strumento basato sulla tecnica dell'incandescenza. L'SP2 è diventato sempre più riconosciuto come uno strumento per quantificare le proprietà del BC refrattario (rBC) perché fornisce simultaneamente più informazioni a livello di singola particella. In primo luogo, misura in modo inequivocabile la massa di rBC nelle singole particelle di aerosol piuttosto che dedurla da misure di proprietà ottiche/di assorbimento dell'aerosol. In secondo luogo, è in grado di fornire informazioni aggiuntive come le distribuzioni dimensionali in massa e in numero di rBC e il mixing state (sia in modo qualitativo che quantitativo) delle singole particelle contenenti rBC. Terzo, poiché lo strumento rileva le singole particelle di aerosol, è in grado di quantificare la massa di rBC anche in ambienti molto puliti, come l'Artico, dove altre tecniche richiederebbero tempi di integrazione proibitivi.

Le domande di ricerca ancora insolte riguardanti la scienza del black carbon, che abbiamo affrontato durante questo lavoro di dottorato sono state le seguenti:

## 1) Misure di concentrazione in massa di black carbon

La quantificazione della concentrazione in massa di black carbon è un'attività molto complicata. Non esiste un metodo di riferimento SI (Sistema Internazionale delle unità di misura), né un adatto materiale di riferimento per quantificarla. Attualmente, la massa di BC è definita operativamente attraverso metodologie che utilizzano proprietà fisico-chimiche e/o ottiche distinte di BC al fine di quantificare la sua concentrazione di massa. Le tre tecniche più comuni sono l'analisi termico-ottica basata su collezione di particolato su filtro; i metodi basati sull'incandescenza (LII) e quelli basati sull'assorbimento della luce. I termini specifici utilizzati per fare riferimento alla massa di BC quantificata da ciascuna di queste tre tecniche sono: carbonio elementare (EC), black carbon refrattario e black carbon equivalente (eBC), rispettivamente.

L'assorbimento ottico dell'aerosol è stato a lungo utilizzato come proxy per la massa di BC, ma può essere influenzato sia dall'aerosol che assorbe alla stessa lunghezza d'onda dello strumento utilizzato (ad esempio, sabbia o brown carbon), sia dall'aumento dell'assorbimento dato dal rivestimento del BC. Inoltre, le misure della massa di eBC si basano su conoscenze a-priori o valori presunti di  $MAC_{BC}$ . Tale conoscenza preliminare non è richiesta per le misure termo-ottiche della massa di EC o per le misure della massa di rBC attraverso la tecnica LII. Molti lavori di intercomparison tra le tecniche BC sono disponibili in letteratura, ma pochissimi riguardano la massa EC e rBC. Ciò significa che il dibattito sulla comparabilità di queste due quantità è ancora in gran parte irrisolto.

Nel primo articolo, abbiamo esaminato e quantificato il livello di accordo o disaccordo tra le concentrazioni in massa di BC misurate dall'analisi termico-ottica e con la tecnica LII. A questo scopo, abbiamo confrontato le misurazioni co-localizzate delle concentrazioni in massa di EC e rBC da campagne di misura eseguite in diversi siti europei (Bologna, Cabauw, Parigi e Melpitz) per campionare diversi tipi di aerosol. Questa prima comparazione multi-sito ci ha permesso di valutare più quantitativamente con che precisione le misure della concentrazione di EC e rBC sono in accordo o in disaccordo tra loro. Inoltre, sono state discusse le potenziali ragioni di tali discrepanze come diversi tagli dimensionali, incertezze di calibrazione e possibili interferenze.

Abbiamo scoperto che l'analisi termico-ottica e la tecnica LII forniscono una misura della massa di BC in buon accordo generale. Tuttavia, in alcuni siti sono state osservate discrepanze sistematiche fino a  $\pm 50\%$ . La mediana dei rapporti di massa osservati tra rBC e EC per l'intero set di dati era 0.92, con una GSD di 1.50. Il rapporto mediano variava da 0.53 a 1.29 da campagna a campagna. Le potenziali ragioni delle discrepanze erano: la risposta SP2 specifica per sorgente, la possibile presenza di particelle di BC al di sotto dell'LDL dell'SP2, differenze nel cut-off superiore dell'SP2 e nella linea di ingresso per il campionamento EC, o nel caso dell'EC varie incertezze e interferenze da specie co-emesse. La discrepanza tra rBC e EC sembra essere sistematicamente correlata alla sorgente di BC, ovvero traffico rispetto alla combustione di legna e/o carbone. Tuttavia, non è stato possibile identificare le cause alla base di questa tendenza a causa di potenziali correlazioni incrociate tra diversi tipi di aerosol e proprietà del BC, rilevanti per poter distinguere potenziali bias.

## 2) La relazione tra le proprietà $MAC_{BC}$ e BC

La comprensione scientifica dei fattori che determinano la variabilità di  $MAC_{BC}$  rimane inadeguata e contribuisce alla grande incertezza associata alla quantificazione della forzante climatica del BC. L'assorbimento della luce da parte del BC mescolato esternamente è ragionevolmente ben caratterizzato, ma il mixing interno tra BC e altri componenti dell'aerosol attraverso processi come la condensazione del gas e la coagulazione può aumentare l'assorbimento da parte del BC. L'impatto del mixing interno non è ben compreso, con disparità tra le osservazioni di laboratorio e gli studi sul campo. Gli studi di laboratorio mostrano tipicamente un forte aumento nell'assorbimento della luce da parte del BC, spesso di un fattore due o più per quantità di rivestimento sufficientemente grandi. Tuttavia, l'aumento dell'assorbimento da parte del BC varia tra gli studi sul campo, con diversi studi che mostrano un aumento dell'assorbimento molto più debole per quantità di rivestimento medie simili. Questa discrepanza tra laboratorio e ambiente si traduce in ambiguità nelle rappresentazioni dei modelli di assorbimento da parte di particelle contenenti BC e, quindi, incertezza nelle previsioni del modello di riscaldamento atmosferico causato dal black carbon.

Sebbene l'intervallo dei valori di  $MAC_{BC}$  della letteratura sia coerente con le osservazioni più recenti, lo spread rimane piuttosto ampio. La variabilità di  $MAC_{BC}$  può essere principalmente spiegata con la variabilità nelle proprietà fisiche e ottiche del BC come: mixing state, dimensione del nucleo di BC, morfologia delle particelle e indice di rifrazione. Tuttavia, dipende anche dalle tecniche di misurazione utilizzate per la concentrazione in massa del BC e per il coefficiente di assorbimento, che possono avere grandi incertezze.

Nel secondo articolo, abbiamo studiato la variabilità spazio-temporale del  $MAC_{BC}$  e la sua relazione con mixing state e il diametro del nucleo BC nella Pianura Padana, in Italia durante il periodo estivo. Inoltre, abbiamo fornito un quadro generale delle proprietà fisico-ottiche del BC più rilevanti, come la concentrazione in massa di rBC, concentrazione in massa di EC, distribuzione dimensionale della massa di rBC, coefficiente di assorbimento del BC, esponente di Ångström di assorbimento e albedo a dispersione singola.

I nostri risultati hanno mostrato che la piccola variazione dei diametri del nucleo di BC trovata durante la campagna non era in grado di spiegare la più ampia variabilità nei valori di  $MAC_{BC}$  osservati, che è stata spiegata meglio con la variabilità del mixing state del BC. Questo risultato fornisce la conferma sperimentale che il lensing effect può aumentare sostanzialmente il MAC del black carbon fino a un fattore di quasi 2. Tuttavia, mentre questo studio fornisce una chiara evidenza degli effetti del mixing state del BC sul  $MAC_{BC}$ , i valori di  $MAC_{BC}$  osservati rimangono contaminati dall'incertezza dovuta alla mancanza di tecniche di misurazione accurate della massa di BC. In effetti, in questo studio, i valori  $MAC_{BC}$  basati sulle concentrazioni di massa di rBC erano del 35% più alti di quelli basati sulle concentrazioni di massa EC. Inoltre, lo studio delle proprietà fisico-ottiche rilevanti del black carbon nella Pianura Padana, ha evidenziato che la Pianura Padana, in estate, contiene un insieme di particelle di BC invecchiate in cui si mescolano le emissioni di BC fresche su brevi scale temporali e spaziali.

### 3) Misure a lungo termine delle proprietà del BC nell'Artico

La descrizione degli impatti del BC sul clima e sulla qualità dell'aria nell'Artico richiede un'accurata comprensione delle proprietà ottiche e microfisiche del BC, dell'interazione aerosol-nube del BC, della deposizione umida e secca, e delle sorgenti. In particolare, l'analisi della variabilità temporale del BC può aiutare a comprendere come i cambiamenti climatici e le attività antropogeniche influenzino il BC. La concentrazione atmosferica di BC nella regione artica è controllata dalle emissioni di BC alle alte e medie latitudini, dalla meteorologia locale e dalla circolazione su larga scala, e dall'efficienza di rimozione del BC attraverso la deposizione umida e secca, che a loro volta sono controllate dalle proprietà microfisiche e dalla meteorologia. Una migliore comprensione di tutti i fattori che controllano la concentrazione atmosferica di BC è un elemento chiave per migliorare la capacità dei modelli di descrivere l'impatto del BC sul clima e ridurre l'incertezza dei futuri scenari climatici. Inoltre, aumentare la copertura temporale delle misure di BC, specialmente durante l'inverno su scala globale e regionale, migliorerebbe la conoscenza dell'impatto climatico del BC nell'Artico.

Le osservazioni a lungo termine alle Svalbard fanno uso di tecniche ottiche su filtro per dedurre la concentrazione di massa BC, come il multi-angle absorption photometer, il photoacoustic absorption photometer e l'Aethalometro. Tuttavia, il coefficiente di assorbimento calcolato con questi strumenti può essere soggetto a grandi incertezze, a causa di effetti di dispersione (multiple scattering effect) ed eccessivo carico del filtro (filter loading effect). Un'incertezza aggiuntiva risulta dalla conversione empirica del coefficiente di assorbimento nella concentrazione in massa di BC equivalente utilizzando un valore di  $MAC_{BC}$  assunto. Grazie al recente sviluppo del Single Particle Soot Photometer, sono state avviate misurazioni dirette del black carbon refrattario anche nell'Artico. Tuttavia, le misurazioni SP2 nell'Artico sono ancora scarse. Migliorare la comparabilità e l'accuratezza delle misurazioni atmosferiche di BC, comprendendo le differenze tra i diversi metodi di monitoraggio, è una necessità urgente nell'Artico.

Per rispondere alla necessità di una caratterizzazione più completa e di serie temporali più lunghe delle proprietà del black carbon nell'Artico, abbiamo misurato le concentrazioni in massa di rBC e le distribuzioni dimensionali in massa di rBC presso l'Osservatorio Zeppelin nelle isole Svalbard, Norvegia, da Aprile 2019 a Marzo 2020. Le misure sono state eseguite con un Single Particle Soot Photometer Extended Range, la

versione più compatta dell'SP2. Per la prima volta in questo lavoro, l'SP2-XR è stato utilizzato per una campagna di monitoraggio remoto a lungo termine. Inoltre, sono state utilizzate analisi della traiettoria (back-trajectories) per stimare le sorgenti di BC. Infine, abbiamo confrontato le concentrazioni di massa di rBC con quelle derivate dal MAAP per indagare sul loro accordo o disaccordo.

Lo studio della variabilità temporale della concentrazione in massa di black carbon refrattario e della distribuzione dimensionale della massa di rBC hanno mostrato una media annuale e mediana della massa di rBC di 8.0 e 3.8 ng m<sup>-3</sup> rispettivamente; mentre le medie mensili variavano da un massimo di 24.7 ng m<sup>-3</sup> a Febbraio, a un minimo di 2.3 ng m<sup>-3</sup> a Ottobre. Il diametro modale medio annuale,  $D_{\text{rBC,mode}}$ , della distribuzione dimensionale di rBC era di 197 nm con valori mensili compresi tra  $D_{\text{rBC,mode}} = 161$  nm in Agosto e  $D_{\text{rBC,mode}} = 233$  nm a Dicembre. Le analisi delle traiettorie pesate con la concentrazione in massa di rBC, hanno mostrato che da Ottobre a Marzo, le concentrazioni di BC allo Zeppelin Observatory erano principalmente influenzate dalle regioni con origine in Russia settentrionale e centrale. Da Aprile a Luglio la massa di BC proveniva dalle zone estreme del Nord: Nord Eurasia e Canada settentrionale, mentre in Agosto e Settembre la concentrazione in massa di BC proveniva principalmente dall'Europa nord-orientale. La presenza inaspettata ma frequente di particelle BC grossolane con un diametro equivalente di massa (mass equivalent diameter) maggiore di 300 nm è stata riscontrata sia nella distribuzione dimensionale di rBC dell'SP2-XR che nell'analisi al microscopio elettronico a trasmissione, prevalentemente in Giugno, Settembre, Ottobre e Novembre.

La concentrazione di rBC è stata confrontata con la concentrazione in massa di eBC misurata con il MAAP. Il rapporto mensile eBC/rBC variava tra 2.9 e 4.0. La ragione principale di tale grande discrepanza è stata spiegata con un troppo basso valore  $\text{MAC}_{\text{BC}}$  applicato ai coefficienti di assorbimento misurati dal MAAP per calcolare la concentrazione in massa di eBC. Un'altra causa di questa discrepanza è stata riscontrata nel limitato range di rilevamento dell'SP2-XR, che non consentiva il rilevamento totale di particelle BC grossolane. In effetti, è stato riscontrato che la frequente presenza di particelle BC grossolane aumentava il rapporto di massa eBC/rBC del 33%.

# Chapter 1: Introduction

## 1.1 The Earth's climate

Climate is usually described in terms of the statistical properties (i.e. mean and variability) of parameters such as temperature, humidity, precipitation and wind, over a period of time, ranging from months to millions of years (the typical period to characterize the climate system is 30 years). The Earth's climate is the result of the properties and interaction of five major components of the climate system: the atmosphere (air), the hydrosphere (including the oceans and all other reservoirs of water in liquid form), the cryosphere (ice and permafrost), the lithosphere (earth's upper rocky layer) and the biosphere (living organisms).

### 1.1.1 Global energy balance and natural climate forcings

Climate change is governed by changes to the global energy balance. The energy that drives the climate system comes from the Sun, located at around  $150 \times 10^6$  km from the Earth. The annual average radiative solar flux reaching the top of the Earth's atmosphere is called solar constant and is approximately  $1360 \text{ W m}^{-2}$  (Dines, 1917). The total amount of energy received per second at the top of the Earth's atmosphere is given by the solar constant times the surface area of the Earth divided by the cross-sectional area of the Earth irradiated by the Sun, which corresponds to one quarter of the solar constant (approximately  $340 \text{ W m}^{-2}$ ). Part of this energy does not reach the surface of the Earth since it is reflected back to space by clouds and the atmosphere; the remaining fraction is absorbed by the Earth's surface or the atmosphere. The energy that reaches the Earth's surface is then re-emitted as long-wave (infrared) radiation. Part of this re-emitted energy is absorbed by clouds and atmospheric gases (such as carbon dioxide,  $\text{CO}_2$ ; methane,  $\text{CH}_4$ ; water vapor,  $\text{H}_2\text{O}$  or nitrous oxide,  $\text{N}_2\text{O}$ ) and then re-emitted again in all directions: this process is known as “greenhouse effect” and keeps the Earth at a habitable temperature (Stephens et al., 2012).

The climate system evolves under the influence of its own internal dynamics and due to changes in external factors that affect the Earth's surface temperature, called “climate forcings”. Natural external forcings include phenomena such as volcanic eruptions, solar activity variations, e.g., the Milankovitch cycles (the changing of the Earth's eccentricity, obliquity and precession), the motion of tectonic plates, the orbital dynamics of the Earth-Moon system and changes in the atmospheric chemical composition.

The cyclic nature of these forcings brought the Earth to undergo different ice age cycles, which are cold glacial periods followed by shorter warm periods (called “interglacial periods”). In the past 740,000 years there have been eight cycles of glacial advance and retreat (EPICA community members, 2004). The last ice age ended about 11,700 years ago and marked the beginning of the modern climate era and of human civilization (Severinghaus, 1999).

### 1.1.2 The climate forcings from the preindustrial era

At present, we are living in an interglacial period, the Holocene, and according to the natural climate forcings, the next glacial period should begin in around 50,000 years. However, the sharp increase in human activities during the last 100–1000 years (Fig. 1.1), which has caused a sharp and accelerating increase in atmospheric greenhouse gases trapping the Sun's heat, may prevent the next glacial period (IPCC, 2013; Ganopolski et al., 2016).

Each of the last three decades has been successively warmer at the Earth's surface than any preceding decade since 1850. The period from 1983 to 2012 was likely the warmest 30-year period of the last 1400 years in the Northern Hemisphere (IPCC, 2013). The globally averaged combined land and ocean surface temperature data as calculated by a linear trend, show a warming of  $+0.85$  ( $+0.65$  to  $+1.06$ )  $^\circ\text{C}$  over the period 1880 to 2012 (Fig. 1.1). The  $\text{CO}_2$  and  $\text{CH}_4$  concentrations have increased by 40% and 150% since 1790 (Lüthi et al., 2008; MacFarling Meure et al., 2006; IPCC, 2013) (Fig. 1.1). However, greenhouse gases are not the only climate forcings of this era.



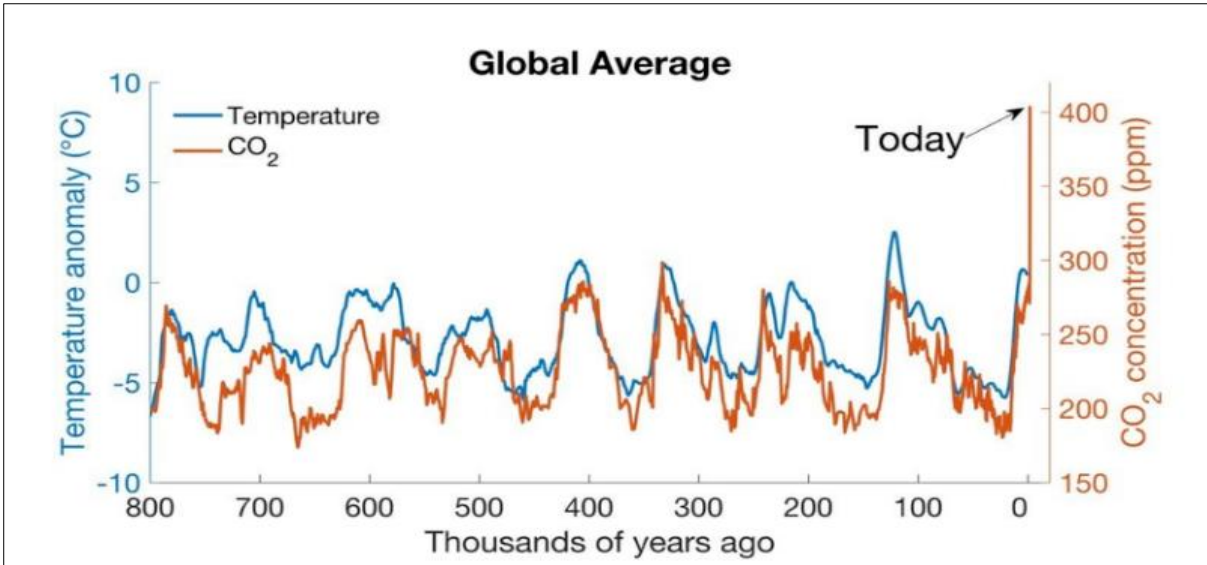


Figure 1.1: Time series of global average temperature and CO<sub>2</sub> concentration from the data by Parrenin et al., 2013; Bereiter et al., 2015; Snyder, 2016 (Image credits: Ben Henley and Nerilie Abram/The Conversation).

The Radiative Forcing (RF) is defined as the change in the net radiative flux due to a change in an external driver, also called a forcing agent or a climate forcer. A forcing is positive when it is related to an incoming energy that exceeds the outgoing energy, resulting in a warming, and vice-versa. Moreover, the recently introduced Effective Radiative Forcing (ERF) takes into account rapid adjustments to perturbations. The individual forcing caused by each climate forcer has been isolated and reported in the last assessment report of the IPCC (IPCC, 2013). Since the great majority of anthropogenic emissions occurred after the beginning of the industrial revolution, during the second half of the 18<sup>th</sup> century, the forcings are compared to the year 1750 (Fig. 1.2).

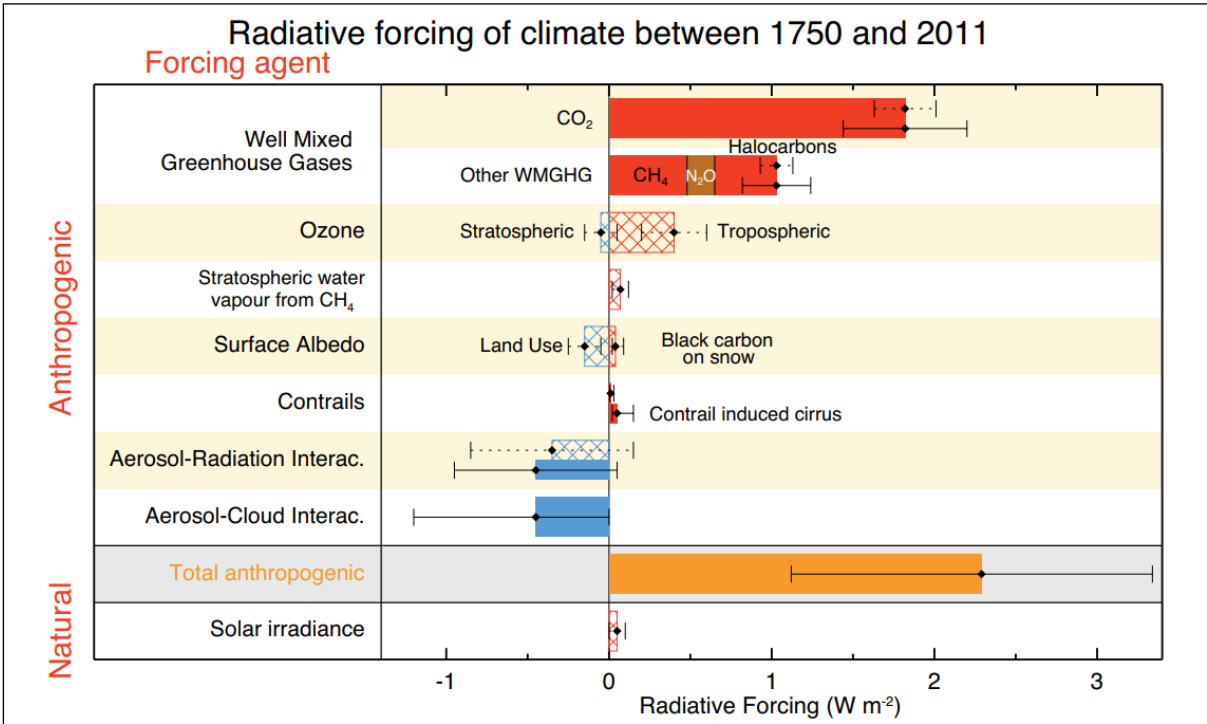


Figure 1.2: Radiative forcing contribution of the various forcing agents between 1750 and 2011 with associated uncertainty range (solid bars are ERF, hatched bars are RF, associated uncertainties are for RF assessed in AR4) (IPCC, 2013).

In addition to GHGs, aerosol particles (definition in Sect. 1.2) are very likely playing a role in climate change. In general, anthropogenic gas emissions have a warming effect while aerosol particles, induce a cooling. When accumulated, the effects of all forcings result in a warming of the climate system since 1750, with an effective forcing of  $2.3 \text{ W m}^{-2}$  (Fig. 1.2). A striking point is that the large 5 to 95% confidence range attached to this number ( $1.1$  to  $3.3 \text{ W m}^{-2}$ ) is mainly caused by the uncertainties on the forcing due to aerosols.

### **1.1.3 Impacts, vulnerability, adaptation and mitigation of climate change**

Even if this global mean temperature increase seems to be rather small, the sensitivity of the climate system and ecosystems is such that this temperature anomaly was found to be responsible for various types of threats and damages. Indeed, global warming is substantially influencing the ecosystems. All five components of the system are affected by climate change and respond in various ways, e.g., increased frequency and intensity of heat waves and droughts, stronger and more frequent extreme rainstorms, sea level rise, enhanced acidification of the oceans, surface melting of ice caps, animal migration, more frequent forest fires and desertification and accelerated biodiversity loss, just to mention some. Climate change has an effect also on the human beings through increased mortality and morbidity. Moreover, climate change increases people's exposure to natural hazards (floods, heat waves cyclones, erosion, ...); generally, this affects more the poor people or those who live in conflict areas (IPCC, 2013).

While the above-mentioned changes of the climate system have already been observed, a large amount of studies aimed at estimating their evolution in the near future. Unsurprisingly, all changes are expected to intensify, and the negative impacts observed on the living world are expected to escalate. However, the overall risk of climate change impacts can be reduced by limiting the rate and magnitude of climate change. This means that to achieve scenarios that estimate concentration levels of 450 ppm equivalent  $\text{CO}_2$  by 2100 (to keep the temperature change below the  $2 \text{ }^\circ\text{C}$  relative to the pre-industrial era) we should cut the anthropogenic greenhouse gas emissions by mid-century through large-scale changes in all systems. A tremendous effort needs to be committed in order to mitigate the impacts of global warming; the two main strategies being the reduction of anthropogenic emissions of greenhouse gases and the improvement of the performance of carbon sinks.

Several international treaties and mitigation strategies have emerged in the last decades. The United Nations Framework Convention on Climate Change (UNFCCC) entered into force in 1994 with the objective to reduce the risks of anthropogenic climate change by stabilizing the atmospheric concentration of greenhouse gases. The organization has become the main forum focusing on climate change mitigation. Every year since 1995, the parties of the UNFCCC have met in the Conference of Parties (COP) to evaluate the progress and fix new objectives. During the COP21 in 2015, the Paris Agreement was ratified, specifying that the increase in global average temperature should be kept below  $2 \text{ }^\circ\text{C}$  and ideally below  $1.5 \text{ }^\circ\text{C}$ , relative to the preindustrial era. To meet the GHG target reduction (without considering the aerosols' role), cuts in emissions of 7.6 % per year from 2020 to 2030 to meet the  $1.5^\circ\text{C}$  goal and 2.7 % per year for the  $2^\circ\text{C}$  goal should be realized.

In this context also the aerosol emissions play a large role in determining the near-term allowable greenhouse gas emissions that will limit future warming to  $2 \text{ }^\circ\text{C}$ , however in the long term, drastic GHG emissions reductions are required under any reasonable aerosol scenario. Larson and Portmann (2019) estimated that, with large future aerosol emissions, similar to present day amounts, GHG emissions need to be reduced by 8 % by 2040 and by 74 % by 2100 to limit warming to  $2 \text{ }^\circ\text{C}$ . Under a more likely low aerosol scenario, GHG emissions need to be reduced by 36 % and 80 % by 2040 and 2100, respectively.

## **1.2 Atmospheric aerosols: definition, properties and effects**

The atmospheric aerosol is a polydisperse collection of solid and liquid particles suspended in the atmosphere, each one maintaining its physical-chemical properties long enough to allow their observation and measurement (Seinfeld and Pandis, 2006). The term "aerosols" is often used for indicating only the aerosol particles. We will use this latter terminology in the thesis. In the last decades, the atmospheric aerosol (also called particulate matter - PM) has raised increasing interest due to its impacts on both the environment and human health (Cao, 2017; Davidson et al., 2005; Fuzzi et al., 2015).

In particular, aerosols can:

- affect the Earth's radiative balance, via its optical properties (scattering and absorption - direct effect) (Moosmüller et al., 2009; Pandolfi et al., 2018) and by changing clouds' lifetime and albedo (indirect effect) (Twomey, 1974);
- act as cloud and ice condensation nuclei (McFiggans et al., 2006; Andreae and Rosenfeld, 2008);
- be a catalyst in chemical reactions taking place in the atmosphere (e.g., Sørensen et al., 2002);
- cause water and soil pollution via dry and wet deposition processes (Barrie and Schemenauer, 1986);
- impair visibility (Appel et al., 1985) and damage cultural heritage (Bonazza et al., 2016)
- be detrimental for human health, entering the respiratory tract and reaching other parts of the body (Dockery et al., 1993; Krewski et al., 2009; Pope et al., 2002).

### 1.2.1 Sources, formation, and life cycle

Atmospheric aerosols are part of a very complex system; they are generated by many different sources and emission processes and they show a significant heterogeneity in terms of chemical composition, size, shape and residence time. They are ubiquitous in the atmosphere but in extremely variable concentrations. The spatial and temporal distribution of aerosols strongly depends on the distribution of sources and sinks and how these interact with their transport in the atmosphere.

Sources of atmospheric aerosol can be natural or anthropogenic. Natural aerosol sources comprise seas and oceans (with produce sea spray), deserts (mineral dust), soil, volcanoes and forests (Fitzgerald, 1991; Durant et al., 2010; Knippertz and Todd, 2012). Among major sources of anthropogenic particles are: energy production, traffic, industrial activities, and domestic heating in urban and industrial areas; biomass burning, livestock and agricultural manure at rural sites. On a global scale, natural aerosol is significantly more abundant (by about one order of magnitude) than anthropogenic ones (Viana et al., 2014). Nevertheless, the percentage of atmospheric particles produced by human activities can increase significantly and become comparable to the one of natural aerosol in densely populated and heavily industrialized areas (Gelencsér et al., 2007).

When aerosol particles are directly emitted into the atmosphere by the sources, they are called primary aerosols. Secondary aerosols are instead the aerosols formed by gas-to-particle conversion. Formation and evolution in time of natural and anthropogenic aerosols are influenced by transitions from the gas phase to the condensed phase. In the formation of a condensed phase from the vapor, three processes are relevant: nucleation, condensational growth, and coagulation.

Nucleation is the transformation of matter from one phase to another phase through the formation of nuclei. For atmospheric aerosols, nucleation refers to the transformation of gas-phase molecules into a cluster of molecules called "aerosol nucleus". The nucleation can be homogenous or heterogeneous. Homogeneous nucleation is the formation of particles from a super-saturated vapor without any condensation nuclei. Otherwise, heterogeneous nucleation leads to the formation of particulate material from a super-saturated vapor in presence of condensation nuclei (Dunning, 1960). This process is more commonly called condensation and is the most important mechanism causing mass transfer from the gaseous to the particulate phase. Growth by condensation takes place when molecular clusters formed by nucleation processes become larger than a critical size: stable atmospheric particles formed this way can increase in size due to condensation of vapor on their surface (Wagner, 1982). Opposite to condensational growth, evaporation leads to more molecules leaving the surface of a particle compared to those that attach to it (Nomura et al., 2000). Finally, coagulation takes place when two particles join together to form a unique and larger particle (Ramabhadran et al., 1976). Consequently, the particle number decreases, and the average diameter increases.

Finally, atmospheric aerosol is removed from the atmosphere via two different deposition pathways: dry deposition and wet deposition. Dry deposition happens when particles are transported to a surface and are then retained by it. Wet deposition, comprises: fog deposition, when particles get embedded in fog or mist droplets; rain-out, i.e. aerosol deposition caused by processes occurring in clouds, where particles serve as condensation

nuclei for water droplets or ice crystals, and wash-out, when aerosol particles are removed below clouds, where they are captured by precipitation (Seinfeld and Pandis, 2006).

During their life-cycle, aerosol particles undergo various atmospheric processing mechanisms which modify their own characteristics, depending also on their native properties such as size and chemical composition, and determine their residence time in the atmosphere. In the following sections, the physical, optical and chemical properties of aerosols will be briefly discussed.

### 1.2.2 Physical properties

Atmospheric aerosols are largely variable in terms of shape which is related to the particle formation pathway. For instance, natural aerosol has usually an irregular shape, whereas anthropogenic particles (especially those produced by high temperature combustion processes) are typically spherical and smaller. Another fundamental aerosol physical feature is the size. Due to the irregular shape of the particles one typically uses equivalent diameters (based on specific aerosol characteristics) in order to describe particles and compare them. Some of the most commonly used equivalent diameters (and the ones used in this thesis work) are:

- Aerodynamic diameter ( $D_{ae}$ ): equivalent diameter of a spherical particle of unit density having the same inertial properties (i.e., the same terminal settling velocity) as the actual particle.
- Volume equivalent diameter ( $D_{veq}$ ): the diameter of a sphere of the same volume as that of the actual particle.
- Optical diameter ( $D_{opt}$ ): equivalent diameter of a spherical particle having the same refractive index as the one of the particles used for the calibration of the optical instrument adopted to determine an aerosol size distribution, that scatters the same amount of light in the measured angle.

The aerosol size distribution is a key property affecting the particles' physical behavior. Since atmospheric aerosols cover a wide range of diameters (from a few nanometers to around 100  $\mu\text{m}$ ), size distributions are usually represented as a function of the logarithm of the diameter itself. Size distributions can be expressed in terms of number, surface area, volume or mass of particles.

An atmospheric aerosol size distribution can be represented by the sum of lognormal distributions, each associated to specific formation, transformation, and deposition processes. For example, the analytical lognormal mass size distribution function is defined as:

$$\frac{dm}{d\ln D_p} = \frac{m}{\ln \sigma_g \sqrt{2\pi}} \exp \left[ -\frac{1}{2} \left( \frac{\ln D_p - \ln \bar{\sigma}_g}{\ln \sigma_g} \right)^2 \right] \quad (1.1)$$

where  $m$  is total particle mass ( $\mu\text{g m}^{-3}$ ),  $D_p$  is the particle diameter,  $\sigma_g$  is the geometric mean diameter, and  $\bar{\sigma}_g$  is the geometric standard deviation.

Depending on particle size, atmospheric aerosols can be classified according to different conventions. Major classifications are based on modes or sampler cut-point. The modal classification ideally divides aerosol particles according to the modal structure of their size distribution (Fig. 1.3):

- Nucleation mode: particles with a diameter of about 10 nm. These particles are formed by nucleation processes from low-volatility vapors and are rapidly removed by coagulation through Brownian motion (resulting in bigger particles);
- Aitken mode: particles with diameters in the range 0.01-0.1  $\mu\text{m}$ . These particles are mainly produced by high temperature combustion and coagulation of smaller particles; they are removed by coagulation;
- Accumulation mode: particles with diameters in the interval 0.1-1  $\mu\text{m}$ . Typical formation processes are combustion, coagulation, and chemical reactions, whereas rain-out and wash-out are common removal pathways in this size range. The accumulation mode is usually divided into two sub-modes: the condensation mode, containing particles growing by condensation, and the droplet mode, with particles that typically represent evaporated droplets after aqueous phase chemistry.

- Coarse mode: particles with diameter larger than 1  $\mu\text{m}$ . Typically with natural origin and mechanically generated. These particles experience negligible diffusion and, due to their higher weight, the removal takes place mainly by gravitational settling.

Classification based on cut-points arises from the sampling of aerosol in a specific size range. Size-selective aerosol samplers are characterized by their 50 % cut point size, i.e., the aerodynamic diameter (in  $\mu\text{m}$ ) at which half of the particles penetrate and the remaining half is rejected. These samplers are commonly used for research and monitoring purposes, and the aerosol size fractions sampled are named  $\text{PM}_x$ , where "x" is the maximum aerodynamic diameter of the considered aerosol population. Following European air quality standards, regulated aerosol fractions are  $\text{PM}_{2.5}$ , i.e., particles with  $D_{ae} < 2.5 \mu\text{m}$ , and  $\text{PM}_{10}$ , i.e., the fraction of particles with  $D_{ae} < 10 \mu\text{m}$ . In this thesis, we will refer to these fractions in Chapter 3.

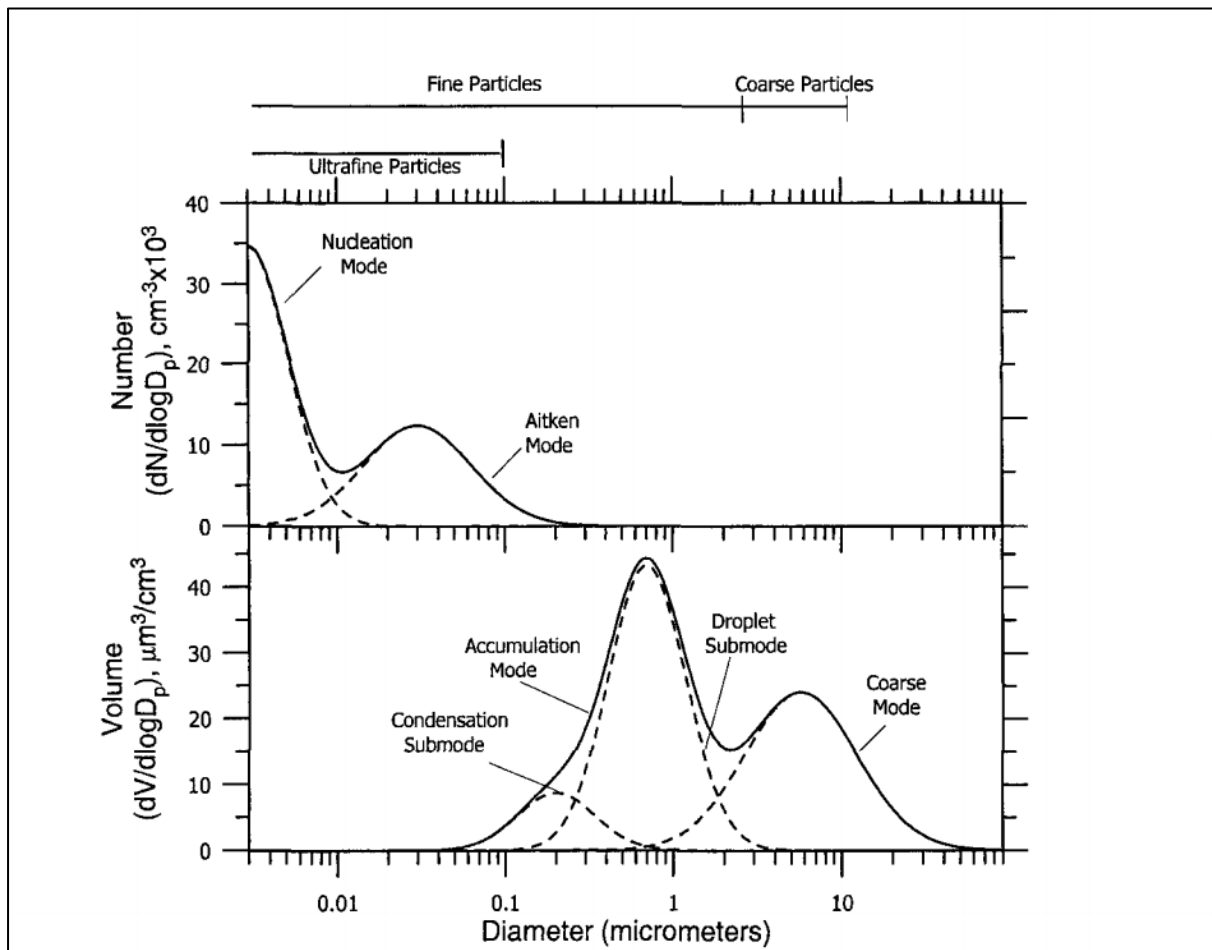


Figure 1.3: Terminology used to describe the modes of atmospheric aerosols (McMurry et al., 2004).

### 1.2.3 Optical properties

The scattering and absorption of light by atmospheric particles are phenomena of great importance because they modify the transfer of solar energy into the atmosphere thus influencing climate change and visibility (Moosmuller et al., 2008).

When a radiation beam of a given intensity  $I_0$  hits an aerosol particle, it causes excitement of its electric charges which are placed in oscillation: these can re-radiate energy in all directions (scattering or diffusion) and convert part of the light energy into thermal energy with subsequent heating of the particles and the environment surrounding (absorption). The law of conservation of energy requires that the light that is removed from the incident beam by the particles, called extinction,  $W_{ext}$ , is equal the sum of the scattered and absorbed parts. The ratio  $W_{ext}/I_0$  is a quantity (unit:  $\text{m}^2$ ) and is called extinction cross section  $\sigma_{ext}$ ; the same holds for scattering and

absorption. For an ensemble of  $n$  particles, the extinction coefficient  $b_{\text{ext}}$  (unit:  $Mm^{-1}$ ) is the sum of individual single  $i$  particle extinction cross sections  $\sigma_{\text{ext},i}$  divided by the volume  $V$  (unit:  $m^3$ ) occupied by the particle ensemble. The extinction coefficient is given by the sum of the scattering and absorption coefficients:

$$b_{\text{ext}} = b_{\text{sca}} + b_{\text{abs}} \quad (1.2)$$

The fraction of light extinction that is due to scattering is called single scattering albedo and in case of a particle ensemble is calculated as follows:

$$\text{SSA} = \frac{b_{\text{sca}}}{b_{\text{ext}}} = \frac{b_{\text{sca}}}{b_{\text{sca}} + b_{\text{abs}}} \quad (1.3)$$

Light extinction depends on the chemical composition of the particle and the surrounding medium, particle size, the wavelength and the polarization state of the incident light, and the shape of the particle (Bohren and Huffman, 1983). Since the analytical solution of the problem of the interaction of light with a particle is very complex, usually a linearly polarized plane electromagnetic wave incident on a spherical particle is assumed. With this assumption of a linearly polarized plane electromagnetic wave incident on a spherical particle, the parameters regulating scattering and absorption by a particle are:

- wavelength  $\lambda$  of the incident radiation;
- size (i.e., particle diameter  $D_p$ ), which is usually included in the so-called size parameter:  $x = \pi D_p / \lambda$ ;
- complex refractive index  $m = n - ik$ , where both terms (real part  $n$  and imaginary part  $k$ ) are functions of the wavelength; the real and imaginary parts at first order approximation are related to the non-absorbing and absorbing behavior of a particle, respectively.

The theory that solves the classical problem of the interaction of light with a spherical particle is the Mie-Debye-Lorentz theory (hereafter called Mie theory). It describes scattering and absorption by a particle of arbitrary size (i.e.  $x$ ) and composition (i.e.  $m$ ) expanding the electromagnetic field inside and outside the particle in vector spherical harmonics and then solving Maxwell's equations with appropriate boundary conditions. The Mie theory gives a complete picture of the phenomena arising from the interaction of radiation with a particle. An extensive discussion of the possible solutions is reported e.g., by Bohren and Huffman (1983).

Depending on the size parameter  $x$ , three light scattering regimes can be identified:

- Rayleigh scattering: the particle is very small compared to the wavelength of the incident light ( $x \ll 1$ );
- Mie scattering: particle size and wavelength of incident radiation are comparable ( $x \approx 1$ );
- Geometric scattering: the particle is large compared to the wavelength ( $x \gg 1$ ).

In the Rayleigh scattering regime (for instance, when  $D_p < 0.1 \mu\text{m}$  in the visible range), it is possible to give an approximate solution of the scattering problem. In this regime, the angular distribution of scattered light is symmetrical in the forward and backward hemispheres and more or less independent of particle shape. For a particle with size comparable to the wavelength of the incident light, no simplifications can be made to solve the problem: therefore, the exact solutions of Maxwell's equations must be found to compute the scattering, absorption, and extinction cross sections. When the particle size is much larger than the wavelength of the incoming light, its optical properties can be described using geometric optics principles of reflection, refraction, and diffraction.

Although not always explicitly indicated, all optical properties are dependent on the wavelength of the incident radiation. The wavelength dependencies of some of the optical parameters defined are important to identify specific aerosol features. Extinction, scattering, and absorption coefficients generally depend on  $\lambda$  following a power law, where the exponents are called extinction, scattering, and absorption Ångström exponents, respectively: EAE, SAE, and AAE. Therefore, considering a wavelength pair  $\lambda_1$  and  $\lambda_2$ , the wavelength dependence follows (for absorption) the following equation:

$$\frac{b_{\text{abs},1}(\lambda_1)}{b_{\text{abs},2}(\lambda_2)} = \left(\frac{\lambda_1}{\lambda_2}\right)^{-\text{AAE}} \quad (1.4)$$

Where  $b_{\text{abs},1}$  and  $b_{\text{abs},2}$  are the aerosol absorption coefficients at the wavelengths  $\lambda_1$  and  $\lambda_2$ .

Another very important aerosol optical property is the mass absorption cross-section (or mass absorption coefficient) (MAC) calculated at a certain wavelength  $\lambda$ . For a certain aerosol component  $x$ , the MAC is given by the ratio between the absorption coefficient,  $b_{\text{abs}}$  and the mass concentration of the component  $x$ ,  $m_x$ , as follows:

$$\text{MAC}(\lambda) = \frac{b_{\text{abs}}(\lambda)}{m_x} \quad (1.5)$$

We will extensively talk about the MAC of black carbon particles,  $\text{MAC}_{\text{BC}}$ , (Sect. 1.3) in Chapter 4.

#### 1.2.4 Chemical properties

The chemical composition of aerosols is a key parameter for two main reasons: first, it is crucial for the aerosol toxicity (Tsai et al., 2000), second it controls the hygroscopicity of the aerosol (i.e. its ability to take up water and grow in size as ambient relative humidity increases) and thus its removal processes (Gysel et al., 2007).

The atmospheric aerosol composition is a mixture of inorganic compounds (sulfates, nitrates, and ammonium), organic material, elemental carbon, crustal species, sea salt, metal oxides, hydrogen ions and water. In the present-day atmosphere, the majority of sulfate, nitrate, ammonium and elemental carbon originate from anthropogenic sources; organic compounds have both substantial anthropogenic and natural sources (Calvo et al., 2013).

The chemical components of aerosols can be externally mixed (particles are chemically pure and the mixture is comprised of particles of different chemical composition) or internally mixed (different chemical species are mixed within each particle). In general, primary emissions are more likely to contain externally mixed particles. Aging and particle processing in the atmosphere result in increased internal mixing.

Internal mixing can affect the optical properties of a particle. As we mentioned in Sect. 1.2.3, different aerosols absorb and scatter radiation in different ways and mixing different elements together within the same particle can alter the refractive index,  $m$ . Specifically, both sulfate and nitrate scatter radiation across the solar spectrum (Pandolfi et al., 2018). Organic aerosols include thousands of different compounds, some of which only scatter solar radiation and some, called brown carbon, can also absorb solar radiation in the UV-Vis region (Andreae and Gelencsér, 2006). However, black carbon particles (for definition see Sect. 1.3) dominate aerosol light absorption. Black carbon particles can become coated with nitrate, sulfate or organics and this leads to an increase of the particle's overall absorption efficiency (Liu et al., 2015b) (Sect. 1.3.2). This effect, known as lensing effect, will be extensively treated in Chapter 4.

#### 1.2.5 Impact on climate

Aerosol optical properties have effects both at global scale on the Earth radiation balance and at local scale on visibility. The effect of atmospheric components on the Earth radiation balance is quantified by the RF (see definition in Sect. 1.1.2). Atmospheric aerosols affect the Earth's radiation balance both directly via scattering and absorption of radiation, and indirectly acting as cloud condensation nuclei (CCN) and ice nuclei (IN), with impacts on cloud albedo and lifetime. These effects on RF are called  $\text{RF}_{\text{ARI}}$  (aerosol-radiation interaction) and  $\text{RF}_{\text{ACI}}$  (aerosol-cloud interaction), respectively. Nevertheless, it is noteworthy that the estimate of RF due to aerosol and its precursors is still affected by a large uncertainty (Fig. 1.2): the best estimate of  $\text{RF}_{\text{ARI}} + \text{RF}_{\text{ACI}}$  is  $-0.9 \text{ Wm}^{-2}$  ( $-1.9 - 0.1 \text{ Wm}^{-2}$ ), attributed with medium confidence (IPCC, 2013).

$\text{RF}_{\text{ARI}}$  is characterized by the modification of the radiative forcing caused by the scattering and absorption of anthropogenic aerosol particles. Particles absorb and scatter solar radiation to different extents depending on their optical properties (Sect. 1.2.3). As we have seen in Sect. 1.2.4, the optical properties of a population of aerosols

depend on the size distribution and the refractive index (which in turn depends on the mixing state and chemical composition of the single particles).

$RF_{ACI}$  is characterized by the modification of radiative forcing caused by the interaction between the anthropogenic aerosol particles and clouds. A cloud forms when the air becomes supersaturated, which occurs when an air mass is cooled to its dew point or when the quantity of water vapor in an air mass increases. As explained in Sect. 1.2.1, aerosol particles provide a surface onto which water vapor can condense long before the supersaturation threshold for homogeneous nucleation and therefore the formation of cloud droplets around aerosol particles (heterogeneous nucleation) is far more common. The particle's ability to act as CCN depends on its chemical composition, with more hygroscopic particles being more likely to act as CCN as well as on the particle size, where bigger particles (accumulation mode particles) are more likely to act as CCN than smaller ones.

Many different processes are part of the indirect effects of aerosols on clouds and many of these effects are highly uncertain (IPCC, 2013). The first effect to be discovered was the Twomey effect (Twomey, 1974): in warm clouds, an increase in the aerosol number concentration results in an increased number of cloud droplets and a smaller average radius for these droplets, which in turn increases the reflectivity of the clouds. Fifteen years after that, the cloud lifetime effect was discovered (Albrecht, 1989): an increase in aerosol number concentration increases cloud lifetime. The associated effect is the reduction of the precipitation efficiency, as smaller particles are less likely to fall out of the cloud as rain (Rosenfeld, 1999). Moreover, aerosol optical properties can affect the way in which they influence clouds: scattering particles act as good CCN while absorbing aerosols have been shown to prevent clouds from forming or if within cloud droplets even cause sufficient warming to lead to cloud evaporation (Chýlek et al., 1996; Huang et al., 2010).

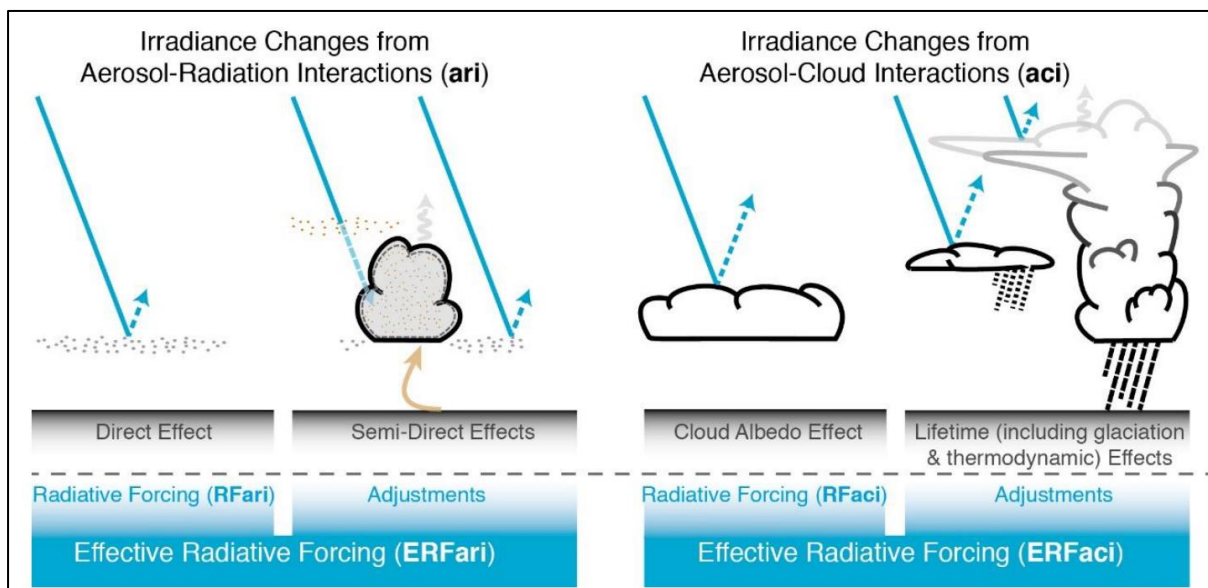


Figure 1.4: A schematic of the mechanisms through which aerosols affect atmospheric radiative transfer via aerosol-radiation interaction (left) and aerosol-cloud interaction (right). The blue arrows illustrate the solar radiation, the grey arrows the terrestrial radiation and the brown arrow symbolizes the couplings between the surface and the cloud layer for rapid adjustments. Black dotted lines with different thickness represent precipitation intensity. (IPCC, 2013).



### 1.2.6 Impact on human health

In 2013, the World Health Organization (WHO) declared PM carcinogenic to humans and estimated 7 million premature deaths every year due to poor air quality, both ambient and indoor (WHO, 2016).

In the human body, the coarse fraction of the aerosol particles is stopped in the upper respiratory system, while the particles of the PM<sub>2.5</sub> fraction penetrate to the lower respiratory tract; furthermore the accumulation mode particles reach the bronchioles (Heinzerling et al., 2016). Exposure to aerosols has been associated with cardiovascular and respiratory morbidity and mortality in numerous epidemiological and toxicological studies (Dockery et al., 1993; Pope et al., 2002; Chung et al., 2015). There is good evidence of the effects of short-term exposure to PM<sub>10</sub> on respiratory health, but for mortality, and especially as a consequence of long-term exposure, PM<sub>2.5</sub> is a stronger risk factor than PM<sub>10</sub>. All-cause daily mortality is estimated to increase by 0.2–0.6% per 10 µg m<sup>-3</sup> increase of PM<sub>10</sub> concentration (Samoli et al., 2008). Long-term exposure to PM<sub>2.5</sub> is associated with an increase in the long-term risk of cardiopulmonary and lung cancer mortality by 4–8% per 10 µg m<sup>-3</sup> of PM<sub>2.5</sub> (Pope et al., 2002).

However, no consensus in the scientific community about which aerosol property (mass, size, number, surface area, composition, etc.) or the component responsible for adverse health effects has been found yet. Even if it is likely that not every PM component is equally important in causing these health effects, the collective evidence has not yet isolated factors or sources that would be unequivocally related to specific health outcomes (Stanek et al., 2011).

## 1.3 Black carbon

Among aerosols, black carbon (BC) particles play a significant role in the Earth's climate system. Black carbon is the strongest light absorber among aerosols (Moosmüller et al., 2009). Moreover, it influences cloud properties in two ways: with the semi-direct effect, altering the thermal structure of the atmosphere by the heat generated from light absorption and indirectly contributing to CCN population (Koch and Del Genio, 2010). In addition, it alters the melting of snow and ice cover (Bond et al., 2013).

BC particles seem to be the second largest positive contribution to anthropogenic climate forcing in the present-day atmosphere after that from CO<sub>2</sub> (Jacobson, 2001; Bond et al., 2013; IPCC, 2013). However, due to their short lifetime compared to CO<sub>2</sub>, BC emission reduction represents a potential mitigation strategy that could reduce global climate forcing from anthropogenic activities in the short term and slow the associated rate of climate change (Takemura and Suzuki, 2019).

### 1.3.1 Nomenclature

There is no universally accepted definition of black carbon, and it is often times referred to as soot, graphitic carbon, and/or elemental carbon. Some definitions have focused on its chemical and/or physical properties, while others are operationally based and reflect the results of measurement and estimation approaches (Janssen et al., 2012; Bond et al., 2013). In general, black carbon is a collective term that describes a range of carbonaceous substances from partly charred plant residues to highly graphitized (i.e., highly ordered molecular carbon structures as found in graphite) soot that are generated as products of incomplete combustion (Shrestha et al., 2010).

Black carbon was defined by the essential works of Bond et al. (2013) and Petzold et al. (2013) as the material which strongly absorbs visible light; volatilizes at ~4000 K; is insoluble in water and organic solvents; exists as aggregates consisting of primary spherules with diameter 10–80 nm and consists primarily of graphitic sp<sup>2</sup>-bonded carbon. BC typically has a wavelength-independent refractive index, which, in combination with its typically open morphology and small size relative to visible/infrared wavelengths, means that it is a strong broadband absorber with an AAE (Eq. 1.4) close to 1.0 when externally mixed.

Corbin et al. (2019) recently split the definition of BC into two categories: soot BC and char BC. While soot BC is the one defined above, char BC is defined with the same properties of soot BC except for the morphology. Indeed, char BC is formed when low-volatility fuel droplets undergo surface graphitization rather than evaporation when heated. As a result of this, char BC particles are bigger than soot BC particles, more spherical and with an AAE close to 0.

Black carbon is usually defined operationally, which means that it is based on the measurement technique used to measure it. The amount of strongly light-absorbing carbon with the approximate optical properties of BC that would give the same signal in an optical instrument (typically at the red or IR wavelengths) as the sample, is defined as equivalent black carbon (eBC) (Andreae and Gelencsér, 2006). The thermal-optical analysis (TOA) measures the mass of carbon that is thermally refractory up to about 800 K (depending on the analysis protocol), after correcting for potential sample pyrolysis, and is called elemental carbon (EC). Finally, black carbon measured by laser-induced incandescence technique (LII), heated to ~4000 K, is named refractory black carbon (rBC). In Chapter 3 the TOA and LII techniques are treated in detail.

### 1.3.2 Sources, formation and life cycle

Black carbon is a primary pollutant emitted from anthropogenic and natural incomplete combustion processes. Major source categories include open biomass burning (e.g., agricultural burning, wildfires, prescribed burning), mobile/transportation sources, electricity generating units and other power production sources, and residential heating and cooking (Bond et al., 2013; Briggs and Long, 2016).

A complex series of reactions involving polycyclic aromatic hydrocarbon molecules forms precursors of BC. These precursors oligomerize to sizes large enough to serve as particle nuclei and grow through reactions on the surface. These freshly formed BC particles consist of small graphitic spheres of tens of nanometres with high carbon-to-hydrogen ratios (Heidenreich et al., 1968). These graphitic spherules coagulate to form aggregates or fractal chain-like structures consisting of hundreds or thousands of spherules (Martins et al., 1998) (Fig. 1.4a). Within a few hours after the emission during their transport in the atmosphere, these particles undergo many different processes like coagulation, condensation and photochemistry. These processes are collectively known as aging and change the morphology, hygroscopicity and mixing state of the particles (Matsui et al., 2013; Weingartner et al., 1997; Peng et al., 2016).

In particular, aging causes individual black carbon particles to become internally mixed with sulfate, nitrate and organic material (Jacobson, 2001; Moteki and Kondo, 2007; Shiraiwa et al., 2010; Lee et al., 2015) (examples of electron microscopy images of Arctic BC internally mixed with sulfate and dust are shown in Chapter 5), increasing their light absorption, size and hygroscopicity thereby increasing their ability to act as CCN, influencing its removal rate (Stier et al., 2006). Aging mainly affects the mass absorption cross-section of BC ( $MAC_{BC}$ ) (Eq. 1.5), which topic will be extensively discussed in Chapter 4.

It is often assumed that non-absorbing material surrounds the BC particles completely and symmetrically, and such configuration is called core-shell geometry (Fig. 1.4c). However, mixing geometries with partial and non-concentric shell may also exist (Adachi et al., 2010; Sedlacek et al., 2012; Dahlkötter et al., 2014) as well as BC cores attached to other non-BC particles (Moteki et al., 2014).

Black carbon is a short-lived aerosol as its global average residence time in the atmosphere is on the order of 5-10 days (Samset et al., 2014; Lund et al., 2018). The dominant sink of BC is wet deposition which is more efficient in removing BC from the atmosphere than dry deposition (Bauer et al., 2010). On a global scale, wet deposition accounts for 80 % of the total deposition (Jurado et al., 2008) and for more than 90 % in certain areas such as in the Arctic (Dou and Xiao, 2016). The relative importance of wet-versus-dry deposition depends on the amount of precipitation at a given site location and atmospheric burden. While wet deposition controls BC lifetime, dry deposition can significantly extend the lifetime of BC in the absence of precipitation (Emerson et al., 2018). BC particles deposited on the surfaces can finally be preserved in soils, snow and ice, water and sediments (Lavanchy et al., 1999; Bisiaux et al., 2012).

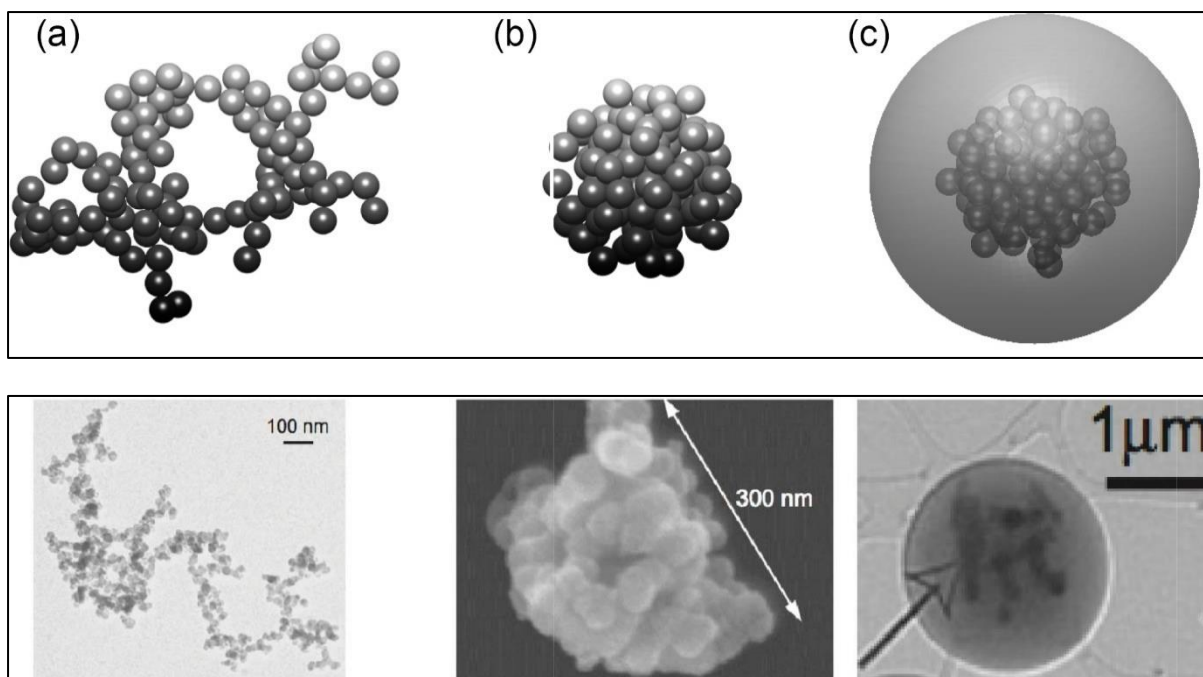


Figure 1.5: Geometries of numerically generated BC aggregates with different particle geometries. In the top figure (a): fresh BC, (b) compact BC, (c) coated BC; in the bottom figure some examples of transmission electron microscopy images of real BC particles for comparison (from left to right: Burr et al., 2012; Lewis et al., 2009; Freney et al., 2010) (Image credit: Liu et al., 2018).

### 1.3.3 Black carbon impact on climate

Black carbon has a huge impact on the climate system. Despite its relatively low particle mass concentration, it has been argued that BC is the second most important atmospheric positive forcer after  $\text{CO}_2$  (Jacobson, 2001; Bond et al., 2013), but a controversy around this notion exists (Feichter et al., 2003). Its effect, according to the IPCC report, can be divided into the direct effect, the semi-direct effect, the snow/ice albedo effect and the indirect effect (IPCC, 2013). The net effective BC radiative forcing was estimated to be around  $+1.1 \text{ W m}^{-2}$  (Bond et al., 2013) and includes aerosol-radiation-cloud interactions with rapid adjustments. This value is, however, affected by an uncertainty of 90%, resulting in an ERF range between  $0.17$  and  $2.1 \text{ W m}^{-2}$  (Myhre et al., 2013).

Direct radiative forcing of black carbon is caused by absorption and scattering of sunlight. Black carbon is the dominant absorber of visible solar radiation in the atmosphere: black carbon heats the atmosphere and reduces the amount of sunlight that reaches the surface and that is reflected back to space. Bond et al. (2013) estimated a global industrial-era (1750 to 2005) direct radiative forcing of black carbon of  $+0.71 \text{ W m}^{-2}$  with 90% uncertainty bounds of  $+0.08$  to  $+1.27 \text{ W m}^{-2}$ .

Black carbon influences the properties of ice clouds and liquid clouds through diverse and complex processes. The semi-direct effect consists in the perturbation of the temperature structure of the atmosphere, with consequent influence of the cloud cover and distribution. This effect can either increase or decrease the cloud cover and the cloud water content depending on many factors such as the position of black carbon particles relative to the cloud and the cloud type (Koch and Del Genio, 2010). The indirect effect refers to their action as CCN when coated with hygroscopic material and as ice nucleating particles (IN), and subsequently altering the cloud albedo. The estimate of the industrial-era climate forcing from black carbon cloud effects is  $+0.23 \text{ W m}^{-2}$  with a  $0.47$  to  $+1.0 \text{ W m}^{-2}$ , 90% uncertainty range (Bond et al., 2013). This estimate is calculated with very low scientific understanding and large uncertainties (IPCC, 2013).

Black carbon particles deposited on high albedo surfaces like ice and snow reduce the total surface albedo available to reflect solar energy back to space. This effect creates a positive feedback because a reduced surface albedo increases the surface temperature, and the increased surface temperature decreases the snow or ice cover and further decreases the surface albedo. The cloud-albedo effect is estimated at  $+0.13 \text{ W m}^{-2}$  with a 0.04 to  $+0.33 \text{ W m}^{-2}$  90% uncertainty range (Bond et al., 2013).

#### **1.3.4 Black carbon impact on human health**

Even if it is not yet clear which role the single aerosol component has in the mortality rate, as explained in Sect. 1.2.6, it is known that the risk may vary among specific  $\text{PM}_{2.5}$  components. Some studies, e.g., Ostro et al. (2007) show the evidence for the hazardous nature of combustion-related PM. Moreover, the exhaust from diesel engines was classified by the International Agency for Research on Cancer as carcinogenic (Group 1) to humans.

In particular, black carbon, as part of the  $\text{PM}_{2.5}$  and as product of the incomplete combustion mechanisms, is particularly harmful to human health. Epidemiological studies found evidence of associations of all causes and cardio-pulmonary mortality with short and long-term average BC exposure (Janssen et al., 2012). Specifically, BC has been linked to several pathologies such as cardiac and ventricular arrhythmias (Rich et al., 2005), lowered heart rate variability (Schwartz et al., 2005), and more generally increased cardiovascular mortality (Maynard Dan et al., 2007). In addition, due to its small size, BC may act as a carrier for a wide variety of chemical constituents of different toxicities (e.g., polycyclic aromatic hydrocarbons; metals and inorganic salts; Contini et al., 2018).

By reducing black carbon, the health risks from air pollution will decline. It is estimated that from 640,000 to 4,900,000 premature human deaths could be prevented every year by utilizing available mitigation measures to reduce black carbon in the atmosphere (WHO, 2016). For example, Janssen et al. (2011) found that a reduction of BC will lengthen human life four to nine times more than a comparable reduction of the  $\text{PM}_{2.5}$  mass.

For all these reasons, the measurement of the size and the mixing state of BC, along with its chemical composition are of high interest for policy makers in order to address more appropriate human health regulations.

#### **1.4 Aim of the work and thesis structure**

In summary, black carbon constitutes a small fraction of the total aerosol; however, it contributes greatly to the overall positive radiative forcing and plays a clear role in the climate warming. Unfortunately, there is still a large number of uncertainties in its quantification and properties, for example regarding its metrology and the uncertainties on the radiative forcing pathways. In this scientific context, during this PhD project, we focused our attention on three different topics. These are discussed in the following chapters.

In Chapter 3, we address an important issue regarding the methodology used to quantify the black carbon mass concentration. Through five field campaigns, we answer the question: are refractory black carbon and elemental carbon mass measurements consistent between each other? This is an important matter, because, as mentioned in Sect. 1.3.1, black carbon is operationally defined and because the debate on the comparability of these two quantities was still largely unresolved. This finding has important implications for studies based on BC mass concentration measurements, for example for the interpretation of uncertainties of inferred BC mass absorption coefficient values, which are required for modelling the radiative forcing of BC.

In Chapter 4, we investigate how the  $\text{MAC}_{\text{BC}}$  values change in relation to the mixing state and size of black carbon particles. Regardless of the uncertainties associated with the  $\text{MAC}_{\text{BC}}$  values, these results are important to mechanistically understand how  $\text{MAC}_{\text{BC}}$  depends on BC particle properties and to demonstrate the debated lensing effect in ambient measurements. In addition, we also gave a picture of the temporal and spatial variability of the most relevant physical and optical properties of black carbon particles, i.e.: rBC mass concentration, EC mass concentration, mass size distribution, absorption coefficient, mixing state, AAE, and SSA. This field experiment was performed in the Po Valley, one of the most polluted sites in Europe, with both stationary and mobile measurements. The study of the spatio-temporal BC properties in this area is fundamental for assessing BC climate impacts.

In Chapter 5, we characterize black carbon properties at the remote site of Zeppelin Observatory, Svalbard, Norway, over one year. Despite its short lifetime, BC can be transported over long distances and, as explained in Sect. 1.3.2, undergo changes of its properties through aging. In this work, we compare the rBC and eBC mass concentration measurements; we examine the seasonal variability of the main BC properties (mass concentrations and mass size distributions) and we identify the geographic regions contributing to the BC measured through back trajectories analysis. Such BC properties are fundamental to derive the optical properties required for radiative forcing estimates in the Arctic, a place that is warming twice as fast as the rest of the world.

Within the studies, filter based thermal-optical analysis; laser induced incandescence technique and aerosol light absorption based methods were used to quantify the BC mass concentration. All these techniques are described in Chapter 2.

## Chapter 2: Methodologies

In this chapter, the main measurement techniques adopted in this work are briefly discussed. These are: the filter-based absorption photometry (Sect. 2.1), the thermal-optical technique (Sect. 2.2) and the laser induced incandescence technique (Sect. 2.3).

### 2.1 Filter-based absorption photometry

The most adopted filter-based photometers for the measurement of aerosol light absorption are: the Aethalometer (Hansen et al., 1984; Magee Scientific, Berkeley, CA), the multi-angle absorption photometer (MAAP; Petzold and Schönlinner, 2004; Thermo Scientific, Franklin, MA), the particle soot absorption photometer (PSAP; Bond et al., 1999; Radiance Research, Seattle, WA) and the continuous soot monitoring system (COSMOS; Miyazaki et al., 2008; Kanomax, Osaka, Japan).

In all of these techniques, the aerosol particles are collected on-line on a filter matrix and the transmitted light (or transmitted and scattered light in the case of the MAAP) is simultaneously detected. The amount of aerosol deposited on the filter is inversely proportional to the transmittance or, directly proportional to the attenuation (*ATN*) defined in Eq. (2.2). From *ATN*, the absorption coefficient can be retrieved using Eqs. 2.3 and 2.4.

However, the use of a filter introduces consistent biases in the absorption coefficient quantification. In fact, the *ATN* measurement is influenced by the interaction of sampled particles with the filter matrix and with other particles. The major effects happening on a filter matrix are:

- multiple scattering effects caused by the scattering by the filter fibers and the scattering by aerosol particles on the filter (Lioussse et al., 1993; Petzold et al., 1997). The scattering due to particles (which depends on the optical properties and size distribution of the deposited aerosol particles) and due to the filter fibers increases the optical path of the light. This in turn leads to an overestimation of the absorption coefficient. Hänel (1987) dealt with the radiative transfer problem for a plane layer that both scatters and absorbs radiation by applying a radiative transfer scheme. Petzold and Schönlinner (2004) developed the MAAP starting from Hänel's approach in order to consider the multiple scattering effects happening in the optical analysis of aerosols deposited on a fiber filter (Sect. 2.1.2).
- filter loading effect: related to the shadowing that deposited aerosol particles cause on each other (Bond et al., 1999; Weingartner et al., 2003). In particular, the accumulation of particles on the filter matrix leads to a saturation of the instrumental response. Moreover, the filter loading effect depends on the optical properties of the particles present on the filter matrix, especially on black carbon particle coating. Weingartner et al. (2003) showed that uncoated BC induces a higher loading effect compared to coated BC and Drinovec et al. (2017) found that the filter loading parameter can be used as a proxy for determination of the particle coating, thus allowing for differentiation between local/fresh and transported/aged particles. Since the filter loading parameter depends on the backscattered fraction of light, it can be parametrized as a function of the SSA (Eq., 1.3) (Collaud Coen et al., 2010; Virkkula et al., 2015).

The optical effects just described take place in every filter-based photometer. Several correction procedures have been developed for the Aethalometer (Weingartner et al., 2003; Virkkula et al., 2007; Collaud Coen et al., 2010; Drinovec et al., 2015), the PSAP (Bond et al., 1999; Ogren, 2010) and the COSMOS (Miyazaki et al., 2008; Nakayama et al., 2010).

After applying these corrections, the absorption coefficient might be converted into an equivalent black carbon mass concentration (check Sect. 1.3.1 for BC nomenclature) using a proper mass absorption cross-section,  $MAC_{eBC}$ .

$$m_{eBC} = \frac{b_{abs}(\lambda)}{MAC_{eBC}} \quad (2.1)$$

In general terms it is important to note that absorption is not a proxy for black carbon mass concentration and the assumption that there is a constant ratio between absorption and BC concentration is only valid when there is no interference from light-absorbing materials other than BC (Bond and Bergström, 2006).

A discussion on the  $MAC_{BC}$  variability is presented in the Introduction of Chapter 4. Because only the Aethalometer and the MAAP were used in this PhD work, we will focus on these two instruments, describing their principle of operation in Sects. 2.1.1 and 2.1.2.

### 2.1.1 The Aethalometer

Among the light attenuation methods, the Aethalometer (Hansen et al. 1984), is the most frequently used technique in the world for real-time measurement of BC mass concentrations. The first Aethalometer was conceptualized and developed in 1979 and currently there are hundreds of these instruments installed worldwide. The first Aethalometer model calculated BC using white light, afterwards distinct wavelengths ranging from the near ultraviolet to the near infrared were added. The multi-wavelength analysis was implemented to gather information about different components of the carbonaceous fraction, particularly organics, which absorb light prevalently at shorter wavelength (Yan et al., 2018).

The Aethalometer measures the change in transmittance of the incoming radiation through a filter on which particles are deposited. The attenuation is defined as the logarithm of the ratio between the light intensity that passes through a pristine part of the filter ( $I_0$ ) and the intensity of the light that passes through the loaded filter ( $I$ ):

$$ATN(\lambda) = \ln\left(\frac{I_0(\lambda)}{I(\lambda)}\right) \quad (2.2)$$

As a consequence, the attenuation coefficient ( $b_{atn}$ ) at a certain wavelength  $\lambda$  is equal to the variation of the attenuation measured at different times multiplied by the spot size area  $A$  ( $m^2$ ) divided by the sample flow rate  $Q$  ( $m^3 s^{-1}$ ) through the filter:

$$b_{atn}(\lambda) = \frac{A}{Q} \frac{ATN(\lambda, t) - ATN(\lambda, t + \Delta t)}{\Delta t} = \frac{A}{Q} \frac{\Delta ATN}{\Delta t} \quad (2.3)$$

It is well known that  $b_{atn}$  may differ significantly from the true aerosol absorption coefficient  $b_{abs}$  of airborne particles. This is because of the multiple scattering and filter loading effects described in Sec. 2.1. This produces significant uncertainties in the assessment of BC concentrations. Several algorithms have been proposed to correct the Aethalometer data for these effects (Weingartner et al., 2003; Virkkula et al., 2007; Collaud Coen et al., 2010). In these works generally two calibration factors ( $C$  and  $R$ ) are introduced, which can be used to convert Aethalometer attenuation measurements into absorption coefficients through the following formula:

$$b_{abs} = b_{atn} \frac{1}{C R(ATN)} \quad (2.4)$$

where  $C$  and  $R(ATN)$  describe the multiple scattering effect and the filter loading effect, respectively.  $C$  mainly depends on the nature of the filter and the apparatus used, is greater than unity and is caused by multiple scattering of the light beam at the filter fibers in the unloaded filter. Any other effects that are caused by deposited particles are described by the empirical function  $R(ATN)$  which varies with (a) the amount of aerosol particles embedded in the filter and (b) optical properties of the deposited particles. For unloaded filters  $R$  is set to unity, i.e.  $R(ATN = 0) = 1$ . With the gradual increase in attenuation due to the accumulating particles in the filter the absorbing particles in the filter absorb a higher fraction of the scattered light which leads to a reduction of the optical path in the filter ( $R < 1$ ) (Weingartner et al., 2003).

Without these corrections, the Aethalometer approach is quite reliable only for thin aerosol layers with a high black carbon mass fraction ( $> 10\%$ ) and a low scattering coefficient of the particles ( $\sim 1000 \text{ cm}^{-1}$ ). These conditions are usually met for samples of an urban aerosol, but they are no longer valid for background aerosols (Petzold and Schönlinner, 2004).

In particular, other than previous Aethalometer versions, whose data needed to be converted afterwards, the AE33 version uses the patented DualSpot™ method to compensate for the loading effect. This is done by making two simultaneous measurements of black carbon ( $BC1$  and  $BC2$ ) on two spots at two different degrees of loadings,  $ATN1$  and  $ATN2$ :

$$\begin{cases} BC1 = BC (1 - k ATN1) \\ BC2 = BC (1 - k ATN2) \end{cases} \quad (2.5)$$

From these two equations both the compensated black carbon,  $BC$  and the ‘loading compensation’ parameter,  $k$ , which may provide additional information about the physical and chemical properties of the aerosol, can be retrieved (Drinovec et al., 2015).

It is important to remember that, in addition to the problem of evaluating  $b_{abs}$  with Eq. (2.4), all optical methods convert light absorption/attenuation using a fixed conversion coefficient (i.e.  $MAC_{eBC}$ , Eq. 2.1) that can bias resulting eBC mass values.

In this PhD thesis the data of the Aethalometer (AE-31 and AE-33 models) (details in Sect. 3.2.4.2 of Chapter 3 and in Sect. 4.2.3 of Chapter 4) were used to calculate the absorption Ångström exponent (Eq. 1.4). This coefficient describes the spectral dependence of the aerosol light absorption coefficient and is commonly used to retrieve an indication on the sources of black carbon (Zotter et al., 2017).

### 2.1.2 The multi-angle absorption photometer

The multi-angle absorption photometer (Petzold and Schönlinner 2004) measures simultaneously the light transmittance in orthogonal direction through a glass-fiber filter as well as back-reflectance at two different angles. The firmware includes a full data inversion, which is based on a two-stream approximation radiative transfer model, to directly infer the absorption coefficient  $b_{abs}$  at 637 nm, whereby the reflectance signals provide the information required to account for the effects of multiple scattering and shadowing.

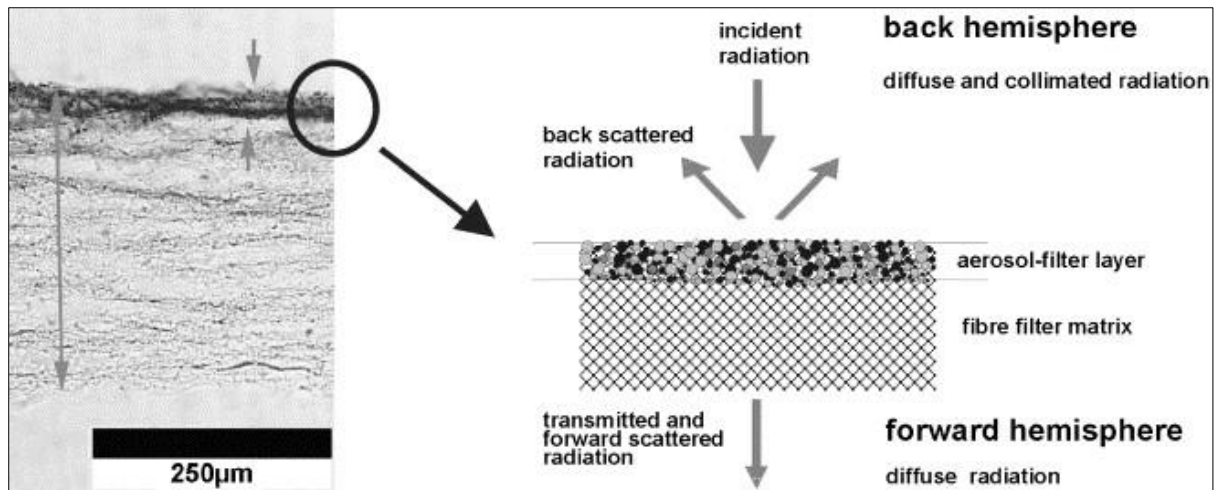


Figure 2.1: Schematic illustration of the two-layer system of particles deposited in a fibrous filter matrix (Petzold and Schönlinner, 2004).

The measurement of the angular distribution,  $S(\theta)$ , of light scattered back and penetrated through a particle-loaded fiber filter showed that the radiation that has penetrated through the filter is completely diffuse and can be parameterized by a cosine law:

$$S(\theta) \propto \cos\theta \quad (2.6)$$

with  $\theta$  being the scattering angle relative to the incident radiation. The back-scattered radiation is described by a combination of a diffusely scattered fraction proportional to  $\cos(\theta - \pi)$ , and a fraction that is parameterized best



by a Gaussian law proportional to  $e^{-\frac{1}{2}(\theta-\pi)^2/\rho^2}$ , with  $\rho$  being a measure for the surface roughness of the aerosol layer deposited on the filter and  $\alpha$  the fraction of diffusely scattered radiation:

$$S(\theta) \propto \alpha \cos(\theta - \pi) + (1-\alpha) e^{-\frac{1}{2}(\theta-\pi)^2/\rho^2}. \quad (2.7)$$

The Gaussian-distributed fraction of the back-scattered radiation can be taken as radiation “reflected” from a rough surface. The distribution of back-scattered radiation between diffuse and Gaussian type depends on the sampled aerosol. The measurement of the radiation penetrating through the filter at the scattering angle  $\theta = 0^\circ$ , and the simultaneous measurement of the radiation scattered back from the filter at two detection angles  $\theta = 130^\circ$ , and  $165^\circ$ , permits the full determination of the irradiances in the forward and back hemisphere relative to the incident light beam.

The exact position of the detection angles was chosen such that the partitioning between diffuse and Gaussian types can be determined with highest resolution. In the MAAP, the determination of the aerosol absorption coefficient  $b_{\text{abs}}$  of the deposited aerosol uses radiative transfer techniques. The particle-loaded filter is treated as a two-layer system (Fig. 2.1): the aerosol-loaded layer of the filter and the particle-free filter matrix. Radiative processes inside the layer of deposited aerosol and between this layer and the particle-free filter matrix are separately taken into account. In this approach, originally developed by Hänel (1987) and modified for this purpose by Petzold and Schönlinner (2004), multiple reflections between the aerosol-loaded filter layer and the particle-free filter matrix are treated by the adding method (Van de Hulst, 1980). Starting from quantities directly measurable, the model resolution gives the two parameters needed to calculate the absorbance *ABS* (fraction of light absorbed in a filter sample):

$$ABS(\lambda) = (1 - SSA)\tau(\lambda) \quad (2.8)$$

Where  $\tau(\lambda)$  is the total optical depth of the particle loaded aerosol-filter layer and SSA is the single scattering albedo, defined in Eq. (1.3).

Therefore,  $b_{\text{abs}}$  is calculated as follows:

$$b_{\text{abs}}(\lambda) = ABS(\lambda) \frac{A}{V} \quad (2.9)$$

where  $A$  is the area of the sample spot to which particles are deposited, and  $V$  the volume of air sampled.

$b_{\text{abs}}$  can be converted into an equivalent black carbon mass concentration using a  $MAC_{\text{eBC}}(637 \text{ nm})$  of  $6.6 \text{ m}^2 \text{ g}^{-1}$ . This value was set by the MAAP manufacturer and was optimized towards fresh BC particles measured in urban areas after some comparisons between MAAP absorption data and EC values (Petzold and Schönlinner, 2004). For this reason when dealing with aged BC aerosols the MAAP  $m_{\text{eBC}}$  may be overestimated.

It is important to note that originally, the operating wavelength of the MAAP was thought to be 670 nm (Petzold et al., 2005), while later, the true value was shown to be  $637 \pm 1 \text{ nm}$ . As a consequence of this, the absorption coefficient determined by the firmware of the MAAP needs to be increased by 5 % assuming an absorption Ångström exponent of 1 to obtain the correct aerosol absorption coefficient at 637 nm (Müller et al., 2011).

In this work the MAAP was used in Chapter 4 to calculate the absorption coefficient of black carbon, while in Chapter 5 it was used to retrieve  $m_{\text{eBC}}$  and to compare it with  $m_{\text{rBC}}$  measured with the SP2.

## 2.2 Thermal optical technique

The thermal-optical technique allows the determination of the total carbon (TC) which is the total carbonaceous aerosol concentration. With the use of a thermal sequence, TC can be split into organic carbon (OC) and elemental carbon, according to their different thermal stability. This technique requires an instrument (OC/EC analyzer) and a thermal protocol.

### 2.2.1 The Sunset EC/OC analyzer

The Sunset EC/OC analyzer manufactured by Sunset Laboratory Inc. (Tigard, OR) (Chow et al., 1993) is the most widespread instrument to perform thermo-optical analysis of the carbonaceous fraction in PM samples. The analysis is based on the different evolution characteristics of EC and OC as a function of the temperature and type of atmosphere and on the quantification of the evolved  $\text{CO}_2$  at the thermal steps chosen for the separation.

A schematic view of the Sunset Laboratory OC/EC analyzer is shown in Fig. 2.2 The instrument consists of a front oven, an oxidizer oven with manganese oxide, a methanator and a flame ionization detector (FID).

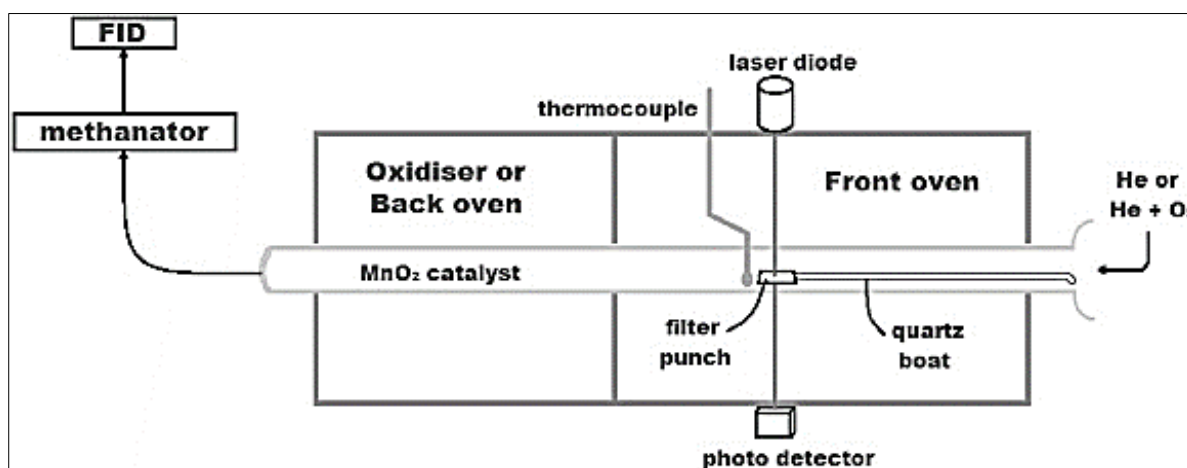


Figure 2.2: Schematic view of the Sunset Laboratory OC/EC analyzer (Ammerlaan et al., 2015).

The procedure for the determination of EC and OC works as follows. A punch from a quartz filter sample is placed in a quartz boat and positioned in the path of a red light diode laser, which is used to monitor the transmittance of the filter during the analysis. A thermocouple at the end of the boat is used to monitor the temperature during analysis. All carbon species evolved from the filter are converted to carbon dioxide in an oxidation oven immediately downstream of the primary oven, and the carbon dioxide is reduced to methane before passing into a FID.

One of the most widespread techniques for the thermal quantification of OC and EC fraction is the Thermal-Optical Transmittance method (TOT) (Birch and Cary, 1996) and consists of two main steps. In the first step, the carbonaceous particles are thermally desorbed in a pure helium atmosphere (inert atmosphere). The components measured in this cycle are called organic carbon. After the first heating step, the oven is cooled down and the carrier gas is switched to a mixture of helium and oxygen (2% oxygen/helium mixture: oxidizing atmosphere). The temperature is increased again and the refractory components that oxidize and volatilize in the second cycle are attributed to elemental carbon. However, in the helium atmosphere, a fraction of OC pyrolyses and produces thermally stable, light absorbing material with the result that not all OC is desorbed in the first heating cycle. In the second cycle, these components, called pyrolytic carbon, oxidize. To correct for this effect the transmission signal is measured continuously. The transmission decreases in the helium cycle and increases again in the oxygen cycle. The point in the second cycle where the optical signal reaches its initial value is called “split point” (Fig. 2.3). In this way the component that is measured in the part of the oxygen phase before the split point, that is the pyrolytic carbon, can be attributed to the organic carbon. This correction is called “charring correction” and can also be done using light reflectance (thermo-optical reflectance method; TOR) instead of transmittance.

The above described assumptions on the optical charring correction are only partially fulfilled, typically leaving charring artefacts as a main source of bias even for optically corrected EC mass data (Chow et al., 2004; Subramanian et al., 2006). More information can be found in Sect. 3.2.2.1 of Chapter 3.

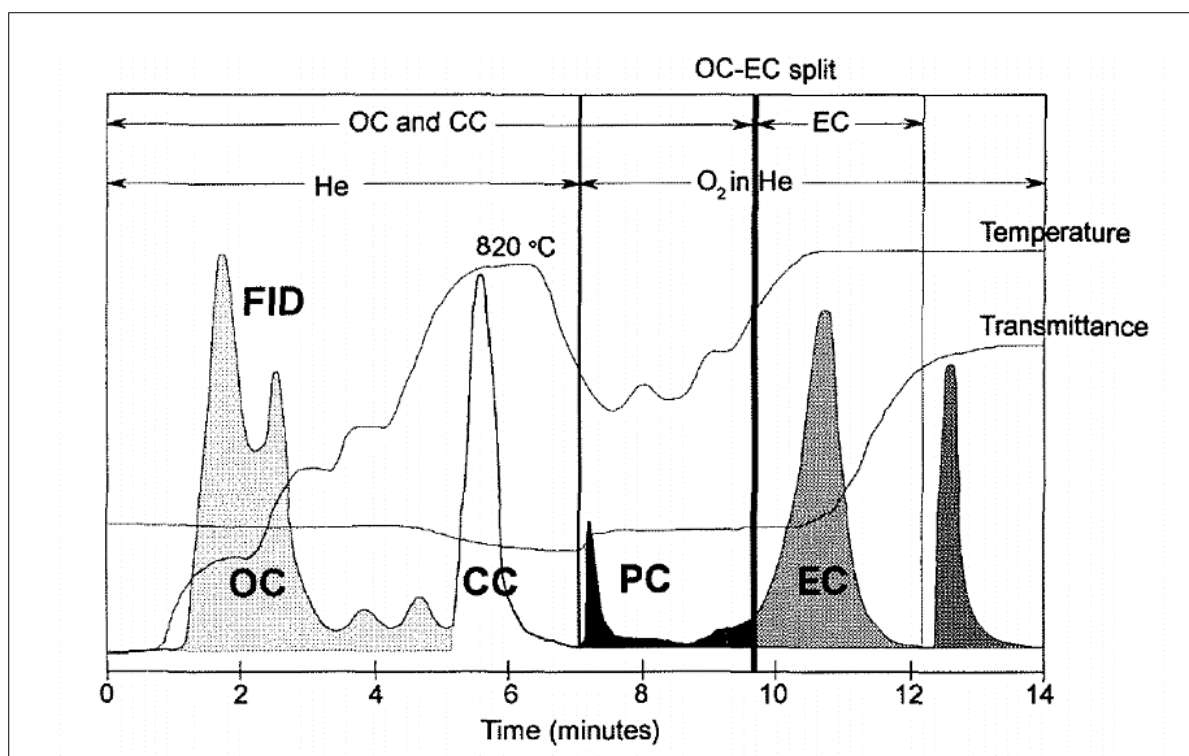


Figure 2.3 Schematic of the thermal-optical OC/EC analyzer (Kvietkus, 2007).

So far, the IMPROVE (Interagency Monitoring of PROTECTED Visual Environments; Chow et al., 1993), NIOSH (National Institute for Occupational Safety and Health; Birch and Cary, 1996) and EUSAAR-2 (European Supersites for Atmospheric Aerosol Research; Cavalli et al., 2010) thermal-optical protocols have been the most widely used ones in the atmospheric science community. Traditionally, the IMPROVE protocol has been applied to samples from non-urban background sites in the US IMPROVE network; in 2005, the IMPROVE network started to apply the IMPROVE-A protocol, an only slightly modified version of IMPROVE thanks to refined measures of the sample temperature (Chow et al., 2007). The NIOSH protocol has been applied to samples from urban sites in USA-EPA's Speciation Trends Network. The protocol NIOSH-5040 was later introduced to be used for the determination of EC from diesel exhaust. These protocols differ in temperature set points – higher for NIOSH (e.g. the highest temperature in He is 900 °C) than for IMPROVE (e.g. the highest temperature in He is 550/580 °C) – and in the residence times at each temperature step – typically longer for IMPROVE than for NIOSH (Table 3.1). Moreover, the IMPROVE protocol uses the reflectance method to correct for charring, while the NIOSH protocol has adopted the transmittance method. In Europe, the EUSAAR-2 protocol has been selected as the European standard thermal protocol to be applied in air quality networks for the measurement of TC, OC, and EC in PM<sub>2.5</sub> samples (European Committee for Standardisation Ambient air, 2017; EN16909:2017).

Table 2.1: Most common thermal protocols: temperature set point and residence time are reported.

Step	NIOSH	NIOSH 5040	IMPROVE	IMPROVE-A	EUSAAR-2
	T, duration [°C, s]	T, duration [°C, s]	T, duration [°C, s]	T, duration [°C, s]	T, duration [°C, s]
He1	310, 60	250, 60	120, 150-580	140, 150-580	200, 120
He2	475, 60	500, 60	250, 150-580	280, 150-580	300, 150
He3	615, 60	650, 60	450, 150-580	480, 150-580	450, 180
He4	900, 90	850, 90	550, 150-580	580, 150-580	650, 180
He/O <sub>2</sub> 1	600, 45	650, 30	550, 150-580	580, 150-580	500, 120
He/O <sub>2</sub> 2	675, 45	750, 30	700, 150-580	740, 150-580	550, 120
He/O <sub>2</sub> 3	750, 45	850, 30	800, 150-580	840, 150-580	700, 70
He/O <sub>2</sub> 4	825, 45	940, 120			850, 80
He/O <sub>2</sub> 5	920, 120				

Previous studies have demonstrated that differences in the temperature and duration steps of the various thermal protocols may significantly alter the measured amounts of OC and EC (Chow et al., 1993). The use of different thermal protocols can result in a wide elemental carbon-to-total carbon variation by up to a factor of five (Cavalli et al., 2010). In general, it has been observed that protocols with a rather low peak temperature in the inert mode like EUSAAR-2 and IMPROVE generally classify more carbon as EC compared to the NIOSH protocol (Karaniou et al., 2015). In Table 3.1 of Chapter 3 the differences between EC measured with EUSAAR-2 and with other protocols reported in previous literature studies are summarized.

In this thesis, EC mass concentrations at several European sites were analyzed with the EUSAAR-2 thermal protocol and compared with co-located measurements of rBC mass concentration. The results are shown in Chapter 3.

### 2.3 Laser induced incandescence

Laser induced incandescence (LII) is an optical technique which enables the detection of black carbon particles. The technique is based on the measurement of the black body thermal radiation emitted by BC particles when heated up by a light source, typically a laser (Michelsen, 2017). There are different instrumental approaches for LII using both pulsed-shot lasers (Michelsen et al., 2015), and continuous-wave lasers, as in the commercially-available Single-Particle Soot Photometer (SP2).

The spectral radiance of a black body is described by Planck's law:

$$B(\lambda, T) = \frac{2hc^2}{\lambda^5 [\exp\left(\frac{hc}{\lambda k_B T}\right) - 1]} \quad (2.10)$$

where  $h$  is the Planck constant,  $c$  is the speed of light in vacuum,  $\lambda$  is the radiation wavelength and  $k_B$  is the Boltzmann constant.

Detection of the LII signal is essentially an integration of Planck's law over a certain spectral detection band, time interval, and particle size distribution. The resulting detected LII signal is expressed by:

$$S_{\text{LII}} = \frac{\Omega}{4\pi} \int_{\Delta t} \int_{\Delta \lambda} C_{\text{emit}}(v, m, \lambda, \text{shape}, \alpha, \beta, \gamma, t) B(\lambda, T) \varepsilon(\lambda) d\lambda dt \quad (2.11)$$

where  $\Delta \lambda$  is the wavelength detection band,  $\Delta t$  is the time interval of detection,  $\Omega$  is the solid angle of detection,  $\varepsilon(\lambda)$  the wavelength-dependent function describing the transmissivity of the optical filter and responsivity of the photodetector,  $C_{\text{emit}}$  the emission cross-section of the thermal emission,  $v$  the particle volume;  $m$  the complex refractive index, and  $\alpha, \beta, \gamma$  the Euler angles of particle rotation.

### 2.3.1 The Single Particle Soot Photometer

The Single Particle Soot Photometer (Droplet Measurement Technologies, DMT, Longmont, CO, USA) (Stephens et al., 2003; Moteki and Kondo, 2007) is based on the LII technique. The SP2 can simultaneously measure the size of the particle and give information on its mixing state at single particle level. The detection of the emitted particle incandescence signal allows the determination of the particle mass. The elastically scattered light provides information about the size of the particle. The schematic of SP2 is shown in Fig. 2.4.

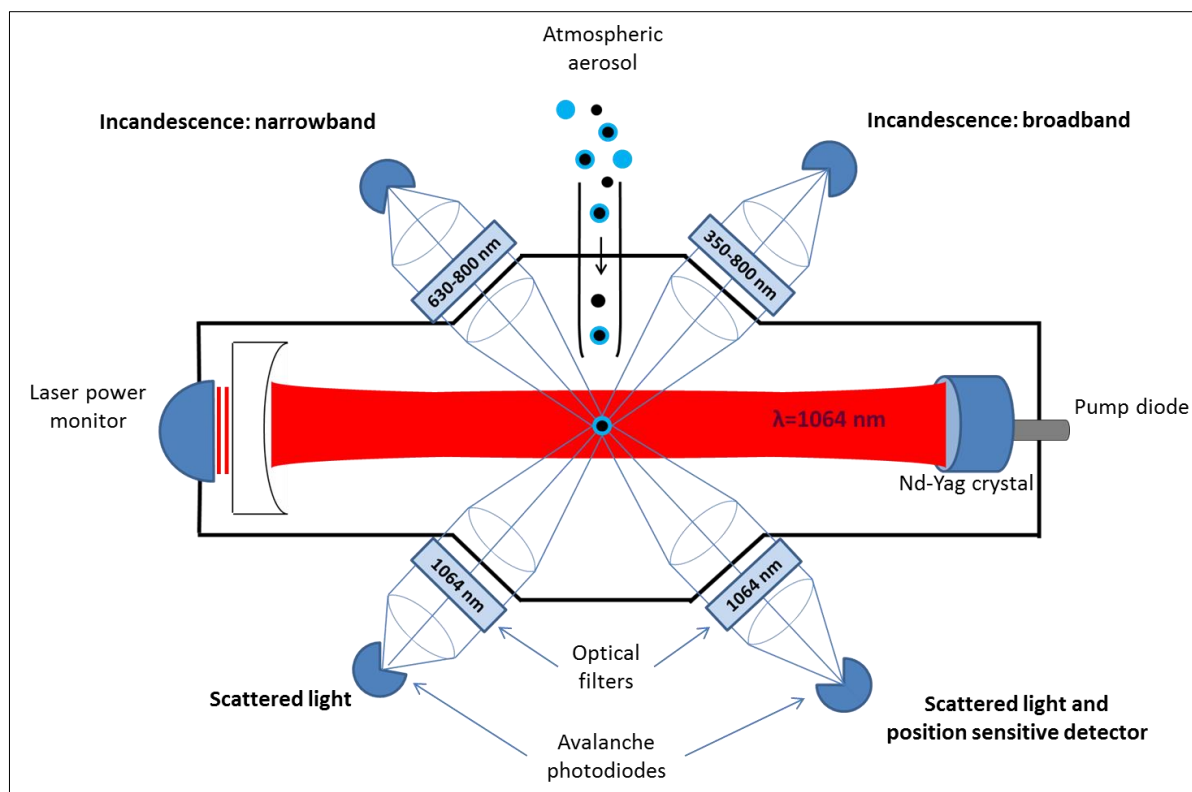


Figure 2.4: Schematic of the measurement chamber of the SP2 (adapted from Schwarz et al., 2006).

An air jet carrying sample aerosol intersects an intense ( $\sim 1 \text{ MW cm}^{-2}$ ) Nd:YAG, intra-cavity, continuous laser beam ( $\lambda = 1064 \text{ nm}$ ) pumped by a diode laser. Two optical lenses are positioned to each capture a solid angle ( $\sim \pi/2 \text{ sr}$ ) of light emitted or scattered by particles in the laser beam, and image it onto an avalanche photodiode (APD). One of the two is used to optically size non-incandescence particles that only scatter light, the second serves for the sizing of the internally mixed black carbon, as described later. Two photomultiplier tubes equipped with optical filters detect incandescent light over either a “broadband” ( $\sim 350\text{--}800 \text{ nm}$ ) or “narrowband” ( $\sim 630\text{--}800 \text{ nm}$ ) wavelength interval and are used to characterize incandescing particles (Schwarz et al., 2006).

Light-absorbing refractory particles such as rBC absorb energy and are heated to their boiling point or vaporization temperatures, emitting thermal radiation. The intensity of the thermal radiation emitted at the rBC vaporization point is a linear function of the refractory volume of the particle. Since rBC is the main atmospheric component remaining at a temperature higher than 4230–4325 K, the technique is selective for refractory black carbon and does not undergo major interferences by non-refractory absorbing materials (information about potential interferences and artefacts can be found in Sect 3.2.3.3 of Chapter 3). The mass of every rBC particle is derived from the measured  $S_{\text{LII}}$  signal (Eq. 2.11), which is proportional to the height of the incandescence peak signal ( $PkHt_{\text{inc}}$ ). The relationship between  $PkHt_{\text{inc}}$  and particle mass is parametrized within the calibration procedure, performed measuring  $PkHt_{\text{inc}}$  when sampling pure rBC particles with a certain mobility diameter or mass (Baumgardner et al., 2012; Laborde et al., 2012a). In case of a mobility-diameter based calibration, the effective

density of the calibration material used is needed to infer the rBC mass from the selected mobility diameter. The effective density of several common SP2 calibration materials was determined by Gysel et al. (2011). An alternative way of performing an incandescence calibration is to introduce particles with a known BC mass into the SP2. During atmospheric measurements, the mass equivalent diameter of rBC particles,  $D_{\text{rBC}}$ , is not directly measured, but derived from the particles mass using a material density of  $1800 \text{ kg m}^{-3}$  (Moteki and Kondo, 2010). Despite the advantages, the SP2 technique has one main disadvantage: the size range. Depending on the SP2 model the size detection range may vary. The lower limit of detection of the different SP2s varies between  $D_{\text{rBC}} = 80 \text{ nm}$  and  $D_{\text{rBC}} = 90 \text{ nm}$  (Schwarz et al., 2010). The higher size limit of detection varies between  $D_{\text{rBC}} = 340 \text{ nm}$  and  $D_{\text{rBC}} = 550 \text{ nm}$  depending on the gain of the analog-digital converter. This higher cut off may result in an important rBC mass underestimation, for this reason the measured rBC mass size distribution is usually fitted with a unimodal lognormal function (Schwarz et al., 2006; Laborde et al., 2013; Chapter 3). The two most commonly used approaches used to extrapolate the measured rBC mass size distribution and correct for the missing rBC mass are explained and compared in a detailed way in Sect. 3.2.3.5 of Chapter 3.

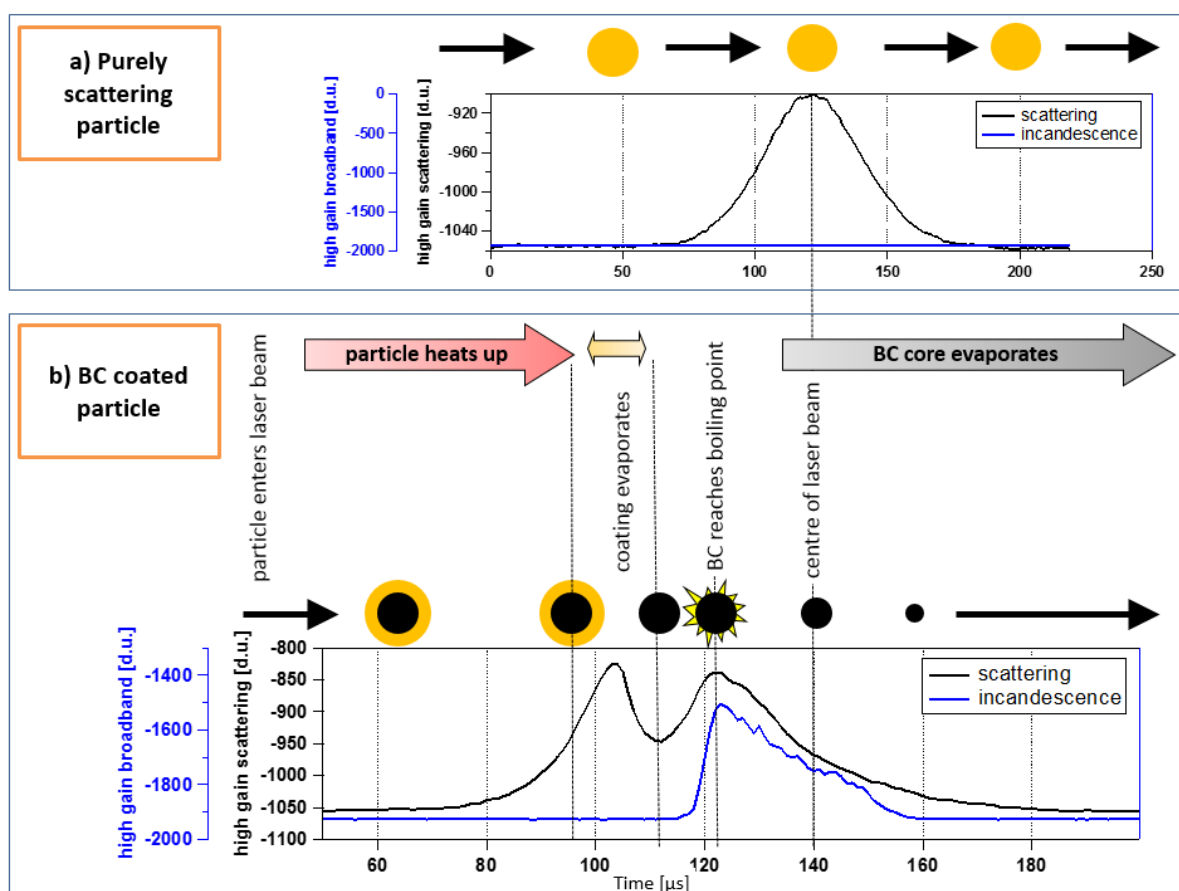


Figure 2.5: Schematic of the signals of a purely scattering particle and a coated BC particle passing through the SP2 (adapted from a schematic prepared by Martin Gysel-Ber).

With the SP2 is also possible to infer the optical diameter of BC-free particles from the measured differential scattering cross section of the single particle ( $\sigma_{sp-meas}(D_p, m)$ ). Assuming a spherical geometry and the refractive index, Mie theory can be used to interpret the SP2 raw signal of the light scattering detectors. The scattering signal  $s(t)$  is proportional to the incident laser intensity and to the scattering cross section and depends on the distribution of the laser intensity. Due to the absence of light absorption, the scattering cross section of an rBC-free particle remains stable throughout the measurement time. As a consequence, the  $s(t)$  is proportional only to the intensity of the laser light at which the particle is exposed and assumes a Gaussian shape peaking with an amplitude of  $PkHt_{\text{scat}}$  at the laser center (Fig. 2.5a). The calibration of the scattering signal is determined by measuring

$PkHt_{scat}$  when sampling non-absorbing, spherical particles of a known diameter,  $D_p$ , and refractive index,  $m$  (e.g.  $m = 1.59$  for polystyrene latex spheres, PSL). Mie theory and the homogeneous spherical particle model is then used to calculate the relationship between  $D_p$  and the corresponding differential scattering cross section ( $\sigma_{sp-Mie}(D_p, m)$ ). The scattering signal calibration factor  $CF_{scat}$  is then calculated, using the SP2 measurement of the integrated laser intensity ( $I_{monitor}$  from the YAG monitor) with the following equation:

$$CF_{scat}(D_p, m) = \frac{PkHt_{scat}}{I_{monitor} \sigma_{sp-Mie}(D_p, m)} \quad (2.12)$$

The scattering signal calibration might be performed calculating the average of the scattering signal calibration factors measured for different particle diameters in order to gain in accuracy. Alternatively, calibration factors might be calculated for a single particle diameter varying the intensity of the laser beam ( $I_{monitor}$ ).

The measured particle scattering cross section  $\sigma_{sp-meas}(D_p, m)$  is then derived from the measurement of  $PkHt_{scat}$ , using the calibration factor and the following equation:

$$\sigma_{sp-meas}(D_p, m) = \frac{PkHt_{scat}(D_p, m)}{I_{monitor} CF_{scat}(D_p, m)} \quad (2.13)$$

The particle's optical diameter is then inferred from  $\sigma_{sp-meas}(D_p, m)$ , using Mie theory, and assuming a certain refractive index.

Due to light absorption, the scattering cross section of an rBC-containing particle decreases during its path in the laser beam. This is due to the evaporation of non-rBC components (the coating) and the core vaporization at incandescence. As a direct consequence, the maximum of the scattering signal does not occur in the middle of the laser beam (Fig. 2.5b). Therefore, the scattering signal is still proportional to the original size of the particle only prior to light absorption by the rBC core and thermal transfer from the rBC core to the non-refractory coating. In this case,  $PkHt_{scat}$  can be reconstructed by fitting the edge of the scattering signal (leading edge only fit, LEO), knowing the laser intensity at the position of the particle in the laser beam profile, compared to the intensity at the center of the profile, corresponding to the signal peak, as explained in Gao et al. (2007). This approach, known as LEO-fit, allows quantifying the thickness of the BC particle coating,  $\Delta_{coat}$ :

$$\Delta_{coat} = \frac{D_p - D_{rBC}}{2}. \quad (2.14)$$

A different approach, known as delay-time method, can be used to obtain a binary classification of the BC mixing state. With the delay-time method the time lag between the first scattering signal peak and the incandescence signal peak is measured (Fig. 2.5b) and utilized as an indication of the coating vaporization time. Particles with a delay time below a certain threshold are classified as bare, thinly or moderately coated, whereas particles with a delay time above this threshold are identified as thickly coated (Schwarz et al., 2006; Laborde et al., 2012b).

In this thesis work, the data from three different SP2s was analyzed (see Table 3.3 of Chapter 3 for more information). Additional information on the incandescence calibrations performed can be found in Sect. 3.2.3.2 and Table 3.3 of Chapter 3 and in Sect. 4.2.3.1 of Chapter 4. In the Bologna campaign the delay-time method for the calculation of the number fraction of thickly coated particles was applied (Sect. 4.2.3.1 of Chapter 4) because it was not possible to perform the LEO-fit method due to misalignment of the position sensitive detector.

### 2.3.2 The Single Particle Soot Photometer Extended Range

The Single Particle Soot Photometer Extended Range (SP2-XR, Droplet Measurement Technologies, DMT, Longmont, CO, USA) is the smaller, simpler and newer version of the SP2. It is based on the same physical principles and allows the users to obtain a real-time output of rBC mass and particle size for individual particles as well as some information on the particle mixing state. Moreover, the software provides real-time results for BC

particle number/mass concentration and size distribution by automatically processing the raw data. The scheme of the SP2-XR optical components is reported in Fig. 2.6.

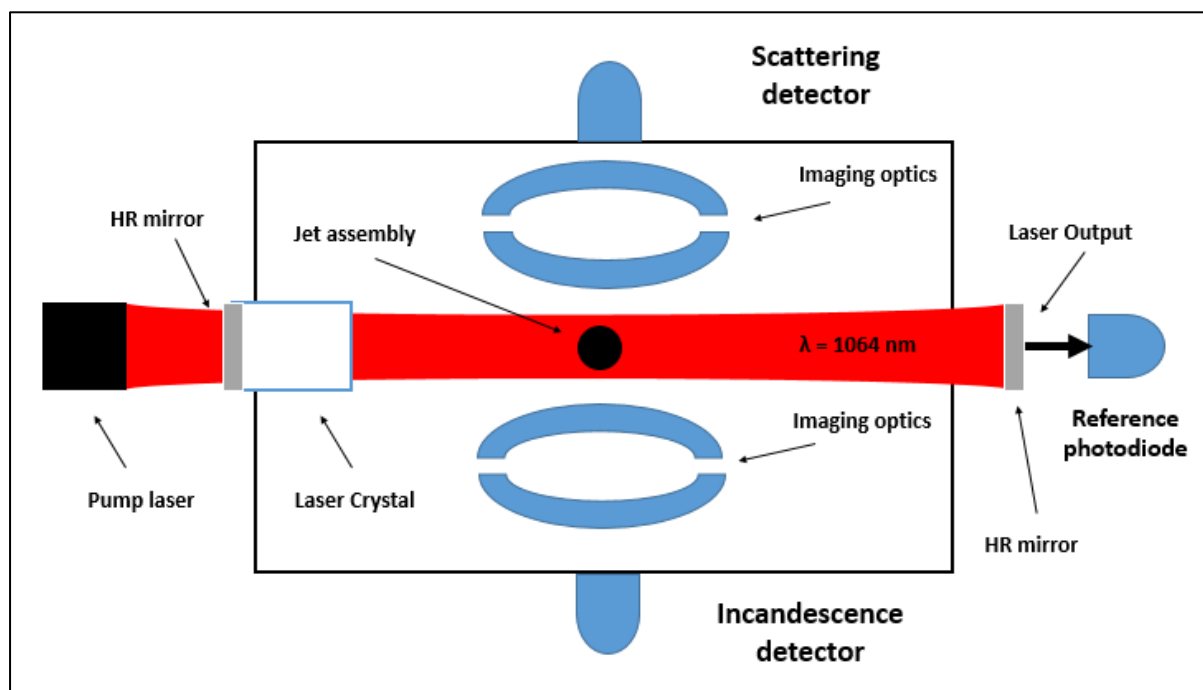


Figure 2.6: Schematic of the measurement chamber of the SP2-XR (figure adapted from the SP2-XR manual).

The flow of aerosol particles is directed through the inlet and the aerosol jet to the center of the Gaussian shape continuous Nd:YAG laser beam ( $\lambda = 1064 \text{ nm}$ ), characterized by an intra-cavity circulating power up to  $1 \text{ MW cm}^{-2}$ . The laser radiation is absorbed and scattered by the particles which consecutively heat up. In the presence of coated black carbon particles this warming removes the coating material in a time period depending on the coating thickness and its chemical composition. The BC cores eventually reach a temperature of approximately 4230-4325 K, incandescing and emitting a thermal/visible signal before vaporizing (Moteki and Kondo, 2010). The peak intensity of the thermal emission at the core boiling point is proportional to the mass of each particle. The incandescence signal passes through a band pass filter, nominally from 400 nm to 750 nm, and it is recorded via a single photomultiplier tube. The SP2-XR has only one detector for the incandescence signal, whereas the SP2 has two: the broadband and the narrowband (Sect. 2.3.1). The incandescence signal from the SP2-XR can be compared to the one from the broadband channel of the SP2.

Similarly to the SP2, the SP2-XR allows the particles optical sizing by recording the elastically scattered light with an avalanche photo diode with a band pass filter centered at 1064 nm. The non-BC particles number concentration and optical size distribution are then derived. The SP2-XR is not equipped with the two element APD, used in the SP2 to evaluate the position of the particles in the laser beam and the particles differential scattering cross section, as described in Gao et al. (2007). This still enables the use of the LEO-fit method (Gao et al. 2007 and Schwarz et al. 2008) to quantitatively determine the coating thickness of black carbon particles. However, two other methods could potentially be applied to infer the BC coating characteristics: the qualitative delay-time method and a quantitative method based on the assessment of the differential scattering cross-section without the use of the two element APD (Moteki and Kondo 2008).



## 2.4 Comparison of BC measuring techniques

Over the last decade, the comparability of black carbon mass concentration obtained from using different techniques has been widely investigated. Since there is not yet a universally accepted BC mass quantification technique, it is extremely important to understand how the various instruments and techniques compare to each other and what the reasons behind these potential differences are.

As mentioned at the beginning of this Chapter, absorption is not a proxy for black carbon mass concentration, unless having the knowledge on the mixing state and optical properties of the sampled aerosols. In this case, one can apply the appropriate corrections needed and the proper BC mass absorption cross sections (which might be calculated using reference techniques such as laser induced incandescence or well calibrated thermal-optical technique) to convert an absorption coefficient into an equivalent black carbon mass concentration. In general, it is very difficult to own all this information during a field campaign because of the necessity of a combination of instruments. In contrast, the thermal optical measurements of EC mass or the LII measurements of rBC mass do not require a prior knowledge or assumed values of the  $MAC_{BC}$ , and for this reason these techniques are recommended to obtain reliable BC mass concentrations measurements.

Numerous works investigated the comparability between eBC and EC mass or the difference between eBC and rBC mass concentrations. Some studies showing the discrepancy between eBC from the MAAP and rBC from the SP2 are discussed in Chapter 5. The lack of intercomparison studies of EC mass and rBC mass and the unresolved direction of the systematic difference between these two quantities was the motivation of the study presented in Chapter 3.

## Chapter 3:

### Comparison of co-located rBC and EC mass concentration measurements during field campaigns at several European sites

Rosaria E. Pileci<sup>1</sup>, Robin L. Modini<sup>1</sup>, Michele Bertò<sup>1</sup>, Jinfeng Yuan<sup>1</sup>, Joel C. Corbin<sup>1,\*</sup>, Angela Marinoni<sup>2</sup>, Bas J. Henzing<sup>3</sup>, Marcel M. Moerman<sup>3</sup>, Jean P. Putaud<sup>4</sup>, Gerald Spindler<sup>5</sup>, Birgit Wehner<sup>5</sup>, Thomas Müller<sup>5</sup>, Thomas Tuch<sup>5</sup>, Arianna Trentini<sup>6</sup>, Marco Zanatta<sup>7</sup>, Urs Baltensperger<sup>1</sup> and Martin Gysel-Beer<sup>1</sup>

<sup>1</sup>Laboratory of Atmospheric Chemistry, Paul Scherrer Institute (PSI), 5232 Villigen PSI, Switzerland

<sup>2</sup>CNR-ISAC—Italian National Research Council, Institute of Atmospheric Science and Climate, via Gobetti 101, 40129 Bologna, Italy

<sup>3</sup>Netherlands Organisation for Applied Scientific Research (TNO), Princetonlaan 6, 3584 Utrecht, the Netherlands

<sup>4</sup>European Commission, Joint Research Centre (JRC), Ispra, Italy

<sup>5</sup>Leibniz Institute for Tropospheric Research (TROPOS), Permoserstrasse 15, 04318, Leipzig, Germany

<sup>6</sup>Regional Agency for Prevention, Environment and Energy, Emilia-Romagna, 40122, Bologna, Italy

<sup>7</sup>Alfred Wegener Institute, Helmholtz Centre for Polar and Marine Research, Bremerhaven, Germany

\*now at: Metrology Research Centre, National Research Council Canada, 1200 Montreal Road, Ottawa K1A 0R6, Canada

*Correspondence to:* R. L. Modini (robin.modini@psi.ch) and M. Gysel-Beer (martin.gysel@psi.ch)

Published in *Atmospheric Measurement Techniques*, <https://doi.org/10.5194/amt-14-1379-2021>.

**Abstract.** The mass concentration of black carbon (BC) particles in the atmosphere has traditionally been quantified with two methods: as elemental carbon (EC) concentrations measured by thermal-optical analysis and as equivalent black carbon (eBC) concentrations when BC mass is derived from particle light absorption coefficient measurements. Over the last decade, ambient measurements of refractory black carbon (rBC) mass concentrations based on laser-induced incandescence (LII) have become more common, mostly due to the development of the Single-Particle Soot Photometer (SP2) instrument. In this work, EC and rBC mass concentration measurements from field campaigns across several background European sites (Palaiseau, Bologna, Cabauw and Melpitz) have been collated and examined to identify the similarities and differences between BC mass concentrations measured by the two techniques. All EC concentration measurements in PM<sub>2.5</sub> were performed with the EUSAAR-2 thermal-optical protocol. All rBC concentration measurements were performed with SP2s calibrated with the same calibration material as recommended in the literature. The observed values of median rBC to EC mass concentration ratios on single campaign level were 0.53, 0.65, 0.97, 1.20 and 1.29, respectively, and the geometric standard deviation (GSD) was 1.5 when considering all data points from all five campaigns. This shows that substantial systematic bias between these two quantities occurred during some campaigns, which also contributes to the large overall GSD. Despite considerable variability of BC properties and sources across the whole data set, it was not possible to clearly assign reasons for discrepancies to one or the other method, both known to have their own specific limitations and uncertainties. However, differences in the particle size range covered by these two methods were identified as one likely reason for discrepancies.

Overall, the observed correlation between rBC and EC mass reveals a linear relationship with a constant ratio, thus providing clear evidence that both methods essentially quantify the same property of atmospheric aerosols, whereas systematic differences in measured absolute values by up to a factor of 2 can occur. This finding for the level of agreement between two current state-of-the-art techniques has important implications for studies based

on BC mass concentration measurements, for example for the interpretation of uncertainties of inferred BC mass absorption coefficient values, which are required for modelling the radiative forcing of BC. Homogeneity between BC mass determination techniques is very important also towards a routine BC mass measurement for air quality regulations.

### 3.1 Introduction

Light absorbing aerosols exert a positive radiative forcing through direct absorption of solar radiation. Moreover, their heating can change the atmospheric dynamics and thereby, cloud formation and lifetime (Samset et al., 2018). Despite the relatively small mass abundance of black carbon (8–17 %; Putaud et al. 2010), it dominates the aerosol light absorption in the atmosphere (Bond et al., 2013). Additional, significant contribution comes from brown carbon (Kirchstetter et al., 2004), tar balls (Adachi et al., 2019) and mineral dust (Sokolik and Toon, 1999).

Black carbon aerosols possess a unique set of properties: they are refractory (Schwarz et al., 2006), strong absorbers of short- and long-wave radiation (Bond and Bergstrom, 2006), insoluble in water (Fung, 1990) and composed primarily of graphene-like sp<sup>2</sup>-bonded carbon (Medalia and Heckman, 1969). The source of black carbon is the incomplete combustion of hydrocarbon fuels, including fossil- and bio-fuels (Bond et al., 2013). BC mass concentration data from atmospheric measurements are used in many applications such as validation of model simulations (Grahame et al., 2014; Hodnebrog et al., 2014) and quantification of the mass absorption coefficient of BC ( $MAC_{BC}$ ). The latter is defined as the ratio of the light absorption coefficient caused by BC to the BC mass concentration, and is a crucial parameter in modelling the BC radiative forcing (Matsui et al., 2018). For these reasons, it is important to assess the accuracy and comparability of different BC mass measurement techniques.

There is neither an SI (International System of Units) traceable reference method nor a suitable standard reference material for quantifying BC mass (Baumgardner et al., 2012; Petzold et al., 2013). This presents a challenge for the long-term, routine monitoring of BC mass concentrations in observation networks such as GAW (Global Atmosphere Watch), ACTRIS (European Research Infrastructure for the observation of Aerosols, Clouds and Trace Gases) and IMPROVE (Interagency Monitoring of PROtected Visual Environments). The lack of a reference method is due to variability in the microstructure of BC produced by different combustion sources (Adachi et al., 2010), the difficulty of isolating BC from other particulate matter, and the lack of direct mass-based methods selective to BC without interferences (Baumgardner et al., 2012).

In practice, the BC mass is defined operationally through methodologies that use distinct physico-chemical and/or optical properties of BC in order to quantify its mass concentration in aerosols. The following three different techniques are most commonly applied: filter based thermal-optical evolved gas analysis (Huntzicker et al., 1982; Chow et al., 2007; Cavalli et al., 2010); laser induced incandescence (LII) (Schraml et al., 2000; Stephens et al., 2003; Schwarz et al., 2006; Michelsen et al., 2015) and aerosol light absorption based methods (Rosen et al., 1978; Hansen et al., 1984; Arnott et al., 2003; Petzold et al., 2005). The specific terms used to refer to the mass of BC quantified by each of these three techniques are: elemental carbon (EC), refractory black carbon (rBC) and equivalent black carbon (eBC), respectively (Petzold et al., 2013). eBC mass measurements are not further addressed here, as they rely on prior knowledge or assumed values of the  $MAC_{BC}$ . Such prior knowledge is not required for thermal optical measurements of EC mass or for LII measurements of rBC mass.

Thermal-optical analysis (TOA) and the LII technique both make use of the high refractoriness of BC to quantify its mass, although in a different manner. In comparing these two techniques, it is essential to define what is meant by BC. The popular Bond et al. (2013) definition of BC is, fundamentally, a summary of the properties of highly-graphitized carbon found in soot particles. There are, however, other forms of light-absorbing carbonaceous particulate matter (PM), with different cross-sensitivities for TOA and LII. Building on earlier studies (e.g. Bond 2001), Corbin et al. (2019) recently proposed a refined classification of light-absorbing carbonaceous PM into four classes: soot-BC, char BC, tar brown carbon and soluble brown carbon, and they provided an overview of the respective physico-chemical properties. This refined classification provides a useful framework in describing the responses of TOA and LII. For example tar brown carbon, an amorphous form of carbon, is sufficiently refractory to contribute to EC mass, whereas it is not sufficiently refractory to cause substantial interference in

rBC (Corbin and Gysel–Beer, 2019). Any work that compares BC measurement techniques should therefore consider the types of carbonaceous material present in the sample.

Very few intercomparisons of EC mass and rBC mass are available in the literature, particularly when it comes to ambient aerosols, despite the fact that both methods are frequently applied these days. This means that the debate on the comparability of these two quantities is still largely unresolved. Some studies have shown that the two quantities can agree to within a few percent (Laborde et al., 2012b; Miyakawa et al., 2016; Corbin et al., 2019), while other studies have shown they can systematically differ by factors of up to 2 to 3 in either direction (e.g. Zhang et al., 2016; Sharma et al., 2017).

In this work, we examined and quantified the level of agreement or disagreement between BC mass concentrations measured by the thermal–optical analysis and the LII technique. For this purpose, we compared co–located measurements of EC and rBC mass concentrations from field campaigns performed at several European sites (Bologna, Cabauw, Palaiseau and Melpitz) in order to sample different aerosol types. Care was taken to harmonize the applied methods: all thermal optical measurements were performed with the same temperature protocol (EUSAAR–2, European Supersites for Atmospheric Aerosol Research; Cavalli et al., 2010) and all SP2 calibrations were done using the same calibration material. This first multi–site intercomparison allows us to more quantitatively assess the extent to which the EC and rBC concentration measurements agree or disagree with each other. Potential reasons for discrepancies such as different size cuts, calibration uncertainties and various interferences are discussed.

## 3.2 Methods

### 3.2.1 Sampling campaigns: measurements sites and experimental setup

The observations presented here include measurements from five field campaigns at four different sites, three of which are part of the ACTRIS network (Aerosols, Clouds and Trace gases Research InfraStructure; [www.actris.eu](http://www.actris.eu)). Basic information (site and country, station code, coordinates, altitude and year/season) of each field campaign is summarized in Table S3.1.

The Melpitz research site of TROPOS (Germany; 51° 32' N, 12° 56' E, 87 m a.s.l.) is located in the lowlands of Saxony, 41 km NE of Leipzig, Germany. The nearest village with about 230 inhabitants is 300 m east of the station. The site is representative for the regional background in Central Europe (Spindler et al., 2012, 2013) since it is situated on a flat meadow, surrounded by agricultural land (Spindler et al., 2010). The area is sometimes influenced by long–range transported air masses from source regions in eastern, south eastern and southern Europe which can contain, especially in winter, emissions from coal heating (van Pinxteren et al., 2019). Two separate field campaigns were performed in summer (from 6 May 2015 to 1 July 2015) and winter (from 2 to 23 February 2017). During the two campaigns, the SP2 was placed behind a nafion dryer (model MD700, Perma Pure) with a PM<sub>10</sub> inlet about 6 m above ground. The PM<sub>2.5</sub> sampler for the OC/EC samples was placed nearby. The meteorological conditions and aerosol characteristics encountered during the campaigns are described by Altstädter et al. (2018) for the summer campaign and by Yuan et al. (2020) for the winter campaign.

The KNMI (Koninklijk Nederlands Meteorologisch Instituut) Cabauw Experimental Site for Atmospheric Research (Netherlands; 51° 58' N, 4° 55' E, –0.7 m a.s.l.) is located in the background area of Cabauw, 20 km from Utrecht, 30 km from Rotterdam and 50 km from the North sea. The nearby region is agricultural in an otherwise densely populated area, and surface elevation changes are at most a few meters over 20 km. During the campaign, the SP2 was placed behind a nafion dryer (model MD700, Perma Pure) with a PM<sub>10</sub> inlet situated 4.5 m above the ground. The PM<sub>10</sub> sampler, from which filters off–line OC/EC analyses were carried out, did not include a dryer in the sampling line in line with the GAW recommendations (GAW Report–No. 227). The measurements at this site were performed from 13 to 28 September 2016. The meteorological conditions and aerosol characteristics encountered during the campaign are described by Tirpitz et al. (2020).

The Bologna measurements were performed at the main seat of CNR–ISAC (Consiglio Nazionale delle Ricerche – Institute of Atmospheric Sciences and Climate), in Bologna (Italy; 44° 31' N, 11° 20' E; 39 m a.s.l.). The site is

classified as urban background and is located in the Po Valley, a European pollution hot spot due to its orography, meteorological conditions and high presence of human activities, resulting in a large number of anthropogenic emission sources (Vecchi et al., 2009; Putaud et al., 2010; Ricciardelli et al., 2017; Bucci et al., 2018). During the campaign, a PM<sub>2.5</sub> sampler, not equipped with a drier, was situated at the ARPAE Supersito (inside CNR–ISAC area). The SP2 was located inside a fully instrumented mobile van in the CNR parking area, about 50 m away from the ARPAE Supersito. The instruments in the van were connected to two inlet lines situated on the top of the vehicle at a height of 3 m and connected to the main inlet line with an inner diameter of 5 cm; no size cut was performed. The sampled air was dried to below 30 % relative humidity using two custom–built, silica–gel–loaded diffusion driers. The data presented in this paper were collected from 7 to 31 July 2017. The meteorological conditions and the aerosol properties of this campaign are described by Pileci et al. (in preparation).

The SIRTA Atmospheric Research Observatory (France; 48° 43' N 2° 12' E; 160 m a.s.l.) is situated in Palaiseau, 25 km South of Paris. The station is characterized as suburban background (Haefelin et al., 2005). This site is influenced both by fresh and aged black carbon mainly originating from the Paris area. It is impacted by road transport emissions all year round and residential wood burning during the winter (Laborde et al., 2013; Petit et al., 2015; Zhang et al., 2018). The SP2 along with many other instruments was installed in an air–conditioned trailer of the SIRTA measurement platform. For the OC/EC measurements, high–volume samplers with a PM<sub>2.5</sub> cut–off were available in the same area. The measurements were performed from 15 January to 15 February 2010. EC and rBC concentrations during this campaign have previously been published in Laborde et al. (2013).

### 3.2.2 Thermal optical analysis

#### 3.2.2.1 Measurement principle, OC/EC split and involved artefacts

In thermal–optical evolved gas analysis (TOA), carbonaceous particles deposited on a filter are thermally desorbed/reacted in order to determine the total carbon mass. This technique further divides the total carbon (TC) into EC and organic carbon (OC) according to the expectation that EC is refractory in an inert atmosphere while OC is not (Chow et al., 1993; Birch and Cary, 1996; Bond, 2001; Chow et al., 2004). Therefore, TOA provides operationally defined OC and EC mass rather than fundamental quantities. This basic binary split does not acknowledge that neither OC nor EC are well–defined materials. Instead, carbonaceous matter in aerosols populates the multidimensional space of chemical and physical properties more or less in a continuous manner (Saleh et al., 2018; Corbin et al., 2020). Nevertheless, the binary split approach aims at providing an operationally defined EC mass that corresponds to “true” BC mass as defined on a conceptual level by Bond et al. (2013) and Corbin et al. (2019) (see Sect. 3.1).

In TOA analysis, the carbonaceous material deposited on a punch of a quartz–fibre filter is thermally desorbed through progressive heating; first in an inert atmosphere of pure helium (He) at multiple moderate temperatures (~500–700 °C) (inert mode) and then in an oxidizing atmosphere (98 % He and 2 % O<sub>2</sub>) at high temperature (~850 °C). The applied duration and the temperature of each step vary between different thermal protocols, as discussed below in Sect. 3.2.2.2. The evolving carbon is catalytically converted first to carbon dioxide (CO<sub>2</sub>) and then to methane (CH<sub>4</sub>). CH<sub>4</sub> is then quantified using a flame ionization detector (FID) and reported as OC (inert mode) and EC (oxidizing mode) mass. The instrument type applied in this study and most commonly used to perform TOA measurements is the OC/EC analyser manufactured by Sunset Laboratory Inc. (Tigard, OR).

Ideally, all OC would desorb in the inert He atmosphere and EC would exclusively burn off in the oxidizing O<sub>2</sub> atmosphere (Chow et al., 1993; Birch and Cary, 1996). In practice, a fraction of carbonaceous matter may be more refractory than the applied separation threshold, while not being BC in a strict sense. This would cause a positive bias in measured EC mass. In addition, a fraction of the OC can pyrolyze in the He step to form pyrolytic carbon (PC), which is thermally stable and only desorbs in the O<sub>2</sub> step, thereby causing a charring artefact in the mutual quantification of OC and EC. To correct for this latter effect a laser at 658 nm is used in combined thermal–optical analysis to monitor the light transmission through the loaded filter before and during the analysis. The measurement principle behind this so-called thermal-optical transmission (TOT) correction approach is explained in Sect. S3.1. The charring correction can also be done using light reflectance (thermo–optical reflectance method;

TOR) instead of transmittance. As reported in the review paper by Karanasiou et al. (2015), EC values of atmospheric samples determined using the TOT method are often up to 30–70 % lower than those determined using the TOR method due to greater evaporation and saturation artefacts in the reflection approach (see Sect. S3.1). Therefore, all EC mass values reported in this study are based on the TOT method.

The above described assumptions on the optical charring correction are only partially fulfilled, typically leaving charring artefacts as a main source of bias even for optically corrected EC mass data (Chow et al., 2004; Subramanian et al., 2006). Pyrolysis depends on many factors, including the amount and type of organic compounds, temperature steps in the analysis and the residence time at each temperature step. This makes the TOA technique sensitive to the aerosol type collected on the filter. Water extraction experiments have shown that water soluble organic carbon (WSOC) compounds are particularly prone to causing charring (Yu et al., 2002; Piazzalunga et al., 2011; Zhang et al., 2012; Giannoni et al., 2016). Samples with a high WSOC content come e.g. from biomass and wood burning (Hitzenberger et al., 2006; Reisinger et al., 2008; Chen et al., 2015). A filter water-washing step prior to TOA can be used to remove WSOC, thereby reducing charring artefacts and improving comparability of different protocols for EC mass measurements (Yu et al., 2002; Piazzalunga et al., 2011). However, filter pre-washing is generally not applied in long-term monitoring TOA measurements for practical reasons (the washing step is time consuming). In these cases, the charring phenomenon can be reduced by adopting a thermal protocol with a sufficiently long residence time at each temperature step in the He atmosphere to allow for maximum OC evolution (Subramanian et al., 2006; Karanasiou et al., 2015).

The OC/EC split can be also biased by EC pre-combustion: EC can thermally evolve in the presence of oxidizing species (Watson et al., 2005; Corbin et al., 2014, 2015), and soluble inorganic compounds (Chow et al., 2001; Yu et al., 2002) and metal salts (Aakko-Saksa et al., 2018) can catalyse EC pre-combustion. If the amount of EC undergoing pre-combustion is significant relative to the amount of PC formed during the analysis, the optical correction (transmittance or reflectance) is not able to account for it and this may cause an underestimation of the EC concentration.

Moreover, soluble brown carbon on filters can affect the laser correction if it was evolving during the OC steps, thereby causing a positive EC artefact. However, soluble brown carbon absorbs much less per unit mass than EC at the red wavelength ( $\lambda = 635$  nm) of the laser used in the thermal-optical instruments, since its absorbance decreases strongly from the blue-UV region of the electromagnetic spectrum towards the red region (Karanasiou et al., 2015). This reduces the potential interference of soluble brown carbon via the introduction of a bias in the optical charring correction. Recently, Massabò et al. (2019) developed a modified Sunset Lab Inc. EC/OC analyser to measure the brown carbon content in the sample by adding a second laser diode at  $\lambda = 405$  nm.

Tar brown carbon only evolves in the oxidizing step of TOA due to its refractoriness (Corbin et al., 2019). Therefore, it is assigned to EC independent of its light absorption properties. This is in contrast to LII, where tar brown carbon only gives marginal contribution to observed rBC mass (Sect. 3.2.3.3).

Further artefacts in TOA analysis can be caused by carbonate carbon, as discussed in Wang et al. (2010), Karanasiou et al. (2015) and Querol et al. (2012). Thermal protocols can be designed to minimize this artefact by having most carbonate carbon evolve as OC (as is the case with the EUSAAR-2 protocol used in this work; Sect 3.2.2.2). However, minor positive, carbonate-related artefacts in EC cannot be excluded (Karanasiou et al., 2011).

### **3.2.2.2 EUSAAR-2 vs other existing protocols**

Many variants of thermal protocols exist for the thermal-optical analysis of EC mass (Bautista et al., 2015). The results presented in this study are based on the EUSAAR-2 protocol, which was developed by Cavalli et al. (2010). The EUSAAR-2 protocol was specifically optimized for aerosol typically encountered at European background sites, and it has recently been selected as the European standard thermal protocol to be applied in air quality networks for the measurement of TC (total carbon), OC, and EC in PM<sub>2.5</sub> (particulate matter) samples (European Committee for Standardisation Ambient air, 2017; EN16909:2017). Besides EUSAAR-2, the IMPROVE-A (Interagency Monitoring of PROtected Visual Environments; Chow et al., 1993, 2007) and NIOSH (National Institute for Occupational Safety and Health; Birch and Cary, 1996) thermal protocols are also

commonly used for TOA analysis. Various NIOSH-like protocols (NIOSH-5040, NIOSH-840, NIOSH-850, and NIOSH-870) exist that are all modified versions of the Birch and Cary (1996) and Birch et al. (1999) protocols.

Table 3.1 summarizes the differences between EC measured with EUSAAR-2 and with other protocols reported in previous literature studies, with a particular focus on the thermal protocols that are considered in this study (e.g. see Fig. 3.6). The use of different thermal protocols can result in a wide elemental carbon-to-total carbon variation by up to a factor of five (Cavalli et al., 2010). In general, it has been observed that protocols with a rather low peak temperature in the inert mode like EUSAAR-2 and IMPROVE generally classify more carbon as EC compared to the NIOSH protocol (Karanasiou et al., 2015). The EnCan-Total-900 protocol has much longer retention time at each temperature step compared to the IMPROVE and NIOSH methods and does not involve a charring correction (Huang et al., 2006; Chan et al., 2010).

Table 3.1: Overview of reported differences between EC calculated with other protocols minus the EC calculated with the EUSAAR-2 protocol: (a) Han et al. (2016); (b) Cheng et al. (2013); (c) Karanasiou et al. (2015).

Protocols	Relative difference compared to EUSAAR-2 (TOT)
IMPROVE (TOR)	~ +25 % (a)
IMPROVE-A (TOR)	~ -10 % (b)
EnCan-Total-900	~ ±25 % (c)

### 3.2.2.3 Variability of EC measurements with the EUSAAR-2 protocol

Given the artefacts involved in TOA analysis, different instruments can measure different EC concentrations for the same sample, even if the same thermal protocol is used. For this reason, the Joint Research Centre (JRC) European Reference Laboratory for Air Pollution (ERLAP) organizes annual instrumental inter-laboratory comparisons in order to harmonize measurements from different Sunset instruments that employ the EUSAAR-2 protocol, which typically include 15 to 30 participants. The measurement performances are evaluated using several PM<sub>2.5</sub> quartz fiber filters collected at a regional background site in Italy. Since the true concentrations of EC or TC in these ambient samples are unknown (due to the lack of suitable reference methods or materials), the expected concentrations are chosen ('assigned') as the robust averages (i.e. with outliers removed) of the TC and EC mass concentrations measured by all participants.

The latest intercomparison yielded an EC/TC ratio repeatability (with the same instrument over time) of 3 % to 8 % and a EC/TC ratio reproducibility (amongst different instruments) of 12 % to 17 % (across 21 participants), where the method precision becomes exponentially poorer toward lower TC contents (<10 µgC cm<sup>-2</sup>) and lower EC/TC ratios (<0.07) (EMEP/CCC-Report 1/2018). Table 3.2 presents EC bias and variability (see Sect. S3.2 of the SI for further information) for the instruments used in each campaign (based on data from the ERLAP intercomparison campaign that occurred most recently before or after the campaign in question). The Palaiseau campaign EC samples were analyzed by the Institut des Géosciences de l'Environnement (IGE, Grenoble), the Cabauw samples were analyzed by the Joint Research Center (JRC, Italy), the Melpitz (summer and winter) samples were analyzed by the Leibniz-Institut für Troposphärenforschung (TROPOS), and the Bologna campaign samples were analyzed by ARPAE. The EC bias and variability of the instrument used for analyzing the Bologna filter samples, which did not participate in a full ERLAP intercomparison, was determined by comparison with the JRC ERLAP reference instrument for nine filter samples from the Bologna campaign. The EC bias found was smaller than 20 % for all applied OC/EC analyzers, which is within the TOA measurement uncertainty. Therefore, we did not correct the EC measurements reported in this work for these biases.

Blank filters were analyzed for all campaigns. The blank value for EC mass was always below detection limit or negligibly small compared to EC mass on loaded filter samples, such that applying a blank correction does not make a difference for the resulting EC mass concentration.

Table 3.2: Description of the methodology for EC mass concentration measurements: thermal protocol, sampling duration, inlet size cut, flow rate and performance during the ERLAP intercomparison, in relative terms for EC bias and variability (Sect. 3.2.2.3 and Eqs. S3.1 and S3.2).

Station code	Thermal protocol for $m_{EC}$	Sampling duration (h)	Inlet size cut	Flow rate	EC bias	EC variability
Palaiseau	EUSAAR-2 (TOT)	12	PM <sub>2.5</sub>	30 m <sup>3</sup> in 12 hours	-6.0 %	11.9 %
Melpitz winter	EUSAAR-2 (TOT)	24	PM <sub>2.5</sub>	30 m <sup>3</sup> h <sup>-1</sup>	-6.0 %	4.3 %
Melpitz summer	EUSAAR-2 (TOT)	24	PM <sub>2.5</sub>	30 m <sup>3</sup> h <sup>-1</sup>	16.1 %	4.4 %
Cabauw	EUSAAR-2 (TOT)	12	PM <sub>10</sub>	27.6 m <sup>3</sup> in 12 hours	-6.7 %	3.0 %
Bologna	EUSAAR-2 (TOT)	24	PM <sub>2.5</sub>	38.3 L min <sup>-1</sup>	1.6 %	6.8 %

Blank filters were analyzed for all campaigns. The blank value for EC mass was always below detection limit or negligibly small compared to EC mass on loaded filter samples, such that applying a blank correction does not make a difference for the resulting EC mass concentration.

### 3.2.3 The Single Particle Soot Photometer (SP2)

#### 3.2.3.1 Principle of measurement

Laser induced incandescence occurs when a high-intensity laser is used to heat light absorbing and highly refractory particles to high enough temperatures for them to emit considerable grey/blackbody radiation. LII can be used to quantify rBC carbon mass concentration in aerosols by detecting the emitted thermal radiation, which is approximately proportional to rBC mass. There are different instrumental approaches for LII using both pulsed-shot lasers (Michelsen et al., 2015), and continuous-wave lasers, as in the commercially-available Single-Particle Soot Photometer (SP2, Droplet Measurement Technologies, Longmont, CO, USA). The SP2 quantifies the rBC mass in individual particles (Stephens et al., 2003; Schwarz et al., 2006; Moteki and Kondo, 2007). When aerosol particles enter the instrument, they are directed into the centre of an intra-cavity Nd:YAG laser beam with a wavelength of 1064 nm where they are irradiated. BC-containing particles absorb the laser light causing them to heat up and incandesce. Since the thermal radiation emitted by individual black carbon particles is proportional to the volume (and mass) of BC in the particle (Moteki and Kondo, 2010), this radiation intensity can be converted to rBC mass using an empirical calibration curve.

#### 3.2.3.2 rBC mass calibration

The relationship between incandescence signal peak amplitude and BC mass depends on the BC type (Moteki and Kondo, 2010; Laborde et al., 2012a), which means the instrument should be calibrated with a material that represents the type of BC one seeks to measure. Unfortunately, many types of BC are found in the atmosphere, such that it is typically not possible to calibrate the SP2 specifically with atmospheric BC. Instead, a fixed calibration using commercial BC materials is commonly applied. Therefore, potential variation in the chemical microstructure of atmospheric BC results in uncertainty in rBC mass measurements.



Table 3.3: Description of the measurement methodology for rBC mass concentration adopted during each campaign, along with SP2 owner (Paul Scherrer Institute (PSI), Alfred Wegner Institut (AWI) and Institut de Géosciences de l'Environnement (IGE), calibration material (fullerene soot batch), calibration method selection, and inlet size cut.

Station code / campaign	SP2 owner	Revision, acquisition card type	Calibration material (fullerene soot batch)	Size selection method for calibration	Inlet size cut	SP2 upper detection limit [nm]
Palaiseau	PSI	C, 14 bits – 2.5 MHz – 8 channels	Fullerene Soot (stock 40971, lot FS12S011)	DMA	PM <sub>10</sub>	439
Melpitz winter	AWI	C, 14 bits – 2.5 MHz – 8 channels	Fullerene Soot (stock 40971, lot W08A039)	APM	PM <sub>10</sub>	722
Melpitz summer	PSI	C, 14 bits – 2.5 MHz – 8 channels	Fullerene Soot (stock 40971, lot FS12S011)	APM	PM <sub>10</sub>	766
Cabauw	IGE	C, 14 bits – 2.5 MHz – 8 channels	Fullerene Soot (stock 40971, lot FS12S011)	DMA	PM <sub>10</sub>	537
Bologna	PSI	C, 14 bits – 2.5 MHz – 8 channels	Fullerene Soot (stock 40971, lot FS12S011)	DMA	No size cut	676

In this study, two different batches of fullerene soot (Alfa Aesar; stock 40971, lots FS12S011 and W08A039) were used. The former is recommended as calibration material (Baumgardner et al., 2012) since it was shown to be suitable for quantifying BC in diesel engine exhaust (agreement within 10 % for rBC cores  $\leq$  40 fg; Laborde et al., 2012b). Calibrations using the latter batch agreed with those using the former batch within 5 %. In this work, three different SP2s (PSI, IGE, AWI) were used to acquire the data. This does however not contribute appreciably to uncertainties, since the reproducibility of measured rBC mass size distributions was shown to be  $\pm$ 10 % during a large SP2 intercomparison involving six SP2s from six different research groups (Laborde et al., 2012b). The SP2 used during the Melpitz campaigns was calibrated using an APM to select the calibration particles by mass. For the other campaigns a DMA was used for size selection and the corresponding particle mass was calculated using effective density data reported in (Gysel et al., 2011). The latter approach results in an additional error of about 10 %.

### 3.2.3.3 Potential interferences and artefacts

One of the strengths of the SP2 is that the incandescence signal is not perturbed by the presence of non-refractory matter internally or externally mixed with BC (Moteki and Kondo, 2007; Slowik et al., 2007). However, other types of highly refractory and sufficiently light-absorbing (at 1064 nm) material can incandesce in the SP2 laser. Therefore, SP2 measurements can potentially contain interferences from metals, metal oxides (Moteki et al., 2017), volcanic ash and dust (rarely) (Kupiszewski et al., 2016). Fortunately, such materials are usually observed only rarely in atmospheric aerosols in large enough quantities to cause significant SP2 measurement artefacts. Furthermore, if they are present, in some cases their presence can be identified and ignored when calculating rBC mass. Specifically, potential interference can be determined with the use of the spectral bandpass filters, which permits the determination of the color temperature of incandescence (Moteki et al., 2017). Recently, Sedlacek et al. (2018) found that rBC-free organic particles that absorb light at 1064 nm can char and form rBC under sufficiently high SP2 laser power, resulting in an rBC overestimate. In general, this artefact is only likely to be relevant in biomass burning plumes that contain organic tar balls that can absorb light at 1064 nm (Sedlacek et al., 2018). Marine engines operated with heavy fuel oil can also produce tar particles, but Corbin and Gysel–Beer

(2019) found that the contribution of such particles to rBC mass was negligible. Furthermore, it is possible to distinguish incandescing tar particles from soot BC with SP2 measurements by examining the ratio of scattering–at–incandescence to incandescence signals (Corbin and Gysel–Beer, 2019).

### 3.2.3.4 SP2 detection efficiency and detection range

The SP2 lower detection limit depends on both physical limitations of the detection technique and instrument parameters chosen by the operator (Schwarz et al., 2010). With optimal setup, the SP2 can reach unit counting efficiency for rBC mass  $m_{\text{rBC}} \approx 0.12$  fg (Schwarz et al., 2010; Laborde et al., 2012a), which corresponds to an rBC mass equivalent diameter of  $D_{\text{rBC}} \approx 50$  nm using a void–free BC bulk density of  $1800 \text{ kg m}^{-3}$  (Moteki and Kondo, 2010). The lower cut–off size for unit counting efficiency can be larger if the SP2 is not optimally setup. Usually the SP2’s counting efficiency is robust down to  $D_{\text{rBC}} \approx 80$  nm ( $m_{\text{rBC}} \approx 0.48$  fg). We only considered the data of particles with BC cores greater than  $D_{\text{rBC}} = 80$  nm in this study, as exact characterization of the cut–off curve was not performed in all campaigns. Note, poor counting efficiency for BC cores with greater mass than this limit has been reported by Gysel et al. (2012). PALAS soot, which is characterized by very small primary sphere size and very low fractal dimension, resulting in relatively enhanced heat loss. However, we are not aware of studies indicating reduced counting efficiency for atmospherically relevant BC particles, which have larger primary spheres and higher fractal dimension, compared to PALAS soot.

The SP2 was operated downstream of inlets with a 50 % cut–off diameter at  $10 \mu\text{m}$  in every campaign except for the Bologna campaign, where no external upper size cut was applied. In addition, the SP2 is unable to quantify rBC mass above a certain limit due to the saturation of the electronics that record the signals. This saturation limit can be varied via detector gains, with typical settings resulting in upper limits of quantification ranging from  $D_{\text{rBC}} \approx 500$  nm to around  $D_{\text{rBC}} \approx 1 \mu\text{m}$ . Consequently, the total BC mass may be underestimated if BC cores greater than the upper limit of quantification contribute substantially to total BC mass. Recently, Schwarz (2019) evaluated an algorithm for reconstructing the peak incandescence intensity from the truncated incandescence signals of large BC cores. We did not apply this approach as it only allows increasing the upper limit of quantification by around 15 % in terms of  $D_{\text{rBC}}$  without introducing substantial uncertainty in the upper limit of quantification.

The SP2 has no lower number concentration detection limit (in the absence of leaks), while particle counting coincidence imposes an upper concentration limit when multiple BC particles cross the laser beam simultaneously. Coincidence only caused negligibly low bias in measured rBC mass concentrations for the concentration ranges that were encountered in this study.

### 3.2.3.5 Methods to correct SP2 data for missing mass below LDL

Two approaches are most commonly used to extrapolate the measured rBC mass size distribution and correct for the missing rBC mass (Schwarz et al., 2006; Laborde et al., 2013). In this study, both methods were applied in order to assess the sensitivity to the correction approach (Sect. 3.3.1); based on this assessment the first of the two methods described below was determined to be preferable. The two methods are based on fitting the measured rBC mass size distribution with a unimodal lognormal function since BC mass size distributions are generally close to lognormally distributed (e.g. Fig. 3.1; and Schwarz et al., 2006; Reddington et al., 2013).

A first approach to correcting SP2 rBC measurements for potentially missed mass is based on extrapolation of the measured size distribution below and/or above the SP2 detection limits. We hereafter refer to this as the “extrapolation method”. The corrected rBC mass,  $m_{\text{rBC,corr}}^{\text{extrap}}$ , is obtained as the sum of the measured mass,  $m_{\text{rBC,meas}}$ , and a correction term,  $\Delta m^{\text{extrap}}$ :

$$m_{\text{rBC,corr}}^{\text{extrap}} = m_{\text{rBC,meas}} + \Delta m^{\text{extrap}} . \quad (3.1)$$

Here,  $\Delta m^{\text{extrap}}$  is obtained by fitting a lognormal function  $\frac{dm_{\text{fit}}}{d\log D_{\text{rBC}}}$  to the measured rBC mass size distribution and only considering potentially missed mass below the lower detection limit (LDL) of the SP2. No correction was applied for potentially missed mass above the upper detection limit (UDL) for two reasons explained in Sect. 3.3.1.1. Using this approach, the correction term simplifies to the integrated mass of the lognormal fit in the size range below the LDL:

$$\Delta m^{\text{extrap}} = \Delta m_{\text{rBC} < \text{LDL}} = \int_0^{D_{\text{LDL}}} \frac{dm_{\text{fit}}}{d\log D_{\text{rBC}}} (D_{\text{rBC}}) d\log D_{\text{rBC}} . \quad (3.2)$$

A second commonly applied approach, hereafter referred to as the “fit method”, is based on the assumption that the true BC mass size distribution in the submicron size range exactly follows a lognormal function. Under this assumption, the corrected rBC mass,  $m_{\text{rBC,corr}}^{\text{fit}}$ , is chosen as the integrated mass,  $m_{\text{fit}}$ , of a lognormal fit to the measured rBC mass size distribution (which includes corrections for contributions below the LDL and above the UDL):

$$m_{\text{rBC,corr}}^{\text{fit}} = m_{\text{fit}} = \int_0^{+\infty} \frac{dm_{\text{fit}}}{d\log D_{\text{rBC}}} (D_{\text{rBC}}) d\log D_{\text{rBC}} . \quad (3.3)$$

The corrected BC mass obtained with this second approach is composed of four terms (Eq. 3.4), which are visualized in Fig. 3.1: i) the measured rBC mass,  $m_{\text{rBC,meas}}$  (black solid line), ii) the rBC mass below the SP2 detection limit,  $\Delta m_{\text{rBC} < \text{LDL}}$  (red shading; Eq. 3.2), iii) the rBC mass above the SP2 detection limit,  $\Delta m_{\text{rBC} > \text{UDL}}$  (blue shading; Eq. 3.5), and iv) the residual area between the fit,  $m_{\text{fit}}$  and the measured rBC mass integrated in the range from  $D_{\text{LDL}}$  to  $D_{\text{UDL}}$  (denoted as  $\Delta m_{\text{fitresid}}$ ; purple shading; Eq. 3.6):

$$m_{\text{rBC,corr}}^{\text{fit}} = \Delta m_{\text{rBC} < \text{LDL}} + \Delta m_{\text{rBC} > \text{UDL}} + m_{\text{rBC,meas}} + \Delta m_{\text{fitresid}} , \quad (3.4)$$

where

$$\Delta m_{\text{rBC} > \text{UDL}} = \int_{D_{\text{UDL}}}^{+\infty} \frac{dm_{\text{fit}}}{d\log D_{\text{rBC}}} (D_{\text{rBC}}) d\log D_{\text{rBC}} \quad (3.5)$$

and

$$\Delta m_{\text{fitresid}} = \int_{D_{\text{LDL}}}^{D_{\text{UDL}}} \frac{dm_{\text{fit}}}{d\log D_{\text{rBC}}} (D_{\text{rBC}}) - \frac{dm_{\text{meas}}}{d\log D_{\text{rBC}}} (D_{\text{rBC}}) d\log D_{\text{rBC}} . \quad (3.6)$$

Note that with this definition  $\Delta m_{\text{fitresid}}$  has a negative value for the example shown in Fig. 3.1. The correction term in the case of the fit method is naturally defined as the difference between the corrected and the measured rBC mass:

$$\Delta m^{\text{fit}} = m_{\text{fit}} - m_{\text{rBC,meas}} . \quad (3.7)$$

From Eqs. (3.4) and (3.7), one can derive:

$$\Delta m^{\text{fit}} = \Delta m_{\text{rBC} < \text{LDL}} + \Delta m_{\text{rBC} > \text{UDL}} + \Delta m_{\text{fitresid}} . \quad (3.8)$$

Comparing the missing mass correction terms of the two approaches given in Eqs. (3.1) and (3.3) shows that the corrected rBC mass differs by the sum of two physically meaningful quantities, the fit residual and the extrapolated rBC mass above the UDL:

$$m_{\text{rBC,corr}}^{\text{fit}} - m_{\text{rBC,corr}}^{\text{extrap}} = \Delta m_{\text{rBC} > \text{UDL}} + \Delta m_{\text{fitresid}} . \quad (3.9)$$

The results of these two approaches are compared and discussed in relation to the different datasets used in this study in Sect. 3.3.1.1. Outside of Sects. 3.3.1.1 and 3.3.1.2, Figs. 3.1, 3.2 and S3.1, and Table 3.4, this manuscript applies the first method (Eq. 3.2) to quantify rBC mass.

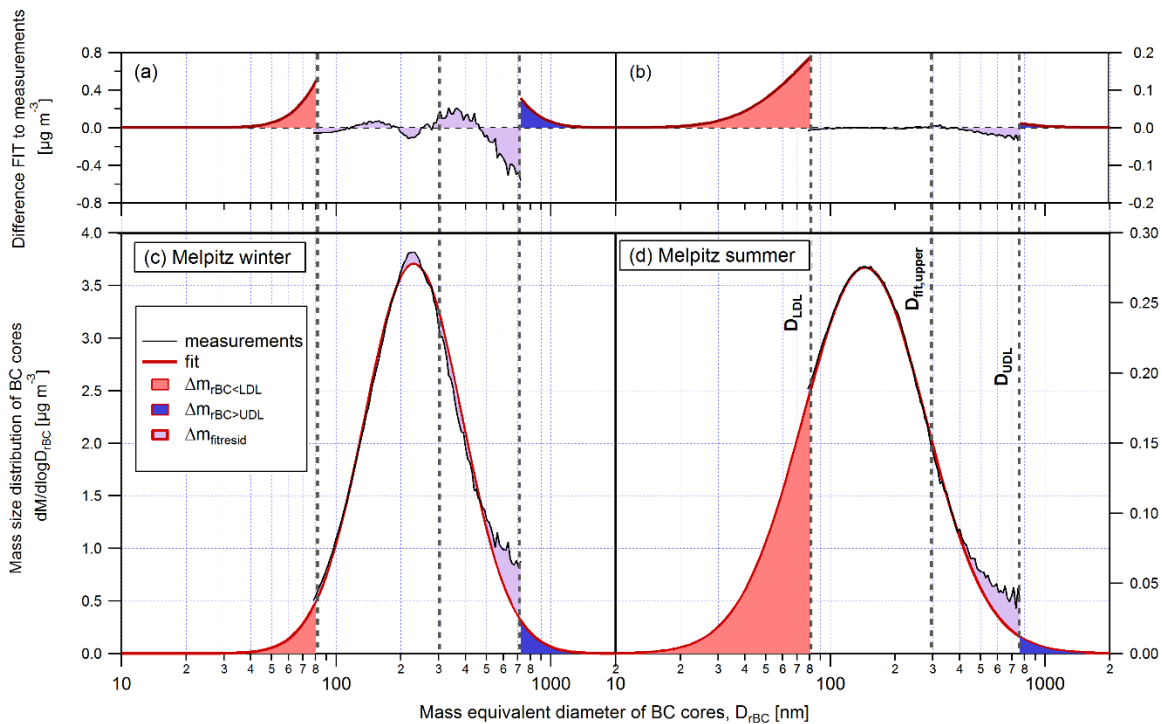


Figure 3.1: Approach to correct for the rBC mass outside the rBC core size range covered by the SP2 for the Melpitz winter (panels a and c) and the Melpitz summer (panels b and d) campaigns. The bottom two panels show the measured rBC mass size distribution as a function of rBC core mass equivalent diameter, including the SP2 detection limits  $D_{LDL}$  and  $D_{UDL}$ . The lognormal functions are fitted between  $D_{LDL}$  and  $D_{fit,upper}$ . The integrated area of the red, purple, and blue shadings correspond to  $\Delta m_{rBC < LDL}$ ,  $\Delta m_{fitresid}$  and  $\Delta m_{rBC > UDL}$ , respectively (see Sect. 3.2.3.5). The top two panels additionally show the same shadings after subtraction of the measured size distribution (and measurement forced to be zero outside the SP2 detection range). The average mass size distributions of the other campaigns are represented in Fig. S3.1.

### 3.2.4 Auxiliary measurements

#### 3.2.4.1 Aerosol size distribution

In the Melpitz winter and summer campaigns, aerosol number size distributions in the diameter range from 3.8 to 770 nm were measured with a mobility particle size spectrometer (MPSS), custom built by Wiedensohler et al. (2012), which consists of a differential mobility analyzer (DMA) and a condensation particle counter (CPC). The DMA was operated with a sheath air flow of  $10 \text{ L min}^{-1}$  and the aerosol number size distribution was measured every 20 minutes. During the Cabauw campaign, a modified version of a commercially available scanning mobility particle sizer (TSI SMPS 3034) provided the number size distribution of the aerosol in the diameter range from 10 to 470 nm. No size information is available for the Palaiseau and Bologna campaigns.

#### 3.2.4.2 Absorption Ångström exponent (AAE) inferred from Aethalometer data

The Aethalometer measures the light attenuation through a sample filter that is continuously loaded with aerosol (Hansen et al., 1984). The raw attenuation coefficient ( $b_{atm}$ ) is calculated from the rate of attenuation change with time. The relationship between attenuation coefficient and absorption coefficient of the deposited aerosol particles is linear for low attenuation values but saturation occurs when the attenuation values are high (Weingartner et al., 2003). Therefore, the measurements must be corrected for this “loading effect” in order to obtain a corrected

attenuation coefficient ( $b_{\text{atn,corr}}$ ) (Virkkula et al., 2007; Drinovec et al., 2015). The attenuation coefficient is greater than the absorption coefficient due to multi-scattering effects within the filter matrix, described with a proportionality constant  $C$ .

From a pair of  $b_{\text{atn,corr}}$  at two different wavelengths,  $\lambda_1$  and  $\lambda_2$ , it is possible to calculate the absorption Ångström exponent,  $\text{AAE}(\lambda_1, \lambda_2)$ , a coefficient commonly used to describe the spectral dependence of the aerosol light absorption coefficient (Moosmüller et al., 2009):

$$\text{AAE}(\lambda_1, \lambda_2) = - \frac{\ln(b_{\text{atn,corr}}(\lambda_1)) \ln(\lambda_2)}{\ln(b_{\text{atn,corr}}(\lambda_2)) \ln(\lambda_1)} \quad (3.10)$$

Note that since the Aethalometer  $C$ -value has only a small spectral dependence (Weingartner et al., 2003; Corbin et al., 2018), it is possible to infer the AAE directly from the corrected attenuation coefficient, as is done in this work.

The AAE provides an indication on the sources of BC (Zotter et al., 2017). The light absorption of particles from traffic emissions is dominated by BC, which has an AAE of  $\sim 1$ . By contrast, wood burning emissions contain a mixture of BC and co-emitted brown carbon. Light absorption by brown carbon has a much stronger spectral dependence than BC, such that the mixture has an AAE between  $\sim 1$  and 3 (Kirchstetter et al., 2004; Corbin et al., 2018). This makes relative apportionment of BC to traffic and wood burning sources based on aerosol AAE possible. However, this simple approach only works in the absence of additional BC sources or light absorbing aerosol components (e.g. from coal combustion).

In this paper the AAE values were calculated with the formula presented in Eq. (3.10) with  $\lambda_1 = 470$  nm and  $\lambda_2 = 950$  nm. Aethalometer AE-31 (Magee Scientific) instruments were used during the Palaiseau and Cabauw campaigns. These measurements were corrected for the loading effect with the algorithm developed by Weingartner et al. (2003). In the other campaigns, Aethalometer AE-33 (Magee scientific) instruments were used. These data did not need further correction since the algorithm developed by Drinovec et al. (2015), which takes into account the filter loading effect, is incorporated in the instrument. However, the AE33 firmware correction was not working properly during Bologna campaign. Therefore, these data were corrected using the Weingartner et al. (2003) correction.

### 3.3 Results and discussion

#### 3.3.1 rBC mass potentially missing below the LDL of the SP2

##### 3.3.1.1 Comparison of two approaches to correct for the truncated rBC mass

In the following, we compare the results from the two different approaches for estimating the missing rBC mass concentration outside the size range covered by the SP2 (see Sect. 3.2.3.5).

Typically, the measured size distributions only approximately followed a lognormal distribution. We chose to infer and present the missed rBC mass estimate based on fitting across the range from 80 nm to 300 nm. In addition, the sensitivity to the fitted range was assessed. The estimated missed rBC mass below the SP2 LDL increased by up to 11 % of the measured mass when increasing the lower fit limit from 80 nm to 100 nm, i.e. around the SP2 LDL. This provides evidence that the extrapolation towards the smallest BC cores is not strongly affected by the SP2 counting efficiency performance, which could potentially be degraded in this range. The fit approach used the total area of a lognormal fit to rBC mass size distributions to obtain the correct rBC mass. Sensitivity analyses done with fitting to a manually prescribed upper limit between 200 nm and 400 nm showed that the fit results were insensitive to the choice of this upper limit for valid fits. Therefore, a fixed fit range from 80 nm to 300 nm, which always provided good match between measured and fitted size distribution around the mode of the distribution, will be used in the remainder of this manuscript for missing mass corrections. The validity of the fits was determined by comparing the fitted peak location with the mode of the measured data. Data

were only fitted to a manually prescribed upper limit, and the fit results were insensitive to the choice of this upper limit for valid fits, while larger deviations occurred for invalid fits.

Table 3.4: Estimates of potentially missed rBC mass for the two methods ( $\Delta m^{\text{extrap}}$  and  $\Delta m^{\text{fit}}$ ), summands contributing to it ( $\Delta m_{\text{rBC}>\text{UDL}}$  and  $\Delta m_{\text{fitresid}}$ ), and modal diameter of the averaged rBC mass size distribution, all separately listed for each campaign. The size range of 80–300 nm rBC mass equivalent diameter was chosen for fitting the measurement. The sensitivity of the results to this choice was negligible, as discussed in the text.

Mass fractions/ Campaigns	$\Delta m^{\text{extrap}}$ [%] ( $:= \Delta m_{\text{rBC}<\text{LDL}}$ )	$\Delta m^{\text{fit}}$ [%]	$\Delta m_{\text{rBC}>\text{UDL}}$ [%]	$\Delta m_{\text{fitresid}}$ [%]	$D_{\text{rBC,mode}}$ [nm]
Bologna	$24.1 \pm 6.4$	$17.8 \pm 7.4$	$0.2 \pm 0.3$	$-6.5 \pm 1.9$	$118.6 \pm 0.3$
Cabauw	$22.4 \pm 4.9$	$19.7 \pm 4.6$	$0.7 \pm 0.3$	$-3.4 \pm 1.0$	$127.2 \pm 0.4$
Melpitz summer	$24.5 \pm 8.5$	$20.5 \pm 7.3$	$0.4 \pm 0.3$	$-4.5 \pm 3.7$	$142.9 \pm 0.3$
Melpitz winter	$2.9 \pm 2.1$	$2.5 \pm 1.4$	$1.1 \pm 0.4$	$-1.5 \pm 1.5$	$227.9 \pm 0.7$
Palaiseau	$20.3 \pm 8.7$	$18.0 \pm 7.0$	$2.5 \pm 2.0$	$-4.9 \pm 2.1$	$136.7 \pm 0.3$

Detailed results of the missing mass correction are listed in Table 3.4. The extrapolation method and the fit method provide comparable results. It can be seen that  $\Delta m^{\text{extrap}}$  varied in the range 3–25 %, while  $\Delta m^{\text{fit}}$  varied between 3–21 %. Considerable variability in missing mass correction between campaigns occurred due to differences in the rBC mass size distribution, especially differences in the average modal diameters, which is also listed in Table 3.4. As shown in Eq. (3.9), the extrapolation and the fit methods for missing mass correction differ by the sum of the fit residual ( $\Delta m_{\text{fitresid}}$ ) and the extrapolated mass above the UDL ( $\Delta m_{\text{rBC}>\text{UDL}}$ ). The opposite signs and comparable magnitudes of these two terms (Table 3.4), shown as purple and blue shadings in Figs. 3.1 and S3.1, have partially compensating effects, resulting on average in only 3 % difference between the two missing mass correction methods.

The systematic difference between measurement and fit for rBC mass equivalent diameters near the UDL of the SP2 (Figs. 3.1 and S3.1) could indicate either the presence of a second lognormal mode that is centered at a larger diameter than the main mode, or an inaccurate extrapolation of the incandescence signal calibration for masses greater than 64 fg ( $D_{\text{rBC}} = 408$  nm). As both effects make extrapolation of the rBC mass size distribution above the UDL uncertain, we decided to apply the extrapolation method in this study. As explained in Sect. 3.2.3.5 (Eqs. 3.1 and 3.2), the extrapolation method only uses the fit below the LDL of the SP2 to estimate missing rBC mass. This ensures a well-defined upper cut-off in terms of rBC core mass for the corrected rBC mass concentration results. In the following, all reported rBC mass concentrations are corrected with the extrapolation method (Eq. 3.2) with fit range chosen from 80 nm to 300 nm, unless otherwise stated.

The missing mass correction results for the Melpitz winter campaign are significantly different from those for the Melpitz summer and all other campaigns (Fig. 3.1, Fig. S3.1 and Table 3.4). Specifically, the missed mass percentage for the Melpitz winter campaign is less than 3 %, while it is between 18 % and 24.5 % for the other campaigns. This is due to the fact that the Melpitz winter rBC core mass size distribution peaks in the middle of the SP2 detection range, with  $D_{\text{rBC,mode}} = 227.9$  nm (Fig. 3.1 and Table 3.4). This is not the case for the other campaigns, where, as shown in Table 3.4, the average rBC mass size distributions have their maximum between 118.6 and 142.9 nm (Figs. 3.1 and S3.1). This could indicate that in Melpitz during the winter the BC source was different from that of the other campaigns of this work. Indeed, with a back-trajectory analysis on the same dataset, Yuan et al. (2020) showed that the period between 5 and 14 February 2017 was characterized by air masses transported from south-east Europe, where coal is still used as fuel (Spindler et al., 2013). Coal combustion

and biomass burning produce rBC size distributions with larger modal diameter than traffic emissions (Bond et al., 2013; Liu et al., 2014; Schwarz, 2019).

### 3.3.1.2 Limits to rBC mass missed in small BC cores imposed by the BC particle number

The presence of an additional mode of small particles below the lower detection limit of the SP2 would introduce an error in the above extrapolation calculations. Indeed, a substantial fraction of nascent soot particles emitted by combustion engines is usually below the detectable size range of the SP2. Count median diameters (CMD) of non-volatile particle size distributions in aircraft turbine exhaust range from 15 to 40 nm (Lobo et al., 2015; Durdina et al., 2017, 2019) while unfiltered gasoline direct injection and Diesel engines have larger CMD values ranging from 50 to 100 nm (Burtscher et al., 2001; Momenimovahed and Olfert, 2015).

The existence of additional modes of BC cores at diameters below the SP2 lower detection limit has been hypothesized based on the observation of ‘upticks’ in rBC mass size distributions at the LDL of the SP2 (i.e. increasing particle concentration with decreasing mass equivalent diameter as the SP2 LDL is approached) (Liggio et al., 2012; Cappa et al., 2019). Cappa et al. (2019) performed multi-modal fits to measured SP2 size distributions with upticks assuming fixed modal diameter (47 nm) and geometric standard deviation (1.63) of the lognormal mode lying below the SP2 LDL. These authors estimated that the campaign average mass concentration of the hypothesized small mode of BC particles was as large as 52 % of the total measured rBC mass concentration. While upticks at the lower end of SP2 size distributions may indicate the presence of an additional mode of small rBC particles, it should be noted that these upticks might also represent measurement artefacts. SP2 measurements of rBC cores with diameters below 100 nm are sensitive to small variations in fitted calibration curves and it is difficult to perform accurate calibration measurements near the LDL of the SP2 (Laborde et al., 2012a). Nevertheless, we cannot exclude presence of an undetected mode with small modal diameter between around 40 nm and 60 nm BC core size in our studies. Even smaller mode diameter is considered unlikely because such small particles can be found only in the proximity of a source (Zhu et al., 2006). Larger mode diameter is unrealistic in our campaigns because we did not see any sign of the upper tail of such a hypothetical mode at the bottom end of the BC size distribution measured by the SP2.

The mass of BC particles below the lower detection limit of the SP2 ( $D_{\text{rBC}} < \sim 80$  nm) can be estimated by measuring the total number concentration of non-volatile particles by thermo-denuded MPSS measurements, assuming that BC particles dominate the number of nonvolatile (NV) particles remaining after thermal treatment (Clarke et al., 2004). Miyakawa et al. (2016) employed this approach to conclude that the fraction of small rBC particles with  $D_{\text{rBC}}$  less than around 80 nm did not contribute substantially to the total rBC mass concentrations measured at an industrial site south of Tokyo, Japan. In the absence of such thermally-treated measurements, we assume 30 % of total measured particle number concentration as an upper limit for total BC particle number concentration (Wehner et al., 2004; Reddington et al., 2013; Cheung et al., 2016). This provides, after subtraction of the BC particle number concentration measured by the SP2, an upper limit ( $n_{\text{limit}}$ ) for the undetected BC particle number concentration.

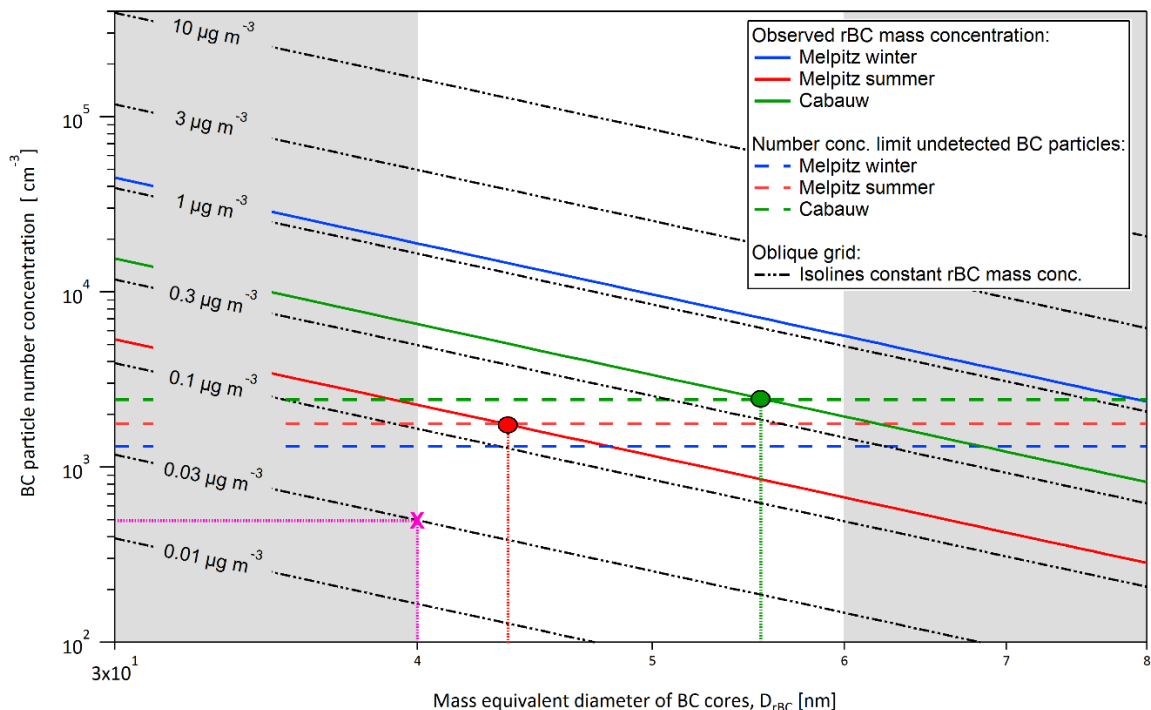


Figure 3.2: Relationship between rBC mass equivalent diameter, BC particle number concentration and rBC mass concentration for perfectly monodisperse BC aerosol (magenta cross and lines illustrate an example of this unambiguous relationship). The oblique dashed–dotted black grid represents isolines of constant rBC mass concentration. The continuous oblique lines represent the observed uncorrected rBC mass concentrations (campaign geometric mean values). The horizontal dashed lines represent the upper number concentration limit ( $n_{\text{limit}}$ ), calculated as difference between assumed maximum minus measured BC particle number concentration. The figure can be read in two ways: the intersects of the horizontal lines with rBC mass concentration isolines provide an upper limit for the maximal undetected rBC mass concentration if the undetected mode peaks at the diameter where the intersect occurs. Alternatively, when the horizontal dashed line crosses the corresponding oblique line of equal color (e.g. red point if we consider Melpitz summer), this corresponds to a maximal contribution of rBC mass concentration in small undetected particles equal to the observed value. If we consider Melpitz summer as an example (red point) this happens for a BC mass mode of 44 nm. The grey shading indicates that the modal diameter of a hypothetical mode undetected by the SP2 is expected to be between 40 nm and 60 nm.

Based on the discussion in Sect. 3.3.1.1, we applied in this study the extrapolation method to correct for estimated rBC mass below the SP2 LDL ( $\Delta m^{\text{extrap}}$  in Table 3.4). The resulting corrections are smaller than the upper limit imposed by BC particle number as discussed here. Hence, it cannot be excluded that the truly missed mass was larger than accounted for. The conservative estimate based on the BC particle number considerations suggests that the missing mass could be as large as 23 % (applied correction: 3 %), 125 % (applied correction: 22 %), 263 % (applied correction: 25 %) for the Melpitz winter, Cabauw and the Melpitz summer campaigns, respectively.

### 3.3.2 Comparison of observed EC and rBC mass concentrations

Here we aim at a quantitative comparison of rBC (after correction using Eq. 3.2) and EC mass concentrations measured by the SP2 and the thermal–optical method, respectively. Figure 3.3 shows a scatter plot of time–resolved data using distinct colours for each campaign (rBC data averaged according to the sampling periods of the EC samples). Figure S3.2 presents the corresponding statistics of the rBC to EC mass ratio and Table 3.5 reports all statistical parameters. The median values of the rBC to EC mass ratio lie between the arithmetic and geometric means, indicating distributions that are between the normal and lognormal distribution (Fig. S3.2). For this reason, we adopted the median when reporting the ratio of the two quantities and in the figures (lines in Figs. 3.3 and 3.6), and the geometric standard deviation (GSD) to report the  $m_{\text{rBC}}/m_{\text{EC}}$  variability (Table 3.5).



Considering all data points from all campaigns, the median value of  $m_{\text{rBC}}/m_{\text{EC}}$  was 0.92 with a GSD of 1.5. That is,  $m_{\text{rBC}}$  was on average 8 % smaller than  $m_{\text{EC}}$ , and 68 % of the individual data points fell into the range within a factor of 1.5 around the geometric mean ratio. Accordingly, the overall statistics for these two quantities agree closely, with geometric mean values (GSD) of 0.41 (2.60)  $\mu\text{g m}^{-3}$  and 0.47 (2.46)  $\mu\text{g m}^{-3}$  for  $m_{\text{rBC}}$  and  $m_{\text{EC}}$ , respectively, both ranging from 0.05 to 3.22  $\mu\text{g m}^{-3}$  (Fig. 3.3).

The above result suggests a very small overall systematic bias between rBC and EC mass on average. However, a look at the statistics calculated for each campaign separately (Table 3.5 and Fig. S3.2) reveals a slightly different picture: the variability of the rBC to EC mass ratio is considerably smaller for individual campaigns, with GSDs typically around 1.2–1.3, and the systematic bias on campaign level is substantially greater than the overall bias, with median ratios ranging from 0.53 to 1.29. During the Melpitz winter campaign,  $m_{\text{rBC}}$  was on average 29 % higher than  $m_{\text{EC}}$  with  $m_{\text{rBC}}$  and  $m_{\text{EC}}$  geometric means of 1.20 (2.64)  $\mu\text{g m}^{-3}$  and 0.97 (2.16)  $\mu\text{g m}^{-3}$ , respectively. During the Melpitz summer campaign,  $m_{\text{rBC}}$  was comparable to  $m_{\text{EC}}$  within 3 %, with respective geometric means of 0.17 (1.57)  $\mu\text{g m}^{-3}$  and 0.18 (1.54)  $\mu\text{g m}^{-3}$ . For the Bologna summer campaign, the median rBC to EC mass ratio was 0.65, with  $m_{\text{rBC}}$  and  $m_{\text{EC}}$  geometric means of 0.40 (1.46)  $\mu\text{g m}^{-3}$  and 0.64 (1.45)  $\mu\text{g m}^{-3}$ . The largest difference was found in Cabauw, with a median rBC to EC mass ratio of 0.53 and geometric means of  $m_{\text{rBC}}$  and  $m_{\text{EC}}$  of 0.46 (1.62)  $\mu\text{g m}^{-3}$  and 0.86 (1.63)  $\mu\text{g m}^{-3}$ , respectively. During the Palaiseau campaign,  $m_{\text{rBC}}$  was 20 % higher than  $m_{\text{EC}}$ ; this value is somewhat higher than the value of 15 % previously published in Laborde et al. (2013), which is explained by the fact that here we used the  $m_{\text{rBC}}/m_{\text{EC}}$  median value instead of the result of the linear fit.

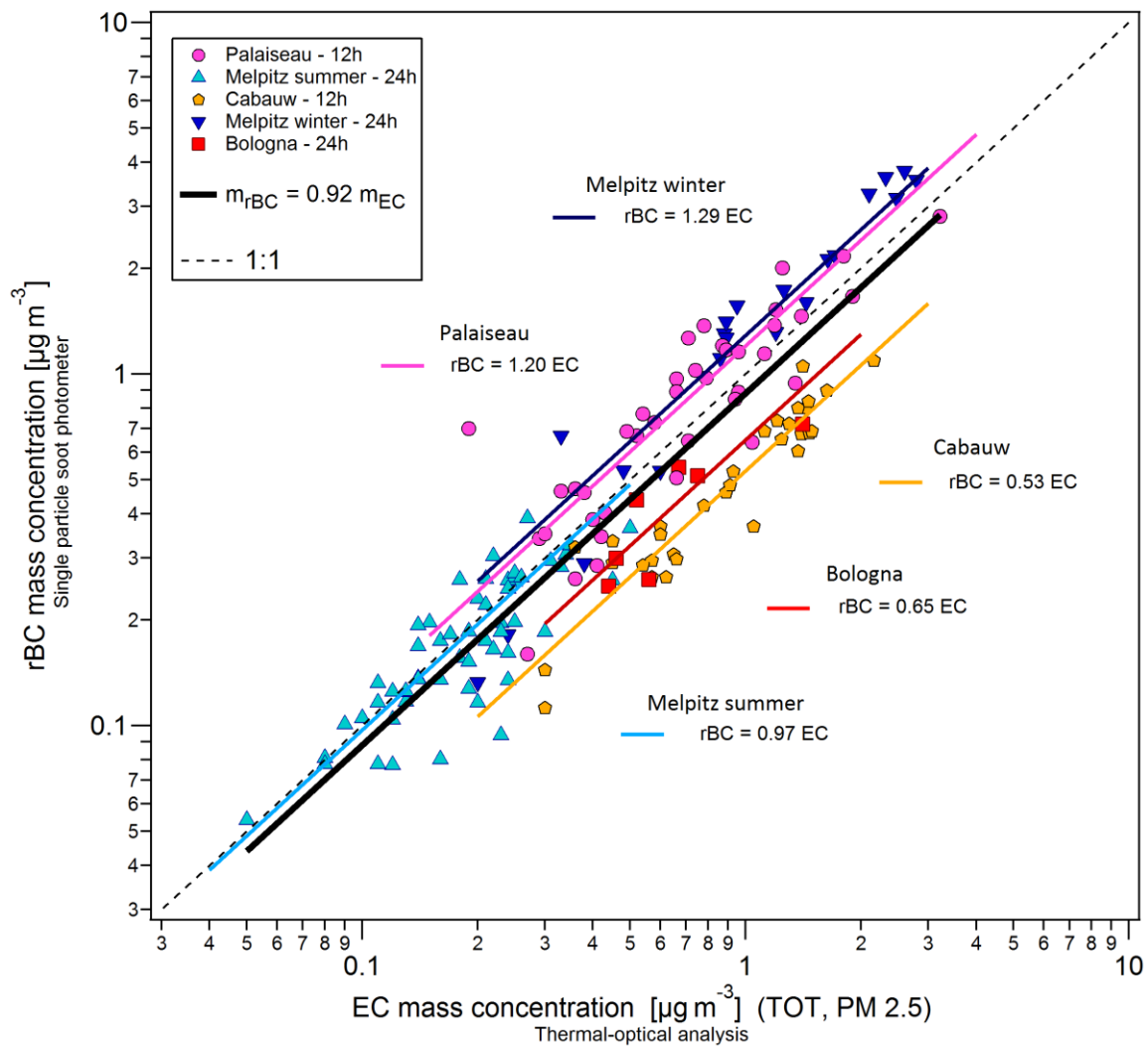


Figure 3.3 rBC mass concentration versus EC mass concentration for the five campaigns studied in this paper. The median rBC to EC mass ratios are shown as lines for each campaign. Uncertainties of EC measurements as a function of EC and TC filter surface loadings as well as EC/TC mass ratio are presented in Fig. S3.3 and discussed in Sect. 3.3.3.2.

Table 3.5:  $m_{\text{rBC}}$  and  $m_{\text{EC}}$  statistics per campaign: median, arithmetic and geometric mean, geometric standard deviation (GSD), standard deviation (SD), 10<sup>th</sup> and 90<sup>th</sup> percentiles and number of data points.

	Palaiseau	Cabauw*	Melpitz summer	Melpitz winter	Bologna	All the campaigns
$m_{\text{rBC}}$ median (10 <sup>th</sup> , 90 <sup>th</sup> ) [ $\mu\text{g m}^{-3}$ ]	0.85 (0.34, 1.55)	0.47 (0.27, 0.83)	0.17 (0.09, 0.29)	1.41 (0.29, 3.56)	0.44 (0.26, 0.61)	0.41 (0.13, 1.44)
$m_{\text{EC}}^*$ median (10 <sup>th</sup> , 90 <sup>th</sup> ) [ $\mu\text{g m}^{-3}$ ]	0.71 (0.32, 1.36)	0.92 (0.45, 1.47)	0.19 (0.11, 0.31)	0.92 (0.45, 1.47)	0.56 (0.45, 1.01)	0.47 (0.14, 1.44)
$m_{\text{rBC}}$ geometric mean (GSD), [ $\mu\text{g m}^{-3}$ ]	0.77 (1.88)	0.46 (1.62)	0.17 (1.57)	1.20 (2.58)	0.40 (1.46)	0.41 (2.60)
$m_{\text{EC}}$ geometric mean (GSD), [ $\mu\text{g m}^{-3}$ ]	0.68 (1.83)	0.86 (1.63)	0.18 (1.54)	0.97 (2.16)	0.64 (1.45)	0.47 (2.46)
$m_{\text{rBC}}/m_{\text{EC}}$ geometric mean (GSD)	1.13 (1.40)**	0.53 (1.19)	0.92 (1.26)	1.23 (1.32)	0.63 (1.23)	0.88 (1.50)
$m_{\text{rBC}}/m_{\text{EC}}$ arithmetic mean (SD)	1.20 (0.51)	0.54 (0.11)	0.95 (0.24)	1.28 (0.33)	0.65 (0.14)	0.96 (0.41)
$m_{\text{rBC}}/m_{\text{EC}}$ median (10 <sup>th</sup> , 90 <sup>th</sup> )	1.20 (0.72, 1.50)	0.53 (0.44, 0.64)	0.97 (0.63, 1.23)	1.29 (0.76, 1.58)	0.65 (0.49, 0.82)	0.92 (0.51, 1.42)
# data points	39	32	55	21	7	154

\* EC mass was measured in PM<sub>2.5</sub>, except for the Cabauw campaign, where PM<sub>10</sub> samples were collected.

\*\* The statistics of the rBC to EC mass ratio for the SIRTAs campaign is strongly influenced by one outlier (see Fig. 3.3). Ignoring this outlier would provide a geometric mean ratio of 1.09 and a GSD of 1.32.

### 3.3.3 Discussion of level of agreement between the rBC and EC mass concentration measurements

In this section, we test different hypotheses for the observed differences between rBC and EC mass.

#### 3.3.3.1 Differences in upper cut-off diameters and in inlet losses

Differences in the upper cut-off diameters for the EC and rBC mass measurements are a potential source of discrepancy. The EC mass measurements presented in Fig. 3.3 relate to an upper 50 % cut-off at an aerodynamic particle diameter  $D_{\text{aero}} = 2.5 \mu\text{m}$  at ambient RH (Table 3.2), except for Cabauw, where a PM<sub>10</sub> inlet was used. The SP2 measurements were mostly taken behind PM<sub>10</sub> inlets. However, the SP2 has a more stringent intrinsic UDL, which varied from  $D_{\text{UDL}} = 439 \text{ nm}$  to  $766 \text{ nm}$  BC core mass equivalent diameter, depending on the campaign (Table 3.3). To explore the possibility that BC particles with diameters between the UDL of the SP2 and  $2.5 \mu\text{m}$  aerodynamic diameter contributed to the discrepancies between  $m_{\text{rBC}}$  and  $m_{\text{EC}}$ , the SP2-related mass equivalent diameters ( $D_{\text{ve}}$ ) were converted to aerodynamic diameters ( $D_{\text{aero}}$ ). This was done by numerically solving Eq. (3.11), where  $C_C$  is the Cunningham slip correction factor,  $\rho_p$  the particle density,  $\rho_0 = 1000 \text{ kg m}^{-3}$  and  $\chi$  is the particle dynamic shape factor (more details in Sects. S3.3 and S3.4 of the SI):

$$D_{ve} = D_{aero} \sqrt{\frac{\rho_o \chi C_C(D_{aero})}{\rho_p C_C(D_{ve})}}. \quad (3.11)$$

During the Melpitz winter campaign, the intrinsic UDL was at  $D_{rBC} = 722$  nm. The aerodynamic diameter of externally mixed bare BC cores of this size varies from around  $D_{aero} = 625$  nm for fractal-like shape to 970 nm for compact shape (Table S3.3). For coated BC particles, the corresponding dry aerodynamic diameter ranges from around 1140 nm to 1660 nm for coating to core mass ratios of 1:1 and 6:1, respectively. The actual BC mixing state was measured by Yuan et al. (2020), though at smaller core diameters. Using these data as a constraint provides around 1320 nm as a best estimate for the dry aerodynamic diameter. However, the impactor for the filter sampling is operated at ambient RH, which means that hygroscopic growth affects the cut-off diameter. Potential hygroscopic growth was assessed as described in Sect. S3.4. Accordingly, the aerodynamic diameter of particles with BC cores size at the SP2 UDL increases up to 1610 nm and 2230 nm at 80 % and 95 % RH, respectively, for the best estimate BC mixing state. Externally mixed bare BC particles are not affected by hygroscopic growth. Based on this analysis, it can be expected that the intrinsic SP2 UDL translates to a cut-off varying between  $PM_1$  and  $PM_{2.5}$ , or even slightly smaller or greater under extreme assumptions. This statement also applies for the Melpitz summer campaign, where the SP2 UDL differed only marginally from that of the Melpitz winter campaign (Table 3.3).

Since during the Melpitz campaigns the EC mass concentrations were measured behind both  $PM_1$  and  $PM_{2.5}$  inlets, we were able to calculate the fraction of EC mass in particles with aerodynamic diameters between 1 and 2.5  $\mu\text{m}$  out of the total EC mass in  $PM_{2.5}$ . Fig. 3.4a and 3.4b indicate that between 10 and 60 % of EC  $PM_{2.5}$  mass was present in the large size fraction (1–2.5  $\mu\text{m}$ , indicated as  $EC_{2.5-1}$ ) for the majority of measurements during both the Melpitz winter and summer. These  $EC_{2.5-1}$  fractions are greater than the longer-term average values at the Melpitz site, which is potentially related to the fact that coal combustion was a likely source of EC particles with diameter between 1 and 2.5  $\mu\text{m}$  at the Melpitz site, at least during the winter campaign (van Pinxteren et al., 2019; Yuan et al., 2020).

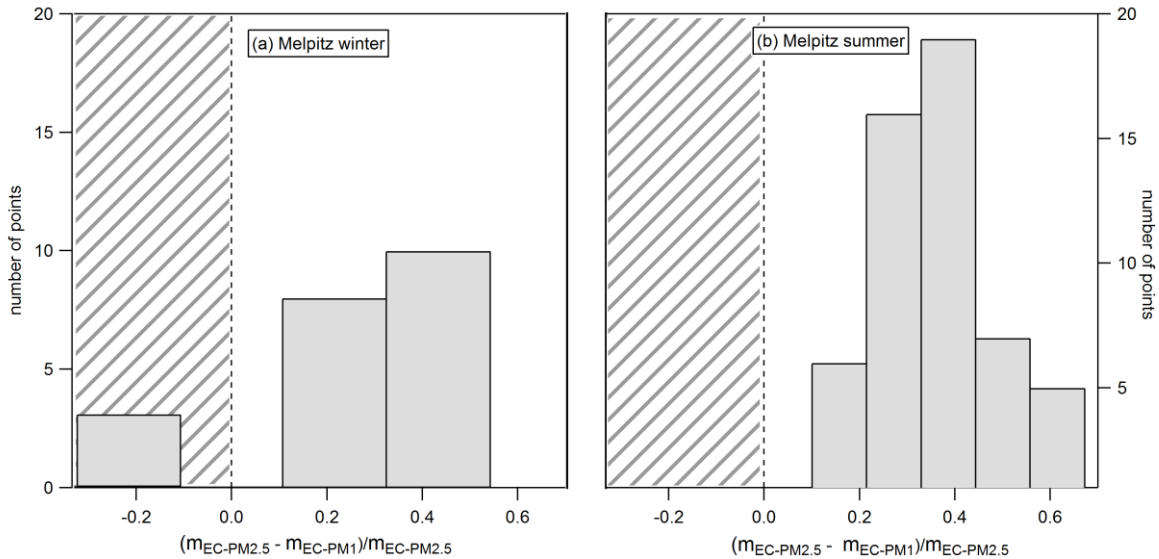


Figure 3.4: Histogram of  $(m_{EC-PM_{2.5}} - m_{EC-PM_1}) / m_{EC-PM_{2.5}}$  for Melpitz winter (panel a, on the left) and summer (panel b, on the right) campaigns. The area with the oblique grey lines indicates the non-physical part in which  $m_{EC-PM_{2.5}} < m_{EC-PM_1}$ , reflecting the uncertainty in the EC measurements.

The facts that the  $EC_{2.5-1}$  fraction contributed on average around 30 to 40 % EC mass in  $PM_{2.5}$  during the Melpitz campaigns, and that the SP2 BC particle cut-off is likely between  $PM_1$  and  $PM_{2.5}$ , makes it possible that upper cut-off related differences contribute to the discrepancies between measured rBC and EC mass seen in Fig. 3.3. However, additional covariance analyses of the  $EC_{2.5-1}$  fraction with the rBC to EC bias did not provide a conclusive result. Furthermore, such cut-off effects should rather result in an rBC mass being lower than the EC

mass, opposite to the result for the Melpitz winter campaign. This indicates the presence of other effects/biases, which over-compensated for the mass between 1 and 2.5  $\mu\text{m}$  that the SP2 was not able to detect.

Concerning Cabauw, the  $\text{EC}_{2.5-1}$  fraction could be a potential cause of the observed low rBC mass to EC mass ratio, given that EC was measured behind a  $\text{PM}_{10}$  inlet and that the SP2 cut-off was at  $D_{\text{rBC}} = 537$  nm, resulting in a wider upper cut-off gap than during the other campaigns. However, the rBC modal diameter measured by the SP2 was the second lowest of all campaigns (Table 3.4 and Fig. S3.1), which makes a potential bias originating from the lower end of the BC size distribution more likely. A closer assessment is however not possible as no  $\text{PM}_{10}$  EC samples are available, which also applies for the other sites.

Differences between  $m_{\text{rBC}}$  and  $m_{\text{EC}}$  can also come from differences in the inlet line losses. Particle losses can be caused by the presence of a dryer in the inlet line to which the SP2 was connected. In this work, the dryer losses are estimated to be less than 10 % (see further details in Sect. S3.5). Although this is, therefore, not the major contributor to the observed discrepancies, it should be addressed in future campaigns.

### 3.3.3.2 Filter loading and EC/TC ratios

Filter overloading with EC can interfere with the optical detection of pyrolytic carbon, potentially leading to a systematically low bias in the reported EC mass concentrations. For aerosol collected at an urban location, Ram et al. (2010) reported that linearity between transmission and EC surface loading was maintained when EC surface loading was kept below 8.0  $\mu\text{g cm}^{-2}$ . Figure S3.3a presents the observed rBC to EC mass ratios as a function of EC surface loading. Several samples collected during the Melpitz winter campaign exceeded the above loading threshold (red shading). However, the rBC to EC mass ratio of these data points was very similar to the other filter samples of the Melpitz winter campaigns with lower surface loading. Moreover, no systematic trend exists between surface loading and rBC to EC mass ratio for all other campaigns, where EC surface loading anyway stayed below the above threshold (Table S3.2). Instead, the bias depends systematically on the campaign as already shown above. Consequently, filter overloading cannot explain the  $m_{\text{rBC}} - m_{\text{EC,PM}_{2.5}}$  discrepancy during the Melpitz winter campaign, or for the other campaigns of this study.

The precision of thermal-optical EC mass measurements has been found to degrade at TC surface loadings  $< 10$   $\mu\text{g cm}^{-2}$  and at low EC to TC mass ratio (Sect. 3.2.2.3). Figure S3.3b presents the observed rBC to EC mass ratios as a function of TC surface loading, which frequently dropped to low values between 2 and 10  $\mu\text{g cm}^{-2}$  during 3 out of the 5 campaigns (Table S3.2). However, this analysis does not suggest increased random noise nor systematic bias caused by low TC surface loading (points within red shaded area). Instead, systematic campaign-dependent bias dominates again.

OC/EC split related artefacts in thermal-optical EC mass are more likely to occur at low EC/TC mass ratios. Figure S3.3c presents the observed rBC to EC mass ratios as a function of EC/TC mass ratio. No systematic dependence on EC/TC was found, except possibly for the Melpitz winter campaign. However, multiple other aerosol properties exhibited covariance with EC/TC on a campaign-to-campaign basis, as will be addressed in Sect. 3.3.4. Causality hence remains elusive.

### 3.3.3.3 Systematic EC and rBC bias due to the presence of particular types of particulate matter such as brown carbon or biomass burning BC

As discussed in Sect. 3.2.3.2, the SP2 sensitivity depends on the BC type. Therefore, differences in the BC properties between the atmospheric rBC samples and the calibration material may result in systematic bias. The AAE of an aerosol provides information on brown carbon co-emitted with BC and through this on potential BC sources (Sect. 3.2.4.2). Figure 3.5 presents the relation of  $m_{\text{EC}}$  and  $m_{\text{rBC}}$ , color-coded by the AAE to investigate a possible influence by the presence of brown carbon. Three zones can be distinguished (see also Table S3.4 for AAE statistics): the upper part of the figure, with  $m_{\text{BC}} > 0.3$   $\mu\text{g m}^{-3}$  and  $m_{\text{rBC}} > m_{\text{EC}}$ , represents data collected during the winter campaigns of Melpitz and Palaiseau, with an AAE above average ( $> 1.2$ ; blue symbols) and geometric mean AAE values of 1.36 and 1.38, respectively. The lower right part of the figure, with  $m_{\text{BC}} >$

$0.3 \mu\text{g m}^{-3}$  and  $m_{\text{rBC}} < m_{\text{EC}}$ , represents data from Bologna and Cabauw, with  $0.8 < \text{AAE} < 1.2$  and geometric mean AAE values of 1.04 (red symbols). The data in the lower left part of the graph, with  $m_{\text{BC}} < 0.3 \mu\text{g m}^{-3}$ , represent Melpitz summer data, with AAEs between 0.93 and 1.28 (up triangle markers). While there is a general increase in the relative difference between  $m_{\text{EC}} - m_{\text{rBC}}$  with increasing AAE when considering all campaigns (Fig. S3.4), it is not explained with the AAE variability within an individual campaign (marked with different colours). Furthermore, tar brown carbon has been shown to be assigned to EC mass (Sect. 3.2.2.1), while it does not contribute to rBC mass (Sect. 3.2.3.3). Such tar brown carbon interference would cause a negative relationship of data points as presented in Fig. S3.4, which was not observed. Hence, the observations do not provide evidence of substantial fraction of tar brown carbon in total EC in daily averaged samples. We conclude that the variation of BC sources and carbonaceous aerosol composition, as implied by AAE variability, may contribute to variations in the discrepancy between  $m_{\text{EC}}$  and  $m_{\text{rBC}}$ , while not being the main driver of it.

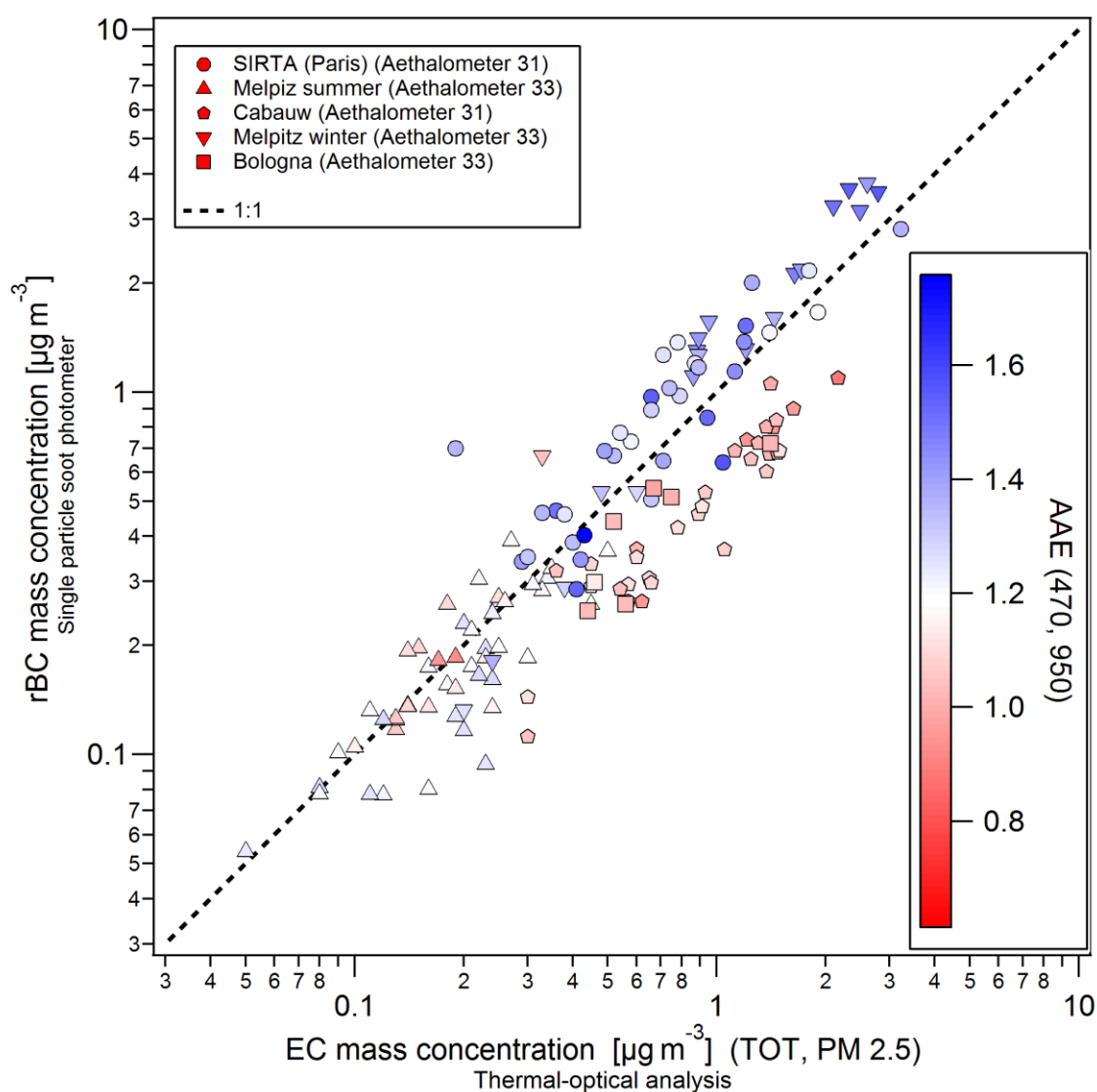


Figure 3.5: rBC mass concentration versus EC mass concentration for all campaigns of this study color-coded by the absorption Ångström exponent of each data point.

### 3.3.4 Reconciliation of sources of discrepancy between rBC and EC mass

The results presented in Fig. 3.3 and discussed in Sect. 3.3.2 showed agreement within 8 % between rBC and EC mass concentrations when averaging over all data points from all campaigns. High correlations were found for individual campaigns, however, with large variability of the campaign median rBC to EC mass ratios, ranging from 0.53 to 1.29. The analyses presented in Sect. 3.3.3.3 (Figs. 3.5 and S3.4) suggest some relationship between observed discrepancy and BC source type. However, many aerosol properties related to potential artefacts are cross-correlated, which makes it difficult to identify causal reasons.

The lowest rBC to EC mass ratios of 0.53 and 0.65 were observed during the Bologna and Cabauw campaigns (Table 3.5). The sampled aerosol during these two campaigns was characterized by smallest BC core sizes, highest EC/TC ratios and lowest AAE of ~1. The latter shows that BC was dominated by traffic sources. This is the type of ambient aerosol, for which the EC mass measurement should be quite reliable (e.g. Khan et al., 2012). The common calibration approach of the SP2 (see Sect. 3.2.3.2) should only cause limited bias in this case, as it was tailored to match the instrument sensitivity of rBC. Coarse BC particles with sizes between the upper cut-off diameter of the SP2 and the PM inlet cut-off diameter of the EC sampling may contribute to the rBC mass being lower than EC mass, though the analyses presented in Sect. 3.3.3.1 did not provide a clear result on the importance of this effect. At the lower end of the BC mass size distribution, rBC mass data were corrected for the missed rBC mass associated with small BC cores (Sects. 3.2.3.5 and 3.3.1.1). However, this correction would not account for an additional BC mode below the SP2 cut-off, as e.g. hypothesized by Liggio et al. (2012) and Cappa et al. (2019), nor could presence of such a mode be excluded by means of particle number-based considerations.

The results for the Melpitz winter campaign are different in many aspects: highest average rBC to EC mass ratio of all campaigns (1.29), largest BC core sizes, highest EC filter loading, and highest AAE (Tables S3.2 and S3.4). Large artefacts from missed rBC mass below the SP2 LDL could be excluded with number-based considerations (Sect. 3.3.1.2). The aerosol contained a substantial fraction of coarse BC, based on parallel EC measurements made with PM<sub>1</sub> and PM<sub>2.5</sub> inlet cut-off diameters. The SP2 might have missed some of these coarse particles. However, this effect likely caused less than 20 % negative bias in rBC mass concentration, which would have made the discrepancy between rBC and EC mass greater rather than smaller. Based on previous studies (van Pinxteren et al., 2019) and measured AAE, the BC contained substantial contributions from coal burning and/or wood burning emissions. For wood burning BC, this could result in rBC mass that is low by less than ~20 % due to potentially lower sensitivity of the SP2 (Laborde et al., 2012a). The sensitivity of the SP2 to BC from coal burning is unknown, but the bias is expected to be <30 %. As for the EC, the analyses presented in Sects. 3.3.3.2 and 3.3.3.3 did not provide evidence of a clear bias of the EC mass measurements in one or the other direction.

An agreement within 15 % between rBC and EC mass was observed for the Melpitz summer and Palaiseau campaigns (Table 3.5), where the pertinent aerosol and BC properties assumed mean values compared to the range covered by data from all campaigns. This finding does not exclude compensating errors in one or both measurements. However, no clear evidence for such errors was observed.

### 3.3.5 Comparison with previous rBC and EC intercomparison studies

In this section, we put our results into context with previous rBC and EC mass intercomparison studies available in the literature. Figure 3.6 contains a compilation of co-located measurements presented as a scatter plot. The data collected in this study are shown with green points, the corresponding median ratio is shown by the green line, and the green area illustrates the 1 GSD range around the geometric mean value. In the same graph, data from previously published ambient, lab and chamber studies are reported, including labels indicating the thermal-optical protocol used for the EC measurements. Further information on the data shown Fig. 3.6 is given in Table S3.5 (SP2 calibration material,  $m_{EC}$  cut-off, TOA thermal protocol, period, location, site characteristics or aerosol source, and average result of the intercomparison).

The data points of the previous studies are scattered around the 1:1 line and the majority of them lie within the 1 GSD range of this study. Therefore, the previous studies confirm the finding that the TOA and the SP2 techniques both provide a consistent measurement of BC mass within the uncertainties of either technique. More specifically, the chamber experiments with CAST soot by Laborde et al. (2012b) show agreement between rBC

and EC mass within 15 % (topmost cyan point in Fig. 3.6). Such close agreement is not surprising as the sample comprised almost pure BC, which simplifies the EC mass measurement, and the BC mass size distribution was almost completely within the range covered by the SP2. Corbin et al. (2019) investigated exhaust from a four-stroke ship diesel engine (brown triangles in Fig. 3.6). Close agreement within a few percent was achieved under engine operation conditions under which the emitted refractory carbon was dominated by soot-BC. By contrast, rBC to EC mass ratios substantially smaller than unity were observed when operating the engine under conditions leading to a high fraction of tar brown carbon in the exhaust. This discrepancy could be attributed to a positive interference in EC mass caused by tar balls. Miyakawa et al. (2016) measured ambient aerosol at an urban location and found very high correlation and close agreement (within 7 %) between rBC and EC mass (after applying line loss corrections, since they found the particle transmission efficiency of the diffusion dryer of the SP2 line to be 84 %). Zhang et al. (2016) reported an average rBC to EC mass ratio of 0.72 for an urban background site, with all data points highly correlated and therefore within the green shading. During the campaign at a remote Arctic site by Sharma et al. (2017), the rBC mass was found to be a factor of 0.51 lower than the EC mass, with half of the data points lying outside the green shading. They attributed this large bias to two potential reasons: first, due to filter loadings being around the limit of quantification of the TOA, and second, due to large charring bias, causing EC mass overestimation despite optical correction. The mean EC mass uncertainty during the campaign was  $\sim 28\%$ , reaching values as high as 80 % during summer due to very low EC mass concentrations.

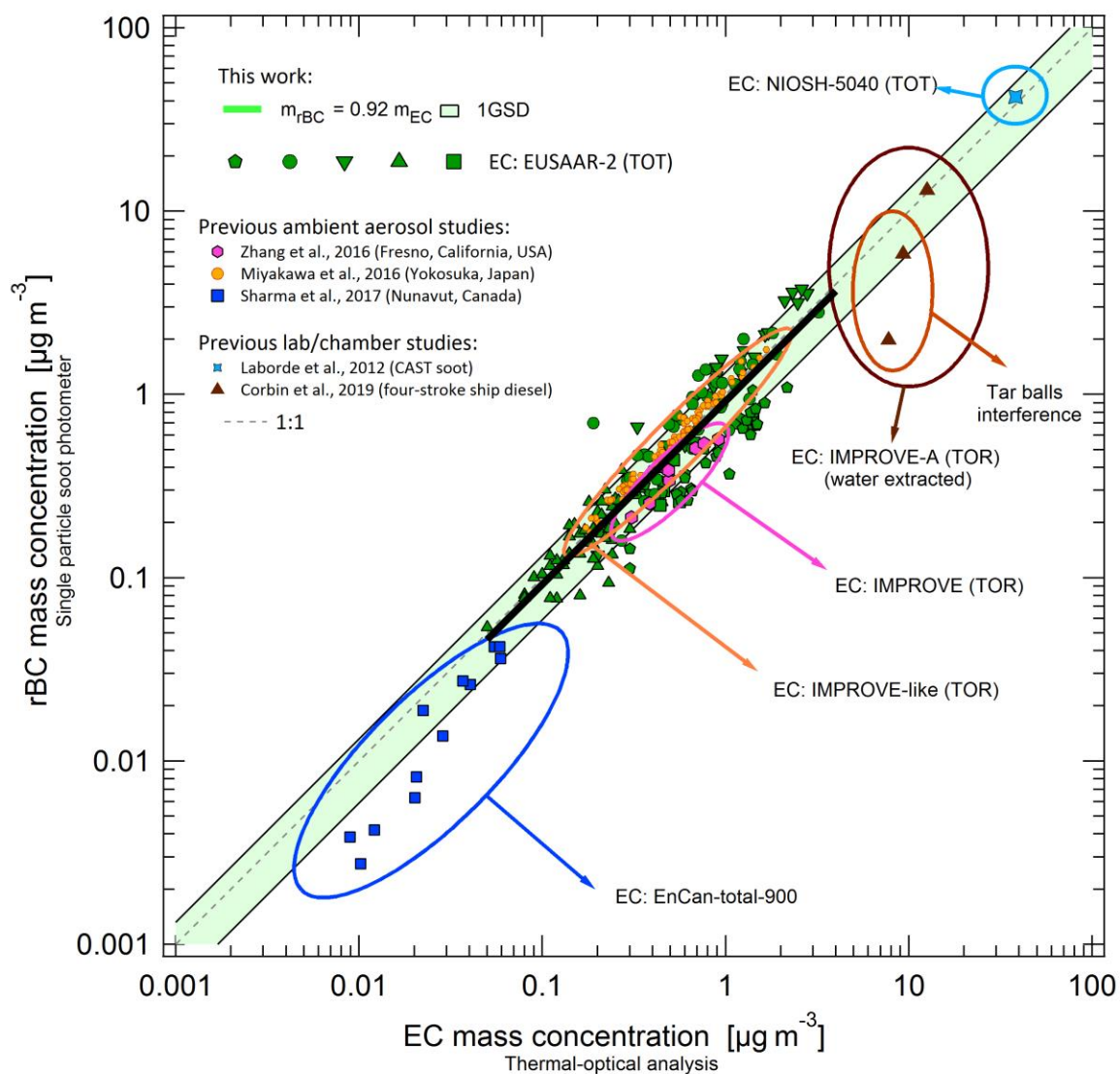


Figure 3.6: EC mass concentration vs rBC mass concentration for the datasets studied in this work and other published data.



As discussed in Sect. 3.2.2.3 and shown in Table 3.1, the difference in the thermal–optical protocols used to quantify  $m_{\text{EC}}$ , can result in a bias of  $\pm 40\%$ . For example, the geometric mean ratio between rBC and EC mass of the Zhang et al. (2016) data points would increase from 0.72 to 0.96, if they had been measured with the EUSAAR–2 protocol, or if the 25 % systematic difference between the IMPROVE and EUSAAR–2 protocols as reported by Han et al. (2016) were applied (see Table 3.1). However, our campaign–to–campaign variability of the rBC to EC mass ratio of roughly  $\pm 50\%$  using the same TOA protocol, (Fig. 3.3), can be even bigger than the variability associated with a different TOA protocol for the same sample. Therefore, the rBC mass measured by the SP2 cannot be used to identify the optimal TOA protocol.

### 3.4 Conclusions

In this work co–located EC and rBC mass concentration measurements from five field campaigns performed in the time period 2010–2017 across several European sites (Palaiseau, Bologna, Cabauw and Melpitz) were collated and examined to identify the differences between BC mass concentrations measured by the thermal–optical analysis and the LII technique. All EC concentration measurements were performed with the EUSAAR–2 thermal protocol, with the TOT technique on quartz filters sampled with high volumes with  $\text{PM}_{2.5}$  cut–off (except for the Cabauw campaign during which  $\text{PM}_{10}$  was sampled). All the OC/EC TOA instruments used to perform the EC analysis were compared at the JRC European Reference Laboratory for Air Pollution (ERLAP) to check the EC bias and variability. All rBC mass concentration measurements were performed with SP2s. Three different SP2 instruments (PSI, IGE and AWI) were used in these campaigns, calibrated with the same standard material, fullerene soot, using two different batches, which produced almost identical calibration curves. The mass of BC cores smaller than the lower SP2 detection limit was calculated for all the campaigns including sensitivity analyses. The estimates of missed rBC mass outside the detection range of the SP2 was found to vary between campaigns due to differences in the size distributions of the BC particles.

The observed rBC and EC mass concentrations correlated well with each other. However, the median of the observed rBC to EC mass ratios varied from 0.53 to 1.29 from campaign to campaign. Potential reasons for discrepancies are as follows: source–specific SP2 response, the possible presence of an additional mode of small BC cores below the LDL of the SP2, differences in the upper cut–off of the SP2 and the inlet line for the EC sampling, or various uncertainties and interferences from co–emitted species in the EC mass measurement. The discrepancy between rBC and EC appears to be systematically related to the BC source, i.e. traffic versus wood and/or coal burning. However, it was not possible to identify causalities behind this trend due to potential cross–correlations between several aerosol and BC properties relevant for potential biases. For future intercomparison studies, it is important to constrain the upper cut–off and potential inlet losses of both methods in such a manner that these can be excluded as a source of discrepancy.

The comparison with already published studies showed that most of the rBC to EC mass ratio data points of the other campaigns were within 1 GSD of the median and GSD found in this work. Although in this work, all EC concentrations were measured by the EUSAAR–2 protocol, we note that our reported variability in the rBC to EC mass ratio is greater than the variability expected between EC concentrations measured by different thermal protocols.

From this study, we conclude that the two methods essentially measure the same quantity, i.e. both provide an operationally defined measure of atmospheric BC mass in good overall agreement. However, systematic discrepancies up to  $\sim \pm 50\%$  were observed at some sites. Lack of a traceable reference method or reference aerosols combined with uncertainties in both of the methods, made it impossible to clearly quantify the sources of discrepancies, or to attribute them to one or the other method.

## **Acknowledgment**

The authors are grateful to Achim Grüner for the technical support during the two Melpitz campaigns. We also thank Claudia Zigola (ARPAE) who performed the TOA analysis of the filters during the Bologna campaign. The logistic support of CNR–ISAC technical staff (Francescopiero Calzolari) during the Bologna campaign is appreciated. Many thanks to the technical support of Günther Wehrle during the Bologna campaign.

## **Financial support**

The authors are grateful to Achim Grüner for the technical support during the two Melpitz campaigns. We also thank Claudia Zigola (ARPAE) who performed the TOA analysis of the filters during the Bologna campaign. The logistic support of CNR–ISAC technical staff (Francescopiero Calzolari) during the Bologna campaign is appreciated. Many thanks to the technical support of Günther Wehrle during the Bologna campaign.

## **Author contributions**

REP, MB and RLM took the rBC measurements and/or analyzed the raw data during the Bologna campaign. AT was responsible for the EC measurements during the Bologna campaign. AM coordinated the Bologna campaign. JY, MZ and RLM took the measurements and/or analyzed the raw data during the Melpitz winter campaign while JCC took the measurements and analyzed the raw data during the Melpitz summer campaign. TT, TM and BW took the data and coordinated the Melpitz campaigns. GS was responsible for the EC measurements during the Melpitz campaigns. BS was responsible for the EC measurements during the Cabauw campaign. REP performed the data analysis, interpreted the results and wrote the manuscript together with RLM and MGB. All co–authors reviewed and commented the manuscript.

## **Data availability**

Data archiving is currently underway. Data will be available on Zenodo if the manuscript is accepted for publication.

## **Competing interests**

The authors declare that they have no conflict of interest.

# Supplement of: Comparison of co-located rBC and EC mass concentration measurements during field campaigns at several European sites

## S3.1. Further details concerning the optical correction in thermal optical analysis (TOA)

During TOA analysis a fraction of the OC can pyrolyze in the He step to form pyrolytic carbon (PC), which is thermally stable and only desorbs in the O<sub>2</sub> step, thereby causing a charring artefact in the mutual quantification of OC and EC. To correct for this latter effect a laser at 658 nm can be used to monitor the light transmission through the loaded filter before and during the analysis. PC is strongly light absorbing, thus leading to a decrease of the transmission signal when it forms upon heating in the inert atmosphere. Later, in the oxidizing atmosphere, both PC and EC are released from the filter resulting in an increase of the transmission signal. The time at which the transmission equals again the initial pre-pyrolysis value is used to separate OC and EC, depending on whether the carbon evolved before or after this “split point”, respectively. This thermal-optical transmittance (TOT) approach to correct for PC eliminates potential charring artefacts if the PC has the same mass-specific attenuation cross section as the atmospheric native EC (Yang and Yu, 2002), and if no other light-absorbing material evolves from the sample.

Instead of using light transmission, the charring correction can also be done with light reflectance (i.e., thermal-optical reflectance, TOR). EC values determined using TOT can be up to 30 – 70 % lower than those determined with TOR (Karanasiou et al., 2015), because the evaporation of non-absorbing particulate matter during heating affects the reflectance to a greater extent than the transmission signal. Furthermore, high loadings of EC result in saturation effects of both optical signals, again to a greater extent for the reflection compared to the transmission method (Chiappini et al., 2014). These two effects result in better reproducibility and accuracy of the TOT based OC/EC split compared to the TOR approach.

## S3.2. Calculation of variability and bias

The variability ( $Q_{AV}$ ) is defined as the relative standard deviation given by the 95 % confidence limit, thus:

$$Q_{AV} = \frac{n}{\sqrt{6}} \left[ \max \left( \frac{RD_i}{T_i} \right) - \min \left( \frac{RD_i}{T_i} \right) \right] \quad (S3.1)$$

Where  $RD_i = L_i - T_i$ , with  $L_i$  and  $T_i$  representing the laboratory and expected concentrations, respectively.

The bias ( $Q_{AB}$ ) is defined as the median of the percentage of the ratio between  $RD_i$  and  $T_i$

$$Q_{AB} = \text{median} \left[ \frac{RD_i}{T_i} \% \right]. \quad (S3.2)$$

## S3.3. The Cunningham slip correction

The Cunningham slip correction factor,  $C_C$ , is used to account for non-continuum effects when calculating the drag force on small particles.  $C_C$  depends on the particle diameter,  $D$ , the mean free path of the surrounding gas,  $\lambda$ , and on the experimental coefficients  $\alpha$ ,  $\beta$  and  $\gamma$  (Cunningham, 1910; Seinfeld and Pandis, 2006).

$$C_C(D) = 1 + \frac{2\lambda}{D} \left[ \alpha + \beta e^{-\frac{\gamma D}{\lambda}} \right] \quad (S3.3)$$

with  $\alpha = 1.257$ ,  $\beta = 0.4$ ,  $\gamma = 1.1$ ,  $\lambda = 6.5 \cdot 10^{-8}$  m

### S3.3. Hygroscopic growth factor

Hygroscopic growth affects the cut-off imposed by impactors operated at ambient RH. Here we provide simplified equations to calculate the volume equivalent diameter growth factor, GF, of BC-containing particles coated with a mixture of organic and inorganic matter. The GF is calculated using  $\kappa$ -Köhler theory (Petters and Kreidenweis, 2007):

$$\text{GF}(\text{RH}) = \left(1 + \kappa_{\text{tot}} \frac{\text{RH}}{1-\text{RH}}\right)^{1/3} \quad (\text{S3.4})$$

where the hygroscopicity parameter of the mixed particle,  $\kappa_{\text{tot}}$ , is obtained with the ZSR-mixing rule written as (Petters and Kreidenweis, 2007):

$$\kappa_{\text{tot}} = \varepsilon_{\text{BC}}\kappa_{\text{BC}} + \varepsilon_{\text{org}}\kappa_{\text{org}} + \varepsilon_{\text{inorg}}\kappa_{\text{inorg}} \quad (\text{S3.5})$$

The hygroscopicity parameters  $\kappa$  of BC, organics and inorganics are assumed to be 0, 0.1 and 0.5, respectively (Engelhart et al., 2012). The volume fraction,  $\varepsilon_x$ , of compound class “x” in the particle can be calculated using:

$$\varepsilon_x = \frac{m_x \rho_{\text{tot}}}{m_{\text{tot}} \rho_x} \quad (\text{S3.6})$$

where  $m_x$  is the mass of “x” in the particle,  $m_{\text{tot}}$  is the total particle mass.  $\rho_x$  is the material density of “x”, which is assumed to be  $1800 \text{ kg m}^{-3}$ ,  $1200 \text{ kg m}^{-3}$  and  $1700 \text{ kg m}^{-3}$  for BC, organics and inorganics, respectively. The mixed particle density,  $\rho_{\text{tot}}$ , is obtained with:

$$\rho_{\text{tot}} = \frac{1}{\frac{m_{\text{BC}}}{m_{\text{tot}}} \rho_{\text{BC}} + \frac{m_{\text{org}}}{m_{\text{tot}}} \rho_{\text{org}} + \frac{m_{\text{inorg}}}{m_{\text{tot}}} \rho_{\text{inorg}}} \quad (\text{S3.7})$$

### S3.4. Dryers and losses

Differences in  $m_{\text{rBC}}$  and  $m_{\text{EC}}$  mass concentration can also come from differences in the losses of the respective sampling inlets. Particle losses can be caused by the presence of a dryer in the inlet line. The dryer technology offers different dryer types including diffusion and membrane dryers. Diffusion dryers use chemical adsorbents such as silica gel for the minimization of aerosol losses. When the aerosol passes through the tube, the silica adsorbs water vapor, therefore this chemical needs to be changed and regenerated on a regular basis. Membrane dryers are elastic tubes based on water vapor-permeable polytetrafluoroethylene (PTFE). Commercially available membranes are products such as Nafion®: a sulfonated tetrafluoroethylene working as permeable membrane in which water vapor molecules are transported.

In any case, particle losses by diffusion across the dryer should be accounted for in the data processing. This is done by calculating an equivalent tube length, which is longer than the actual dryer length (Wiedensohler et al., 2012).

In this work we calculate the diffusion losses when dryers were present in the inlet lines. A diffusion dryer was placed in front of the SP2 line during the Bologna campaign; while the EC line had none. The particle transmission efficiency of the diffusion dryer for a flow rate of  $2 \text{ L min}^{-1}$  was evaluated to be less than 10 % on average on the size range of the SP2 measurements. Nafion dryers (model MD-700, Perma Pure) were set in front of the SP2s in the Melpitz and Cabauw campaigns. The diffusion losses through them were calculated with the hypothesis of laminar flow and were found to be negligible. The particle loss due to the presence of a dryer in the inlet line does not seem to be the main reason of the  $m_{\text{rBC}}$  and  $m_{\text{EC\_PM}_{2.5}}$  discrepancies for the campaigns of this study. For this reason we did not correct the rBC mass concentrations for this effect.

Table S3.1: site, station code, coordinates, altitude and year/season of the field campaigns presented in this work.

Site (country)	Station code	Coordinates	Altitude	Year/season
Palaiseau (FR)	Palaiseau	48.713° N 2.208° E	160	2010/winter
Melpitz (DE)	Melpitz	51°32' N, 12°56' E	86	2017/winter and 2015/summer
Cabauw (NE)	Cabauw	51° 58' N, 4° 55' E	-0.7	2016/autumn
Bologna (IT)	Bologna	44° 31' N, 11° 20' E	39	2017/summer

Table S3.2: The first three columns show median, 10<sup>th</sup> and 90<sup>th</sup> percentiles of EC, TC and EC/TC filter loading. The last four columns show minima and maxima of EC and TC filter loadings for the field campaigns of this study.

Station code	EC filter loading median (10 <sup>th</sup> , 90 <sup>th</sup> ) [ $\mu\text{g cm}^{-2}$ ]	TC filter loading median (10 <sup>th</sup> , 90 <sup>th</sup> ) [ $\mu\text{g cm}^{-2}$ ]	EC/TC filter loading median (10 <sup>th</sup> , 90 <sup>th</sup> ) [ $\mu\text{g cm}^{-2}$ ]	Min EC filter load [ $\mu\text{g cm}^{-2}$ ]	Max EC filter load [ $\mu\text{g cm}^{-2}$ ]	Min TC filter load [ $\mu\text{g cm}^{-2}$ ]	Max TC filter load [ $\mu\text{g cm}^{-2}$ ]
Palaiseau	1.66 (0.76, 3.19)	9.79 (5.02, 24.03)	0.14 (0.09, 0.30)	0.44	7.53	3.72	37.56
Melpitz winter	4.30 (1.50, 11.08)	44.73 (9.77, 110.72)	0.11 (0.09, 0.17)	0.93	12.53	5.45	115.03
Melpitz summer	0.90 (0.48, 1.43)	12.47 (6.93, 19.08)	0.08 (0.05, 0.10)	0.25	2.30	4.76	24.43
Cabauw	1.47 (0.71, 2.34)	6.87 (3.78, 14.95)	0.18 (0.12, 0.29)	0.48	3.44	2.92	19.10
Bologna	2.49 (1.84, 2.66)	15.50 (13.20, 17.72)	0.16 (0.11, 0.19)	1.63	2.74	12.46	18.42

Table S3.3: In this table the aerodynamic particle diameter  $D_{aero}$  corresponding to the upper SP2 cut-off, which depends on the BC mass equivalent diameter,  $D_{ve}$  (calculating starting from the BC core mass equivalent diameter,  $D_{rBC}$ , knowing the particle mixing state), is given for different extreme hypotheses concerning particle shape ( $\chi$ ), mixing state and relative humidity (RH). The calculations are made with the hypothesis of fixed density of BC core  $\rho_{rBC} = 1800 \text{ kg m}^{-3}$  and with the hypothesis of coating made by half organic material with  $\kappa_{org} = 0.1$  and  $\rho_{org} = 1200 \text{ kg m}^{-3}$  and half inorganic material with  $\kappa_{inorg} = 0.5$  and  $\rho_{inorg} = 1700 \text{ kg m}^{-3}$ . From these hypothesis and knowing the ratio between the mass of the coating material,  $m_{coat}$  and the mass of the BC core,  $m_{rBC}$ , the total particle density,  $\rho_p$ , can be calculated. The mixing state of the last example particle is constrained with SP2 measurements during the Melpitz winter campaign.

	$D_{rBC}$ [nm]	$\rho_p$ [kg m <sup>-3</sup> ]	$\kappa_{tot}$	$D_{ve}$ [nm] Dry	GF (RH = 80 %)	$D_{ve}$ [nm] (RH = 80 %)	GF (RH = 95 %)	$D_{ve}$ [nm] (RH = 95 %)	$D_{aero}$ [nm] Dry	$D_{aero}$ [nm] (RH = 80 %)	$D_{aero}$ [nm] (RH = 95 %)
Fractal-like pure BC: $\chi = 2.4$ (Park et al., 2003)	722.0	1800.0	0.0	722.0	1.0	722.0	1.0	722.0	625.3	625.3	625.3
Spherical pure BC: $\chi = 1$	722.0	1800.0	0.0	722.0	1.0	722.0	1.0	722.0	968.7	968.7	968.7
Coated BC: $\chi = 1$ , $m_{coat} = m_{rBC}$	722.0	1579.4	0.1	909.7	1.2	1063.1	1.6	1423.4	1143.2	1336.0	1788.8
Coated BC: $\chi = 1$ , $m_{coat} = 6m_{rBC}$	722.0	1452.2	0.2	1381.1	1.2	1722.4	1.8	2432.5	1664.4	2075.6	2931.3
Coated BC with coating as observed during the Melpitz Winter campaign: $\chi = 1$ , $m_{coat} = 2.33$ [0.99–3.17] $m_{rBC}$	722.0	1505.2	0.2	1078.2	1.2	1310.4	1.7	1815.9	1322.8	1607.7	2227.9

Table S3.4: AAE (470,950) statistics for the campaigns in this study: median, geometric mean, 10<sup>th</sup> and 90<sup>th</sup> percentiles and number of data points.

	Palaiseau	Cabauw	Melpitz summer	Melpitz winter	Bologna
AAE median (10, 90)	1.35	1.05	1.19	1.40	1.03
	(1.24, 1.53)	(0.97, 1.12)	(1.09, 1.26)	(1.28, 1.50)	(1.01, 1.07)
AAE geometric mean	1.36	1.04	1.18	1.38	1.04
# points	34	32	49	20	7

Table S3.5: Summary of site name, country, SP2 calibration material,  $m_{EC}$  cut-off and TOA thermal protocol, sampling period, site characteristics and geometric mean of the  $m_{rBC}/m_{EC}$  ratio for all the data. \*One data point

	SP2 Calibration Material	$m_{EC}$ cut-off/ TOA Thermal technique	Site name, country	Season/year and site characteristics	$m_{rBC}/m_{EC}$ median
Palaiseau	Fullerene Soot	PM <sub>2.5</sub> / EUSAAR-2	Paris, France	Jan/Feb 2010 suburban background	1.20
Cabauw	Fullerene Soot	PM <sub>10</sub> / EUSAAR-2	Cabauw, Netherlands	Oct 2016 rural background	0.53
Bologna	Fullerene Soot	PM <sub>2.5</sub> / EUSAAR-2	Bologna, Italy	July 2017 urban background	0.65
Melpitz winter	Fullerene Soot	PM <sub>2.5</sub> / EUSAAR-2	Melpitz, Germany	Feb 2017 rural background	1.29
Melpitz summer	Fullerene Soot	PM <sub>2.5</sub> / EUSAAR-2	Melpitz, Germany	July 2015 rural background	0.97
Zhang et al. (2016)	Fullerene Soot	PM <sub>2.5</sub> / IMPROVE	Fresno, California, USA	Jan/Feb 2013 urban background	0.70
Miyakawa et al. (2016)	Fullerene Soot	PM <sub>2.5</sub> / IMPROVE-like	Yokosuka, Japan	Summer 2014 June 17 – 27 urban	1.07
Sharma et al. (2017)	Aquadag scaled to Fullerene Soot	PM <sub>1</sub> / EnCan-Total-900	Nunavut, Canada	From Mar 2011 to Dec 2013 remote site	0.55
Corbin et al. (2019)	Fullerene Soot	PM <sub>1</sub> / IMPROVE-A (washed)	–	Chamber study – four-stroke ship diesel engine	1.03*
Laborde et al. (2012b)	Fullerene Soot	NIOSH-5040	–	Chamber study – CAST soot	1.10*

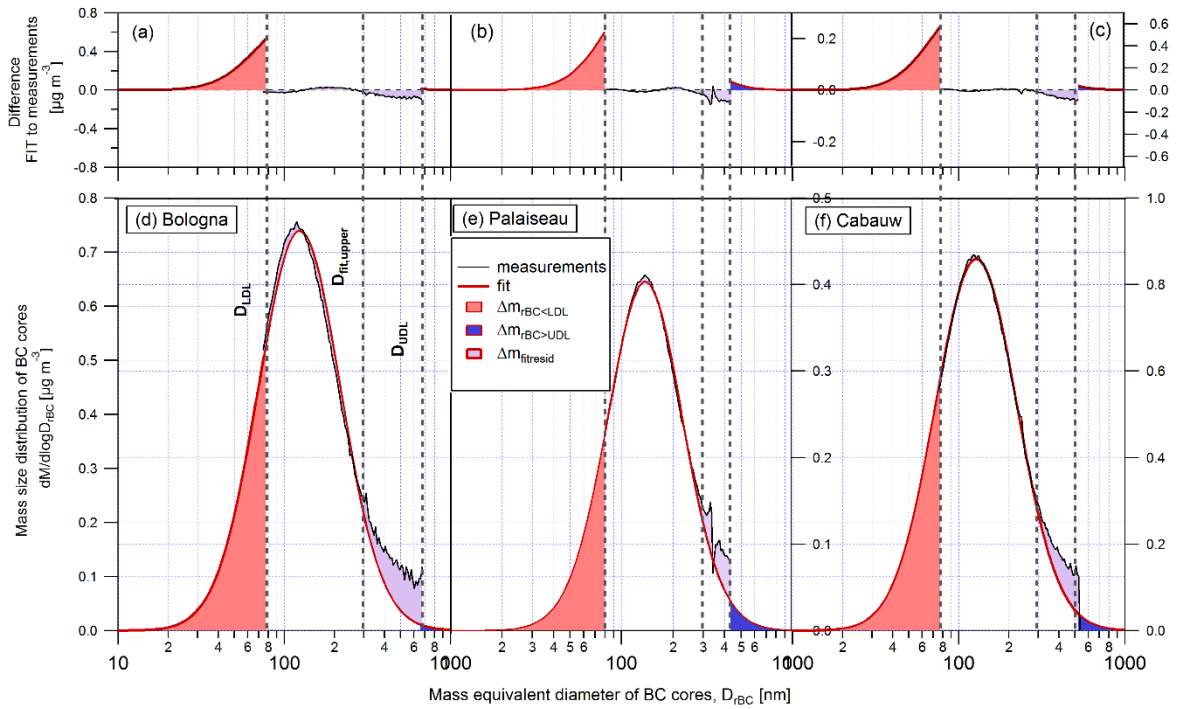


Figure S3.1: Approach to correct for the rBC mass outside the rBC core size range covered by the SP2 for the Bologna (panels a and d), the Palaiseau (panels b and e) and the Cabauw (panels c and f) campaigns. The bottom three panels show the measured rBC mass size distribution as a function of rBC core mass equivalent diameter, including the SP2 detection limits  $D_{LDL}$  and  $D_{UDL}$ . The lognormal functions are fitted between  $D_{LDL}$  and  $D_{fit,upper}$ . The integrated area of the red, purple, and blue shadings correspond to  $\Delta m_{rBC < LDL}$ ,  $\Delta m_{fitresid}$  and  $\Delta m_{rBC > UDL}$ , respectively (see Sect. 3.2.3.5). The top three panels additionally show the same shadings after subtraction of the measured size distribution (and measurement forced to be zero outside the SP2 detection range).

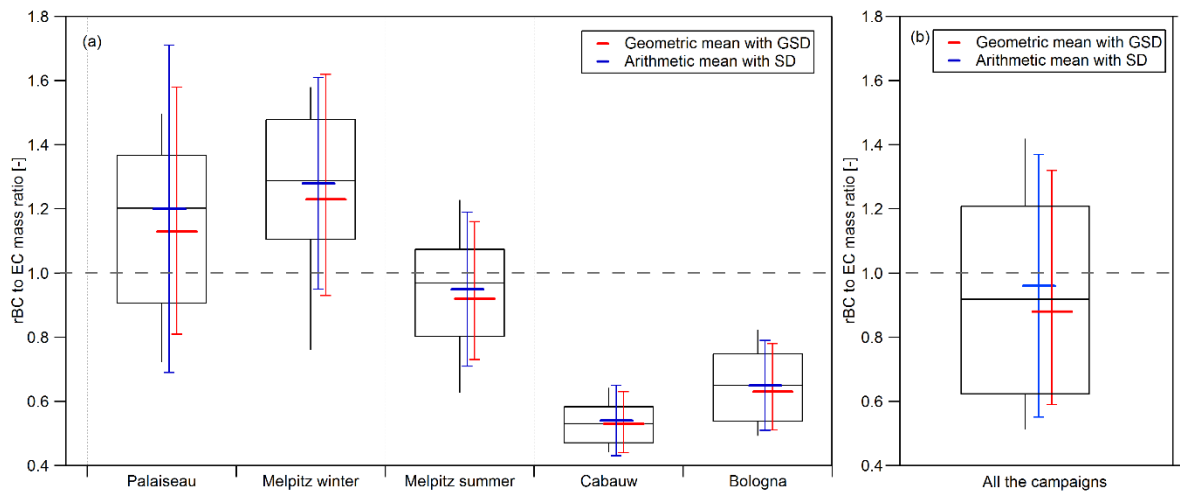


Figure S3.2: Statistics (10<sup>th</sup>, 25<sup>th</sup>, 50<sup>th</sup>, 75<sup>th</sup> and 90<sup>th</sup> percentiles, arithmetic and geometric means, SD and GSD) of the rBC to EC mass ratio ( $m_{rBC}/m_{EC}$ ) per campaign (panel a) and with all the campaigns of this work (panel b).



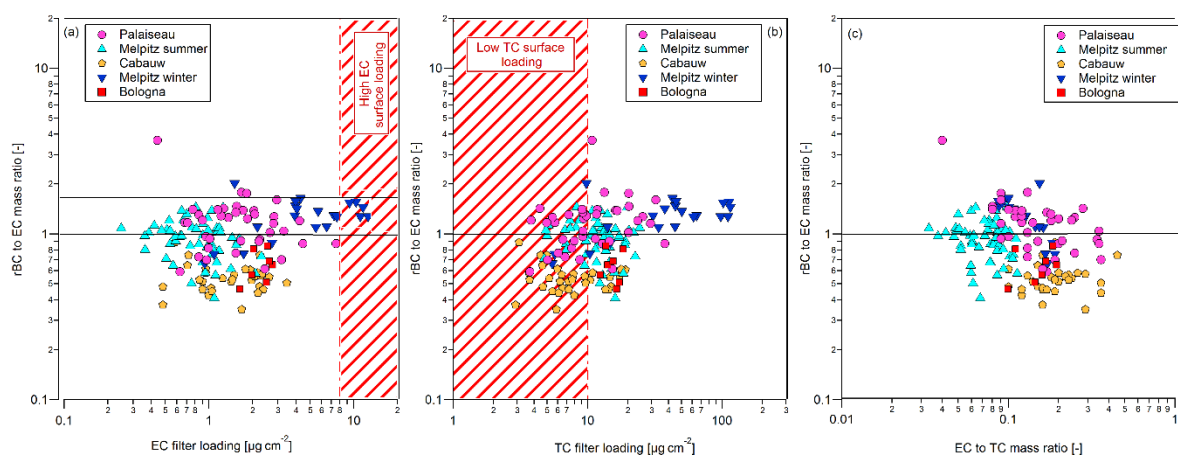


Figure S3.3: rBC mass concentration versus EC filter loading (panel a), TC filter loading (panel b) and EC/TC mass ratio (panel c). The red shaded areas in panel (a) and (b) indicate the high EC surface loading and the low TC surface loading areas respectively.

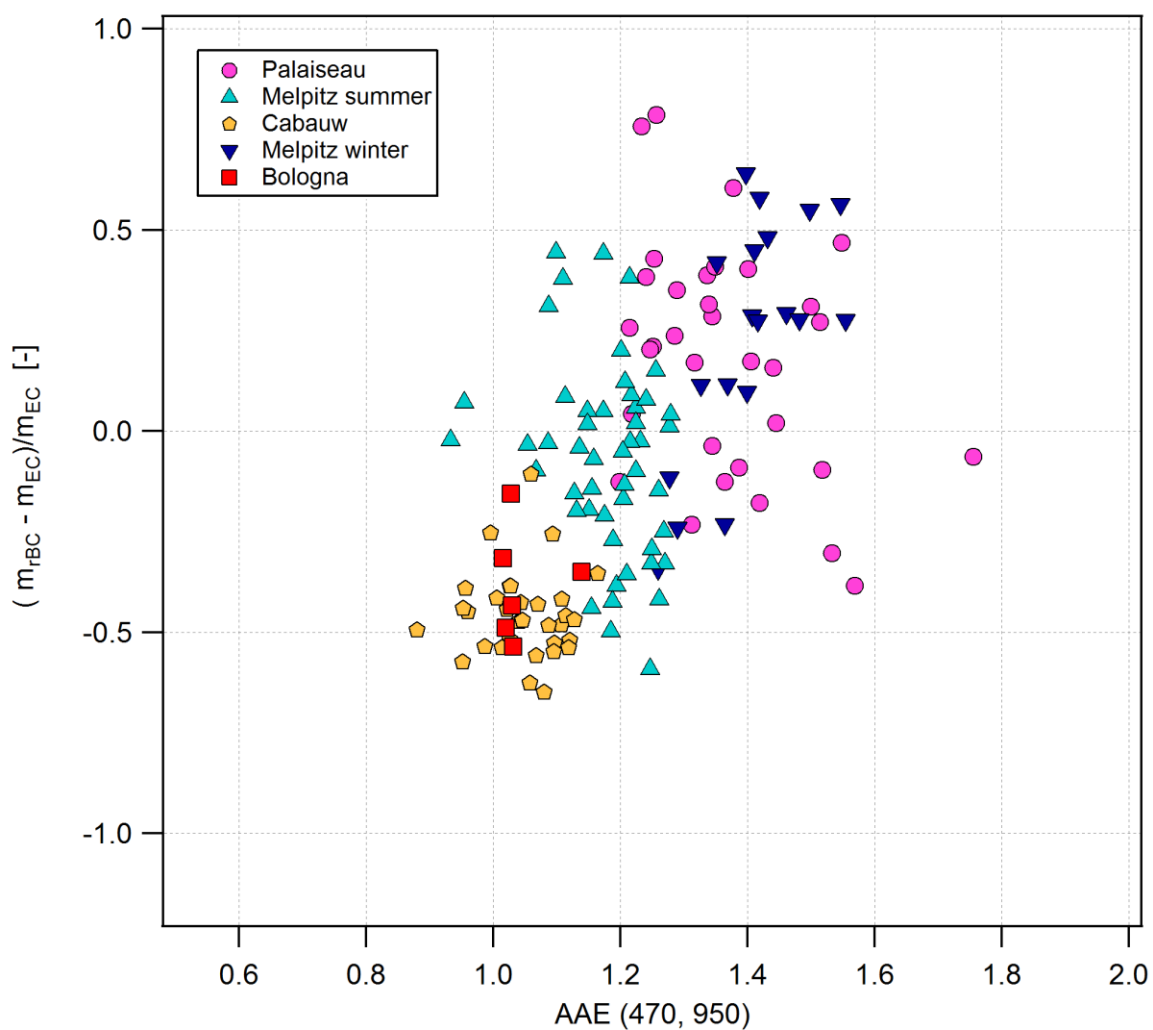


Figure S3.4: Relative difference between  $m_{rBC}$  and  $m_{EC}$  versus the AAE(470,950) coloured by campaign.

## Chapter 4:

# Variability of physical and optical properties of freshly emitted and aged black carbon particles determined from stationary and mobile measurements in the Po Valley (Italy), during summertime

Rosaria Erika Pileci<sup>1</sup>, Michele Bertò<sup>1</sup>, Robin L. Modini<sup>1</sup>, Stefania Gilardoni<sup>2\*</sup>, Matteo Rinaldi<sup>2</sup>, Douglas Orsini<sup>2</sup>, Angela Marinoni<sup>2</sup>, Urs Baltensperger<sup>1</sup> and Martin Gysel–Beer<sup>1</sup>

<sup>1</sup> Laboratory of Atmospheric Chemistry, Paul Scherrer Institute (PSI), 5232 Villigen, Switzerland

<sup>2</sup> CNR–ISAC—Italian National Research Council, Institute of Atmospheric Science and Climate, via Gobetti 101, 40129 Bologna, Italy

\*now at: ISP–CNR – Italian National Research Council, Institute of Polar Sciences, via Gobetti 101, 40129 Bologna, Italy

*Correspondence to:* Modini (rob.modini@psi.ch) and Gysel–Beer (martin.gysel@psi.ch)

Manuscript in preparation for submission to *Atmospheric Chemistry and Physics*.

**Abstract.** Black carbon (BC) particles are the main light–absorbing component of atmospheric aerosols. They affect the climate system globally and regionally, and are damaging to human health. The characterization of the spatio–temporal variability of the physical and optical properties of black carbon particles is of great importance in evaluating their climate and health effects; this is particularly relevant in the Po Valley (in the northern part of Italy), one of the most polluted regions in Europe and home to almost 20 million inhabitants.

Optical properties of atmospheric aerosol indicated that the main BC source contribution in summer in the Valley occurred by traffic emissions. The stationary measurements at the CNR site indicated that the diurnal cycles of BC properties were dominated by the interplay of local sources, wind direction changes, and planetary boundary layer (PBL) dynamics. For instance, the average mass absorption cross–section of refractory BC at 637 nm ( $MAC_{rBC}^{637\text{ nm}}$ ) increased from 12.2 to 16.0 m<sup>2</sup> g<sup>−1</sup> based on SP2 measurements, and from 8.1 to 11.5 m<sup>2</sup> g<sup>−1</sup> based on thermal–optical elemental carbon (EC) measurements ( $MAC_{EC}^{637\text{ nm}}$ ); the minima occurred in the morning when fresh traffic emissions dominated the aerosol loading, and the maxima occurred in the afternoon when PBL height increased and aged particles dominated BC mass.

The spatial variability was investigated by driving on two different types of roads (highways and provincial roads) which were 10 km distant and roughly parallel to each other. The  $MAC_{rBC}^{637\text{ nm}}$  values increased by 39 % from the highway to the provincial roads. The observation of the average rBC mass size distributions and the absorption Ångström exponent (AAE) supported the hypothesis that mixing of freshly emitted BC with aged background BC was the dominant process responsible for this  $MAC_{rBC}^{637\text{ nm}}$  difference. Moreover, the results from aerosol mass spectrometry confirmed this interpretation, showing that it is more likely to find externally mixed organic aerosol (OA) on the highway, and more internally mixed OA on the provincial roads.

A clear positive relationship was found between the number fraction of thickly coated BC particles and the  $MAC_{rBC}^{637\text{ nm}}$  value, while the variation in BC core size was too small to explain the variations in the  $MAC_{BC}$  values. Therefore, the variation in BC mixing state was the main factor driving the  $MAC_{BC}$  variability, indicating that atmospheric aging increases the  $MAC_{BC}$  value via the “lensing–effect” by up to a factor of 2.

## 4.1 Introduction

Black carbon (BC) is a type of carbonaceous material emitted from anthropogenic and natural combustion processes. Although BC represents a small fraction (around 10 % by mass) of the total atmospheric aerosol (Lanz et al., 2010; Putaud et al., 2010), it plays an important role in the Earth system, impacting living organisms and climate (Soto et al., 2008; Grahame et al., 2014). Black carbon is the main light-absorbing component of atmospheric aerosols (Moosmüller et al., 2009; Liu et al., 2020). It influences Earth's climate by both aerosol-radiation interactions and aerosol-cloud interactions (Jacobson, 2001; Bond, 2013). Through these effects and the interaction with the cryosphere, black carbon particles are the second largest contributor after CO<sub>2</sub> to anthropogenic climate forcing in the present-day atmosphere. In particular, the BC direct radiative effect (DRE) at the top of the atmosphere ranges between +0.08 and +1.4 W m<sup>-2</sup> (Jacobson, 2001; Bond, 2013). The high uncertainty in the DRE originates from the low level of confidence in understanding BC-related processes (Myhre et al., 2013). For this reason, an improved understanding of the spatio-temporal variations of BC physical and optical properties is a critical step for reducing uncertainties in estimating the impacts of BC on climate (Schulz et al., 2006).

Freshly emitted BC particles are often externally mixed fractal-like aggregates of primary spherules (Bond et al., 2006). During atmospheric aging, the fractal aggregates become mixed with other particulate species (internally mixed), such as sulphates or organics (Weingartner et al., 1997; Riemer et al., 2009; Bond et al., 2013b; Matsui et al., 2013; Bhandari et al., 2019). The aging changes the size and composition of the coated BC particles thus modifying their hygroscopicity and morphology (Fierce et al., 2015). Moreover, aging is known to enhance the black carbon mass absorption cross-section (MAC<sub>BC</sub>), which is the value describing the BC absorption cross section per unit mass of BC (Jacobson, 2001; Schnaiter M. et al., 2005; Peng et al., 2016) (see Sect. 4.2.1 for the operational definition of the MAC<sub>BC</sub>). The enhancement of the MAC<sub>BC</sub> by coating of BC particles with condensable material is known as the “lensing effect” (Fuller et al., 1999).

Many theoretical studies have shown that the lensing effect can substantially increase BC absorption by up to a factor of two (Bond et al., 2006; Zhang et al., 2018a). Mie theory with a core-shell assumption for homogeneous spherical particles, and assuming the refractive indexes of the BC core and coating materials, is the simpler and most common method to represent a coated BC particle in models. The absorption enhancement of BC due to coating has been confirmed by controlled laboratory experiments which showed a good agreement with the core-shell Mie model (Cross et al., 2010; Lack and Cappa, 2010; Shiraiwa et al., 2010; Bueno et al., 2011; Metcalf et al., 2013). In contrast, field experiments showed contradictory results: some observed a large absorption enhancement (Knox et al., 2009; Naoe et al., 2009; Cui et al., 2016; Chen et al., 2017; Yuan et al., 2020); while others observed much smaller enhancement, or no enhancement at all (Cappa et al., 2012; Lan et al., 2013; Healy et al., 2015; Liu et al., 2015; Cappa et al., 2019). Three main hypotheses made by Cappa et al. (2019) attempted to explain this range of results: the variability of the core refractory BC (rBC) to coating mass fraction among individual particles (Fierce et al., 2016), the different mixing morphologies (Adachi et al., 2010); and the variation in chemical composition of the coating material (Zhang et al., 2018b). However, the relative importance of these effects remains poorly understood.

Bond and Bergström (2006) proposed a representative MAC<sub>BC</sub><sup>550 nm</sup> value of 7.5 m<sup>2</sup> g<sup>-1</sup> for freshly generated BC and a range from 5 m<sup>2</sup> g<sup>-1</sup>, for collapsed but uncoated BC, to 11 m<sup>2</sup> g<sup>-1</sup> for aged and coated BC (Bond and Habib, 2006). In a harmonization work at nine rural background sites across Europe, Zanatta et al. (2016) found an average MAC<sub>BC</sub><sup>637 nm</sup> value of 10 m<sup>2</sup> g<sup>-1</sup>. Although the range of the MAC<sub>BC</sub> values found in the literature is consistent with more recent observations (Ram and Sarin, 2009; Cui et al., 2016; Zanatta et al., 2016), the spread remains rather large. The MAC<sub>BC</sub> value's variability can be primarily explained with the variability in BC physical and optical properties such as mixing state, BC core size, particle morphology and refractive index (Bond et al., 2006; Dastanpour et al., 2017). However, it also depends on the measuring techniques used for the BC mass concentration and the absorption coefficient (Arnott et al., 2003; Pileci et al., 2021), which can have large uncertainties (up to 30–70 %), due to the lack of appropriate reference methods and calibration materials (Petzold et al., 2013; Zanatta et al., 2016).

BC concentrations, as well as physical and optical properties, are modified by dilution through PBL dynamics and atmospheric aging. For instance, Zhao et al. (2018) found that highly turbulent air conditions, observed during hot seasons in the North China Plain around the Beijing megacity, largely diluted the BC mass concentration to background levels. Furthermore, BC properties also depend on the emission source (Andreae and Gelencsér, 2006). The main black carbon sources are fossil fuel combustion and biomass burning (Chow et al., 2001; Briggs and Long, 2016), with different seasonal contributions. The source apportionment of black carbon can be done based on the absorption Ångström exponent (AAE), a coefficient that describes the spectral dependence of the aerosol absorption coefficient (Kirchstetter et al., 2004; Sandradewi et al., 2008; Kirchstetter and Thatcher, 2012). AAE values close to 1 are associated with aerosols from fossil fuel burning, while larger values indicate aerosols from biomass/biofuel burning (Moosmüller et al., 2009; Sandradewi et al., 2008; Zotter et al., 2017). In addition, as reported by Schwarz et al. (2008), particles from fossil fuel combustion generally have smaller volume equivalent diameters (70–140 nm) than particles produced by biomass burning (140–200 nm).

The  $MAC_{BC}$  value depends on particle size, morphology and mixing state, and can hence also depend on source and combustion conditions. Both absolute and relative differences between the  $MAC_{TR}$  ( $MAC_{BC}$  from traffic) and the  $MAC_{WB}$  ( $MAC_{BC}$  from wood burning) decrease with increasing wavelength (Forello et al., 2019). Zotter et al. (2017) found a  $MAC_{TR}$  to  $MAC_{WB}$  ratio of 0.97 at 880 nm, while Laborde et al. (2013) reported a ratio of 0.94 (with  $MAC_{BC}^{880\text{ nm}} = 7.3\text{ m}^2\text{ g}^{-1}$  for traffic and  $7.8\text{ m}^2\text{ g}^{-1}$  for biomass burning).

Black carbon particles are an environmental issue in the Po Valley of Northern Italy, which is a territory encircled by mountains exceeding altitudes 2500 m above sea level on three sides and often characterized by meteorological conditions that inhibit air pollution dispersion (Bigi et al., 2017; Bucci et al., 2018). In a review paper on the spatial and seasonal variability of carbonaceous aerosol across Italy, Sandrini et al. (2014) found an average annual elemental carbon (EC) concentration of  $1.7\text{ }\mu\text{g m}^{-3}$  at some Po Valley urban background sites and  $4.5\text{ }\mu\text{g m}^{-3}$  at a traffic affected monitoring station in Milan. These values are substantially higher than at other European sites (Zanatta et al., 2016), confirming that the Po Valley is one of the most important pollution hotspot regions in Europe (Vecchi et al., 2009; Putaud et al., 2010; Bernardoni et al., 2011). Moreover, this BC load enhances local atmospheric heating in the valley with consequences on atmospheric dynamics; for instance Ferrero et al. (2014) found that BC below the upper boundary of the mixed layer has the potential to increase the dispersion of pollution by decreasing the atmospheric stability over the Po Valley. For these reasons, studying the spatio-temporal BC properties in this area is fundamental for assessing BC climate impacts.

In this work we investigate the spatio-temporal variability of the  $MAC_{BC}$  value and its relation during summertime with the mixing state and BC core diameter in the Po Valley. Moreover, we provide an overall picture of the most relevant physical-optical black carbon properties, such as the refractory BC mass concentration ( $m_{rBC}$ ), elemental carbon mass concentration ( $m_{EC}$ ), rBC mass size distribution, BC absorption coefficient, AAE, and single scattering albedo (SSA). In order to sample black carbon particles with different degree of aging, both stationary and mobile measurements were performed. The stationary measurements were taken at a sub-urban monitoring site of the Regional Agency for Prevention, Environment and Energy (ARPAE), in Bologna; at the background site of San Pietro Capofiume, and at the remote, high altitude site of Monte Cimone. The mobile measurements were performed driving along the Valley with a mobile van (Bukowiecki et al., 2002; Wolf et al., 2015) where the route planning was performed such that a comparison of the aerosol properties on the highway and provincial roads was possible.

## 4.1 Methods

### 4.1.1 Measurements period and sites

The field campaign was carried out in the Po Valley (Italy, Fig. 4.1) between 7 and 31 July 2017. The stationary measurements were performed with a mobile laboratory (described in Sect. 4.1.2), which was mostly parked nearby the regional network monitoring cabin of ARPAE, a suburban site in Bologna ( $41^{\circ}54\text{ N}$ ,  $12^{\circ}30\text{ E}$ ; 54 m a.s.l.). Some stationary measurements were also carried out at the background site of San Pietro Capofiume ( $44^{\circ}390\text{ N}$ ,  $11^{\circ}370\text{ E}$ ; 11 m a.s.l.) and at the remote, high altitude site of Monte Cimone ( $44^{\circ}120\text{ N}$ ,  $10^{\circ}420\text{ E}$ ; 2165 m a.s.l.). Mobile measurements took place between the stationary measurements throughout the campaign.

Three different types of drives were performed: from Bologna to the Southeast of Milan (Lodi), from Bologna to Monte Cimone, and from Bologna to Chioggia, approximately 50 km South of Venice. Table 4.1 provides the details of all trips during the campaign.

Table 4.1: Details of all mobile trips completed during the campaign.

Date	Trip	Time Start	Time Stop
07.07.2017	Bologna – Lodi	05:42	17:05
08.07.2017	Bologna – Lodi	05:51	15:18
11.07.2017	Bologna – S.Pietro – Chioggia	09:00	19:05
13.07.2017	Bologna – Monte Cimone	10:08	20:02
14.07.2017	Bologna – Monte Cimone	09:19	20:34
18.07.2017	Bologna – Monte Cimone	09:01	23:40
20.07.2017	Bologna – S.Pietro – Monte Cimone	08:45	19:55
22.07.2017	Bologna – Lodi	07:15	15:48
24.07.2017	Bologna – S.Pietro – Chioggia	12:12	19:38
25.07.2017	Bologna – Lodi	06:40	15:01
27.07.2017	Bologna – Monte Cimone	07:18	10:03

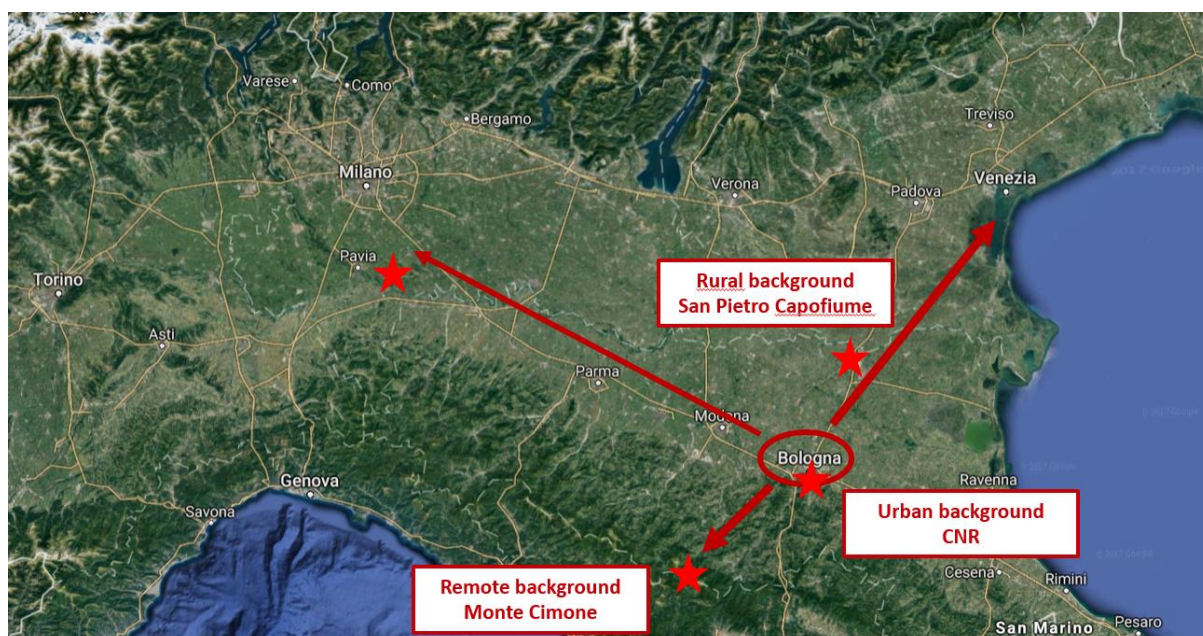


Figure 4.1: Map of the study region, with stars indicating the sites of the stationary measurements (the urban background site in Bologna, the rural background site of San Pietro Capofiume and the remote high–altitude background site of Monte Cimone). The arrows indicate the drives for the mobile measurements (Map data ©2020 Google).

#### 4.1.2 The mobile laboratory

The PSI mobile measurement van termed “MOSQUITA” (Measurements Of Spatial Quantitative Imissions of Trace Gases and Aerosols) was used in this field campaign. The first version of the van was built in 2000 (Bukowiecki et al., 2002), then modified by Weimer et al. (2009), and most recently included an aerosol mass spectrometer (Wolf et al., 2015). The version used for this project was equipped with a set of instruments to characterize physical, optical, and chemical aerosol properties and to determine trace gas concentrations with high time resolution (a description of the instruments is given in the Sect. 4.1.3). In addition, sensors were used to measure ambient temperature, pressure, and relative humidity. A Global Positioning System (GPS) was employed to track the driving routes. The instruments were connected to two inlet lines, each with a diameter of 5 cm at 3 m

above the ground located on top of the vehicle; these lines subsequently connected to the main inlet (Fig. 4.2). The air sampling velocity was about  $13 \text{ m s}^{-1}$  as a compromise to provide steady sampling conditions at different driving speeds (Bukowiecki et al., 2002). A blower drew in the sample air from the front of the van with a constant flow rate of  $4000 \text{ L min}^{-1}$  (Weimer et al., 2009). For aerosol measurements, the sampled air was dried using two silica-gel-filled diffusion driers, to keep the relative humidity (RH) below 30 %.

Table 4.2: List of the instruments inside MOSQUITA, related variables measured and wavelength of the measurement.

Instrument	Measured variable	Additional information
Aethalometer	Attenuation coefficient and absorption Angstrom exponent	$\lambda = 370; 470; 520; 590; 660; 880; 950\text{nm}$
MAAP	Absorption coefficient	$\lambda = 637 \text{ nm}$
CAPS-PM <sub>SSA</sub>	Scattering and extinction coefficients	$\lambda = 780 \text{ nm}$
PAX	Scattering and absorption coefficients	$\lambda = 870 \text{ nm}$
UHSAS	Size distribution	—
SP2	rBC mass concentration rBC size distribution mixing state	$\lambda = 1064 \text{ nm}$ (excitation), $\lambda = 350\text{--}800 \text{ nm}$ broadband incandescent light detection
LI-7000 CO <sub>2</sub> Analyzer	CO <sub>2</sub> –Carbon dioxide	—
Ozone monitor	O <sub>3</sub> –Ozone	—
HR–ToF–AMS	Non–refractory chemical composition	—
CPC	Particle number concentration	—

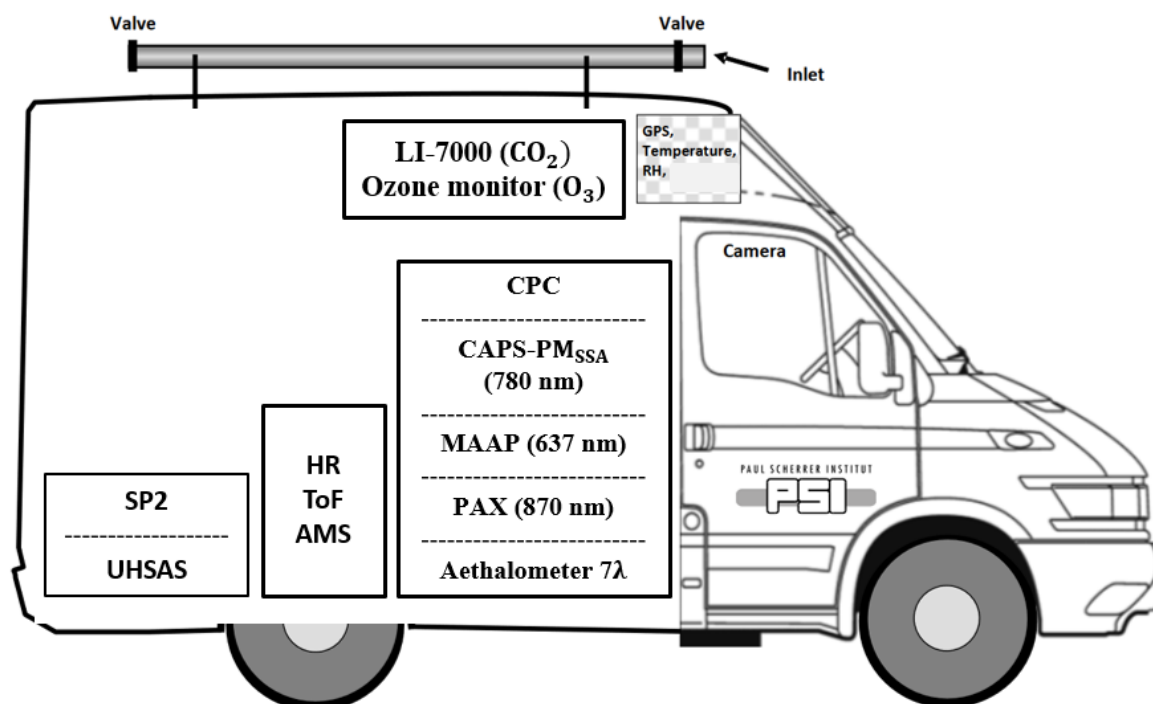


Figure 4.2. Location of the instruments inside the mobile van. The variables measured by these instruments are listed in Table 4.2. The instrument details are provided in Sect. 4.1.3.

### 4.1.3 Instruments used to measure aerosol optical properties

#### 4.1.3.1 Absorption based instruments

Table 4.2 presents an overview of all deployed instrumentation and measured variables. The following instruments were used to measure aerosol optical properties.

The Cavity Attenuated Phase Shift based single scattering albedo monitor (CAPS-PM<sub>SSA</sub>) combines cavity attenuated phase shift spectroscopy with an integrating sphere within the optical path of the cavity. It simultaneously measures the extinction and the scattering coefficients of an aerosol sample in its natural suspended state (Onasch et al., 2015). The absorption coefficient of the aerosol is obtained by subtracting the scattering from the extinction coefficient (known as the extinction-minus-scattering method). The CAPS-PM<sub>SSA</sub> is not subject to filter-based artefacts and it is capable of measuring optical coefficients at high time resolution (1 s). However, all integrating nephelometers exhibit a response bias which is a function of the sampled particles' scattering phase function (i.e., angular distribution), this is called truncation error and must be taken into account to correct the scattering coefficients (Müller et al., 2011; Onasch et al., 2015).

In this work, the CAPS-PM<sub>SSA</sub> data was corrected and used to calculate the single scattering albedo (SSA):

where  $b_{\text{sca}}$  and  $b_{\text{ext}}$  are the aerosol scattering and extinction coefficients, respectively.

$$\text{SSA} = \frac{b_{\text{sca}}}{b_{\text{ext}}} \quad (4.1)$$

The Multi-Angle Absorption Photometer (MAAP, Thermo Fisher Scientific, Waltham, USA) (Petzold et al., 2005) measures the transmitted and reflected light at multiple angles from an aerosol-laden filter and then applies a two-stream-approximation radiative transfer model to infer the absorption coefficient of the deposited aerosol sample. The instrument explicitly treats the light-scattering effects caused by the interaction between the aerosol sample and the filter matrix, which is an important improvement with respect to other filter-based optical instruments.

In this work, the MAAP was used to calculate the absorption coefficient  $b_{\text{abs}}(\lambda)$  at 637 nm using the following equation:

$$b_{\text{abs}}(637 \text{ nm}) = m_{\text{eBC}} \cdot \text{MAC}_{\text{eBC}}^{637 \text{ nm}} \cdot 1.05 \quad (4.2)$$

where  $m_{\text{eBC}}$  is the equivalent mass concentration of BC reported by the instrument,  $\text{MAC}_{\text{eBC}}^{637 \text{ nm}} = 6.6 \text{ m}^2 \text{ g}^{-1}$  is the mass absorption cross section used in the firmware of the MAAP. The factor 1.05 corrects for a difference between the actual wavelength (637 nm) and the nominal wavelength (670 nm) applied by the data inversion scheme implemented in the firmware (Müller et al., 2011).

The Aethalometer (AE33 model, Magee Scientific, Berkeley, USA) (Hansen et al., 1984; Drinovec et al., 2015), measures the rate of light transmittance change through an aerosol-laden filter per deposited sample air volume unit, from which the attenuation coefficient ( $b_{\text{atn}}$ ) of the aerosol sample is inferred at 7 wavelengths (370; 470; 520; 590; 660; 880; 950 nm) (Weingartner et al., 2003; Virkkula et al., 2007; Collaud Coen et al., 2010). By measuring the attenuation of two parallel filter spots simultaneously from the same air beam but with different flow rates and hence different filter loading, as implemented in the AE33, it is possible to correct the measured  $b_{\text{atn}}$  for filter loading artefacts in real time (Drinovec et al., 2015), obtaining  $b_{\text{atn,corr}}$ . Since the AE33 firmware correction was not working properly, the data was corrected for filter loading using the Weingartner et al. (2003) correction. The measured attenuation coefficients are related to the absorption coefficients through a factor accounting for multiple scattering effects known as the  $C$ -value, which is instrument and aerosol-dependent (Weingartner et al., 2003; Saturno et al., 2017). Therefore, it is not recommended to use AE33 attenuation

measurements to infer aerosol absorption coefficients without adequate knowledge of the  $C$ -value in a particular experiment.

For the purpose of this work, the AE33 data was used to calculate AAE using the following equation:

$$AAE(\lambda_1, \lambda_2) = - \frac{\ln(b_{\text{atn},1,\text{corr}}(\lambda_1)) \ln(\lambda_2)}{\ln(b_{\text{atn},1,\text{corr}}(\lambda_2)) \ln(\lambda_1)} \quad (4.3)$$

where  $b_{\text{atn},1,\text{corr}}(470)$  and  $b_{\text{atn},1,\text{corr}}(950)$  are the aerosol attenuation coefficients at the wavelengths 470 nm and 950 nm, respectively. Applying Eq. (1.4) to infer the AAE implicitly contains the assumption that during this study the AE33  $C$ -value did not depend on wavelength.

#### 4.1.3.2 The Single Particle Soot Photometer for BC particles

rBC mass concentrations, rBC particle mass size distributions and the number fractions of thickly coated particles were measured using a Single Particle Soot Photometer (SP2) (Droplet Measurement Technology, Boulder, CO, USA). The SP2 instrument (Stephens et al., 2003; Schwarz et al., 2006; Moteki and Kondo, 2010; Laborde et al., 2012a) employs a high-intensity continuous-wave intra-cavity Nd: YAG laser ( $\lambda = 1064$  nm) to make BC particles incandesce until they vaporize. The rBC mass in single particles is quantified by applying an empirical calibration curve to the measured peak intensity of the thermal emission from the rBC core at its vaporization point. Previous studies have shown that the sensitivity of the SP2 incandescence signal to BC particle mass (i.e. the SP2 calibration curve) depends on the BC type (Moteki and Kondo, 2010; Baumgardner et al., 2012; Laborde et al., 2012a). The SP2 is similarly sensitive (within  $\pm 10$  % for rBC mass  $\leq 40$  fg) to fullerene soot and ambient BC dominated by emissions from diesel engines (Laborde et al., 2012a). To calibrate the incandescence signal of the SP2 in this study, size-selected aerosols from fullerene soot (stock 40971, lot FS12S011) were generated with a differential mobility analyzer (DMA). Three incandescence calibrations were performed during the campaign and were found to be stable and in agreement, within 5 % of the previous calibrations performed in the laboratory and in previous field works. rBC mass size distributions were generated by converting the rBC mass of each BC-containing particle to an rBC mass equivalent diameter ( $D_{\text{rBC}}$ ) (assuming a void-free BC material density of  $\rho_{\text{BC}} = 1.8$  g cm<sup>-3</sup>) and binning the particles by  $D_{\text{rBC}}$ . The SP2 measurements during this field study covered the size range  $80$  nm  $\leq D_{\text{rBC}} \leq 676$  nm with unit detection efficiency. The rBC mass concentration measured in this BC core size range was corrected adding the estimated rBC mass concentration below the lower SP2 limit of quantification (here,  $D_{\text{rBC}} \leq 80$  nm). This mass was determined using an extrapolation method based on lognormal fits to the measurement between 80 nm and 300 nm BC core diameter, as described in Pileci et al. (2021). This missing rBC mass correction was found to be, on average,  $24.1 \pm 6.4$  % of the total measured rBC mass concentration. The SP2 detection efficiency was close to unity for  $D_{\text{rBC}} \geq 80$  nm (which corresponds to  $m_{\text{rBC}} > 0.48$  fg).

The SP2 is equipped with an avalanche photodiode, which detects the particles' scattering signals and is used for the optical sizing of the particles. For BC free particles, the peak scattering intensity is translated to an optical diameter assuming a fixed refractive index and spherical particle shape. The scattering calibration in this work was performed using spherical polystyrene latex size standards (PSL) with diameters of 150 and 269 nm.

The optical sizing of BC-containing material can be executed with the LEO-fit method (Gao et al., 2007; Laborde et al., 2012b). In this work, it was not possible to perform the LEO-fit method due to misalignment of the position sensitive detector). A different approach, known as the "delay-time method" can be used to obtain qualitative mixing state information. With the delay-time method the time lag between the scattering signal peak and the incandescence signal peak is measured. Particles with a delay time below a certain threshold (2  $\mu$ s in this study) are classified as bare, thinly or moderately coated, whereas particles with a delay time above this threshold are identified as thickly coated (Schwarz et al., 2006; Laborde et al., 2012b). The number fraction of thickly coated particles (NFTCP) is the quantity used as the proxy of BC mixing state in this work (see Sect. 4.3). It represents the number of thickly coated particles out of the total number of BC-containing particles based on the delay-time method.



#### 4.1.3.3 The thermal optical transmittance analysis for EC

EC mass measurements were performed with the thermal optical transmittance analysis (TOT) by the Regional Agency for Prevention, Environment and Energy (ARPAE). The ARPAE monitoring station was situated at 100 m distance from the MOSQUITA van.

During the thermal optical analysis, the carbonaceous material, deposited on a punch of a quartz–fibre filter, is thermally desorbed, through progressive heating: first in an inert atmosphere of pure helium (He), which allows for organic carbon (OC) volatilization, and then in an oxidizing atmosphere at high temperature to favor the total combustion of EC. The distinction between OC and EC is based on their difference in refractoriness (Birch and Cary, 1996; Chow et al., 1993, 2004). However, during the volatilization, part of the OC is transformed into pyrolytic carbon (PyC), a refractory component similar to the EC, giving rise to the phenomenon of charring (or pyrolysis). This effect may lead to interference in the reported OC and EC mass concentrations, even if optical corrections based on transmittance are applied (Chow et al., 2004).

The EC mass measurement used in this study are based on the EUSAAR–2 heating protocol with transmittance correction (Cavalli et al., 2010) on high–volume PM<sub>2.5</sub> filter samples. This protocol was specifically developed for aerosol typically encountered at European background sites and it was recently selected as the European standard thermal protocol to be applied in air quality networks for the measurements of TC (total carbon), OC and EC in particulate matter samples (European Committee for Standardisation Ambient air, 2017; EN16909:2017). The OC/EC analysis was performed by ARPAE, and some filters were sent after the campaign to the JRC ERLAP to validate the instrument performance (EMEP/CCC–Report 1/2018). Additional detail is provided in Pileci et al. (2021).

#### 4.1.4 The aerosol mass spectrometer for chemical composition

The chemical composition of the non–refractory submicron aerosol was monitored with an Aerodyne high–resolution time–of–flight aerosol mass spectrometer (HR–ToF–AMS) (Jayne et al., 2000; DeCarlo et al., 2006). The HR–ToF–AMS was operated in V–mode during the entire experiment to reach the highest sensitivity at 1–minute time resolution. It measured simultaneously the concentration and size distribution of sulfate, nitrate, ammonium, chloride, and organic aerosol. In the same way, as for the other aerosol instruments, the sampled air mass was dried to an RH below 30 % with a Nafion drier before measurement. High resolution mass spectra were analyzed with AMS data analysis software SQUIRREL 1.52F and PIKA 1.11G (D. Sueper, University of Colorado–Boulder, Boulder, CO, USA) within IGOR Pro 6.36 (WaveMetrics, Lake Oswego, OR). The collection efficiency was calculated based on the measured aerosol chemical composition according to Middlebrook et al. (2012). The HR–ToF–AMS measurements were validated against off–line PM<sub>1</sub> gravimetric mass and sulfate concentration measurements during the stationary measurement period in Bologna (slope=0.95,  $r=0.69$ ) as suggested by the “Guidelines for comparison of ACSM measurements with co–located external data” (COST Action CA16109 COLOSSAL Chemical On–Line cOmposition and Source and Apportionment of fine aerosoL, Working Group 1, 2019).

#### 4.1.5 Gas monitors

The carbon dioxide concentration (CO<sub>2</sub>) was measured by an LI–7000 CO<sub>2</sub>/H<sub>2</sub>O Gas Analyzer (LI–COR Biosciences, Lincoln, NE, USA). The LI–7000 is a high performance, dual–cell, differential gas analyzer. It uses a dichroic beam splitter and two separate detectors to measure simultaneously infrared absorption by CO<sub>2</sub> and H<sub>2</sub>O in the same gas stream.

The ozone concentration (O<sub>3</sub>) was measured by the Model 205 Dual Beam (2B Technologies, Boulder, CO, USA). The Dual Beam Ozone Monitor measures UV light intensity measurements  $I_o$  (ozone–scrubbed air) and  $I$  (unscrubbed air) simultaneously. Ozone concentration is then calculated from  $I_o$  and  $I$  according to the Beer–Lambert Law.

## 4.2 Data treatment

### 4.2.1 Black carbon mass absorption cross-section

The black carbon mass absorption cross-section is defined by the following equation:

$$\text{MAC}_{\text{BC}}^{\lambda}(\lambda) = \frac{b_{\text{abs}}(\lambda)}{m_{\text{BC}}} \quad (4.4)$$

where  $b_{\text{abs}}(\lambda)$  is the BC absorption coefficient and  $m_{\text{BC}}$  is the black carbon mass concentration. In this work the absorption coefficient was  $b_{\text{abs}}(637 \text{ nm})$ , calculated from the MAAP while  $m_{\text{BC}}$  was either taken from the SP2 or TOA in which cases we use the specific symbols  $\text{MAC}_{\text{rBC}}^{637 \text{ nm}}$  or  $\text{MAC}_{\text{EC}}^{637 \text{ nm}}$ , respectively. The statistical uncertainties associated with the average  $\text{MAC}_{\text{rBC}}^{637 \text{ nm}}$  values in this work were calculated as standard error of the means. However, as we will see in Sect. 4.3.6, the uncertainty associated with the BC mass measurement technique used is much higher than the statistical uncertainty of the average  $\text{MAC}_{\text{BC}}$  value.

### 4.2.2 Positive matrix factorization

To investigate organic aerosol sources we applied positive matrix factorization (PMF) analysis (Paatero and Tapper, 1994) on the organic aerosol mass spectra (Lanz et al., 2007; Ulbrich et al., 2009; Zhang et al., 2011) using the algorithm implemented in the source Finder tool (SoFi 6.36) (Canonaco et al., 2013). PMF analysis was run in robust mode, and  $\text{CO}_2$  related peaks were down-weighted.

PMF analysis was run in unconstrained mode and solutions with 2 up to 5 factors were investigated. The three-factor solution identified a hydrocarbon-like organic aerosol (HOA) component and two oxygenated organic aerosol (OOA) factors: a less oxidized OOA (LO-OOA) and a more oxidized OOA (MO-OOA). The four- and five-factor solutions were disregarded since they split the MO-OOA factor into more than one component, while the two-factor solution was excluded as it identified only a single OOA factor, in contradiction with previous observations in the Po Valley in summer (Wolf et al., 2015). The rotational ambiguity was investigated varying the  $f_{\text{peak}}$  parameter between  $-1$  and  $1$  with an increment of  $0.1$ . For this data set we chose  $f_{\text{peak}}$  equal to  $0$  ( $Q/Q_{\text{exp}} = 2.5$ ). Factor interpretation was supported by correlation analysis of factor spectra with reference mass spectra and correlation of factor time series with time series of external tracers. Time series and mass spectra profiles are reported in panels a, b, c, d, e and f of Fig. S4.1. Figure S4.1g shows the relative mass fraction of the 3 PMF profiles, and Fig. S4.1h the pie chart of their relative contribution to the total OA mass. Table S4.1 reports the Pearson correlation coefficients ( $r$ ) of factor time series with time series of external tracers and factor profiles of other literature works, together with their elemental ratios.

## 4.3 Results and Discussion

### 4.3.1 Meteorological Parameters

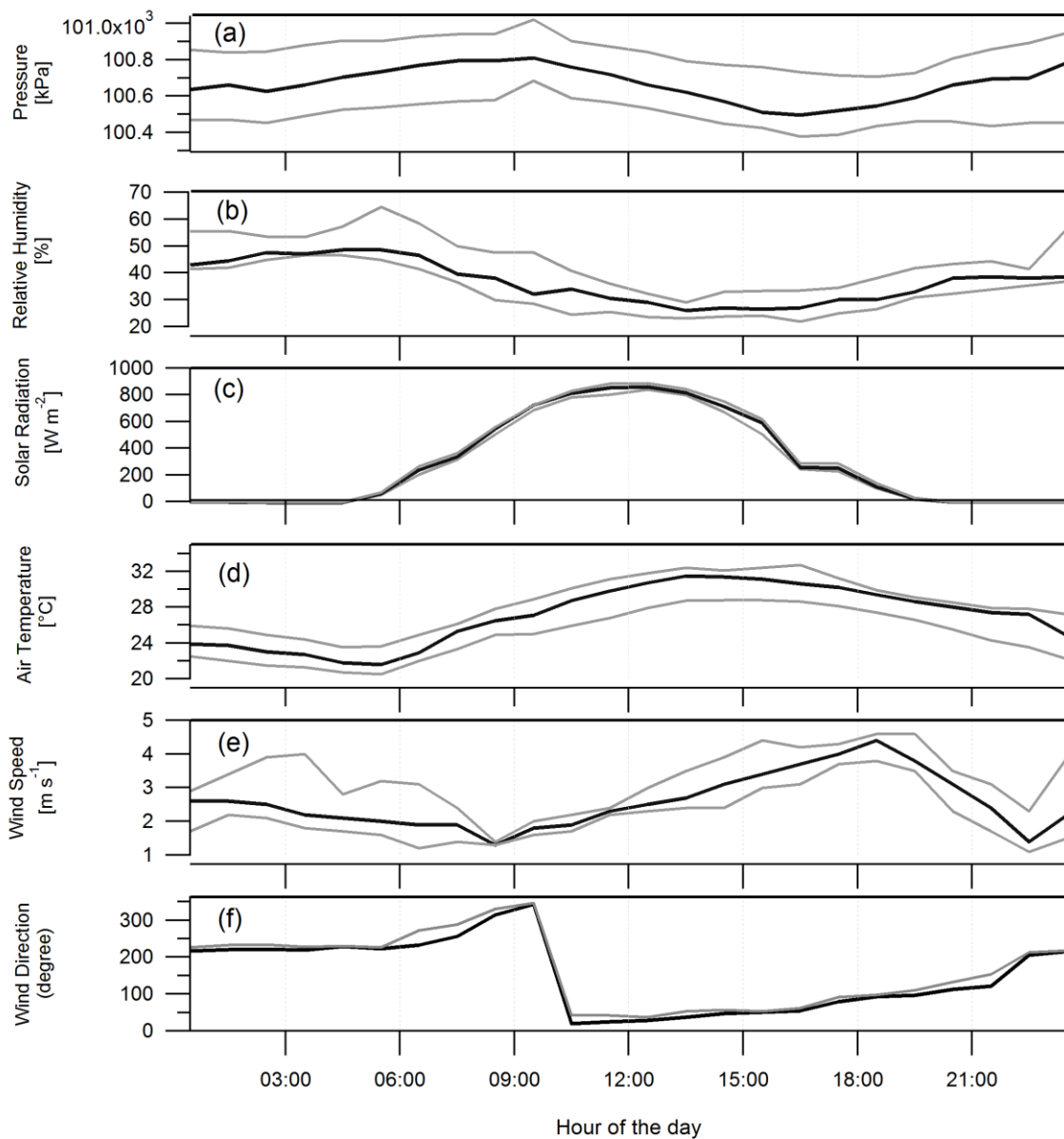


Figure 4.3: Diurnal profiles (1 h time resolution) of pressure, relative humidity, solar radiation, air temperature, wind speed and wind direction at the Bologna site. The black lines represent the medians and the two grey lines the 25<sup>th</sup> and 75<sup>th</sup> percentiles. Note that these diurnal profiles are calculated with 8 days, 5 of which are weekend days.

Summer 2017 was the second warmest summer in Italy since records began in 1800 with a +2.5 °C temperature anomaly relative to the 1971–2000 mean (<http://www.isac.cnr.it/en/content/2018-warmest-year-italy-1800>). July 2017 in the Po Valley featured a high number of high–pressure fields. This meteorological context resulted in recurrent atmospheric stability, clear–sky and high temperatures, enhancing photochemical activity. These meteorological conditions are typical of summers in Northern Italy. Figure 4.3 shows the daily profiles of the principal meteorological quantities: pressure, relative humidity (RH), solar radiation, air temperature, wind speed and wind direction at the suburban CNR–site in Bologna. The black lines represent the medians, while the grey lines represent the 25<sup>th</sup> and 75<sup>th</sup> percentiles. The data were recorded and validated by ARPAE.

### 4.3.2 Aerosol chemical composition

The pie chart in Fig. 4.4 presents the average aerosol chemical composition (non-refractory matter in PM1 plus rBC in total aerosol) measured in Bologna during the stationary measurement periods when the MOSQUITA was parked at CNR. The organic aerosol contribution is divided into the three factors obtained from PMF (Sect. 4.2.2). Overall, the total aerosol mass concentration during the considered period was  $8.8 \mu\text{g m}^{-3}$ . On average, organic aerosol was by far the largest PM component, accounting for 79 % of the total aerosol mass, followed by sulfate (8.9 %), rBC (5.3 %), ammonium (4.2 %), nitrate (2.3 %), and chloride (0.3 %) (Fig. 4.4). Wolf et al. (2015) had sampled the aerosol chemical composition of non-refractory matter in the Po Valley in the summer 2012, also with an HR-ToF-AMS. They also found that the aerosol average chemical composition was dominated by organic aerosol (49.7 %), followed by sulfate (27.1 %), nitrate (12.7 %), ammonium (9.9 %) and chloride (0.5 %). In this work, the PMF factors primary organic aerosol (HOA) and secondary organic aerosol (LO-OOA + MO-OOA) accounted for 5.9 % and 73.1 %, respectively of the total aerosol mass. HOA, LO-OOA, and MO-OOA represented 8 %, 37 %, and 55 % of the OA, respectively (Fig. S4.1h). Compared to Wolf et al. (2015), we found a higher degree of oxygenation for our OOA fractions (see Table S1), and did not retrieve a cooking organic factor.

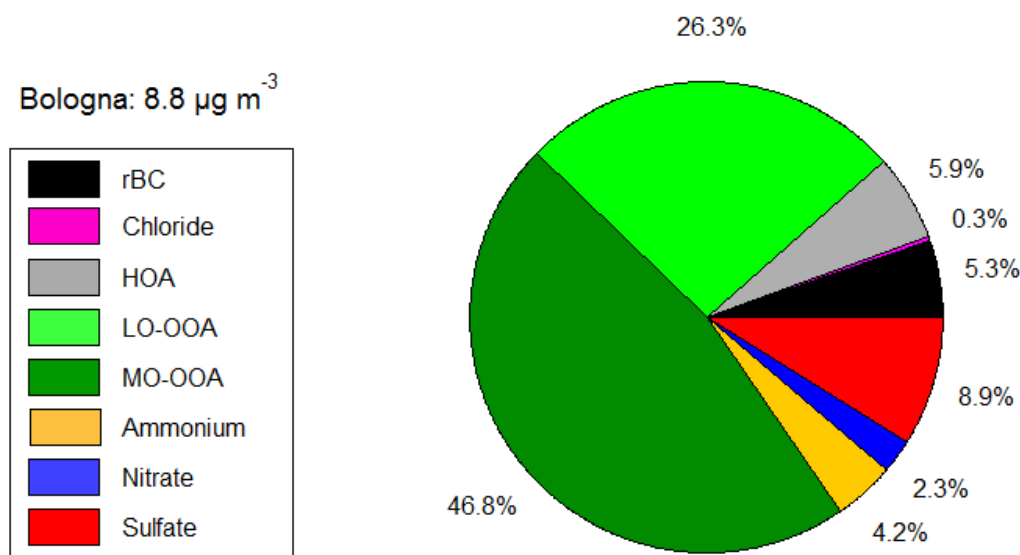


Figure 4.4: Pie chart of the average aerosol chemical composition (non-refractory PM1 plus refractory black carbon of the total aerosol) measured at CNR during the stationary measurements. OA is presented as its three PMF factors: HOA, LO-OOA and MO-OOA.

The HOA factor is unambiguously identified based on high intensity of peaks at mass to charge ratios  $m/z$  43 ( $\text{C}_3\text{H}_7^+$ ),  $m/z$  55 ( $\text{C}_4\text{H}_7^+$ ),  $m/z$  57 ( $\text{C}_4\text{H}_9^+$ ),  $m/z$  69 ( $\text{C}_5\text{H}_9^+$ ), and  $m/z$  71 ( $\text{C}_5\text{H}_{11}^+$ ), typical of aliphatic hydrocarbons (Fig. S4.1b). The HOA mass spectrum correlates with the HOA reference spectra from Crippa et al. (2013) ( $r=0.98$ ), Crippa et al. (2014) ( $r=0.99$ ) and Mohr et al. (2012) ( $r=0.98$ ). HOA is a surrogate of primary OA emitted by traffic, and its time series (Fig. S4.1a) moderately correlates with the BC concentration ( $r = 0.40$ ) (Table S4.1).

The mass spectrum of the OOA factor in Fig. S4.1d is dominated by  $m/z$  29 ( $\text{CO}^+$ ) and  $m/z$  44 ( $\text{CO}_2^+$ ), showing the typical features of more oxidized-oxygenated organic aerosol (MO-OOA). This MO-OOA spectrum correlates with the less volatile OOA mass spectra from Mohr et al. (2012) ( $r=0.98$ ) and Aiken et al. (2009) ( $r=0.96$ ), and resembles the highly oxygenated organic aerosol factor (HOOA) identified by Wolf et al. (2015), both having the highest degree of oxidation. Further, it correlates best with sulfate ( $r=0.74$ ) which is attributed to regional/aged secondary aerosol (Table S4.1).

The OOA spectrum in Fig. S4.1f is characterized by high  $m/z$  43 ( $C_2H_3O^+$ ) and  $m/z$  44 ( $CO_2^+$ ) and is identified as a less oxidized – oxygenated organic aerosol (LO–OOA). This LO–OOA factor identified in this study is also characterized by a relatively high oxygen to carbon ratio though less than the MO–OOA factor (Table S4.1), and it exhibits similarity to the low-volatility oxygenated organic aerosol (LVOOA) identified by Wolf et al. (2015). The LO–OOA mass spectrum correlates with the SVOOA average mass spectrum observed across Europe during EUCAARI (Crippa et al., 2014,  $r = 0.86$ ) and the average SVOOA reported for multiple ambient data sets (Ng et al., 2011,  $r=0.84$ ). Correlation coefficients of LO–OOA with nitrate and sulfate are higher and lower, respectively, compared to those of MO–OOA (Table S4.1), indicating that LO–OOA is likely from local origin.

### 4.3.3 Diurnal variability in BC mass concentrations and properties

The diurnal variability in the physical and optical properties of BC particles was investigated with measurements at the suburban site of Bologna. Only days with a maximum of 2 hours of missing data were included in this analysis (8 days were available at this site, 5 of which were weekend days; see Figs. S4.2–S4.9 for the individual diurnal profiles of different properties). Figure 4.5 displays the median diurnal profiles and inter–quartile range of the rBC mass concentration, the absorption coefficient at 637 nm, the  $MAC_{rBC}^{637\text{ nm}}$  value, the NFTCP, the rBC mass equivalent diameter of BC cores ( $D_{rBC}$ ), and the SSA. In addition, the median diurnal profiles of  $O_3$  (blue line in top panel) and the solar radiation are shown (light grey area in each panel).

Figures 4.5a and b show that rBC mass concentration and absorption coefficient peak during the morning rush hour period between 05:00 and 09:00, reaching their maxima ( $0.8 \mu\text{g m}^{-3}$  and  $12.1 \text{ Mm}^{-1}$ ) around 05:30 when primary emissions from traffic are intense and the planetary boundary layer (PBL) height is relatively low. With increasing PBL height during the day, rBC mass concentrations and absorption coefficient decrease due to dilution of the fresh primary emissions by air mixing from aloft. In the afternoon, at 15:00, the median values of the rBC mass concentration and absorption coefficients are  $0.2 \mu\text{g m}^{-3}$  and  $3.6 \text{ Mm}^{-1}$ , respectively. As pointed out by many studies (Vecchi et al., 2007; Saarikoski et al., 2012; Rinaldi et al., 2015), the PBL dynamics play a key role in the Po Valley during summertime. During the night, a reduced mixing layer height allows for accumulation of pollutants, while during the day a highly convective atmosphere with a mixing layer of up to 2 km results in dilution and mixing. From Figs. S4.2 and S4.3 it appears that all weekdays and weekend days have a distinct morning peak occurring somewhere between 05:00. and 10:00 apart from the Sundays 23/07 and 30/07, which have a very flat diurnal profile. In Fig. 4.5a, the rBC mass concentration is plotted together with the  $O_3$  concentration. Ozone is titrated by NO from traffic emissions, therefore, its diurnal profile shows a minimum at approximately 05:30, in correspondence with the traffic peak; subsequently, with the increase of photochemical reactions involving  $NO_x$  and VOCs, ozone increases, reaching its maximum of 70 ppb around 15:00. The diurnal behavior of the  $MAC_{rBC}^{637\text{ nm}}$ , shown in Fig. 4.5c, appears to be influenced by the wind direction (Fig. 4.3f); indeed the  $MAC_{rBC}$  is oscillating with values between 12.2 and  $14.7 \text{ m}^2 \text{ g}^{-1}$  overnight and during the early morning and starts increasing only after 09:30 when the wind direction changes from NW to N. It reaches the maximum value of  $16.5 \text{ m}^2 \text{ g}^{-1}$  around 10:00, afterwards it slightly decreases during the day. This indicates the possibility that the change in wind direction results in a change from fresh BC from local emissions to aged BC transported from northern parts of the Po Valley. Fig. S4.4 shows that the morning to afternoon difference in  $MAC_{rBC}$  is quite pronounced on most days, with 16/07 (a Sunday) being a noticeable counter–example, which dampens the effect in the averaged diurnal pattern. In Fig. 4.5d the number fraction of thickly coated particles (NFTCP) is shown. It presents a minimum during the traffic morning peak between 05:30 and 06:30 due to the fresh BC particles emitted during that time, and thereafter starts increasing slightly from 5 % to 10 % during the day. Also in this case the increase of NFTCP appears to be related to the change in the air mass at approximately 09:30 in the morning. Figure 4.5e shows the  $D_{rBC}$  diurnal profile with values ranging from 112 to 130 nm, where the change in wind direction seems to result in slightly larger BC cores on average. In Fig. 4.5f the SSA diurnal profile is shown, with values between 0.6 and 0.8 and a minimum around 06:00 simultaneously with the peak in the absorption coefficient. The diurnal profile of the SSA was calculated with 11 days, 6 of which were in common with the other diurnal profiles, in order to increase the statistics.

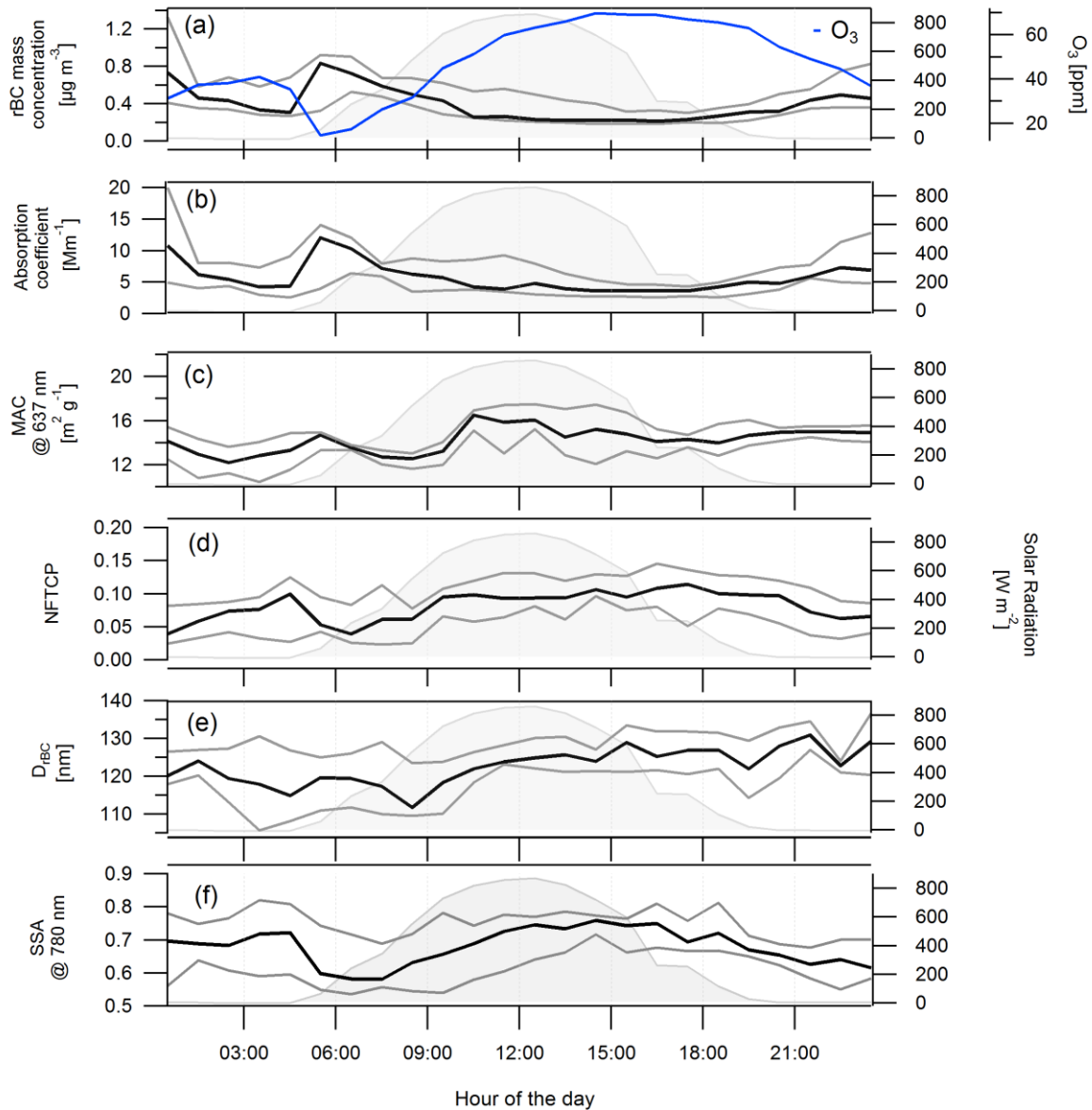


Figure 4.5: Diurnal profiles (1h time resolution) of rBC mass concentration, absorption coefficient,  $MAC_{rBC}^{637\text{ nm}}$ , NFTCP,  $D_{rBC}$  and  $SSA(780\text{ nm})$  for Bologna during the stationary measurement periods. The  $O_3$  diurnal profile is reported on top of the rBC mass concentration. The black lines represent the medians of and the two grey lines the 25<sup>th</sup> and 75<sup>th</sup> percentiles. In addition, the solar radiation daily profile is shown as grey area. Note that these diurnal profiles are calculated with 8 days, 5 of which are weekend days, (corresponding to the single daily profiles in Figs. S4.2, S4.3, S4.4, S4.5, S4.6, S4.7 and S4.9). The SSA diurnal profile is based on a different subset of data, with 6 out of 11 days in common with the other diurnal profiles, see Fig. S4.7.

#### 4.3.4 Spatial variability of BC optical and physical properties

The spatial variation of BC optical and physical properties over the Po Valley was investigated with mobile measurements. The results from the four drives between Bologna and Lodi (just south of Milan), as illustrated in Table 4.1 and Fig. 4.1, using the MOSQUITA mobile laboratory are presented in this section. The distance between Bologna and Lodi was covered in two ways, either by driving on the highway (Autostrada A1) or on a series of smaller, provincial roads which run roughly parallel to the highway at a distance of about 10 km (Fig. 4.6). The traffic density on the provincial roads was substantially lower than on the highway. The wind direction on these days was approximately parallel to the route from Milano towards Bologna, such that aging of BC emitted in the Milano area could potentially be probed. Only measurements taken during the morning hours

(between 06:00–09:30) were included in the results presented hereafter in order to minimize potential effects from distinct diurnal patterns in aerosol properties.

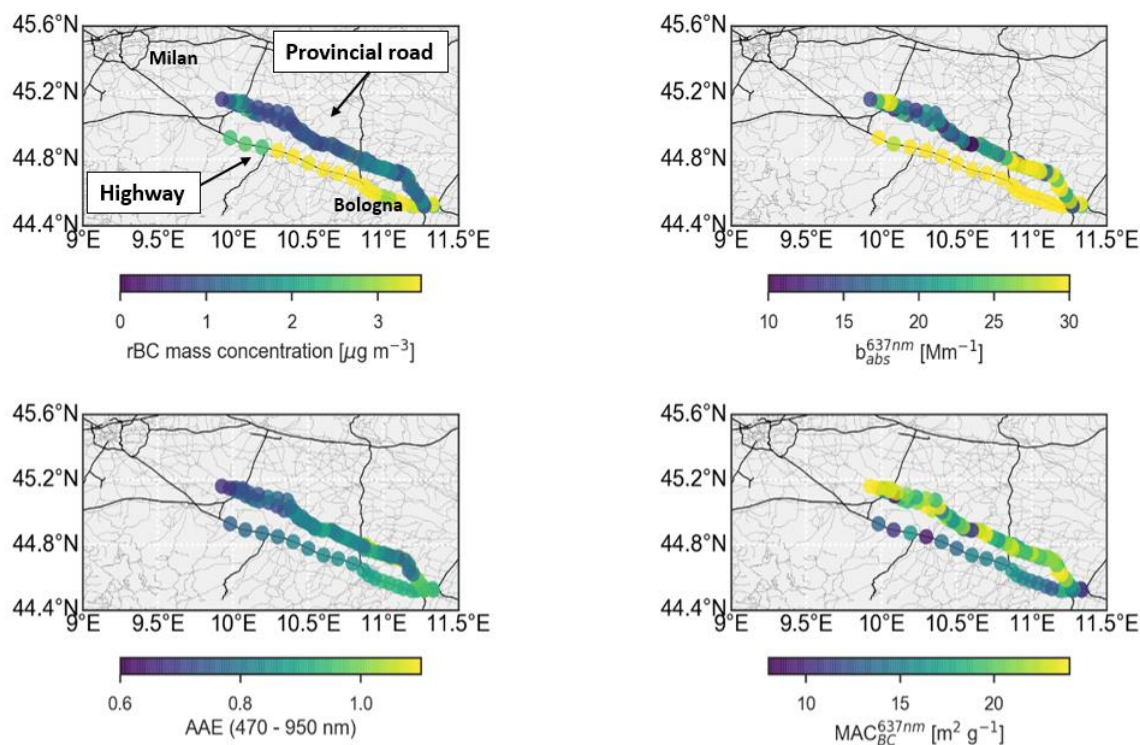


Figure 4.6: Spatial variability (5 min time resolution) of rBC mass concentration, absorption coefficient, AAE and  $MAC_{rBC}^{637\text{ nm}}$  for highway (Southern points) and provincial roads (Northern points) during the Bologna–Lodi trips. Data are averaged from 4 days: two per the highway and two per provincial road drives (Table 4.1). Thick black lines indicate highway roads, thin grey lines smaller roads.

Spatially resolved average values of rBC mass concentrations, absorption coefficients,  $MAC_{rBC}^{637\text{ nm}}$  and AAE measured during the four drives along this route are presented in Fig. 4.6 and Table 4.3. The AAE median values in both cases were close to 1 (between 0.8 and 0.9; Table 4.3), which agrees with the expectation that the main source of BC in both cases was traffic emissions. Median rBC mass concentrations and absorption coefficients were  $3.6\ \mu\text{g m}^{-3}$  and  $53.2\ \text{Mm}^{-1}$  on the highway and  $1.1\ \mu\text{g m}^{-3}$  and  $21.9\ \text{Mm}^{-1}$  on the provincial roads, respectively (Table 4.3), indicating a substantial increment from the highway emissions (BC removal can be excluded as a driver for this difference). Figure 4.7 shows the rBC mass size distributions normalized by their total area for the highway and provincial roads. The rBC mass size distributions of highway and provincial roads peaked at almost equal modal diameters of  $D_{rBC} \approx 108\text{ nm}$  and  $115\text{ nm}$ , respectively. The fraction of BC mass found at larger core sizes ( $D_{rBC} \geq 156\text{ nm}$ ) was slightly larger on the provincial roads compared to the highway, resulting in a slightly higher median ( $115\text{ nm}$  vs.  $108\text{ nm}$ ). The high similarity of the two size distributions is a good basis for assessing BC mixing state effects on  $MAC_{BC}$ . Furthermore, potential artefacts from very large BC cores with sizes above the SP2 upper detection limit of quantification are expected to be small in the Po Valley. Indeed, Matta et al. (2003) demonstrated, in a previous study conducted in Bologna, that the fraction of EC mass found in the coarse mode is negligible. The NFTCP was very low on the highway (3 %) and more than a factor of three higher on the provincial road (10 %; Table 4.3), confirming a higher fraction of internally mixed BC particles. This suggests that the BC observed along the provincial roads was more aged than the BC measured on the highway. Indeed, the  $MAC_{BC}$  values were substantially lower on the highway than along the provincial roads, i.e.,  $14.9\ \text{m}^2\ \text{g}^{-1}$  compared to  $19.8\ \text{m}^2\ \text{g}^{-1}$  (Table 4.3 and Fig. 4.6).

Table 4.3: 25<sup>th</sup>, 50<sup>th</sup> and 75<sup>th</sup> percentiles of rBC mass concentration, absorption coefficient,  $MAC_{rBC}^{637\text{ nm}}$  and AAE, number fraction of thickly coated particles and median equivalent diameter of BC cores for highway and provincial roads.

	$m_{rBC}$ [ $\mu\text{g m}^{-3}$ ] 50 <sup>th</sup> (25 <sup>th</sup> , 75 <sup>th</sup> )	$b_{\text{abs}}$ (637 nm) [ $\text{Mm}^{-1}$ ] 50 <sup>th</sup> (25 <sup>th</sup> , 75 <sup>th</sup> )	$MAC_{rBC}^{637\text{ nm}}$ [ $\text{m}^2\text{ g}^{-1}$ ] 50 <sup>th</sup> (25 <sup>th</sup> , 75 <sup>th</sup> )	AAE 50 <sup>th</sup> (25 <sup>th</sup> , 75 <sup>th</sup> )	NFTCP [%]	$D_{rBC}$ [nm]
Highway	3.6 (3.0, 4.0)	53.2 (43.3, 61.9)	14.9 (13.2, 15.4)	0.9 (0.8, 0.9)	3	108
Provincial roads	1.1 (0.9, 1.6)	21.9 (17.2, 29.8)	19.8 (17.2, 22.3)	0.8 (0.8, 0.9)	10	115

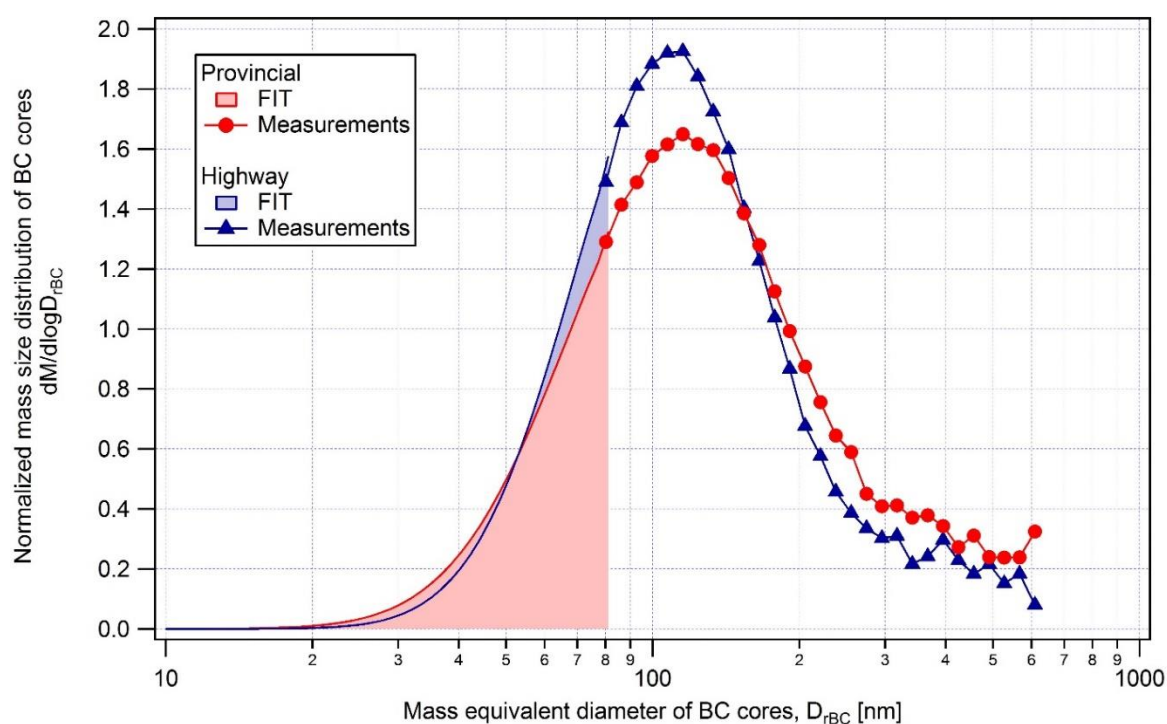


Figure 4.7: Normalized rBC mass size distributions of BC cores averaged for highway and provincial roads (drives from Bologna to Pavia indicated in Table 4.1). The red and blue markers denote the SP2 measurements while the red and blue lines are lognormal fits of the size distributions. The total rBC mass concentrations are obtained with the extrapolation method explained in Pileci et al. (2021). The two size distributions are normalized by their total area.

The particle time of flight (PToF) mode of the AMS provides a tool to explore the size distributions of individual fragments of the mass spectrum (Lee et al., 2015). Figure 4.8 shows the mass size distributions of Org57 (organic mass at  $m/z = 57$  corresponding mainly to the mass fragment  $\text{C}_4\text{H}_9^+$ ) representing the fresh organic aerosol from traffic, and Org44 (organic mass at  $m/z = 44$ , corresponding to  $\text{CO}_2^+$ ) as a proxy of the aged organic aerosol. Since measurements in the PToF mode were limited, only singular cases are shown, one for the highway and two for the provincial roads. On the highway, a mode of Org57 aerosol is seen at small sizes ( $D < 100$  nm) that is not present for Org44 aerosol, suggesting externally mixed fresh emissions in the smaller diameter range (Fig. 4.8a). On the provincial roads, the size distribution of fresh organics, represented by fragment Org57, is still characterized by a peak below 100 nm, but is associated with a shoulder at larger diameters which intensifies from provincial road 1 to provincial road 2. These results suggest that it is more likely to observe internally mixed fresh



and aged particles on the provincial roads (Fig. 4.8b and Fig. 4.8c). Still the scarcity of cases and the noisy signal make it difficult to draw firm conclusions.

Observed differences in particle mixing state between the highway and the provincial roads can result from two possible processes, namely BC aging by condensation and coagulation or different mixing ratios of freshly emitted BC with aged background BC. The former would not alter BC mass concentration, whereas the latter comes with a reduction of BC mass concentration along the trajectory. The lack of systematic spatial trends of BC mass concentration and MAC value along the provincial road where local traffic influence is minor (except for the vicinity of Bologna), clearly suggests that the potential plume from Milan did not make a substantial contribution to BC relative to the background concentration, despite wind blowing from Milan in parallel to the drives. The fact that mass concentrations observed on the provincial road were comparable to those observed at the background sites (San Pietro Capofiume and Monte Cimone) (Fig. 4.9) combined with wind direction being parallel to the highway and provincial routes makes it unlikely that BC aging during transport between the two routes adds to the observed differences in BC mixing state and  $MAC_{BC}$ . Furthermore, the 10 km distance between the two routes is too short to make BC aging plausible as models usually estimate a time scale of about few hours (2 to 8 h) to convert hydrophobic BC to hydrophilic BC (Riemer et al., 2004; Koch et al., 2009; Fierce et al., 2015). All these factors support the hypothesis that dilution of fresh BC emissions with aged background BC is the dominant process responsible for the differences in BC properties between the highway and provincial roads and variations along these, whereas BC aging occurs on time scales slower than that of dilution with background air under the probed conditions. This makes it impossible to infer approximate BC aging time scales by comparison of these measurements.

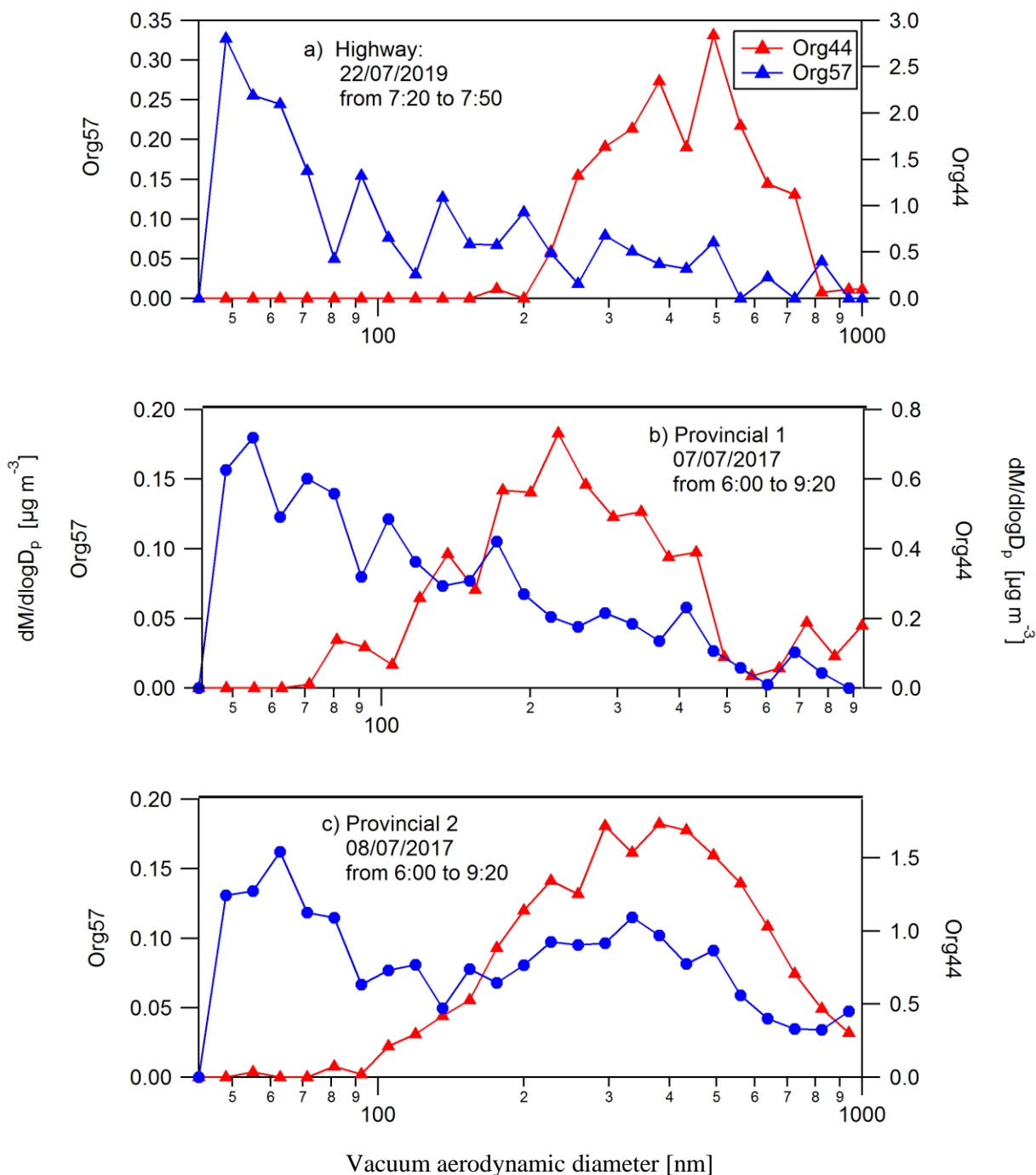


Figure 4.8: Mass size distributions of Org44 (organic mass at  $m/z = 44$ , corresponding to  $\text{CO}_2^+$  and representing the aged organic aerosol) and Org57 (organic mass at  $m/z = 57$ , corresponding mainly to the mass fragment  $\text{C}_4\text{H}_9^+$  and representing the fresh organic aerosol from traffic) from the AMS in PToF mode for the highway trip and the two provincial road trips. The trips correspond to the ones shown in Figs. 4.6 and 4.7 and Table 4.3, apart from one of the highway trips during which the AMS was not working.

#### 4.3.5 Mechanisms driving $\text{MAC}_{\text{BC}}$ variability

As described in the introduction, the  $\text{MAC}_{\text{BC}}$  variability depends on the BC properties i.e., particle size, mixing state, shape and refractive index. In this work only the dependence on particle size and mixing state was explored. Figure 4.9 shows the relation between the  $\text{MAC}_{\text{rBC}}^{637 \text{ nm}}$  and mixing state, using the fraction of thickly coated

particles as a proxy of the mixing state (see Sect. 4.1.3.2 for the definition). The NFTCP was calculated for particles with  $D_{rBC}$  between 102 nm and 295 nm. It is seen that at sites exposed to traffic, such as heavily trafficked roads in Bologna and on the highway (red squares), when the number fraction of thickly coated particles is low, with values between 1 and 5 %, the  $MAC_{rBC}^{637\text{ nm}}$  value is in the range 12.0–15.7  $\text{m}^2\text{ g}^{-1}$ . At the background sites (San Pietro Capofiume and Monte Cimone) (green triangle points), the number fraction of thickly coated particles is much higher, with values between 15 % and 30 %, and the  $MAC_{rBC}^{637\text{ nm}}$  value is higher as well, between 18.9 and 21.7  $\text{m}^2\text{ g}^{-1}$ . The grey circles in the graph represent values at the suburban site Bologna (1 h time resolution), which receives a variable mixture of fresh emissions and aged background air (see Sect. 4.3.3 on diurnal profiles). The observed NFTCP span the entire range of values between 1 % and 25 %, with corresponding  $MAC_{rBC}^{637\text{ nm}}$  values from 6.7 to 23.6  $\text{m}^2\text{ g}^{-1}$ , with a linear increase of  $MAC_{rBC}^{637\text{ nm}}$  with increasing NFTCP.

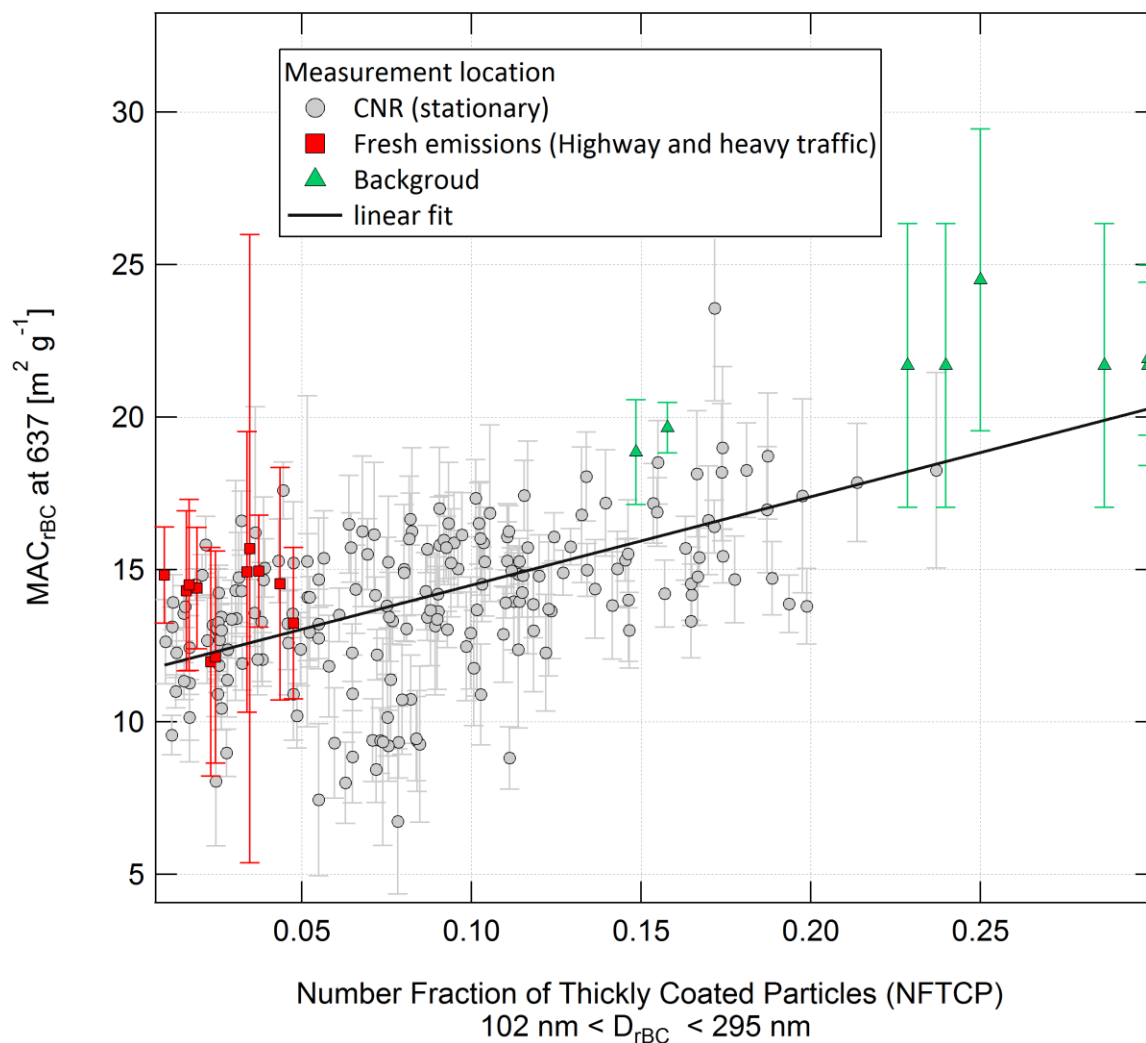


Figure 4.9: Relation between the number fraction of thickly coated particles (NFTCP) calculated for BC core size between 102 nm and 295 nm and the  $MAC_{rBC}^{637\text{ nm}}$ . Grey circles represent stationary measurements at CNR (1 h time resolution); red squares indicate mobile measurements of fresh BC emissions (highway and heavily trafficked roads in Bologna) with varying time resolution; green triangles show stationary measurements performed at background sites (San Pietro Capofiume and Monte Cimone) with varying time resolution. The black line represents a linear fit to the data.

In Fig. 4.10, the relationship between the  $MAC_{BC}$  and BC core size is explored using the modal diameter of the lognormal fit to the BC core ( $D_{rBC}$ ) mass size distribution measured by the SP2 for each time interval. The dashed line shows the theoretical  $MAC_{BC}$  for a polydisperse distribution of fractal-like aggregates consisting of several BC primary spheres described by Mackowski (1994). His analysis employed the superposition formulation for radiative interactions among spheres, in which the total field from the cluster is expressed as a superposition of vector spherical harmonic expansions about each of the spheres in the cluster. According to this theory, the  $MAC_{BC}$  is rather constant for the BC core sizes range of our observations ( $86 < D_{rBC} < 170$  nm) (dashed line in Fig. 4.10) and can not explain the much higher variability in the observed  $MAC_{BC}$  values, which was better explained by a change in BC mixing state. The fact that the variation in  $MAC_{BC}$  associated with variation in the mixing state dominates over the calculated uncertainties provides experimental confirmation that the lensing effect in atmospheric BC measurements can substantially increase the MAC of black carbon by up to a factor of almost 2, as shown by the linear fit represented by the black line in Fig. 4.9.

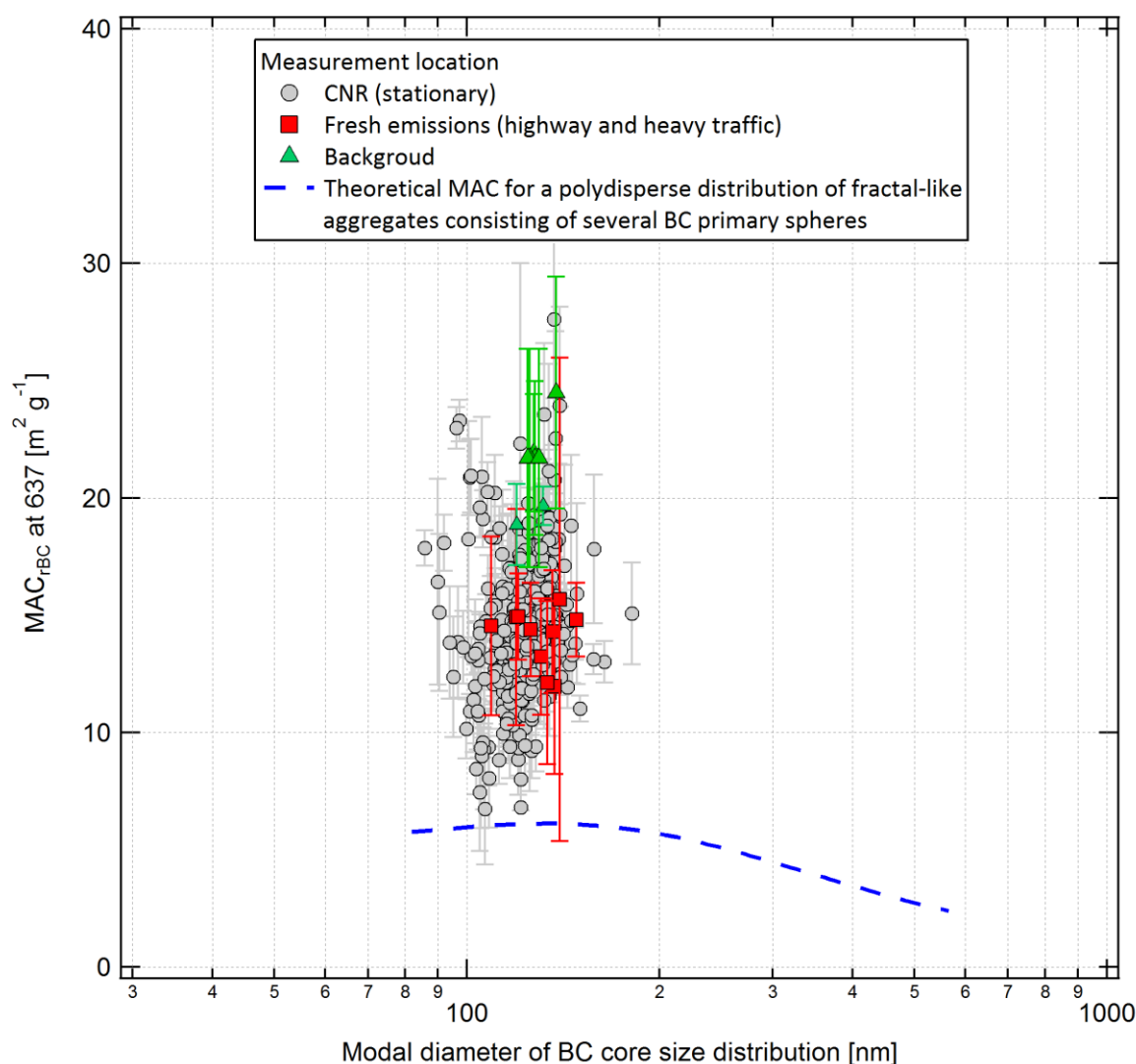


Figure 4.10: Relation between  $MAC_{rBC}^{637\text{nm}}$  and the modal diameter of the BC core mass size distribution (lognormal fit to the SP2 measurement in terms of  $D_{rBC}$ ). The dashed line represents the theoretical  $MAC_{BC}$  for a polydisperse distribution of black carbon spheres. Grey circles represent stationary measurements at CNR with 1 h time resolution); red squares indicate mobile measurements of fresh BC emissions with varying time resolution; green triangles show stationary measurements performed at background sites with varying time resolution.

### 4.3.6 Dependence of $MAC_{BC}$ on using EC and rBC mass measurements

The calculated  $MAC_{BC}$  is also affected by the technique used to measure the BC mass concentration and absorption coefficient (based on Eq. 4.16). In this work, we compared the  $MAC_{BC}$  results obtained by using two different instruments for BC mass calculation: the SP2 and the thermal–optical technique. The  $MAC_{BC}$  comparison was performed for 8 out of the 25 days when the MOSQUITA remained stationary at the Bologna site for the full day, which made comparison with the EC mass concentration from the daily filter samples at the ARPAE site possible.

Figures 4.11a and 4.11b show the individual daily values of  $MAC_{rBC}^{637\text{ nm}}$  and  $MAC_{EC}^{637\text{ nm}}$  calculated with using the MAAP data for the absorption coefficient and the thermal optical EC or SP2 derived rBC data for BC mass, respectively (as explained in Sect. 4.2.1). The  $MAC_{rBC}^{637\text{ nm}}$  values varied from 12.2 to 16.0  $\text{m}^2\text{ g}^{-1}$ , and the  $MAC_{EC}^{637\text{ nm}}$  varied from 8.1 to 11.5  $\text{m}^2\text{ g}^{-1}$ . On average, the  $MAC_{rBC}^{637\text{ nm}}$  value amounts to 14.1  $\text{m}^2\text{ g}^{-1}$ , which is 35% higher than the  $MAC_{EC}^{637\text{ nm}}$  value of 10.2  $\text{m}^2\text{ g}^{-1}$  because  $m_{rBC}$  is on average 35 % smaller than the corresponding  $m_{EC}$  that.

Pileci et al. (2021) compared collocated rBC and EC mass measurements at different European sites, including the Bologna dataset of this study. While they found good agreement when averaging over all studies, they found systematic discrepancies between rBC and EC, by up to ~50 %, when separately averaging data sets from individual sites. In that paper, the authors could not clearly assign the reasons for the discrepancies to one or the other method, both known to have their own specific limitations and uncertainties. However, they found in the different particle size range covered by these two methods one likely reason for the discrepancies, but in this study, we do expect the presence of a BC coarse mode to be negligible.

While the values of  $MAC_{rBC}^{637\text{ nm}}$  reported here are the first ones for the Po Valley, shows the variability of the  $MAC_{EC}^{637\text{ nm}}$  of this work, lies within the previous range of  $MAC_{EC}^{\lambda}$  values encountered in the Po Valley (Bernardoni et al., 2017; Bigi et al., 2017; Forello et al., 2019; Renzi et al., 2019), as shown in Fig. 4.11c. The average  $MAC_{EC}^{637\text{ nm}}$  of the Po Valley studies (red circle in Fig. 4.11c), is  $10.6 \pm 1.9\text{ m}^2\text{ g}^{-1}$  (in close agreement to the value of  $10.2\text{ m}^2\text{ g}^{-1}$  reported above). This value is also comparable to the average  $MAC_{EC}^{637\text{ nm}}$  of the European sites collected in Zanatta et al. (2016), with  $10.0 \pm 1.3\text{ m}^2\text{ g}^{-1}$  (red triangle in Fig. 4.11d).

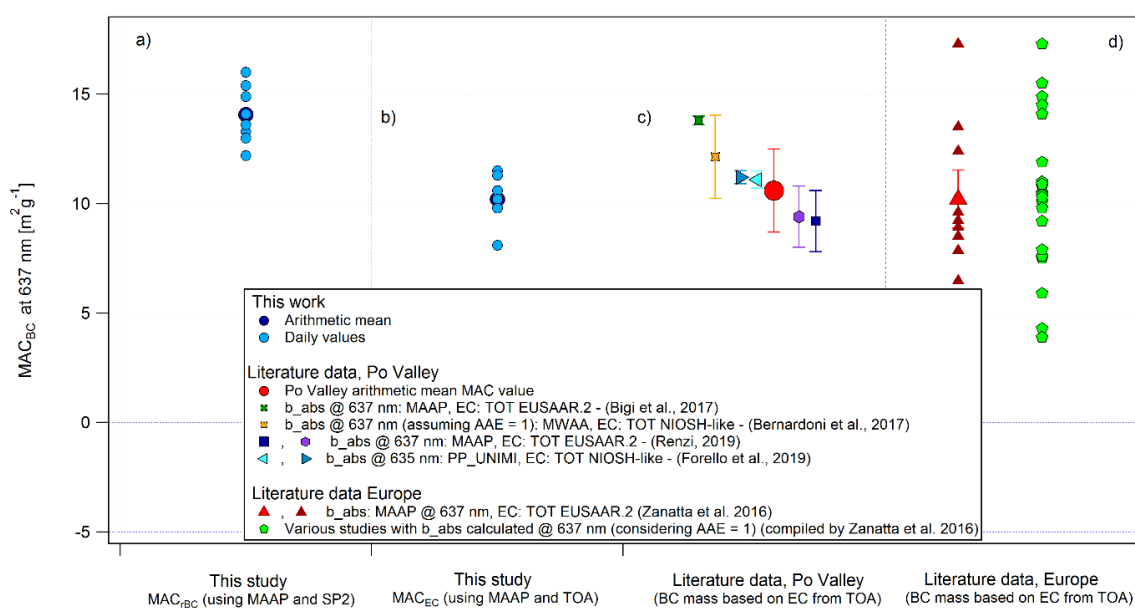


Figure 4.11: In panels a) and b) the daily values of  $MAC_{rBC}^{637\text{ nm}}$  and  $MAC_{EC}^{637\text{ nm}}$  and the arithmetic mean are presented as blue circles. Panels c) and d) present literature data from Po Valley and European studies, respectively. Applied measurement techniques are listed in the legend.

#### 4.4 Conclusions

In this work, we investigated the spatio-temporal variability of physical and optical properties of freshly emitted and aged black carbon particles in the Po Valley during summertime, sampled by a combination of stationary and mobile measurements. The stationary measurements were taken at a sub-urban site in Bologna, at the background site of San Pietro Capofiume and on the remote, high altitude site of Monte Cimone. Mobile measurements were performed driving along the Valley from Bologna to Lodi with a mobile van.

The measured parameters included the following variables: rBC size distribution, rBC mass concentration, BC absorption coefficient, AAE, number fraction of thickly coated particles, geometric mass equivalent diameter, and SSA. Moreover, we calculated the  $MAC_{BC}$  and investigated its dependence on the mixing state, the BC core size diameter and the applied technique to determine the mass concentration of BC or EC. The diurnal variability in the physical and optical properties of BC particles was investigated with stationary measurements at the sub-urban site of Bologna. All the properties studied showed a strong influence of the PBL dynamics and the meteorology. For example, the  $MAC_{BC}$  value and AAE changed only when the wind direction drastically changed. The spatial variability of BC optical and physical properties over the Po Valley was investigated with mobile measurements. The focus was set on the difference in properties between freshly emitted BC particles, sampled on the highway, and aged BC particles, sampled on provincial roads. The  $MAC_{BC}$  values were substantially lower on the highway than along the provincial roads. Moreover, the AAE was rather constant and the rBC mass size distributions were very similar on the two types of roads, while organic aerosol proxy size distributions suggest that the BC particle mixing state was different on the highway and the provincial roads. Both diurnal and spatial observations gave evidence that the Po Valley, in summer, contains a 'pool' of aged BC particles into which fresh BC emissions are mixed on short temporal and spatial scales.

The  $MAC_{BC}$  variability was explored in relation to particle size and mixing state. As proxy for the mixing state, the number fraction of thickly coated particles was used. The small variation of BC core diameters found during the campaign was not able to explain the much greater variability in the observed  $MAC_{BC}$  values, which was better explained with the variability of the BC mixing state. This result provides experimental confirmation that the lensing effect can substantially increase the MAC of black carbon by up to a factor of almost 2. However, while this study provides clear evidence of BC mixing state effects on  $MAC_{BC}$ , the observed  $MAC_{BC}$  values remain tainted with considerable uncertainty due to the lack of absolutely accurate mass measurement techniques. Indeed, in this study, the  $MAC_{BC}$  values based on rBC mass concentrations were 35 % higher than those based on EC mass concentrations.

## **Acknowledgment**

We thank Claudia Zigola (ARPAE) who performed the TOA analysis of the filters during of the campaign. The logistic support of CNR–ISAC technical staff, Francescopiero Calzolari, during the campaign is appreciated. Many thanks to the technical support of Günther Wehrle during and before the campaign.

## **Financial support**

PSI received financial support from the ERC (grant ERC–CoG–615922–BLACARAT) and from the ACTRIS–2 project (EU H2020–INFRAIA–2014–2015, grant agreement no. 654109; and Swiss State Secretariat for Education, Research and Innovation, contract number 15.0159–1; the opinions expressed and arguments employed herein do not necessarily reflect the official views of the Swiss Government).

## **Author contributions**

MGB acquired the funding. MGB and RLM conceived the field experiment. REP, MB and RLM took the rBC measurements and/or analyzed the raw data during the Bologna campaign. SG and MR were responsible for the HR–ToF–AMS measurements during the campaign. SG analyzed the HR–ToF–AMS data and performed the PMF. DO helped with logistics and instrument calibrations during the campaign. AM coordinated the Bologna campaign. REP performed the data analysis, interpreted the results and wrote the manuscript together with RLM and MGB. All co–authors reviewed and commented the manuscript.

## **Competing interests**

The authors declare that they have no conflict of interest.

## Supplement of: Variability of physical and optical properties of freshly emitted and aged black carbon particles determined from stationary and mobile measurements in the Po Valley (Italy), during summertime

Table S4.1: Elemental composition of PMF factors, based on (Aiken et al., 2009); Pearson correlation coefficients ( $r$ ) of factor time series with time series of external tracers and factor profiles of other literature works.

	HOA	MO-OOA	LO-OOA
O/C	0.07	0.85	0.48
H/C	1.91	1.25	1.41
OM/OC	1.27	2.25	1.77
Time series correlation coefficients			
$r$ with NO <sub>3</sub>	0.18	0.16	0.27
$r$ with SO <sub>4</sub>	0.13	0.74	0.33
$r$ with eBC	0.40	0.06	0.14
$r$ with CO <sub>2</sub>	0.35	-0.23	0.00
$r$ with O <sub>3</sub>	-0.35	0.44	-0.03
Profile correlation coefficients			
Mexico City (Aiken et al., 2009)	0.98	0.96	0.95
Barcelona (Mohr et al., 2012)	0.97	0.98	0.90
EUCAARI (Crippa et al., 2014)	0.99	0.84	0.86
Paris (Crippa et al., 2013)	0.98	0.98	
Multiple campaigns (Ng et al., 2011)	0.99	0.84	0.83



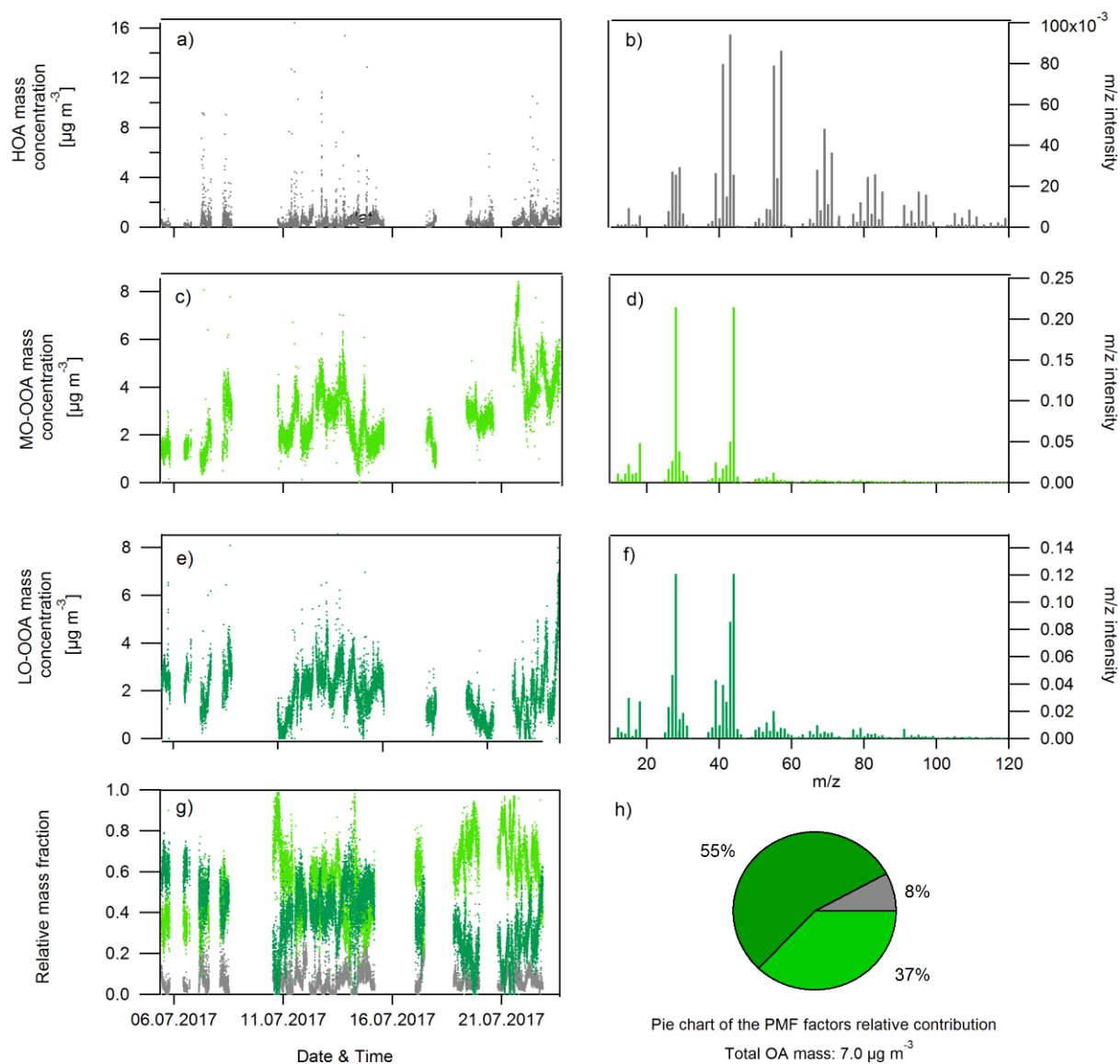


Figure S4.1: Panels a and b, c and d, e and f show the time series and normalized mass spectra profiles of HOA, MO-OOA and LO-OOA, respectively. Panel g presents the relative mass fractions of the 3 PMF factors and panel h their relative contributions to the total OA mass.

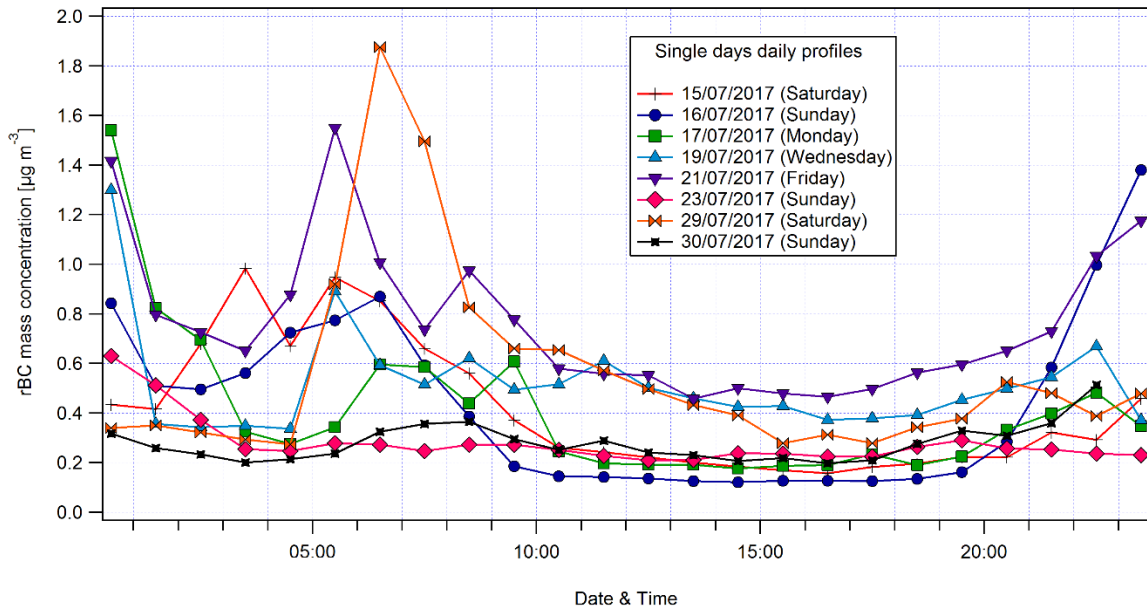


Figure S4.2: Diurnal profiles of the rBC mass concentration from the stationary measurements at CNR.

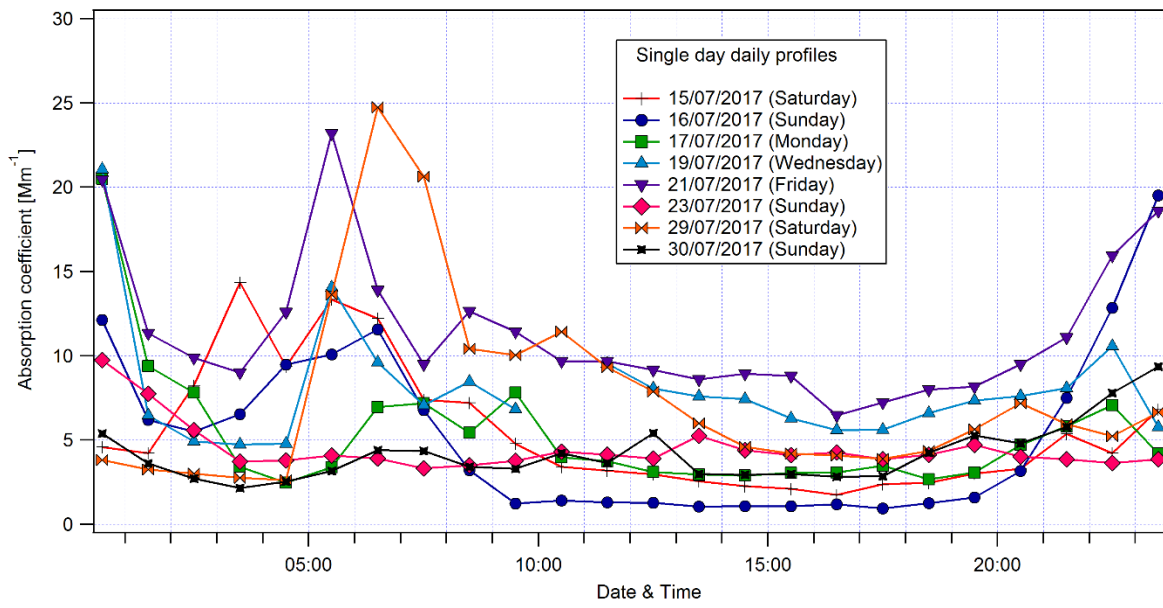


Figure S4.3: Diurnal profiles of the absorption coefficient at 637 nm from the stationary measurements at CNR.

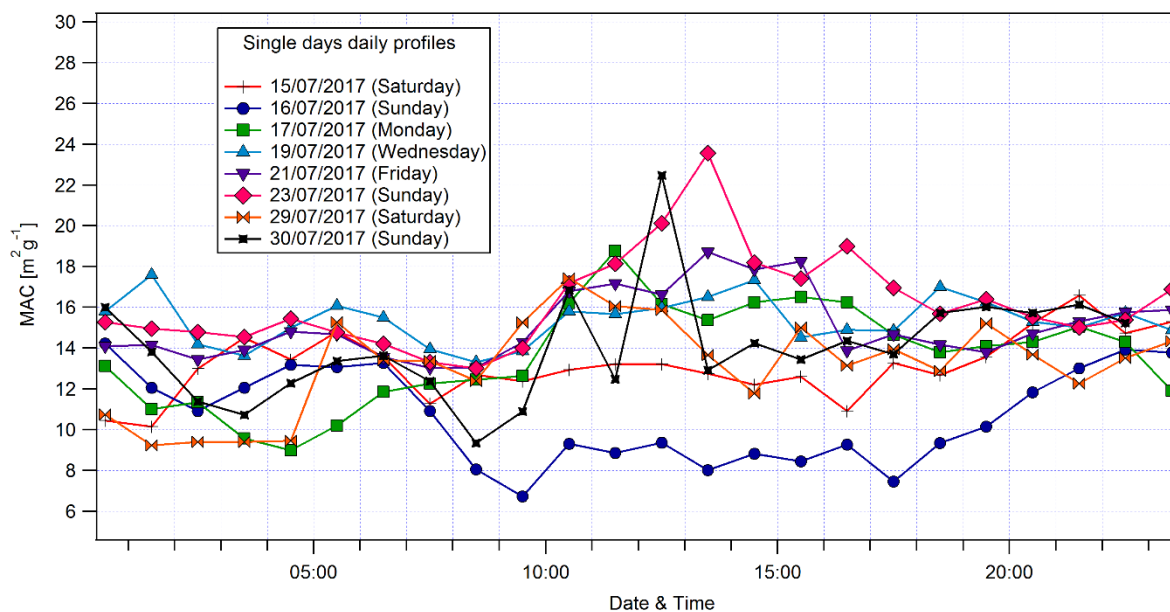


Figure S4.4: Diurnal profiles of the black carbon mass absorption cross section at 637 nm from the stationary measurements at CNR.

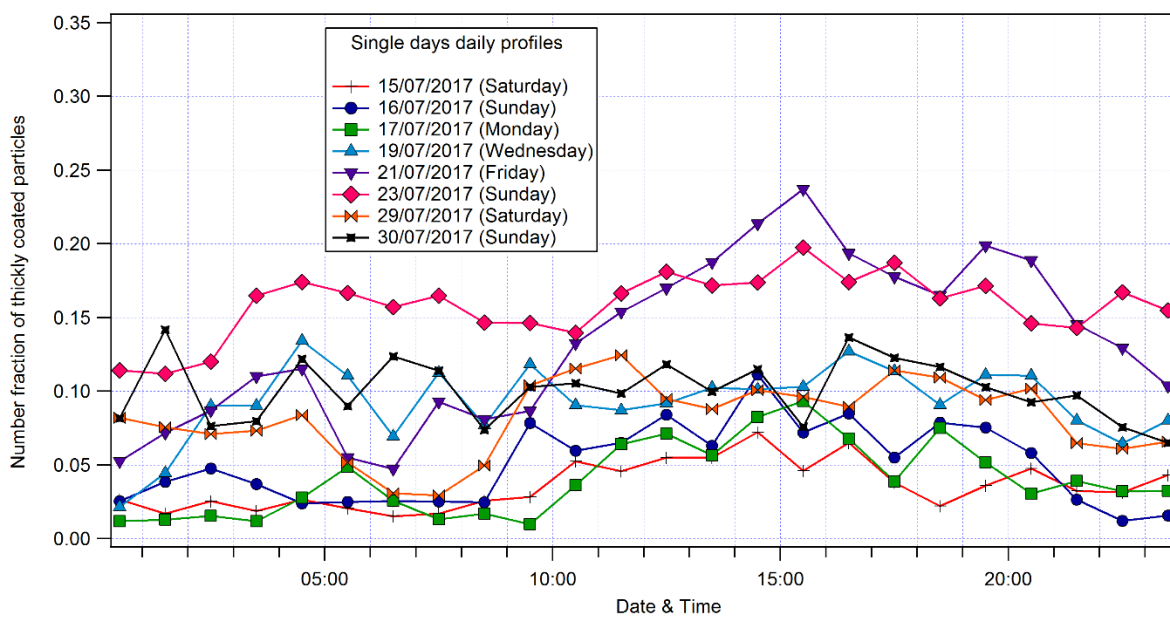


Figure S4.5: Diurnal profiles of the number fraction of thickly coated particles from the stationary measurements at CNR.

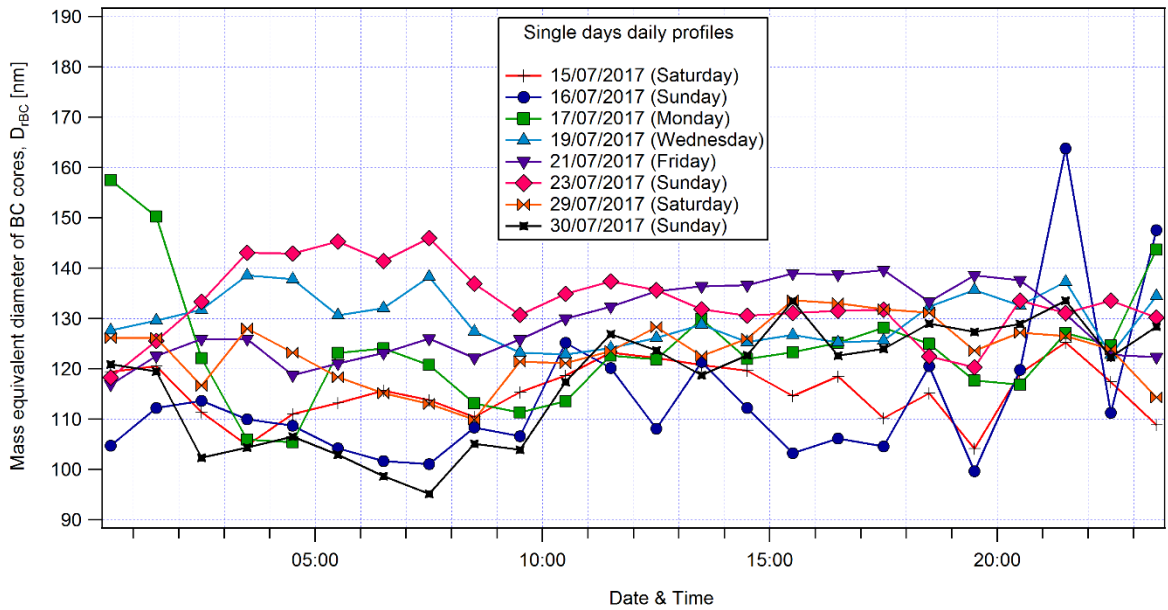


Figure S4.6: Diurnal profiles of the mass equivalent diameter of BC cores ( $D_{rBC}$ ) from the stationary measurements at CNR.

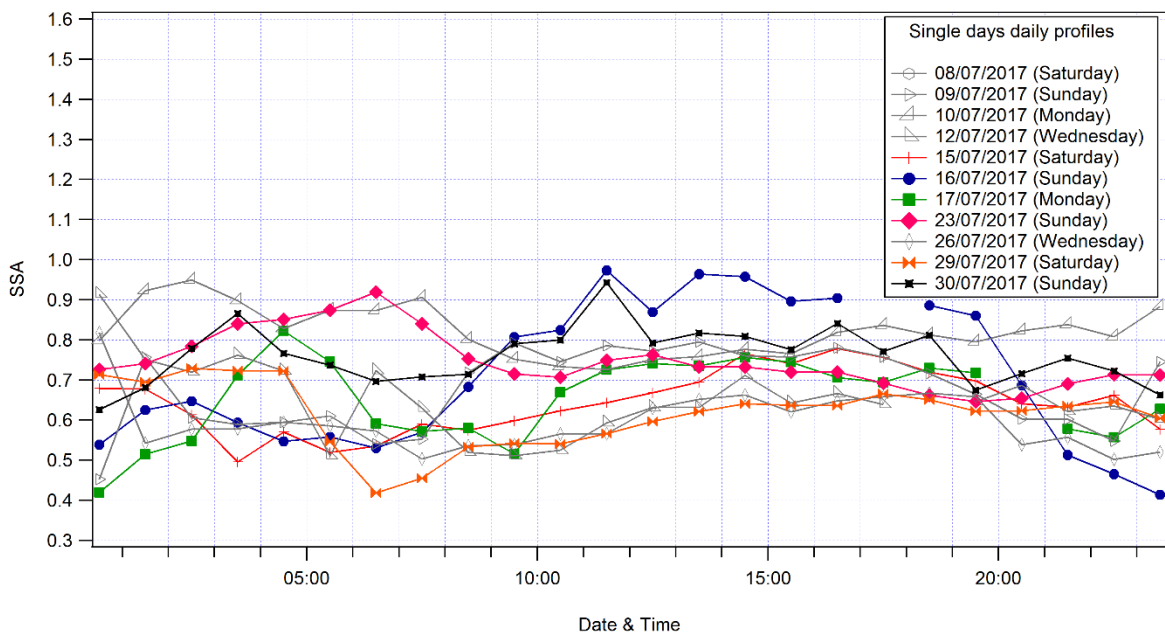


Figure S4.7: Diurnal profiles of the SSA at 780 nm from the stationary measurements at CNR. The grey open symbols are additional days, not in common with the other profiles. The SSA diurnal profile shown in Fig. 4.5 was calculated considering all the days displayed in this figure.

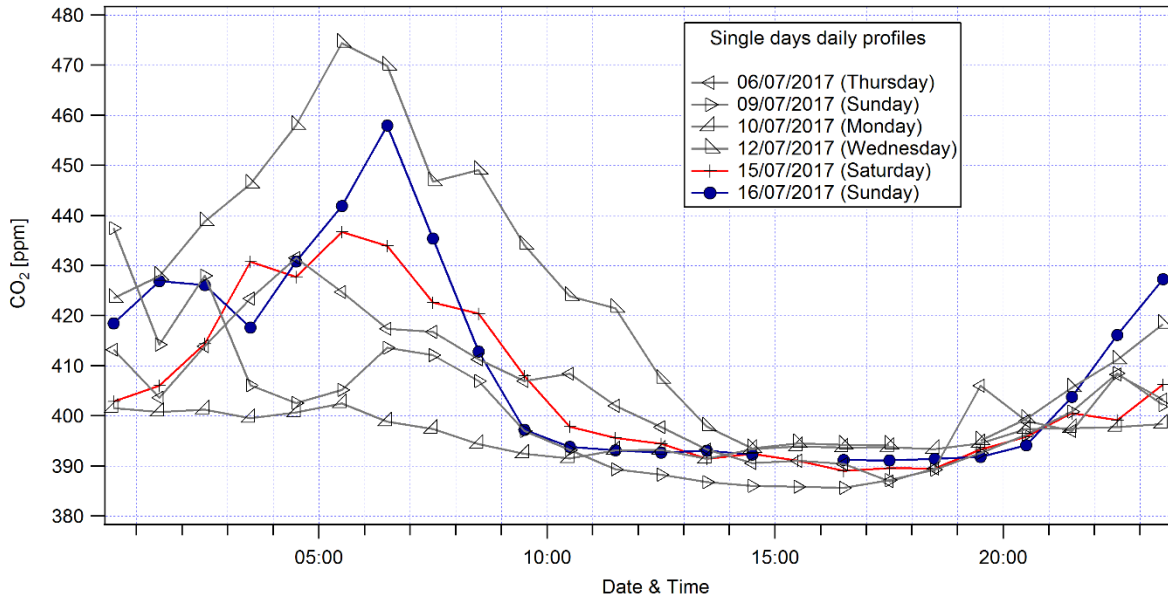


Figure S4.8: Diurnal profiles of the CO<sub>2</sub> mixing ratio from the stationary measurements at CNR. The grey open symbols are additional days, not in common with the other profiles. Since only 2 out of 8 days were in common with the other quantities, the CO<sub>2</sub> the average diurnal profile is not shown.

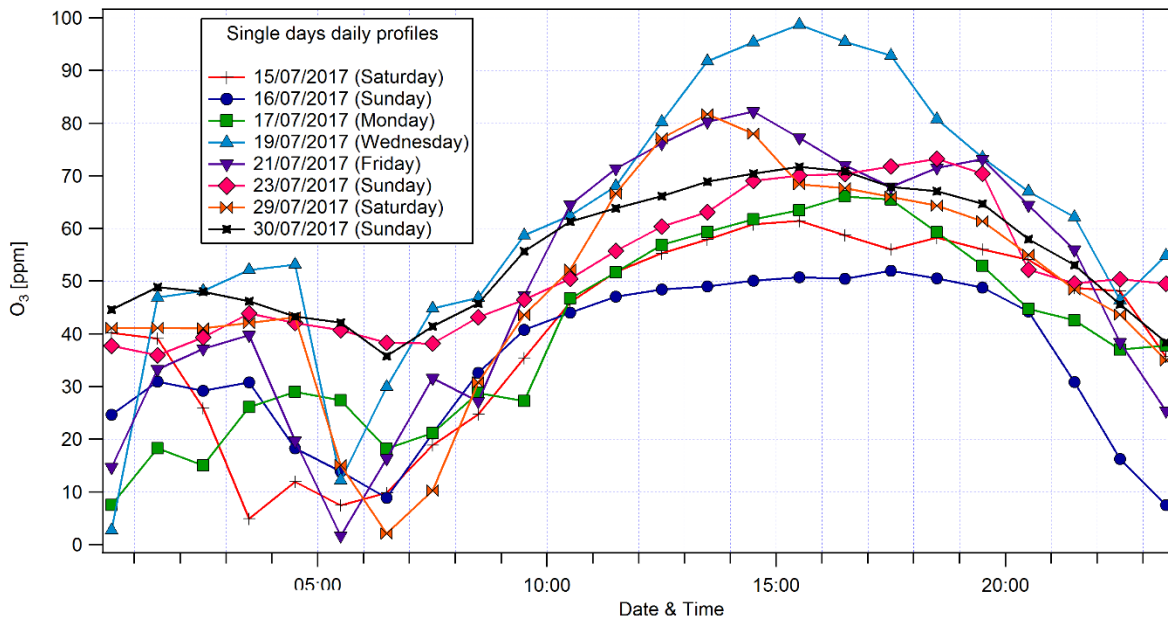


Figure S4.9: Diurnal profiles of the O<sub>3</sub> mixing ratio from the stationary measurements at CNR.

## Chapter 5:

### Yearly characterization of the Arctic Black Carbon sampled on Zeppelin Observatory, Svalbard

Rosaria E. Pileci<sup>1</sup>, Robin L. Modini<sup>1</sup>, Paul Zieger<sup>2</sup>, Radovan Krejci<sup>2</sup>, Kouji Adachi<sup>3</sup>, Urs Baltensperger<sup>1</sup> and Martin Gysel–Beer<sup>1</sup>

<sup>1</sup> Laboratory of Atmospheric Chemistry, Paul Scherrer Institute (PSI), 5232 Villigen PSI, Switzerland

<sup>2</sup> Department of Applied Environmental Science, Stockholm University, 106 91 Stockholm, Sweden

<sup>3</sup> Meteorological Research Institute, Tsukuba, Ibaraki, Japan

*Correspondence to:* R. L. Modini (robin.modini@psi.ch) and M. Gysel–Beer (martin.gysel@psi.ch)

Manuscript in preparation

**Abstract.** Black carbon particles play an important role in the direct and indirect radiative forcing of climate in the Arctic. However, the magnitude of the net radiative forcing is strongly dependent on the physical properties of black carbon (BC) particles, such as mass concentration and size distribution. Long-term and direct measurements of black carbon mass concentration are required to develop, assess, and improve emission inventories, transport models, and mitigation strategies designed to reduce the warming of the Arctic.

For one year (from April 2019 to March 2020), measurements of refractory black carbon (rBC) mass concentration and size distribution were conducted at the Zeppelin Observatory, Svalbard, with a Single Particle Soot Photometer Extended Range (SP2-XR). Annual average and median rBC mass concentrations were 8.0 and 3.8 ng m<sup>-3</sup>, respectively, while monthly averages ranged from a maximum of 24.7 ng m<sup>-3</sup> in February, to a minimum of 2.3 ng m<sup>-3</sup> in October. The annual average modal diameter,  $D_{\text{rBC,mode}}$ , of the rBC mass size distribution was 197 nm with monthly values between  $D_{\text{rBC,mode}} = 161$  nm in August and  $D_{\text{rBC,mode}} = 233$  nm in December.

rBC concentration weighted trajectory (CWT) analyses indicated that from October to March, BC concentrations at Zeppelin were mainly influenced by source regions in Northern and Central Russia. From April to July the BC mass came from extreme northern areas in Eurasia and Canada, while in August and September BC was it originated mainly from North-Eastern Europe.

Unexpected but frequent occurrence of large BC cores with rBC mass equivalent diameter bigger than 300 nm was found prevalently in June, September, October and November. The presence of such large BC particles was confirmed by transmission electron microscopy analysis, which found coarse black carbon particles internally mixed with sulfate, sea salt and dust. The relative contribution of these coarse BC particles to the total rBC mass concentration was found to be inversely proportional to the total rBC mass concentration. This supported two main hypotheses: the production of the large BC cores during atmospheric transport rather than direct emissions or the presence of a weak source of coarse BC particles that became relatively important if the concentration of other transported BC was very low.

The rBC mass concentration was compared with the equivalent black carbon (eBC) mass concentration measured with a MAAP. The monthly eBC/rBC mass ratio varied between 2.9 and 4.0. The principal reason of such large discrepancy was explained with the too low  $\text{MAC}_{\text{BC}}$  value applied to the absorption coefficients measured by the MAAP to calculate the equivalent black carbon mass concentration. Another cause of this discrepancy was found to be the limited detection range of the SP2-XR, which did not allow the total detection of coarse BC particles. Indeed, the presence of coarse BC particles was found to increase the eBC/rBC mass ratio by 33 %.

## 5.1 Introduction

The Arctic is one of the most sensitive regions to climate change, and is warming at twice the global rate over recent decades (Serreze and Barry, 2011). To slow down this warming trend, there is growing interest in reducing the impact from short-lived climate forcers, such as black carbon (BC), because the benefits of its mitigation are seen more quickly relative to CO<sub>2</sub> emission reduction (Shindell et al., 2012).

Indeed, black carbon is the most efficient light-absorber in atmospheric aerosols and can exert a strong warming effect on global and regional climate (Bond et al., 2013; Myhre et al., 2013; Cherian et al., 2017). An absorbing aerosol, over a highly reflective surface, typical of the Arctic, results in a warming at altitudes above and within the particle layer. The added atmospheric heating subsequently increases the downward longwave radiation to the surface, warming it (Shaw and Stamnes, 1980). Moreover, black carbon interacts with clouds to affect their microphysical and radiative properties (Twomey, 1974; Jacobson, 2001; Andrews et al., 2011), further modulating the radiation budget of the region. BC-containing aerosols have an additional forcing mechanism when deposited on snow and ice surfaces. Such deposition enhances the absorption of solar radiation at the surface which can warm the lower atmosphere and induce snow and ice melting (Flanner et al., 2007).

In the Arctic, these BC climate effects have a strong seasonal variation. In fact, while in summer the Arctic is mostly influenced by local activities (Hirdman et al., 2010); in winter and spring the phenomenon called “Arctic haze” takes place (Shaw, 1995). Due to the large-scale air movements, polluted air (rich of BC, sulfate, organic matter, ammonium, nitrate and mineral dust, etc.) coming principally from Eurasia and North America reaches the Arctic (Sharma et al., 2006; Huang et al., 2010; Dutkiewicz et al., 2014), perturbing the surface-atmosphere radiation balance (Blanchet, 1989).

A large number of studies have performed statistical analyses of trajectories combined with atmospheric BC concentration data. These methods tried to identify the regions from which high measured BC concentrations were coming. For instance, Polissar et al. (1999), Sharma et al. (2004, 2006) and Eleftheriadis et al. (2009) studied the source regions of BC measured at Barrow, Alert and Svalbard using trajectory statistics. However, it is important to mention that the assumption of the trajectory method is based on the inertia of the tracer and the fact that chemical or other removal processes do not affect it. This hypothesis can sometimes introduce large uncertainties to the BC source apportionment (Liu et al., 2015a). Black carbon particles can be transported into the Arctic via three principal pathways: low-level transport followed by ascent in the Arctic, low-level transport alone, and uplift outside the Arctic, followed by descent in the Arctic. The last pathway is frequent for pollution originating from North America and Asia, whereas European pollution can follow all three pathways in winter, and pathways one and three in summer (Stohl, 2006). The time for transport of BC from extra-Arctic source regions to the Arctic is typically of the order of several days to weeks (Heidam et al., 2004). This interval is appreciably longer than the time needed for BC aging that is the BC conversion from a hydrophobic to a hydrophilic particle. For this reason, BC particles that reach the Arctic usually have grown by condensation and coagulation, and this can be seen by an increase to a bigger modal diameter of the BC mass size distribution relatively to the emission point (Shiraiwa et al., 2008), moreover they are found to be internally mixed with soluble material (Zanatta et al., 2018). However, long-range transport can also change the BC mass size distribution to a smaller size due to preferential wet removal of larger BC cores (Moteki et al., 2012).

Very long time series of BC mass concentration in the Arctic have been measured with filter-based absorption instruments, such as the multi-angle absorption photometer (MAAP), the particle soot absorption photometer (PSAP) and the Aethalometer (Sharma et al., 2004, 2006; Eleftheriadis et al., 2009). However, the absorption coefficient calculated with these instruments can be prone to large uncertainties, due to multiple scattering and filter loading effects (Weingartner et al., 2003; Backman et al., 2017). Additional uncertainty results from the empirical conversion of the absorption coefficient to an equivalent black carbon mass concentration ( $m_{eBC}$ ) (Petzold et al., 2013) using an assumed mass absorption cross-section ( $MAC_{BC}$ ). This coefficient depends on the composition and morphology of the particles used in the calibration of the instrument, and on the specific technique used to quantify the black carbon mass (Slowik et al., 2007; Pileci et al., 2021).

Thanks to the recent development of the Single Particle Soot Photometer (SP2), which is an instrument based on the laser-induced incandescence (LII) technique, direct measurements of black carbon, in this case named refractory black carbon (rBC) (Petzold et al., 2013) have started also in the Arctic. Sharma et al. (2017) measured the mass concentration of refractory black carbon ( $m_{\text{rBC}}$ ) in the Canadian Arctic from March 2011 to December 2013. Shorter term measurements of  $m_{\text{rBC}}$  were carried out in the European Arctic (Liu et al., 2015a; Raatikainen et al., 2015; Taketani et al., 2016; Zanatta et al., 2018).

These long-term measurements have demonstrated that BC concentration has declined since 1980 thanks to the implementation of climate and air quality policies in Europe and United States which have efficiently contributed to fossil fuel BC emission reductions. At the same time, emissions of BC from wood burning from residential heating in winter and exceptionally high emissions of BC from forest fires in summer have increased over the last 20 years (Chin et al., 2014).

In general, current models fail to reproduce the seasonal cycles of BC mass in the Arctic, with large underestimation during Arctic haze and overestimation in summer (Shindell et al., 2008; Koch et al., 2009; Eckhardt et al., 2015; Winiger et al., 2017). This may be due to multiple reasons: incorrect spatial or temporal distribution of emissions in the inventories used for the modeling in certain areas, poor characterization of BC optical and chemical properties such as its size distribution and mixing state, and uncertainties in the mechanisms associated with BC wet removal and BC interaction with clouds. For instance, Vignati et al. (2010) found that varying BC microphysical properties, mass size distributions and removal rates can result in simulated BC concentrations that differ by more than an order of magnitude in remote regions such as the Arctic. This then also results in substantial uncertainties in the estimation of the BC radiative forcing.

To answer the need for a more complete characterization and longer time series of black carbon properties in the Arctic, we measured the rBC mass concentrations and the rBC size distributions at Zeppelin Observatory in Svalbard, Norway, from April 2019 to March 2020. The measurements were performed with a Single Particle Soot Photometer Extended Range (SP2-XR), the more compact version of the SP2. For the first time, the SP2-XR was used for a long-term remote monitoring campaign. In addition, trajectory analyses were used to identify the source regions of BC. Finally, we compared the rBC mass with eBC mass concentrations measured by the MAAP to investigate their agreement/disagreement.

## **5.2 Methods**

### **5.2.1 Measurement site**

The field campaign took place between 1 April 2019 and 31 March 2020, at the Zeppelin Observatory, (475 m a.s.l.; 78°54' N, 11°53' E), Svalbard, Norway. The Norwegian Polar Institute owns the station, and is responsible for development, maintenance, daily management and safety. The Norwegian Institute for Air Research (NILU) is responsible for the scientific coordination. Moreover, the Zeppelin Observatory is part of the Global Atmosphere Watch network.

This site is representative of remote Arctic background and considered to be within the planetary boundary layer most of the time (Tunved et al., 2013). During the Arctic haze period, Ny Ålesund is mainly influenced by long-range transport over the Arctic Ocean from Siberia, Eurasia and the European subcontinent (Tunved et al., 2013). Minimal local pollution reaches the site (Beine et al., 2001; Ström et al., 2003).

### **5.2.2 Inlets and instruments**

#### **5.2.2.1 Inlets**

Black carbon particles were sampled through two different inlets during the whole campaign (Fig. 5.1): a total inlet and a total counter-flow virtual impactor inlet (CVI, Brechtel Manufacturing Inc., USA, Model 1205). The total inlet sampled interstitial (not activated) particles, cloud droplets and ice crystals when mixed-phase clouds were present. The CVI inlet used opposing air flows to filter out particles with low inertia (i.e. interstitial particles), so that only activated particles (i.e. droplets and ice crystals) were sampled (Noone et al., 1988). A detailed technical description of the CVI inlet at Zeppelin Observatory can be found in Karlsson et al. (2020).



During this campaign, the CVI was only operated when there was a cloud at the station. The CVI automatically turned on when the visibility dropped below 1 km (the WMO’s definition of fog). Once the CVI was on, the SP2-XR was switching between total inlet and CVI inlet every 10’ as shown in Fig. 5.1. This allowed getting quasi-parallel information of both the activated BC and total BC.

In this work we only used the SP2-XR data when the instrument was sampling on the total inlet. Both the MAAP (Sect. 5.2.2.32.1.2) and the transmission electron microscopy data (Sect. 5.2.2.4) presented in this work were collected when sampling on the total inlet.

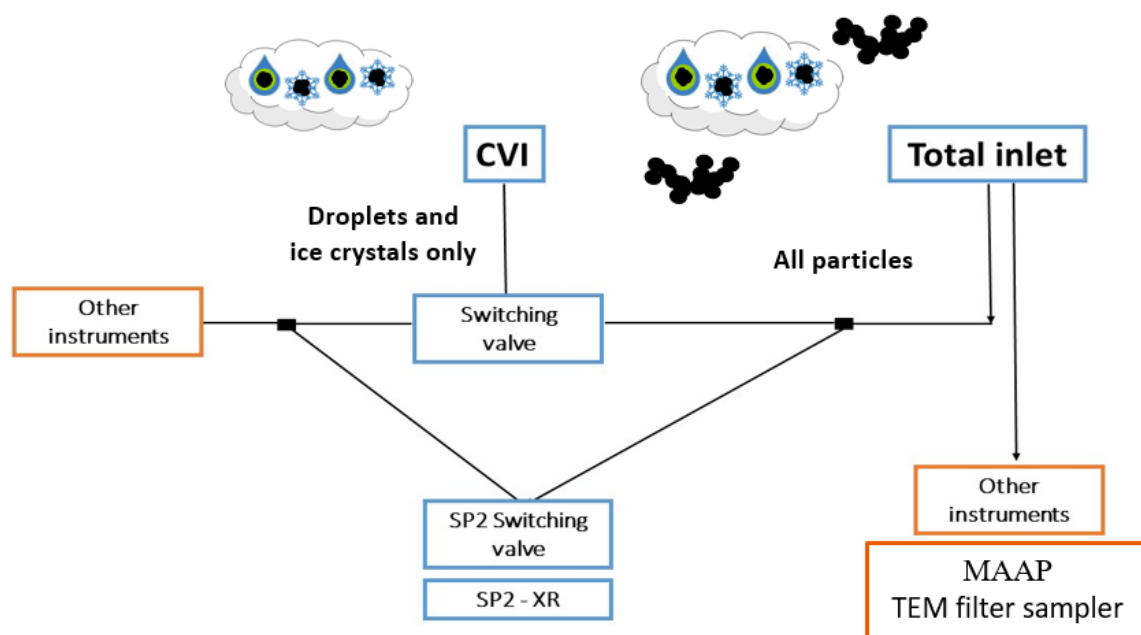


Figure 5.1: Schematic illustration of the experimental set-up at Zeppelin Observatory.

### 5.2.2.2 Single Particle Soot Photometer Extended Range (SP2-XR)

A Single Particle Soot Photometer Extended Range (SP2-XR, Droplet Measurement Technologies, DMT, Longmont, CO, USA) was used in this work to measure the refractory black carbon mass concentration and rBC particle mass size distribution. The SP2-XR uses a high-intensity continuous Nd: YAG laser beam ( $\lambda = 1064 \text{ nm}$ ), characterized by an intra-cavity circulating power up to  $1 \text{ MW cm}^{-2}$ , to make BC particles incandesce and emit a thermal/visible signal until they vaporize. The incandescence signal passes through a band pass filter, nominally from 400 nm to 750 nm, and is recorded via a single photomultiplier tube. The intensity of the thermal radiation emitted at the rBC vaporization point is a linear function of the refractory volume of the particle. In this study the calibration of the incandescence signal was done using size selected aerosols from fullerene soot (stock 40971, lot FS12S011), generated with a differential mobility analyzer (DMA) in accordance with recommended SP2 calibration procedure (Baumgardner et al., 2012; Laborde et al., 2012a). Two incandescence calibrations were performed during the campaign, in June and in November 2019 and were found to be very stable (within a few percent). rBC mass size distributions were generated by converting the rBC mass of each BC-containing particle to an rBC mass equivalent diameter ( $D_{\text{rBC}}$ ) (assuming a void-free BC material density of  $\rho_{\text{BC}} = 1.8 \text{ g cm}^{-3}$ ) and binning the particles by  $D_{\text{rBC}}$ . The SP2-XR measurements during this field campaign covered the size range  $70 \text{ nm} \leq D_{\text{rBC}} \leq 700 \text{ nm}$  with unit detection efficiency. The rBC mass concentration was corrected adding the estimated rBC mass concentration below the lower SP2 limit of quantification (here,  $D_{\text{rBC}} \leq 70 \text{ nm}$ ) using an extrapolation method based on lognormal fits to the measurement, as described in Pileci et al. (2021). No correction was applied for BC cores larger than the upper limit of quantification.

### 5.2.2.3 Multi-angle absorption photometer (MAAP)

A multi-angle absorption photometer (MAAP, Thermo Fisher Scientific, Waltham, USA) (Petzold et al., 2005) was used to determine the equivalent black carbon mass concentration  $m_{\text{eBC}}$ . The MAAP measures the transmitted and reflected light at multiple angles from an aerosol-loaded filter and then it applies a two-stream-approximation radiative transfer model to infer the absorption coefficient of the deposited aerosol sample. Moreover, the reflectance signals provide the information required to account for the effects of multiple scattering and shadowing.

The  $m_{\text{eBC}}$  is then calculated using the following equation:

$$b_{\text{abs,corr}}(637 \text{ nm}) = b_{\text{abs,default}}(670 \text{ nm}) \cdot 1.05 \quad (5.1)$$

$$m_{\text{eBC}} = \frac{b_{\text{abs,corr}}(637 \text{ nm})}{\text{MAC}_{\text{eBC}}^{637 \text{ nm}}} \quad (5.2)$$

where  $\text{MAC}_{\text{eBC}}^{637 \text{ nm}} = 6.6 \text{ m}^2 \text{ g}^{-1}$  is the mass absorption cross section used in the firmware of the MAAP,  $b_{\text{abs,default}}(670 \text{ nm})$  is the aerosol absorption coefficient output of the instrument measured at 670 nm, and  $b_{\text{abs,corr}}(637 \text{ nm})$  is the aerosol absorption coefficient corrected for the difference between the operating wavelength (637 nm) and the nominal wavelength (670 nm) (Müller et al., 2011).

### 5.2.2.4 Transmission Electron Microscope (TEM)

A 120 kV transmission electron microscope (TEM; JEM-1400, JEOL, Tokyo, Japan) was used for the TEM images. A TEM with a scanning mode (scanning transmission electron microscopy; STEM) equipped with an energy-dispersive X-ray spectrometer (EDS; X-max 80, Oxford Instruments, Tokyo, Japan) was also used for the element mapping images of representative particles. The element mapping images were obtained using the STEM-EDS with ~ 30 min of acquisition time.

Aerosol samples were collected using a TEM aerosol sampler (AS-16W, Arios, Tokyo, Japan), which has two impactor stages that collect particles with ~0.1-0.7 and > 0.7  $\mu\text{m}$  aerodynamic diameter (50 % cutoff diameter) on TEM grids (200 mesh Cu grids with Formvar carbon substrates U1007, EM-Japan, Tokyo, Japan). Thirty-min collection times at a  $1.0 \text{ L min}^{-1}$  flow rate were used. From the available samples, the following ones were chosen because they were matching events with high fraction of large BC cores based on SP2-XR data: 16:22-16:52, on 26 April and 0:00-0:30 and 3:00-3:30 on 30 July 2019.

Particle composition and the shapes of individual particles were measured to manually find soot particles from all TEM grid areas. Although particles are mixtures of several components (e.g., dust, sea salt, sulfate, and soot), soot particles can be explicitly identified based on both their fractal-like shapes and C-rich composition.

### 5.2.2.5 Concentration weighted trajectory analysis (CWT)

In this work, we applied Zefir (Petit et al., 2017), an Igor-based package specifically designed to achieve a comprehensive geographical air mass origin analysis using a single statistical tool in combination with back-trajectories from the NOAA Hysplit model (Draxler and Hess, 1997). The results of this analysis are presented in the form of concentration weighted trajectory (CWT) graphs. The CWT analysis was used to determine potential source regions of the black carbon measured at the Zeppelin Observatory. In the CWT method, a weighted concentration is assigned to each grid cell by averaging the sample concentrations that have associated trajectories crossing that grid cell, as follows:

$$C_{ij} = \frac{1}{\sum_{l=1}^M \tau_{ij}} \sum_{l=1}^M C_l \tau_{ij} \quad (5.3)$$

Where  $C_{ij}$  is the average weighted concentration (of rBC, in this case) in the grid cell  $(l, j)$ ,  $l$  is the index of the trajectory,  $M$  is the total number of trajectories,  $C_l$  is the concentration observed at the sampling location (receptor site) on arrival of trajectory  $l$ , and  $\tau_{ij}$  is the residence time (time spent) of the trajectory  $l$  in the grid cell  $(l, j)$ . Thus, the weighted concentration  $C_{ij}$  obtained at each grid cell provided evidence of high BC source strength in this grid cell. In this work, the model was run at the receptor site of Zeppelin Observatory calculating 5, 8 and 10 days back-trajectories every 3 hours. Different altitude thresholds (no altitude limit, 3 km, 2 km and 700 m) for the trajectories were set. Results were discarded for all grid cells with fewer than 3, 5 or 10 trajectories crossings (at altitudes below the threshold).

### 5.3 Results and discussion

#### 5.3.1 rBC mass concentration and size distribution

The total rBC mass concentration measured by the SP2-XR was corrected by adding the estimated rBC mass concentration below the lower SP2 limit (here,  $D_{\text{rBC}} = 70$  nm),  $\Delta m_{\text{rBC} < \text{LDL}}$  (light blue area in Fig. S5.1), calculated using an extrapolation method based on applying a lognormal fit ( $\frac{dm_{\text{fit}}}{d\log D_{\text{rBC}}}$ , blue line in Fig. S5.1) to the measurement ( $\frac{dm_{\text{meas}}}{d\log D_{\text{rBC}}}$ , blue full circles in Fig. S5.1), as described in Pileci et al. (2021). The monthly mean rBC mass size distributions from April 2019 to March 2020, normalized by the total measured monthly rBC mass concentration, are shown in Fig. 5.2. Given to the peculiar shape of these size distributions, which in some cases show a large presence of coarse mode BC particles, the quantity  $\Delta m_{\text{meas}-\text{fit}}$  (dark blue area in Fig. S5.1) was calculated.  $\Delta m_{\text{meas}-\text{fit}}$  represents the integrated difference between measured rBC mass size distribution and lognormal fit in the range 300-700 nm relative to total measured rBC mass and was calculated as follows:

$$\Delta m_{\text{meas}-\text{fit}} = \frac{1}{m_{\text{meas}}} \left( \int_{D_1}^{D_2} \frac{dm_{\text{meas}}}{d\log D_{\text{rBC}}} (D_{\text{rBC}}) - \frac{dm_{\text{fit}}}{d\log D_{\text{rBC}}} (D_{\text{rBC}}) d\log D_{\text{rBC}} \right) \quad (5.4)$$

In Fig. S5.1 the modal diameter of rBC mass size distributions,  $D_{\text{rBC,mode}}$ , is also shown. In Table 5.1, the monthly  $m_{\text{rBC}}$  statistic (arithmetic mean, standard deviation – SD, median, 25<sup>th</sup> and 75<sup>th</sup> percentiles and the data availability),  $D_{\text{rBC,mode}}$ ,  $\Delta m_{\text{rBC} < \text{LDL}}$  and  $\Delta m_{\text{meas}-\text{fit}}$  are listed.

Table 5.1: Monthly corrected  $m_{\text{rBC}}$  arithmetic mean, standard deviation (SD), median, 25<sup>th</sup> and 75<sup>th</sup> percentiles, data availability, modal diameter of rBC mass size distributions  $D_{\text{rBC,mode}}$ , estimated rBC mass concentration below the lower SP2 limit  $\Delta m_{\text{rBC} < \text{LDL}}$  and area of the fitted and integrated difference between measured rBC mass size distribution and lognormal fit in the range 300-700 nm relative to total measured rBC mass,  $\Delta m_{\text{meas}-\text{fit}}$ , are shown.

	Apr 19	May 19	Jun 19	Jul 19	Aug 19	Sep 19	Oct 19	Nov 19	Dec 19	Jan 20	Feb 20	Mar 20
$m_{\text{rBC}}$												
arithmetic mean (SD)	7.6	6.9	2.8	5.3	3.6	3.1	2.3	2.6	14.0	17.1	24.7	12.7
[ng m <sup>-3</sup> ]	(4.2)	(4.2)	(2.8)	(7.0)	(7.8)	(6.4)	(2.2)	(2.0)	(15.0)	(15.9)	(21.9)	(9.4)
$m_{\text{rBC}}$												
median	6.2	6.2	1.5	2.6	2.2	1.1	1.4	1.9	8.1	14.1	18.3	10.6
(25 <sup>th</sup> , 75 <sup>th</sup> )	(4.9,	(3.9,	(0.9,	(1.1,	(1.1,	(0.6,	(0.9,	(1.1,	(5.0,	(5.6,	(7.8,	(5.8,
[ng m <sup>-3</sup> ]	8.6)	9.7)	3.8)	4.5)	3.3)	1.9)	2.9)	3.9)	21.0)	21.0)	31.5)	16.9)
Data availability												
[%]	100	100	93	87	100	83	100	100	81	84	89	48
$D_{\text{rBC,mode}}$												
[nm]	189	189	180	209	161	165	212	203	233	231	226	220
$\Delta m_{\text{rBC} < \text{LDL}}$												
[%]	4.1	3.6	4.1	3.9	7.2	5.3	3.0	3.1	1.1	0.7	0.9	1.3
$\Delta m_{\text{meas}-\text{fit}}$												
	0.04	0.04	0.12	0.01	0.04	0.05	0.07	0.08	0.02	0.01	0.01	0.01

The monthly rBC mass size distributions can be grouped into four categories with similar characteristics, Fig. 5.2b-e, i.e., similar modal diameter and presence or absence of a distinct BC coarse mode. August and

September had  $D_{rBC,mode} = 161$  nm and  $D_{rBC,mode} = 165$  nm. Moreover,  $\Delta m_{meas-fit}$  is 0.04 in August and 0.05 in September, indicating the presence of a second BC mode with modal diameter bigger than the upper detection limit of the SP2-XR (Fig. 5.2b). In June, October and November the presence of super-micron BC particles seemed to be even more important. In fact,  $\Delta m_{meas-fit}$  were 0.12, 0.07 and 0.08, respectively. However, while in October and November  $D_{rBC,mode}$  were 212 nm and 203 nm, in June it was smaller, with  $D_{rBC,mode,June} = 180$  nm and similar to April, May and July. In April and May, the rBC size distributions had both  $D_{rBC,mode} = 189$  nm and  $\Delta m_{meas-fit} = 0.04$ . The rBC size distribution was very symmetric during the winter months of December, January, February and March with  $D_{rBC,mode}$  of 233, 231, 226 and 220 nm, respectively and  $\Delta m_{meas-fit}$  of 0.01 a part from December which had  $\Delta m_{meas-fit} = 0.02$ . Even if it sits in the third group, the month of July was different from all the others. Its rBC size distribution was very symmetric, as the winter months, with  $\Delta m_{meas-fit} = 0.01$ , but  $D_{rBC,mode,July} = 209$  nm, similar to October and November.

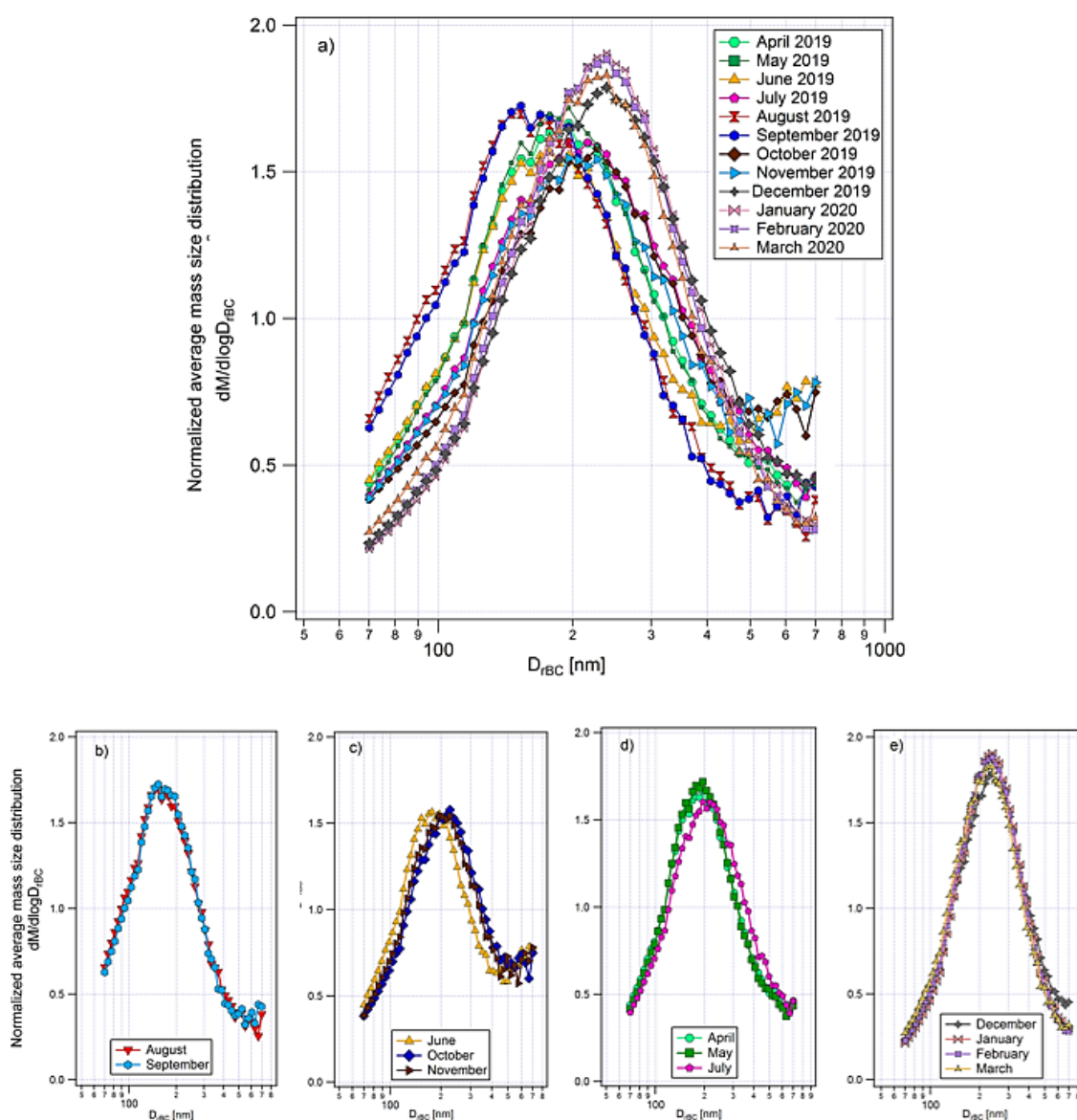


Figure 5.2: Normalized monthly mean rBC mass size distributions from April 2019 to March 2020 (a). The monthly size distributions are normalized by their total measured rBC mass concentration. In the bottom panels, months with similar rBC mass size distributions are grouped together: August and September (b), June, October and November (c), April, May and June (d), December, January, February and March (e).

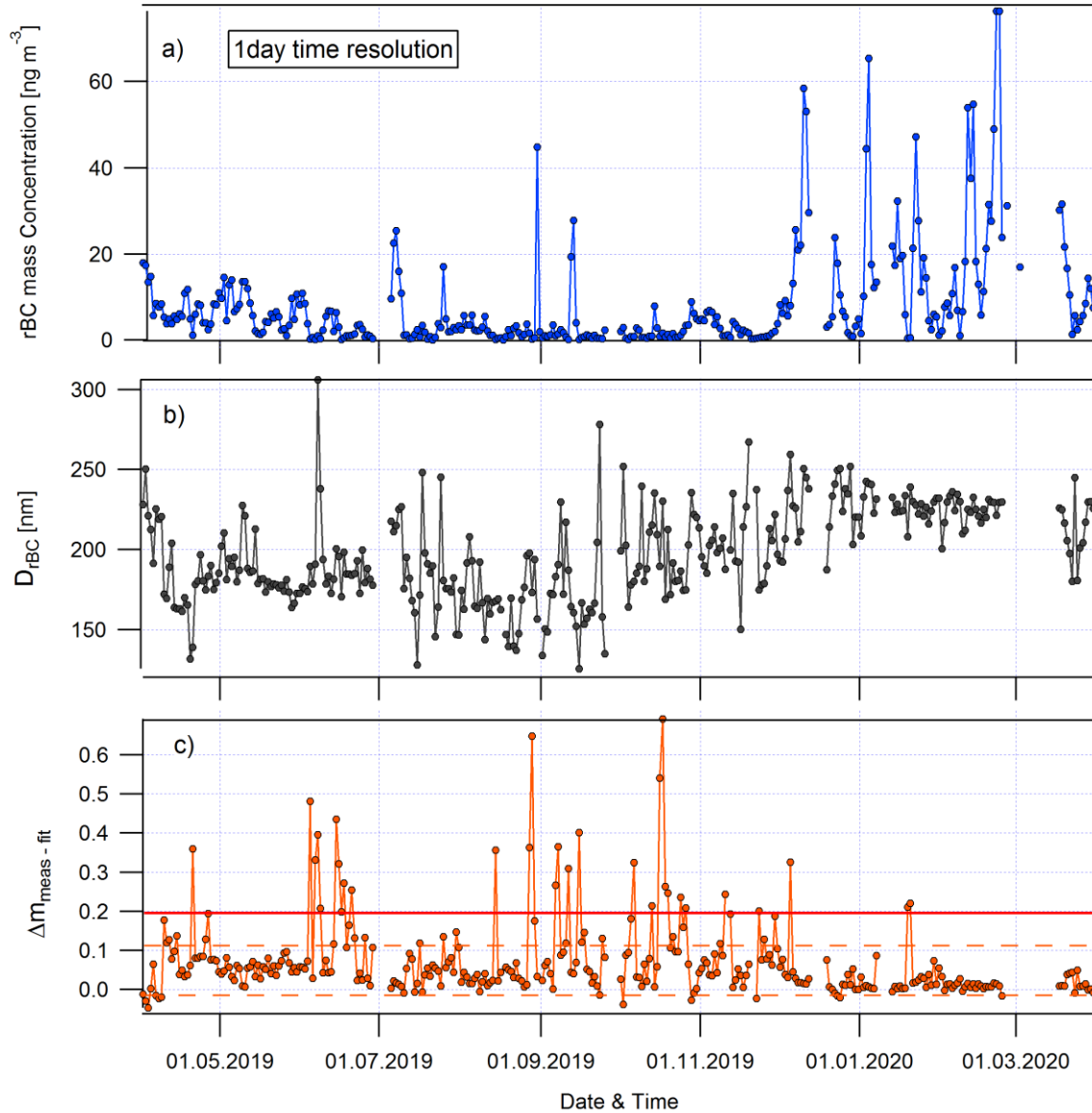


Figure 5.3: Daily averages from April 2019 to March 2020 of rBC mass concentration (a), rBC modal diameter (b) and integrated difference between measured rBC mass size distribution and lognormal fit in the range 300 - 700 nm relative to total measured rBC mass (c).

$D_{\text{rBC,mode}}$  varied between 125 nm and 306 nm as shown in Fig. 5.3b. These values are generally comparable to previous SP2 observations in the Arctic regions. Sharma et al. (2017) found on average a modal mass diameter of 225 nm during winter, and around 170 nm during summer, similar to our results. Raatikainen et al. (2015) found an average modal mass diameter of 194 nm with values ranging from 140 nm and 260 nm during winter 2012. Taketani et al. (2016) found the median values of modal rBC size distribution around 170 nm, in September, very similar to our observations. Zanatta et al. (2018) reported  $D_{\text{rBC,mode}} = 240$  nm, during spring, higher values than in this work.

$\Delta m_{\text{meas-fit}}$  varied between roughly -0.05 and 0.70 (Fig. 5.3c). The rBC mass size distributions with  $-0.05 < \Delta m_{\text{meas-fit}} < 0.05$  were quite symmetric (see the dashed lines in Fig. 5.3c). For this reason, we considered a substantial presence of coarse BC particles when  $\Delta m_{\text{meas-fit}} > 0.05$ . Size distributions with  $\Delta m_{\text{meas-fit}} > 0.2$  (see the red line in Fig. 5.3c) were characterized by an important presence of coarse BC particles. Virtually no such events during the period with high rBC mass concentrations from around December to March were present. Frequent occurrence of such events was found during periods with low rBC mass concentration from around April to November (with May and July being event-free exceptions).

Five months had 100 % of data coverage (April, May, August, October and November) and only one month (March 2020) had less than 50 % data availability. In Fig. S5.1 the modal diameter of the rBC mass size distribution,  $D_{\text{rBC,mode}}$ , is also shown. Table 5.1 lists the monthly  $m_{\text{rBC}}$  statistics (arithmetic mean, standard deviation – SD, median, 25<sup>th</sup> and 75<sup>th</sup> percentiles and the data availability),  $D_{\text{rBC,mode}}$ ,  $\Delta m_{\text{rBC}<LDL}$  and  $\Delta m_{\text{meas-fit}}$ .

The winter and spring months exhibited frequent episodes of high rBC mass concentrations. The daily maximum occurred on 23 February reaching a value of  $76 \text{ ng m}^{-3}$ . In comparison, in summer and autumn, the rBC mass concentrations were generally lower with occasional high BC events (such as on 30 August, with  $m_{\text{rBC}} \approx 40 \text{ ng m}^{-3}$ ). The rBC mass concentration median was smaller than  $7 \text{ ng m}^{-3}$  from April 2019 to November 2019, while it was higher than  $8 \text{ ng m}^{-3}$  in the winter months between December 2019 and March 2020. February was the month with the highest rBC mass concentration (median value of  $18.3 \text{ ng m}^{-3}$ ).

The observed rBC mass concentration can be compared to that observed at Arctic sites from previous SP2 studies. Raatikainen et al. (2015) reported an average rBC mass concentration of  $26 \text{ ng m}^{-3}$  at the Pallas Global Atmosphere Watch station ( $68^\circ \text{ N}$ , Finland) between December 2011 and February 2012. Liu et al. (2015) presented rBC measurements performed in the low and middle troposphere in the European Arctic in spring 2013, when the rBC mass concentration varied between 20 and  $100 \text{ ng m}^{-3}$ . Taketani et al. (2016) investigated the spatial variability in rBC at sea level between the North Pacific and Arctic oceans during September 2014, finding an average rBC mass concentration of  $1.0 \pm 1.2 \text{ ng m}^{-3}$  at latitudes higher than  $75^\circ \text{ N}$ . Sharma et al. (2017), based on a long time series of SP2 measurements between March 2011 and December 2013 at the Global Atmosphere Watch baseline observatory in Alert, Nunavut ( $82.5^\circ \text{ N}$ ), calculated seasonal rBC mass concentration averages of  $33 \text{ ng m}^{-3}$ ,  $25 \text{ ng m}^{-3}$ ,  $6 \text{ ng m}^{-3}$  and  $8 \text{ ng m}^{-3}$  for winter, spring, summer and fall, respectively. Zanatta et al. (2018) reported an average mass concentration of  $39 \text{ ng m}^{-3}$  at Zeppelin Observatory between 22 March and 11 April 2012. Our observations are comparable to the ones of the previous studies except for the spring months. In fact, the rBC mass concentration we measured in March, April and May was substantially smaller than the one reported by the earlier studies. This can be due to the decrease in BC mass concentrations due to the implementation of air quality policies or to particular seasonal meteorological conditions.

### 5.3.2 Presence of coarse BC particles in the TEM analysis

Confirmation of such large BC particles was obtained by TEM analysis (Sect. 5.2.2.4). Only two TEM samples overlapped with the days with significant presence of coarse BC particles. Large BC particles were searched in the TEM coarse mode stage, which collected particles with aerodynamic diameter bigger than 700 nm. A fractal-like BC particle with aerodynamic diameter bigger than 700 nm corresponds to a particle with mass equivalent diameter  $D_{\text{rBC}}$ , bigger than roughly 750 nm, considering a fixed BC core density of  $\rho_{\text{rBC}} = 1800 \text{ kg m}^{-3}$ . Internally mixed BC particles with aerodynamic diameters ranging from 1 to several  $\mu\text{m}$  correspond approximatively to mass equivalent diameters bigger than 700 nm. Hence, those particles constituting the coarse mode of BC particles in the BC mass size distribution measured by the SP2-XR are indeed expected to be collected in the TEM coarse mode stage.

The first TEM sample was collected between 03:00 and 03:30 on 30 July 2019. Figure 5.4a shows the normalized rBC mass size distribution on 30 July with the presence of a coarse BC mode ( $\Delta m_{\text{meas-fit}} = 0.19$ , Fig. 5.3c). Figure 5.4b shows TEM examples of particles containing a large amount of BC mass, which makes it plausible that these particles showed up at rBC mass equivalent diameter  $> \sim 300 \text{ nm}$  if they had been sampled by the SP2-XR. The presence of carbon was confirmed by the carbon signal in the elemental mapping image (Fig. S5.2) and the peculiar (compacted) fractal-like shape in the TEM images (when particles did not overlap each other), which was found throughout the particles, as indicated by the orange arrows in Fig. 5.4b. The occurrence of small particles around the central big particle suggested that the original particle possibly had some volatile liquid material such as water, which was spread around the sample when collected and then evaporated. Figure S5.2 suggests that K, Ca, and N were associated with sulfate in the particle. A dust particle was also attached to the particles, as indicated by Al and Si mapping. The EDS mapping of the bottom half of this particle was difficult to analyze because the particle was too thick resulting in a possible EDS shadowing effect.

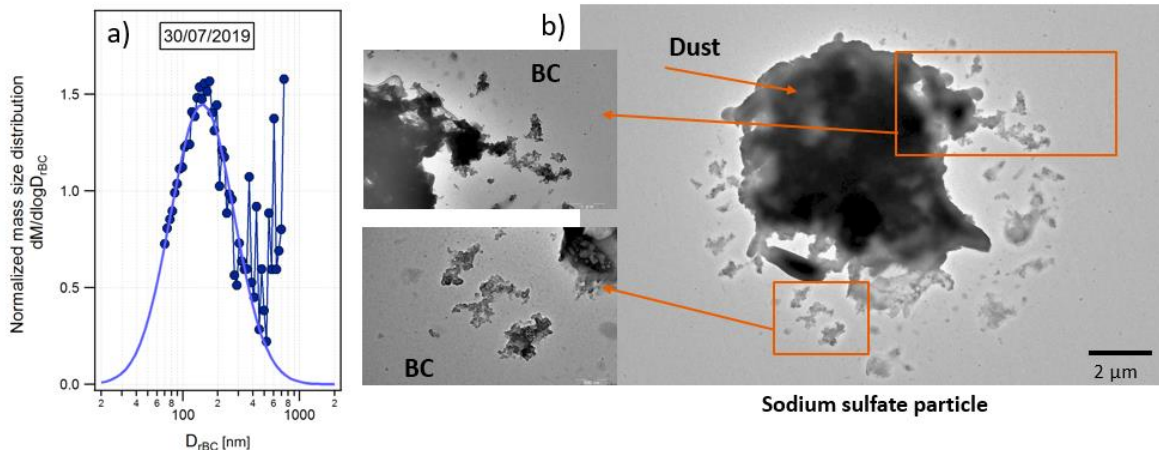


Figure 5.4: normalized rBC mass size distribution (a) and TEM analysis on the 30<sup>th</sup> July 2019 (b).

The second TEM sample was collected between 16:22 and 16:52 on 26 April 2019. Fig. 5.5a shows the normalized rBC mass size distribution on 26 April and Fig. 5.5b shows the presence of large BC particles and as shown in Fig. 5.3,  $\Delta m_{\text{meas-fit}} = 0.20$ . The TEM (Fig. 5.5b) and EDS (Fig. S5.3) results confirm the SP2 findings by showing the presence of a large amount of BC internally mixed with a potassium particle as well as dust (Al, Si, Fig. S5.3) and organic carbon (C, O, Fig. S5.3).

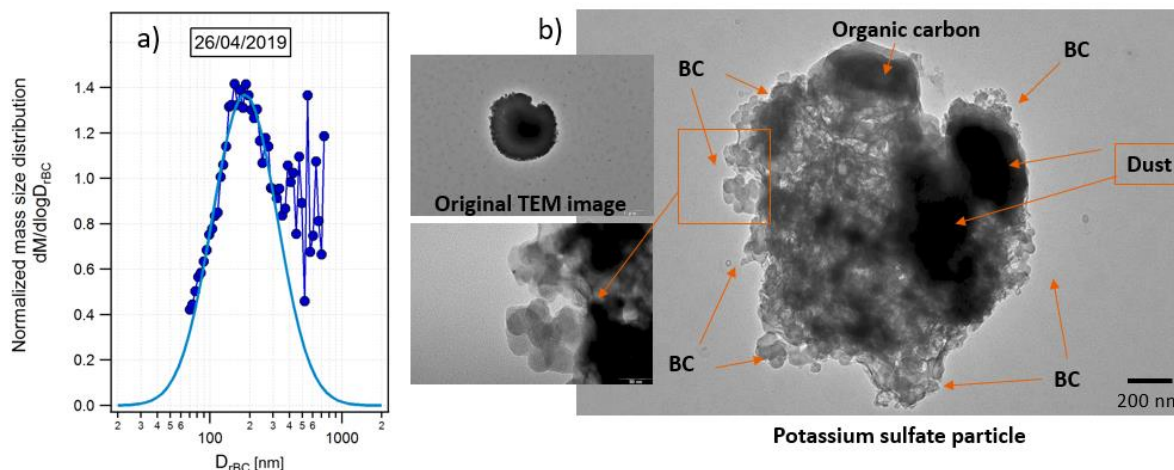


Figure 5.5: normalized rBC mass size distribution (a) and TEM analysis on the 26<sup>th</sup> April 2019 (b).

The TEM analysis corroborated the presence of relatively large soot particles although the limited statistics do not allow for a quantitative comparison with the rBC mass size distribution from the SP2-XR. Soot particles mostly occurred as several aggregates within single mixed particles consisting of sulfate, seas salt and dust principally. Those BC internally mixed particles ranged from 1 to several  $\mu\text{m}$  of geometric diameters and can be compared with BC particles with mass equivalent diameters bigger than 700 nm.

### 5.3.3 Determination of BC source regions

#### 5.3.3.1 Seasonal rBC concentration weighted trajectories

In order to find the source regions of black carbon at Zeppelin, the BC concentration weighted trajectories analysis was applied to the back-trajectories, as explained in Sect. 5.2.2.5. In the literature, different approaches were used to analyze rBC CWT over the year to find specific seasonal BC contributions. For instance, Eleftheriadis et al. (2009) separated summer (May to October) from winter (November to April). Sharma et al. (2006) ran the rBC CWT analysis separately for the winter months from January to April and the summer months from June to

September. In this work, the separation between months was decided based on the rBC mass size distributions presented in Fig. 5.2 and based on the outputs of the rBC CWT analysis. The winter period was considered between December and March. April was analyzed together with May, June and July, October with November and August with September.

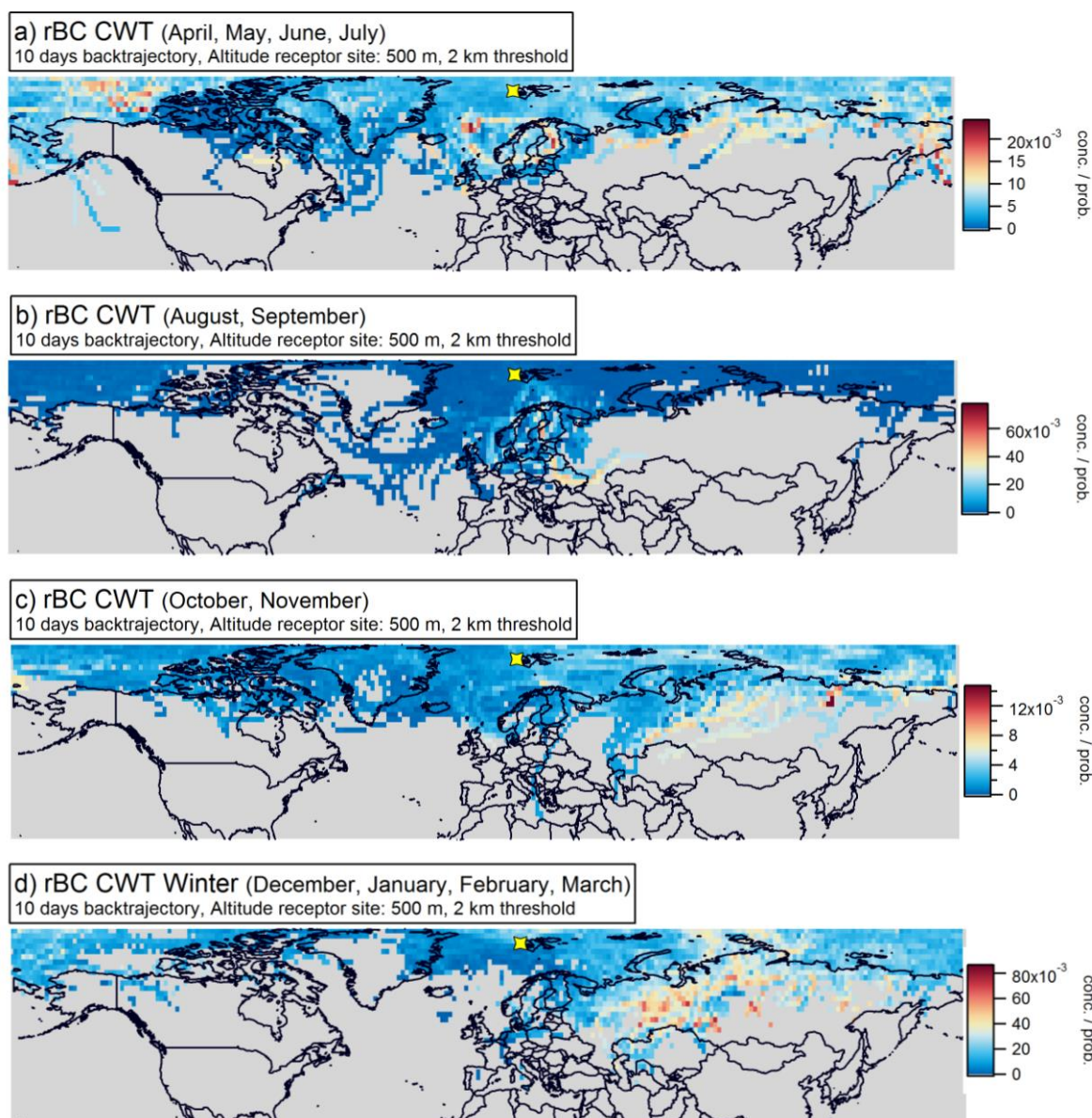


Figure 5.6: Black carbon concentration weighted trajectories graphs based on 10 days back-trajectories calculated every three hours during: April, May, June, July (a); August, September (b); October, November (c) and December, January, February and March (d). The altitude threshold was set at 2 km and only cells with at least three trajectories passing through them were considered. The altitude of the receptor site is 500 m, the altitude of Zeppelin Observatory.

Figure 5.6 shows that during the winter months and during October and November, long-range transport of black carbon from Russia arrived in the Arctic. The maps exhibit high BC CWT regions in a broad area extending from the Volga and Urals Federal Districts over Siberia to the Extreme-Oriental District. In a BC emission inventory reconstruction in Russia, Huang et al. (2015) identified three major BC hot spot regions: the European part of Russia, the Southern Central part of Russia where human population densities are relatively high, and the Urals Federal District where Russia's major oil and gas fields are located but with sparse human population. From April to July the BC CWTs show weighted BC concentrations trajectories coming from extreme northern areas: North



Russia and Europe, such as Finland as well as Greenland Sea and Beaufort Sea together with a hot spot in the Norwegian Sea near Island. In August and September, the CWT map shows that the BC mass concentration originated mainly from North-East Europe, Finland, Belarus and Ukraine. However, the results suggests that there was not sufficient variability in the trajectory paths. Hence, we can conclude that BC was picked up somewhere along that path in Northen-East Europe.

During summer, in the Arctic, the high continental pressure disappears and the transport from medium latitudes becomes less relevant. Thus, any emission related to biomass burning or to anthropogenic sources within the Arctic vortex (e.g., increasing of shipping emissions/gas flaring) becomes very important. The contribution of local sources, both land-based and ship emissions to the mean concentration of atmospheric BC over Svalbard is still an open question. However, while some influence of local sources at Ny-Ålesund village and harbor was seen by local stations, for instance in Gruvebadet, this was constrained in the lower layers of the troposphere and did not affect the high-altitude site such as Zeppelin Observatory (Gilardoni et al., 2019). In contrast, biomass burning episodes are becoming a very important source of BC for the Arctic region, in spring and summer (Warneke et al., 2010; Ritter et al., 2018; Zielinski et al., 2020). Gogoi et al. (2016) found that forest fire burning in Alaska and Canada led to strong increases in BC concentrations over Svalbard.

### 5.3.3.2 Concentration weighted trajectories during large BC particles occurrence

For understanding the origin of the BC coarse mode particles, the CWT analysis was ran exclusively on days that presented a prevalence of coarse BC particles. In order not to bias the analysis with high BC concentration days, the CWT was run on the relative contribution of BC coarse particles  $\Delta m_{\text{meas}-\text{fit}}$ , not on the total rBC mass concentration. In Fig. 5.7, the CWT analyses with choosing  $\Delta m_{\text{meas}-\text{fit}}$  as weighing factor is shown. Figure 5.7a) includes all trajectories of days with  $\Delta m_{\text{meas}-\text{fit}} > 0.05$  and panel b) with  $\Delta m_{\text{meas}-\text{fit}} > 0.20$ . 10-day back-trajectories with an altitude threshold at 2 km were calculated for the maps shown in Fig. 5.7. The 5-day back-trajectories maps are shown in Fig. S5.4.

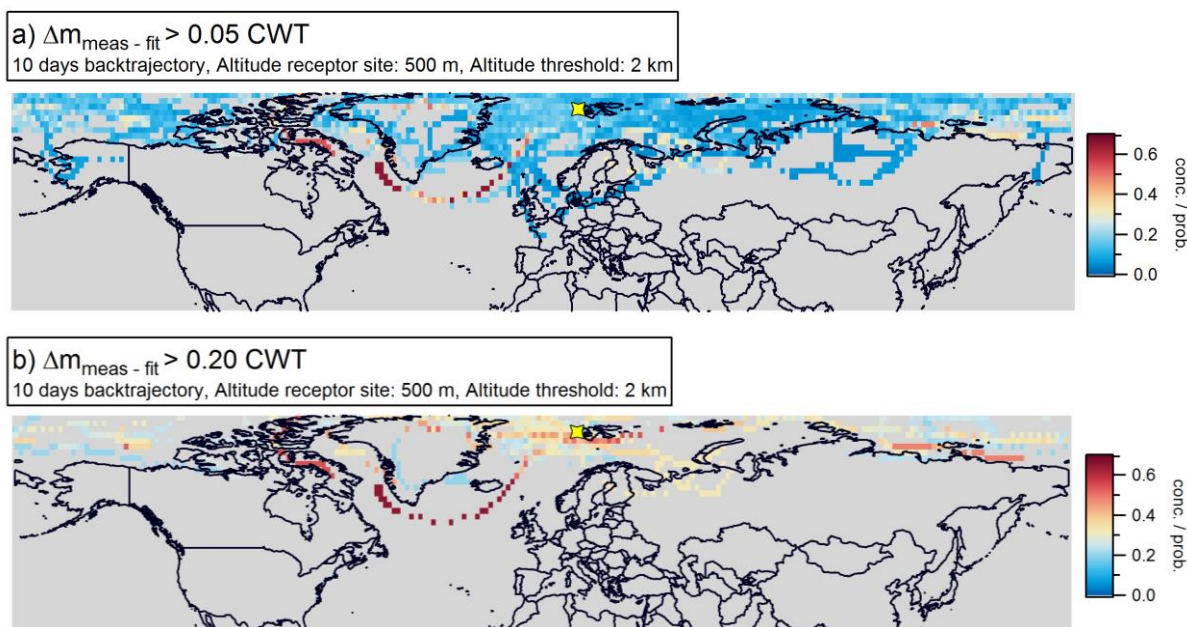


Figure 5.7: CWT analysis run with choosing  $\Delta m_{\text{meas}-\text{fit}}$  as weighing factor. The top panel includes all trajectories of days with  $\Delta m_{\text{meas}-\text{fit}} > 0.05$  and the bottom panel with  $\Delta m_{\text{meas}-\text{fit}} > 0.20$ . 10-day back-trajectories with altitude threshold at 2 km and at least three trajectories crossing a cell. The trajectories are ending at 500 m at Zeppelin Observatory.

The maps in Fig. 5.7 show that the relative contribution of BC during days characterized by the presence of large BC cores was mainly coming from Northern Canada, Greenland and from the Labrador sea. Some trajectories were passing closer to Iceland and some were coming from Siberia. We found significant occurrence of coarse BC particles in spring, summer and early autumn and June was the month characterized by the biggest value of  $\Delta m_{\text{meas-fit}}$  (Table 5.1). As mentioned in Sect. 5.3.3.1, biomass burning episodes are becoming a very important source of BC for the Arctic region, in spring and summer and in June 2019, more than 100 long-lived and intense wildfires blazed within the Arctic Circle. Most of them burned in Alaska and Siberia, and few raged even in Greenland.

Biomass burning produces rBC size distributions with larger modal diameter than traffic emissions with  $D_{\text{rBC,mode}}$  ranging from 200 to 300 nm (Bond et al., 2013; Schwarz, 2019), but there is no published study to the best of our knowledge that found such large presence of biomass burning coarse BC particles. If those particles were emitted by wildfires and transported over the Arctic, we would expect  $\Delta m_{\text{meas-fit}}$  to increase with the total rBC mass concentration. However, Fig. S5.5 shows an inverse relationship between  $\Delta m_{\text{meas-fit}}$  and  $m_{\text{rBC}}$ . Moreover, large BC particles would be mainly removed by wet deposition (Vignati et al., 2010) after an average atmospheric lifetime of 7.3 days (Schulz et al., 2006). Indeed, multiple studies found biomass burning aerosols internally mixed with ammonium, nitrate, and sulfate, which are hydrophilic substances (Pratt et al., 2010).

Anyway, Figs. 5.7 and S5.4 show too few trajectories to be able to draw any valid conclusions. The only pertinent conclusion is that the mode of coarse BC cores is only relevant in relative terms when the rBC mass concentration is low, consistently with Fig. S5.5. This supports two main hypotheses: the production of the large BC cores during atmospheric transport rather than direct emissions or the presence of a weak source of coarse BC particles that becomes relatively important if concentration of other transported BC is very low.

### 5.3.4 Correlation between coarse mode BC particles and presence of clouds

In Sect. 5.3.3.2, we speculated on the hypothesis that the large BC particles we measured in the rBC mass size distributions were produced from a certain source and were then transported over the Arctic. However, Fig. S5.5 shows an inverse correlation between  $\Delta m_{\text{meas-fit}}$  and  $m_{\text{rBC}}$ . This can be an indication that those particles were not transported but were the result of some local or regional process taking place.

Schwarz et al. (2013) found BC mass size distributions shifted to larger sizes in snow than the one seen in the atmosphere. They attributed this effect to three possible processes: 1) the agglomeration in the atmosphere of water-bound BC; 2) long-duration in-cloud residence times and prolonged exposure to collision coalescence in a small fraction of cloud parcels; 3) agglomeration of snow bound BC due to thaw-freeze cycles on the ground. Very recently, Ding et al. (2019) observed for the first time at the micro-scale the phenomenon of BC release from pre-existing liquid droplets during ice/snow particle formation. He proposed a mechanism whereby BC particles are accumulated by droplet collision before being released back to the air in a more aggregated form (with larger BC cores) during the Wegener–Bergeron–Findeisen (WBF) process (Bergeron, 1928; Findeisen, 1938; Wegener, 1911). The WBF process refers to the rapid growth of ice crystals at the expense of surrounding cloud droplets, which frequently occurs in atmospheric mixed-phase clouds and may play an important role on releasing some of the BC particles contained in droplets. The process proposed by Ding et al. (2019) may explain large model-measurement discrepancies such as the underestimates of BC concentration at high latitude and altitude areas dominated by mixed-phase or ice clouds (Qi et al., 2017).

To investigate if clouds could have played a role in the formation of coarse mode BC particles, we plotted  $\Delta m_{\text{meas-fit}}$  together with the hours of cloud occurrence at Zeppelin Observatory, indicated by the grey shadow area in Fig. 5.8. The graph does not show a clear correlation between the presence/duration of clouds and the presence of coarse BC particles. In Fig. S5.6 a case study shows what happened to the rBC mass size distribution during a sequence of “in cloud – out of cloud”. Also, in this case there is no evident correlation between the two variables. However, this does not exclude that the process described by Ding et al. (2019) or some other BC-cloud interaction process is taking place. Many more parameters such as the type of cloud, the meteorological parameters and hours in cloud along the backtrajectory should be investigated. Moreover, also the mixing between the already

transported BC with “freshly” long-range transported BC particles might play an important role abating the relative importance of the coarse BC particles potentially created by the process explained by Ding et al. (2019).

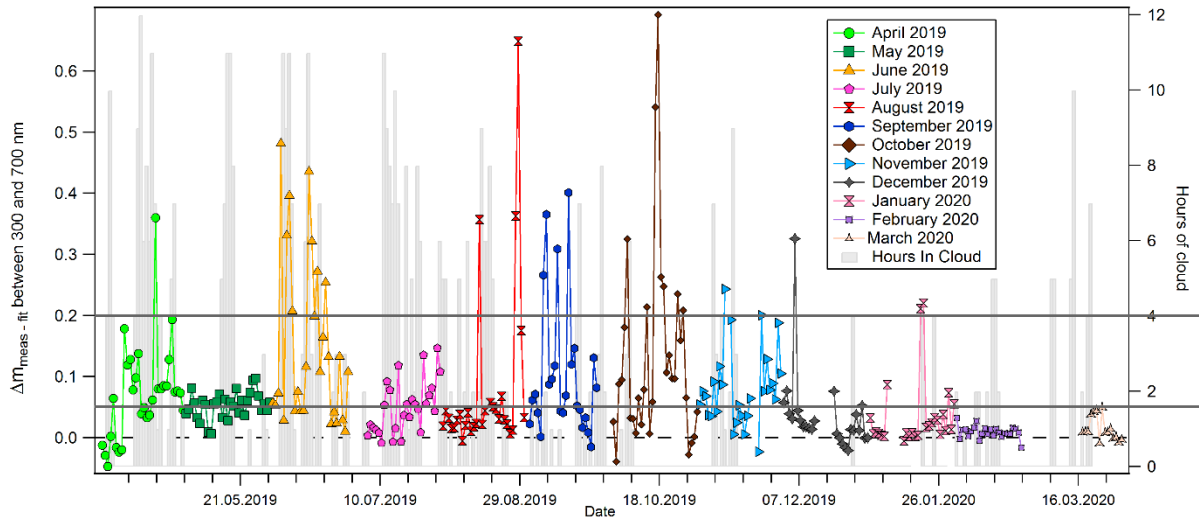


Figure 5.8:  $\Delta m_{\text{meas-fit}}$  with different colors and markers per month plotted together with the hours per day Zeppelin Observatory was in a cloud, indicated by the grey shadow area.

### 5.3.5 Comparison between rBC and eBC mass concentrations

In this paragraph, we show the yearly intercomparison between the rBC mass concentration measured by the SP2 and the eBC mass concentration obtained with the MAAP. The  $m_{\text{eBC}}$  was obtained by Eq. (5.2) with  $\text{MAC}_{\text{eBC}}^{637\text{ nm}} = 6.6 \text{ m}^2 \text{ g}^{-1}$ . Figure 5.9 illustrates the monthly averaged and standard deviations of the rBC, eBC mass concentration (Fig. 5.9b) and the eBC/rBC ratio (Fig. 5.9a). The eBC/rBC mass ratio varied from a minimum of 2.9 in June and December to a maximum of 4.0 in September (the full statistics with arithmetic average, standard deviation – std, median, 25<sup>th</sup> and 75<sup>th</sup> percentiles are shown in Table 5.2). This ratio is slightly higher in summer and autumn, between July and October, than in winter and spring (Table 5.2).

Literature studies found eBC/rBC mass ratios between 1.2 and 5. Raatikainen et al. (2015) showed comparisons between the SP2, the Aethalometer and the MAAP measurements over a 2-month period (December 2011 to January 2012) in Pallas, Northern Finland and found that eBC from the MAAP was a factor of five larger than the rBC mass from the SP2. Since the eBC/rBC mass ratio was practically constant during the campaign, they did not attribute this difference to the time dependent aerosol properties such as mixing state. The difference between eBC and rBC was explained with three possible reasons: the presence of brown carbon (not detected by the SP2 but detected by the MAAP), the limited SP2 size range, and the  $\text{MAC}_{\text{eBC}}$  value used (the default value:  $6.6 \text{ m}^2 \text{ g}^{-1}$ ). Slowik et al. (2007) compared an SP2 and a MAAP using well-characterized fractal soot particles. The default  $\text{MAC}_{\text{eBC}}$  value of  $6.6 \text{ m}^2 \text{ g}^{-1}$  at  $\lambda = 670 \text{ nm}$  was used to calculate eBC mass. For uncoated soot (OA/BC = 0.1 – 0.7), the eBC mass was  $\sim 50 \%$  higher than the rBC mass. This study also tested the instruments at higher OA/BC ratios by applying a coating with oleic acid and anthracene. Three different soot coatings were used: a very thin organic 10 nm coating, a 50 nm oleic acid coating and a 60 nm thick coating of anthracene. Thin organic coatings ( $\sim 10 \text{ nm}$ ) did not affect the instrument readings, while for the 50 nm coating the ratio of the eBC mass increased by  $\sim 20 \%$ . The difference between eBC and rBC for uncoated particles was attributed to the too low  $\text{MAC}_{\text{eBC}}$  while the difference between eBC and rBC for coated particles was explained by the absorption enhancement due to the lensing effect.

In the present study, the large discrepancy between eBC and rBC mass concentration could be the result of an interplay of causes, as highlighted by the previous studies: the principal one is the too low  $\text{MAC}_{\text{eBC}}$  value used to convert the absorption coefficient to eBC mass concentration. Moreover, the possible presence of species other than BC that absorb light at the MAAP wavelength, such as brown carbon (only a small interference is expected, except if a high fraction of tar balls was present, Pósfai et al., 2004; Adachi and Buseck, 2011). All these possible

causes lead to an eBC mass overestimation. With the assumption that the lensing effect was around a factor of 2 for the aged aerosol found at the Zeppelin site, then eBC/rBC mass ratio would become between 1.5 and 2. This means either that the lensing factor of 2 is too low, there were other factors responsible for the eBC/rBC discrepancy or a combination of both hypotheses.

Table 5.2: eBC/rBC mass ratio statistics with arithmetic mean, standard deviation (SD), median, 25<sup>th</sup> and 75<sup>th</sup> percentiles.

	Apr 19	May 19	Jun 19	Jul 19	Aug 19	Sep 19	Oct 19	Nov 19	Dec 19	Jan 20	Feb 20	Mar 20
$m_{\text{eBC}}/m_{\text{rBC}}$												
arithmetic												
mean	3.3	3.3	2.9	3.5	3.4	4.0	3.5	3.2	2.9	3.1	3.0	3.2
(SD)	(0.5)	(0.3)	(0.8)	(1.2)	(1.3)	(1.4)	(1.4)	(0.7)	(0.6)	(1.2)	(1.0)	(9.4)
$m_{\text{eBC}}/m_{\text{rBC}}$												
median	3.1	3.2	3.1	3.2	3.3	3.9	3.1	3.0	2.7	2.8	2.8	2.8
(25 <sup>th</sup> , 75 <sup>th</sup> )	(3.0, 3.4)	(3.1, 3.5)	(2.7, 3.4)	(2.9, 3.6)	(2.5, 3.9)	(3.3, 4.7)	(2.7, 3.7)	(2.7, 3.7)	(2.6, 3.1)	(2.6, 3.1)	(2.7, 3.0)	(2.7, 3.0)

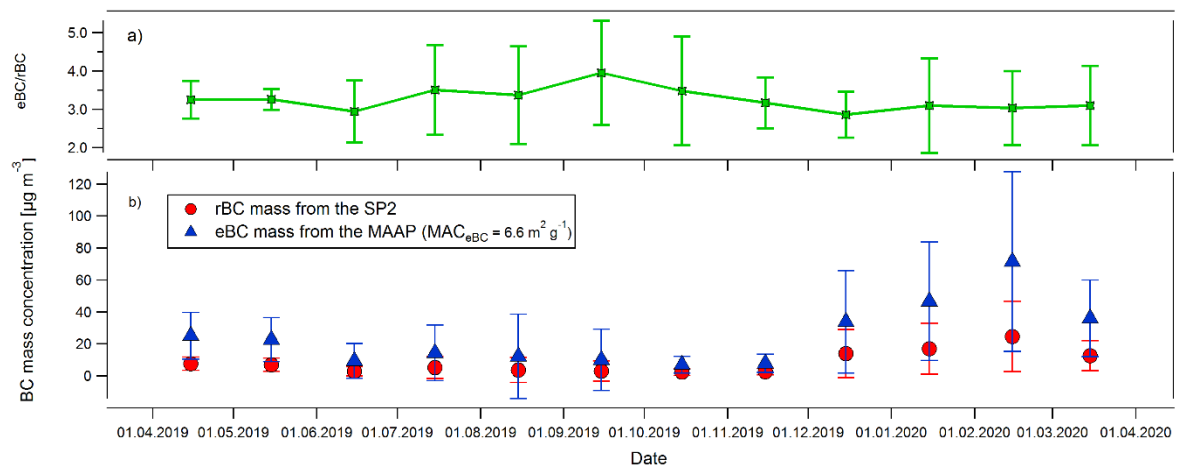


Figure 5.9: rBC/eBC mass concentration ratio (a) and  $m_{\text{rBC}}$  and  $m_{\text{eBC}}$  monthly statistics (arithmetic average  $\pm$  SD) (b).

As found in previous studies, also the limited SP2 detection range can lead to an underestimation of the rBC mass concentration. To investigate if the eBC-rBC mass discrepancy could be also partially explained by the large presence of coarse BC particles, which are detected by the MAAP but not totally by the SP2 due to its limited size detection range, we plotted the box plots of the eBC/rBC mass ratios for different  $\Delta m_{\text{meas-fit}}$  ranges, i.e.,  $\Delta m_{\text{meas-fit}} < 0.05$ ,  $0.05 < \Delta m_{\text{meas-fit}} < 0.10$ ,  $0.10 < \Delta m_{\text{meas-fit}} < 0.15$  and  $\Delta m_{\text{meas-fit}} > 0.15$ . The results in Fig. 5.10 show that the median eBC/rBC mass ratio increased from 3.0 for  $\Delta m_{\text{meas-fit}} < 0.05$  (Fig. 5.10a) to 4.0 for  $\Delta m_{\text{meas-fit}} > 0.15$  (Fig. 5.10d). This means that the presence of coarse BC particles increased the eBC/rBC ratio by roughly 33 %. The same result is also shown in a scatter plot of daily eBC vs rBC values colored by  $\Delta m_{\text{meas-fit}}$  in Fig.S5.7. Panels a) and b) illustrate the points with  $0.05 < \Delta m_{\text{meas-fit}} < \text{max}$  and  $0.05 < \Delta m_{\text{meas-fit}} < 0.2$ , respectively. In both these figures the bias between  $m_{\text{rBC}}$  and  $m_{\text{eBC}}$  shows a  $\Delta m_{\text{meas-fit}}$  dependence.

From these results, we can speculate that at high latitude sites dominated by mixed-phase or ice clouds (and possibly also at high altitude with similar cloud types), coarse BC particles not detected by the SP2 can play an important role in the discrepancy between the mass concentration measured by filter-based instruments and the rBC measured by the SP2. This, together with the low  $\text{MAC}_{\text{eBC}}$  coefficient used, and possibly the presence of other non-BC absorbing species can explain the large bias between  $m_{\text{eBC}}$  and  $m_{\text{rBC}}$  found here as well as in previous studies in Arctic areas (e. g. Raatikainen et al., 2015; Sharma et al., 2017).

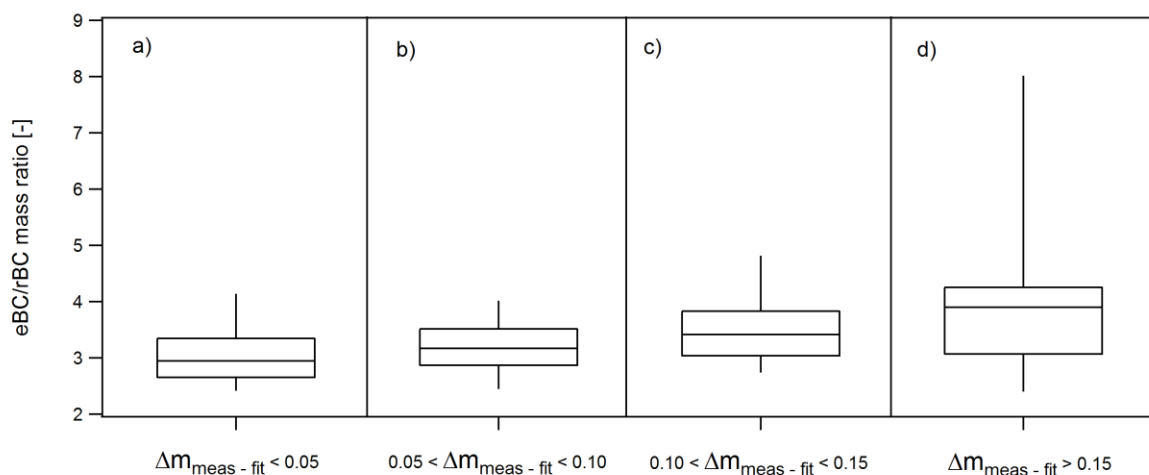


Figure 5.10: Box plots (showing 10<sup>th</sup>, 25<sup>th</sup>, 50<sup>th</sup>, 75<sup>th</sup> and 90<sup>th</sup> percentiles) of the eBC/rBC mass ratios for different intervals of  $\Delta m_{\text{meas}-\text{fit}}$ .

## 5.4 Conclusions

To answer the need of long-term and direct black carbon measurements in the Arctic, a year-long field campaign from April 2019 to March 2020 was conducted at the Zeppelin Observatory in Svalbard, Norway. Refractory black carbon mass concentration and size distribution measurements were measured with a Single Particle Soot Photometer Extended Range (SP2-XR).

Annual average and median rBC mass concentrations were 8.0 and 3.8 ng m<sup>-3</sup>, respectively, while monthly averages ranged from a maximum of 24.7 ng m<sup>-3</sup> in February, to a minimum of 2.3 ng m<sup>-3</sup> in October. The annual average modal diameter,  $D_{\text{rBC,mode}}$  of the rBC size distribution was 197 nm with monthly values between  $D_{\text{rBC,mode}} = 161$  nm in August and  $D_{\text{rBC,mode}} = 233$  nm in December.

Weighted BC concentration trajectory analyses were run for the Zeppelin altitude using 5 and 10 days back-trajectories. The outputs showed that from October to March, BC concentrations at Zeppelin were mainly influenced by source regions in Northern and Central Russia. From April to July the BC mass came from extreme northern areas: North Eurasia and Northern Canada while in August and September BC mass concentration originated mainly from North-East Europe.

Frequent occurrence of coarse BC particles with rBC mass equivalent diameter bigger than 300 nm was found, prevalently in June, September, October, and November. Their presence was quantified calculating the integrated difference between measured rBC mass size distribution and lognormal fit in the range 300-700 nm relative to total measured rBC mass. The presence of such large BC particles was corroborated by transmission electron microscopy analysis, which found coarse black carbon particles from 1 to several  $\mu\text{m}$  internally mixed predominantly with sulfate, seas salt and dust.

The CWT analysis was also run on the days that presented a prevalence of large BC cores. The back-trajectories were weighted with the relative contribution of BC coarse particles, in order not to influence the analysis by high concentration data. However, the scarcity of trajectories made it impossible to identify a BC source area. We found the relative contribution in mass of these coarse BC particles to be inversely proportional to the total rBC mass concentration. This supported two main hypotheses: the production of the large BC cores during atmospheric transport rather than direct emissions or the presence of a weak source of coarse BC particles that becomes relatively important if concentration of other transported BC is very low. In other words, it is more likely that these coarse BC particles were a local or regional product, possibly given by the interaction of BC with clouds during the atmospheric transport or when reaching Svalbard.

We did not find any correlation between coarse BC particles presence and number of hours in clouds. However, this does not exclude that some BC-cloud interaction process was taking place. Many more parameters such as the type of cloud and the meteorological parameters should be investigated before drawing any conclusion.

The rBC mass concentration was compared with the equivalent black carbon mass concentration measured with the MAAP. The monthly eBC/rBC mass ratio varied between 2.9 in June and December and 4.0 in September. The principal reason of such large discrepancy was the too low  $MAC_{BC}$  applied to convert the absorption measurement by the MAAP in equivalent black carbon mass. Moreover, the presence of coarse BC particles, detected by the MAAP and out of the SP2 detection range, was found to increase the eBC/rBC ratio by 33 %.

## Supplement of: Yearly characterization of the Arctic Black Carbon sampled on Zeppelin Observatory, Svalbard

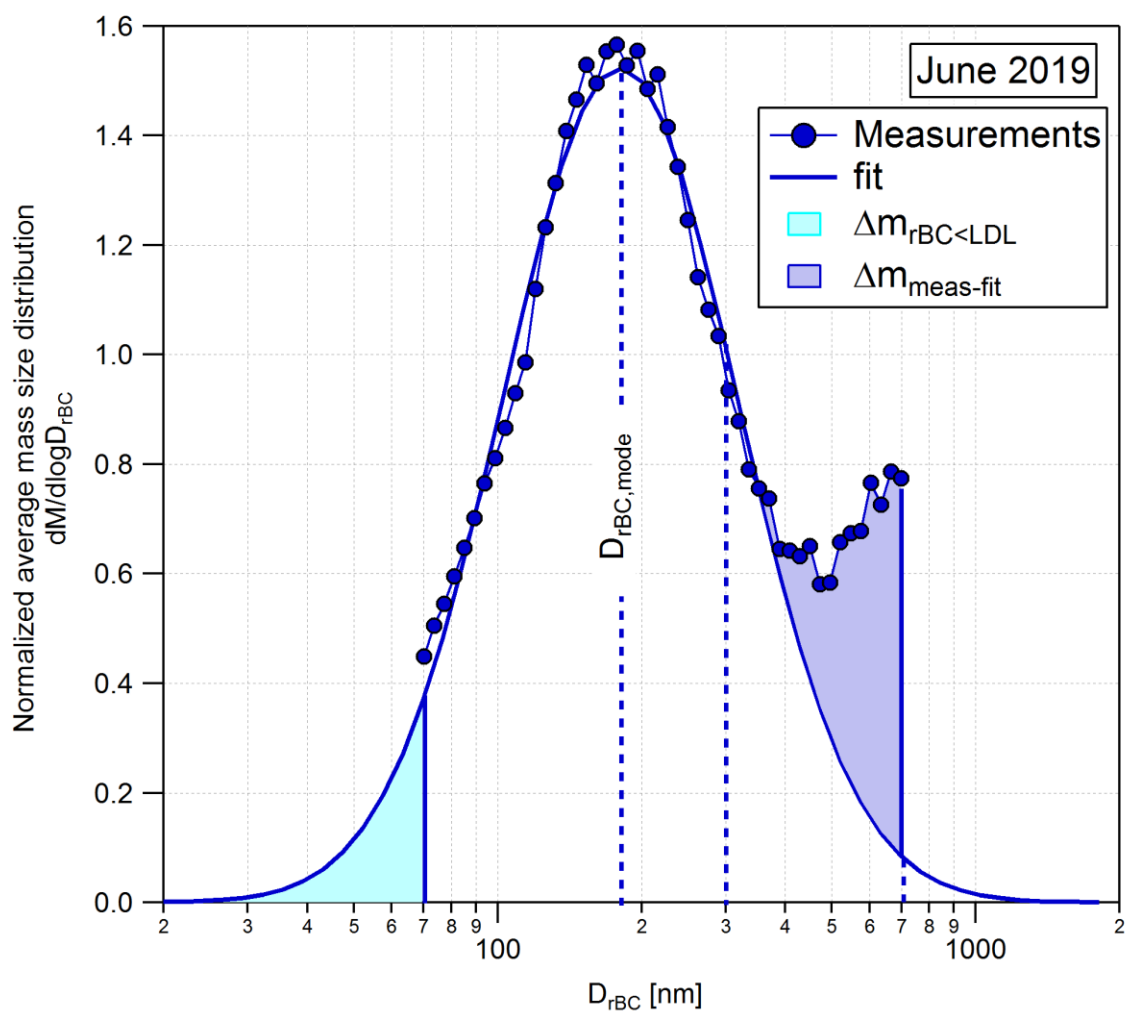


Figure S5.1: Measured rBC mass size distribution (blue full circles) as a function of rBC core mass equivalent diameter. The blue line represents the lognormal fit of the measurements. The integrated area of the cyan and blue shadings correspond to  $\Delta m_{rBC < LDL}$  and  $\Delta m_{meas-fit}$ .

July 30, 2019 (03:00-03:30) #1

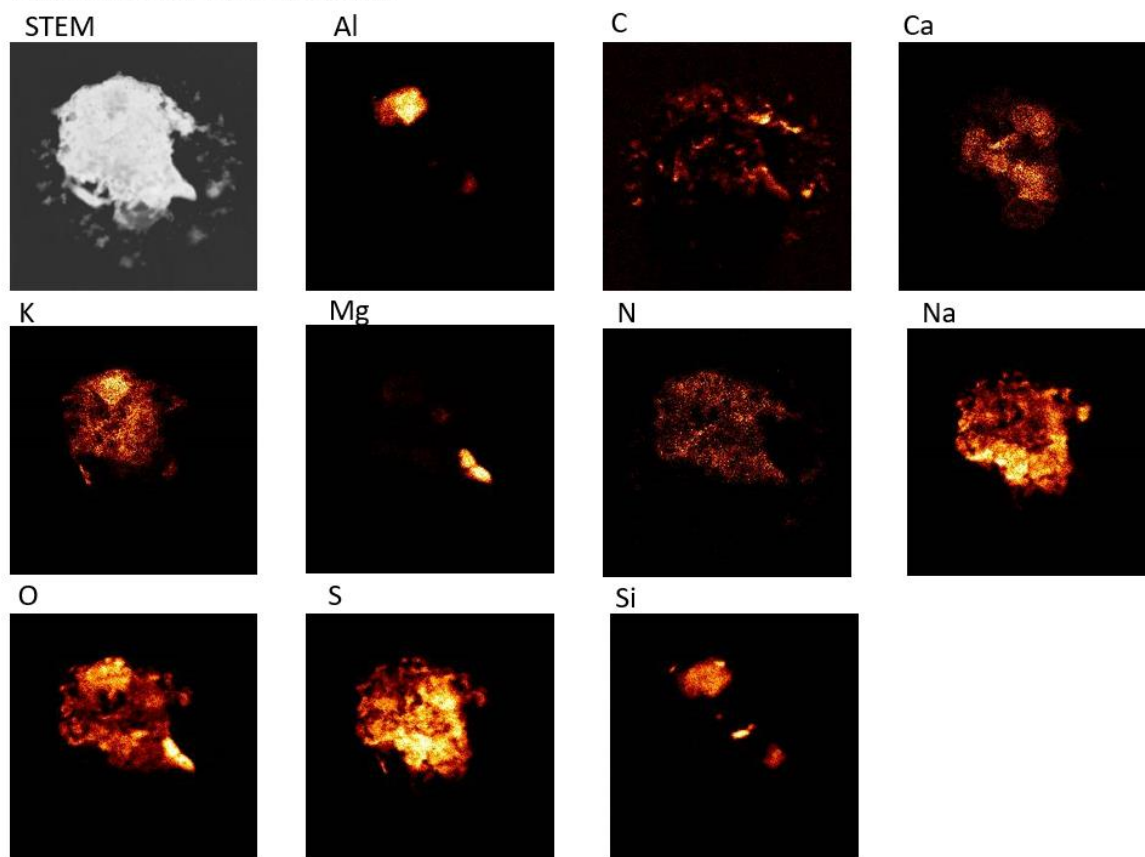


Figure S5.2: Element mapping with the EDS of the particle seen with the STEM (on the top left of the figure) on July 30 2019 between 03:00 and 03:30. Al, C, Ca, K, Mg, N, Na, O, S and Si are present in the particle. Colors indicate normalized EDS intensities for each element.



April 26, 2019 (16:22-16:52) #5

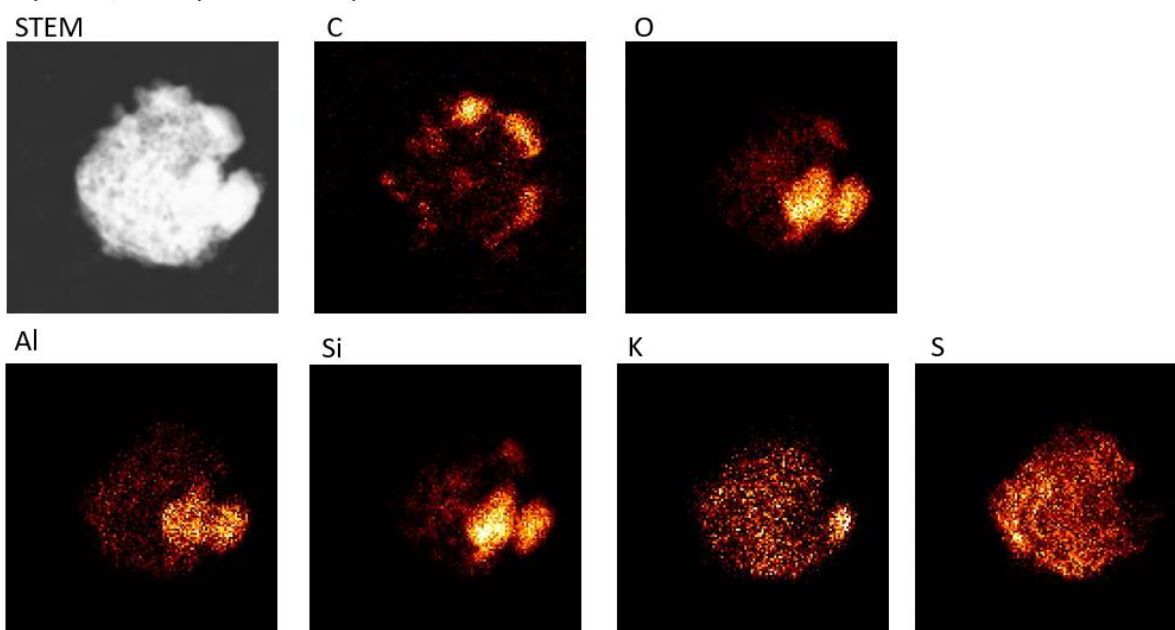


Figure S5.3: Element mapping with the EDS of the particle seen with the STEM (on the top left of the figure) on July 30 2019 between 03:00 and 03:30. Al, C, Ca, K, Mg, N, Na, O, S and Si are present in the particle. Colors indicate normalized EDS intensities for each element.

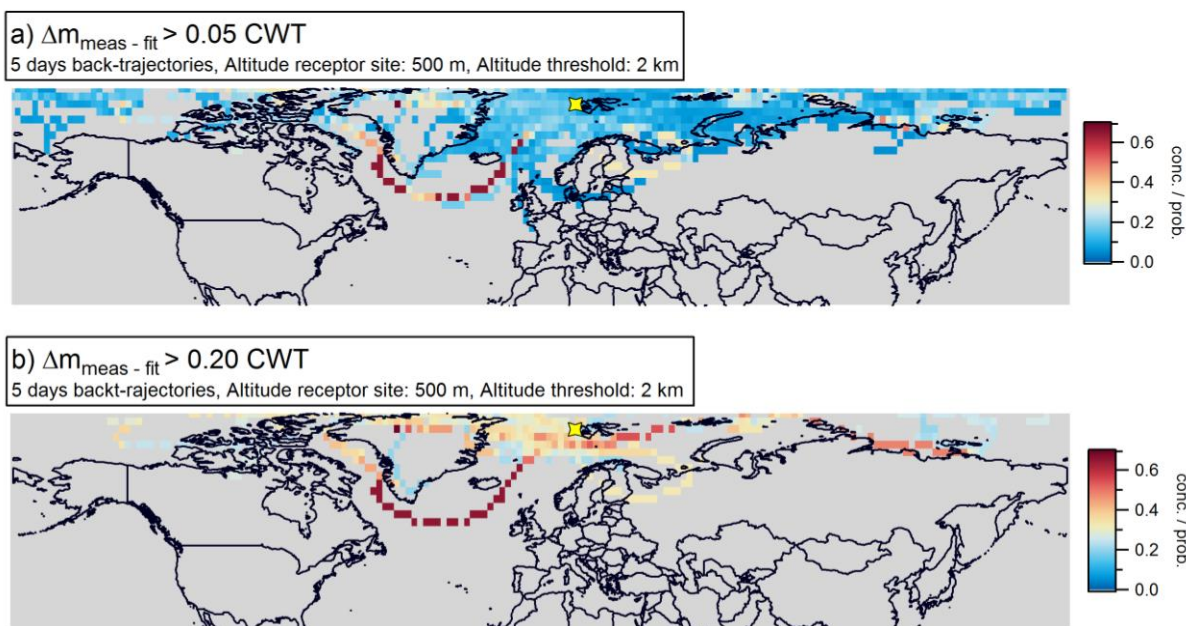


Figure S5.4: CWT analysis run on the relative contribution of the rBC mass between 300 nm and 700 nm per days with  $\Delta m_{\text{meas-fit}} > 0.05$  (a) and  $\Delta m_{\text{meas-fit}} > 0.20$  (b). 5-day back-trajectories with altitude threshold at 2 km, receptor site: Zeppelin Observatory and at least three trajectories crossing a cell.

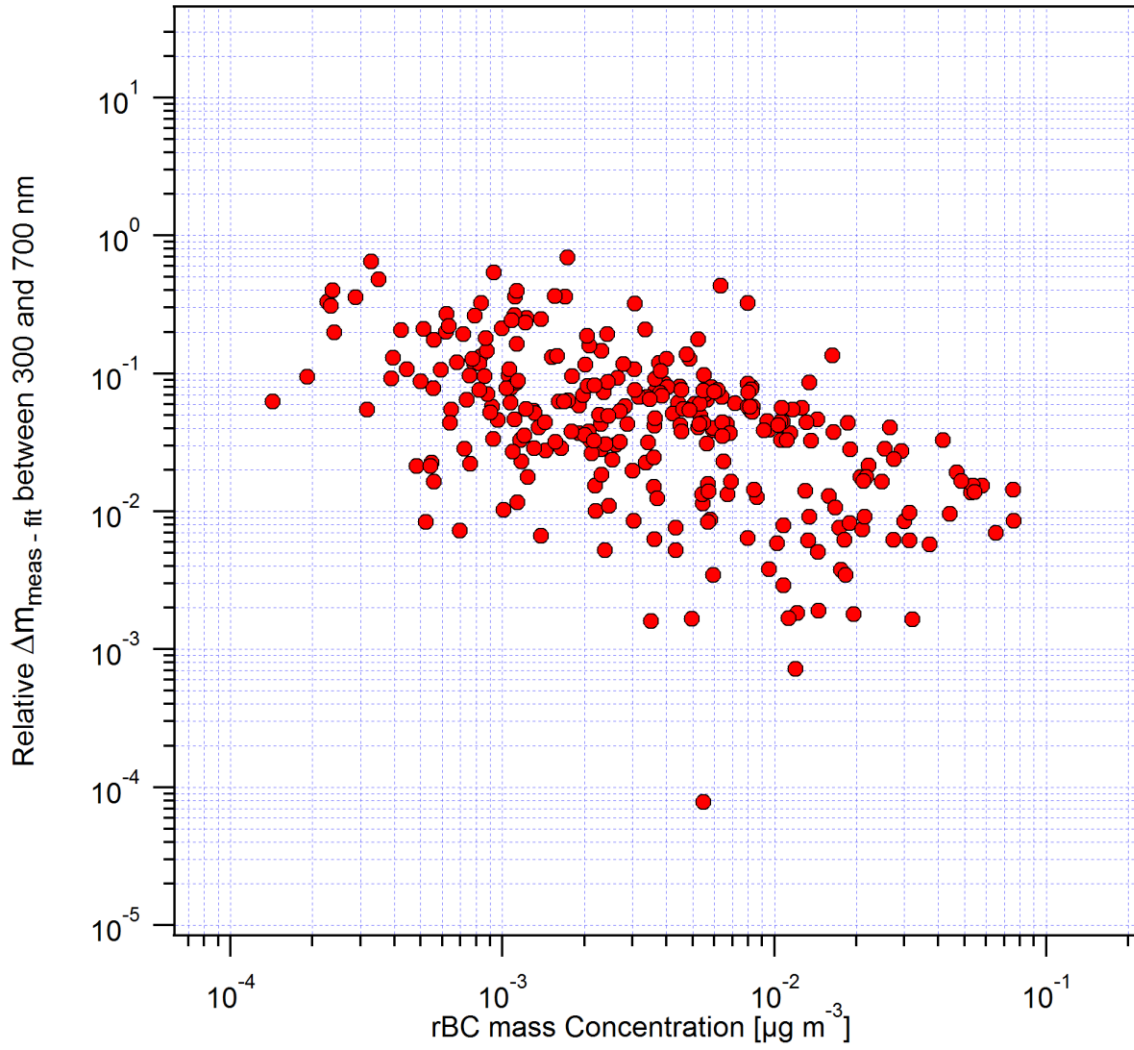


Figure S5.5: Scatter plot of  $\Delta m_{\text{meas}-\text{fit}}$  vs the total BC mass concentration at daily time resolution.

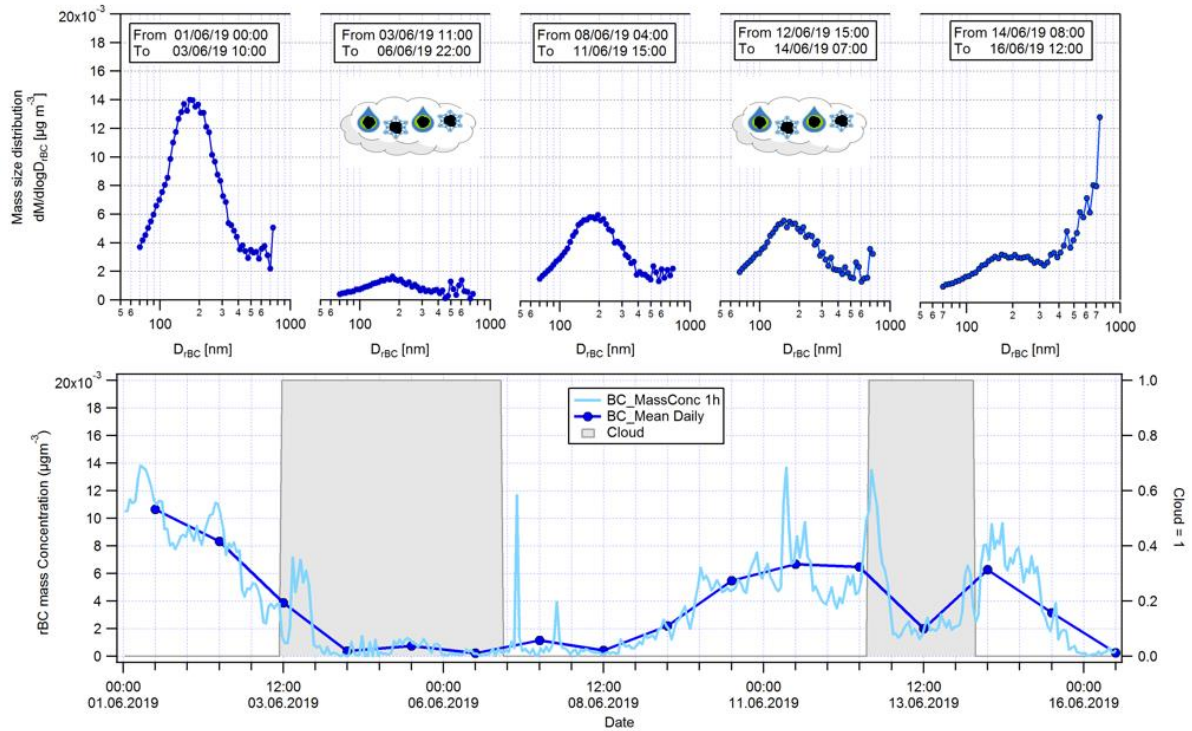


Figure S5.6: rBC size distributions (top) and rBC mass concentrations (1h and daily averages) (bottom) during a sequence of “in cloud – out of cloud” from 1 to 16 June 2019.

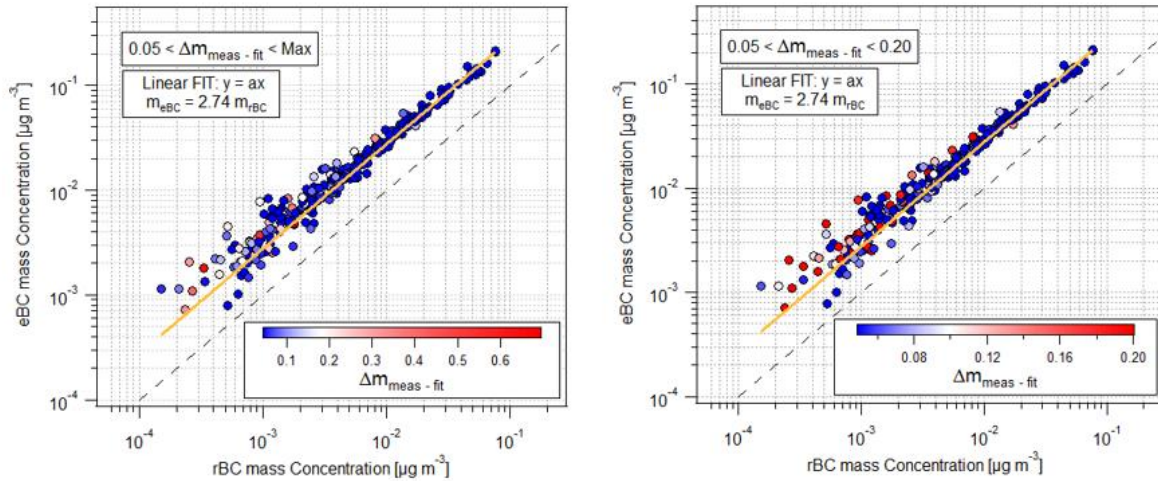


Figure S5.7: eBC-rBC mass scatter plot. The points are colored by  $\Delta m_{\text{meas-fit}}$ . Data with  $0.05 < \Delta m_{\text{meas-fit}} < \text{Max}$  are presented on the left panel, and data with  $0.05 < \Delta m_{\text{meas-fit}} < 0.20$  are presented on the right panel.

## Chapter 6: Conclusions and perspectives

Black carbon (BC) has a great impact on the Earth's climate. However, the lack of a deep knowledge on its properties leads to a large uncertainty in the estimation of its global radiative forcing. The motivation of this thesis was to contribute to reducing the uncertainties related to BC radiative forcing, filling some gaps present in black carbon science, with the following investigations:

- intercomparison measurements of BC mass concentration performed with the three most used techniques: filter based thermal-optical evolved gas analysis; laser induced incandescence and aerosol light absorption based methods. These investigations were done with a large intercomparison study between EC and rBC across four European background sites and with a yearly intercomparison study between eBC and rBC in the Arctic;
- characterization of BC properties with a month-long campaign in the very polluted area of the Po Valley and with a year-long campaign in a very clean environment, in the Arctic;
- investigation of the variability of  $MAC_{BC}$  as a function of mixing state, BC particle size and BC mass measurement technique in the Po Valley where both fresh and aged BC were sampled.

Hereafter the major findings of this thesis work are summarized:

- 1) EC and rBC mass concentration measurements from four field campaigns performed across several European sites (Paris, Bologna, Cabauw and Melpitz) were collated and examined to identify the similarities and differences between BC mass concentrations measured by the two techniques. All EC concentration measurements were performed with the EUSAAR-2 thermal protocol, with the TOT technique on quartz filters sampled with high volumes with a  $PM_{2.5}$  cut-off (except for the Cabauw campaign during which  $PM_{10}$  was sampled). All rBC mass concentration measurements were performed with three different SP2s, calibrated with the same standard material, fullerene soot. The two methods provide an operationally defined measure of atmospheric BC mass in good overall agreement. However, systematic discrepancies up to  $\sim\pm 50\%$  were observed at some sites. The median of the observed rBC to EC mass ratios for the whole dataset was 0.92, with a GSD of 1.50. The median ratio varied from 0.53 to 1.29 from campaign to campaign. Potential reasons for the discrepancies were: source-specific SP2 response, the possible presence of an additional mode of small BC cores below the LDL of the SP2, differences in the upper cut-off of the SP2 and the inlet line for the EC sampling, or various uncertainties and interferences from co-emitted species in the EC mass measurement. The discrepancy between rBC and EC appears to be systematically related to the BC source, i.e. traffic versus wood and/or coal burning. However, it was not possible to identify causalities behind this trend due to potential cross-correlations between several aerosol and BC properties relevant for potential biases.

A yearly intercomparison between eBC and rBC mass concentration measurements was performed at Zeppelin Observatory, in Svalbard, Norway, from April 2019 to March 2020. The eBC mass concentration measurements were performed with a multi-angle absorption photometer, using a  $MAC_{BC}$  of  $6.6 \text{ m}^2 \text{ g}^{-1}$  to convert the light absorption to eBC mass concentration. The rBC mass measurements were performed with an SP2-XR, calibrated with fullerene soot. The monthly eBC/rBC mass ratio varied between a minimum of 2.9 in June and December and a maximum of 4.0 in September. Large overestimation of the eBC mass concentration is expected because of the assumed  $MAC_{BC}$  (too low for measurement in the Arctic, where internally mixed BC is sampled). The presence of light-absorbing materials other than BC, like brown carbon (if large presence of tar balls is present) might cause eBC overestimation. Cause of this discrepancy was found to be the limited detection range of the SP2-XR, which did not allow the total detection of coarse BC particles. Indeed, the presence of coarse BC particles, detected by the MAAP and out of the SP2 detection range, was found to increase the eBC/rBC ratio by 33 %.

**Recommendations and perspectives:** the use of a direct BC measurement is always preferred and suggested in order to avoid the choice of a proper  $MAC_{BC}$  value to convert light absorption to eBC mass. However, both EC and rBC based techniques have their uncertainties and limitations. The thermal–optical evolved gas analysis is mainly influenced by pyrolysis and by the presence of inorganics and light-absorbing organics such as brown carbon on the filter. Moreover, this technique is prohibitive at low BC concentration sites because of the long integration times needed. On the contrary, the SP2 is a very valuable tool to use in very clean environments because it has no lower number concentration detection limit. This instrument gives also information on other BC properties such as the rBC mass and number size distributions and mixing state at single particle level. However, with this work we demonstrated that its limited detection range can sometimes be an important limit towards a correct rBC mass quantification. An absolutely accurate mass concentration measurement is still a limit of the aerosol techniques in general. The recommendation for the field campaigns is to adopt the most suitable technique based on the level of accuracy and information needed and based on the typology of the measurement site.

- 2) The spatio–temporal variability of physical and optical properties of freshly emitted and aged black carbon particles was investigated during summertime, in July 2017, in the Po Valley, Italy with stationary and mobile measurements. The diurnal variability in the physical and optical properties of BC particles was investigated with stationary measurements at a sub–urban site of Bologna. All the properties studied showed a strong influence of the PBL dynamics and the meteorology. For example, the  $MAC_{BC}$  value and AAE changed only when the wind direction drastically changed. For instance, the average mass absorption cross–section of refractory BC at 637 nm ( $MAC_{rBC}^{637\text{ nm}}$ ) increased from 12.2 to 16.0  $m^2\ g^{-1}$  based on SP2 measurements, and from 8.1 to 11.5  $m^2\ g^{-1}$  based on thermal–optical elemental carbon (EC) measurements ( $MAC_{EC}^{637\text{ nm}}$ ); the minima occurred in the morning when fresh traffic emissions dominated the aerosol loading, and the maxima occurred in the afternoon when the PBL height increased and aged particles dominated the BC mass. The spatial variability of BC optical and physical properties over the Po Valley was investigated with mobile measurements. The focus was set on the difference in properties between freshly emitted BC particles, sampled on the highway, and aged BC particles, sampled on provincial roads. The  $MAC_{rBC}^{637\text{ nm}}$  values increased by 39 % from the highway to the provincial roads. The observation of the average rBC mass size distributions ( $108\text{ nm} < D_{rBC,mode} < 115\text{ nm}$ ) and the absorption Ångström exponent (AAE  $\approx 1$ ) supported the hypothesis that mixing of freshly emitted BC with aged background BC was the dominant process responsible for this  $MAC_{rBC}^{637\text{ nm}}$  difference. Both diurnal and spatial observations gave evidence that the Po Valley, in summer, contains a 'pool' of aged BC particles into which fresh BC emissions are mixed on short temporal and spatial scales.

The temporal variability of refractory black carbon mass concentration and rBC mass size distribution was investigated in the Arctic at the Zeppelin Observatory in Svalbard, Norway, during a year-long field campaign from April 2019 to March 2020 with the use of an SP2-XR. Annual average and median rBC mass concentrations were 8.0 and 3.8  $ng\ m^{-3}$ , respectively, while monthly averages ranged from a maximum of 24.7  $ng\ m^{-3}$  in February, to a minimum of 2.3  $ng\ m^{-3}$  in October. The annual average modal diameter,  $D_{rBC,mode}$  of the rBC size distribution was 197 nm with monthly values between  $D_{rBC,mode}= 161$  nm in August and  $D_{rBC,mode}= 233$  in December. Weighted BC concentration trajectory analyses showed that from October to March, BC concentrations at Zeppelin were mainly influenced by source regions in northern and central Russia. From April to July the BC mass came from extreme Northern areas: North Eurasia and Northern Canada while in August and September the BC mass concentration originated mainly from North-Eastern Europe. Unexpected but frequent occurrence of large BC cores with rBC mass equivalent diameter bigger than 300 nm were found, prevalently in June, September, October and November. Their presence was quantified calculating the integrated difference between measured rBC mass size distribution and lognormal fit in the range 300-700 nm relative to total measured rBC mass. Large BC particles internally mixed with sulfate, sea salt and dust were found by transmission electron microscopy analysis. The relative contribution in mass of these coarse BC particles was found to be inversely proportional to the total rBC mass concentration. This supported two main hypothesis: the production of the large BC cores during atmospheric transport rather than direct emissions or the presence of a weak source of coarse BC particles that becomes

relatively important if concentration of other transported BC is very low. In other words, it is more likely that these coarse BC particles were a local or regional product, possibly given by the interaction of BC with clouds during the transport or when reached Svalbard. We did not find any correlation between coarse BC particles and number of hours in cloud, however, we could not exclude that some BC-cloud interaction process was taking place.

**Recommendations and perspectives:** a more complete characterization and longer time series of black carbon properties are still required worldwide in order to improve the accuracy of global aerosol models. This need is even stronger in the Arctic, where these measurements are scarce. Our study revealed a distinctive rBC mass size distribution in the Arctic, with marked presence of coarse BC particles. Future studies should focus on understanding the source of these particles or the mechanisms behind their formation.

- 3) The variability of  $MAC_{BC}$  as a function of mixing state, BC particle size and BC mass measurement technique was investigated in the Po Valley where both fresh and aged BC were sampled. As a proxy for the mixing state, the number fraction of thickly coated particles was used. The small variation of BC core diameters found during the campaign was not able to explain the much greater variability in the observed  $MAC_{BC}$  values, which was better explained with the variability of the BC mixing state. This result provides experimental confirmation that the lensing effect can substantially increase the MAC of black carbon by up to a factor of almost 2. However, while this study provides clear evidence of BC mixing state effects on  $MAC_{BC}$ , the observed  $MAC_{BC}$  values remain tainted with considerable uncertainty due to the lack of absolutely accurate mass measurement techniques. Indeed, in this study, the  $MAC_{BC}$  values based on rBC mass concentrations were 35 % higher than those based on EC mass concentrations.

**Recommendations and perspectives:** this result confirmed that lensing effects in ambient measurements can increase the MAC of black carbon by up to a factor of 2. However, an accurate absolute measurement of the  $MAC_{BC}$  value is not possible given the uncertainty related to the BC mass concentration. Future studies should focus on addressing the effects that the coating composition would have in the  $MAC_{BC}$  variability. Moreover, the behavior of  $MAC_{BC}$  as a function of the particle morphology remains an experimental challenge.

## References

- Aakko-Saksa, P., Koponen, P., Aurela, M., Vesala, H., Piimäkorpi, P., Murtonen, T., Sippula, O., Koponen, H., Karjalainen, P., Kuittinen, N., Panteliadis, P., Rönkkö, T. and Timonen, H.: Considerations in analysing elemental carbon from marine engine exhaust using residual, distillate and biofuels, *J. Aerosol Sci.*, 126, 191–204, doi:10.1016/j.jaerosci.2018.09.005, 2018.
- Adachi, K., Chung, S. H. and Buseck, P. R.: Shapes of soot aerosol particles and implications for their effects on climate, *J. Geophys. Res. Atmos.*, 115(D15), D15206, doi:10.1029/2009JD012868, 2010.
- Adachi, K. and Buseck, P. R.: Atmospheric tar balls from biomass burning in Mexico, *J. Geophys. Res. Atmos.*, 116(D5), doi:10.1029/2010JD015102, 2011.
- Adachi, K., Sedlacek, A. J., Kleinman, L., Springston, S. R., Wang, J., Chand, D., Hubbe, J. M., Shilling, J. E., Onasch, T. B., Kinase, T., Sakata, K., Takahashi, Y. and Buseck, P. R.: Spherical tarball particles form through rapid chemical and physical changes of organic matter in biomass-burning smoke, *Proc. Natl. Acad. Sci.*, 116(39), 19336–19341, doi:10.1073/pnas.1900129116, 2019.
- Aiken, A. C., Salcedo, D., Cubison, M. J., Huffman, J. A., DeCarlo, P. F., Ulbrich, I. M., Docherty, K. S., Sueper, D., Kimmel, J. R., Worsnop, D. R., Trimborn, A., Northway, M., Stone, E. A., Schauer, J. J., Volkamer, R. M., Fortner, E., Foy, B. de, Wang, J., Laskin, A., Shutthanandan, V., Zheng, J., Zhang, R., Gaffney, J., Marley, N. A., Paredes-Miranda, G., Arnott, W. P., Molina, L. T., Sosa, G. and Jimenez, J. L.: Mexico City aerosol analysis during MILAGRO using high resolution aerosol mass spectrometry at the urban supersite (T0) – Part 1: Fine particle composition and organic source apportionment, *Atmos. Chem. Phys.*, 9(17), 6633–6653, doi:https://doi.org/10.5194/acp-9-6633-2009, 2009.
- Albrecht, B. A.: Aerosols, Cloud Microphysics, and Fractional Cloudiness, *Science*, 245(4923), 1227–1230, doi:10.1126/science.245.4923.1227, 1989.
- Altstädter, B., Platis, A., Jähn, M., Baars, H., Lücknerath, J., Held, A., Lampert, A., Bange, J., Hermann, M. and Wehner, B.: Airborne observations of newly formed boundary layer aerosol particles under cloudy conditions, *Atmos. Chem. Phys.*, 18(11), 8249–8264, doi:10.5194/acp-18-8249-2018, 2018.
- Ammerlaan, B. A. J., Jedynska, A. D., Henzing, J. S. and Holzinger, R.: On a possible bias in elemental carbon measurements with the Sunset thermal/optical carbon analyser caused by unstable laser signal, *Atmos. Environ.*, 122, 571–576, doi:10.1016/j.atmosenv.2015.09.076, 2015.
- Andreae, M. O. and Gelencsér, A.: Black carbon or brown carbon? The nature of light-absorbing carbonaceous aerosols, *Atmos. Chem. Phys.*, 6(10), 3131–3148, doi:https://doi.org/10.5194/acp-6-3131-2006, 2006.
- Andreae, M. O. and Rosenfeld, D.: Aerosol–cloud–precipitation interactions. Part 1. The nature and sources of cloud-active aerosols, *Earth-Sci. Rev.*, 89(1–2), 13–41, doi:10.1016/j.earscirev.2008.03.001, 2008.
- Andrews, E., Ogren, J. A., Bonasoni, P., Marinoni, A., Cuevas, E., Rodríguez, S., Sun, J. Y., Jaffe, D. A., Fischer, E. V., Baltensperger, U., Weingartner, E., Coen, M. C., Sharma, S., Macdonald, A. M., Leaitch, W. R., Lin, N.-H., Laj, P., Arsov, T., Kalapov, I., Jefferson, A. and Sheridan, P.: Climatology of aerosol radiative properties in the free troposphere, *Atmos. Res.*, 102(4), 365–393, doi:10.1016/j.atmosres.2011.08.017, 2011.
- Appel, B. R., Tokiwa, Y., Hsu, J., Kothny, E. L. and Hahn, E.: Visibility as related to atmospheric aerosol constituents, *Atmos. Environ.*, 19(9), 1525–1534, doi:10.1016/0004-6981(85)90290-2, 1985.
- Arnott, W. P., Moosmüller, H., Sheridan, P. J., Ogren, J. A., Raspert, R., Slaton, W. V., Hand, J. L., Kreidenweis, S. M. and Collett Jr., J. L.: Photoacoustic and filter-based ambient aerosol light absorption measurements: Instrument comparisons and the role of relative humidity, *J. Geophys. Res. Atmos.*, 108(D1), doi:10.1029/2002JD002165, 2003.
- Backman, J., Schmeisser, L., Virkkula, A., Ogren, J. A., Asmi, E., Starkweather, S., Sharma, S., Eleftheriadis, K., Uttal, T., Jefferson, A., Bergin, M., Makshtas, A., Tunved, P. and Fiebig, M.: On Aethalometer measurement uncertainties and an instrument correction factor for the Arctic, *Atmos. Meas. Tech.*, 10(12), 5039–5062, doi:10.5194/amt-10-5039-2017, 2017.

Barrie, L. A. and Schemenauer, R. S.: Pollutant wet deposition mechanisms in precipitation and fog water, *Water, Air, Soil Pollut.*, 30(1), 91–104, doi:10.1007/BF00305178, 1986.

Bauer, S. E., Menon, S., Koch, D., Bond, T. C. and Tsigaridis, K.: A global modeling study on carbonaceous aerosol microphysical characteristics and radiative effects, *Atmos. Chem. Phys.*, 10(15), 7439–7456, doi:10.5194/acp-10-7439-2010, 2010.

Baumgardner, D., Popovicheva, O., Allan, J., Bernardoni, V., Cao, J., Cavalli, F., Cozic, J., Diapouli, E., Eleftheriadis, K., Genberg, P. J., Gonzalez, C., Gysel, M., John, A., Kirchstetter, T. W., Kuhlbusch, T. A. J., Laborde, M., Lack, D., Muller, T., Niessner, R., Petzold, A., Piazzalunga, A., Putaud, J. P., Schwarz, J., Sheridan, P., Subramanian, R., Swietlicki, E., Valli, G., Vecchi, R. and Viana, M.: Soot reference materials for instrument calibration and intercomparisons: A workshop summary with recommendations, *Atmos. Meas. Tech.*, 5, 1869–1887, doi:10.5194/amt-5-1869-2012, 2012.

Bautista, A. T., Pabroa, P. C. B., Santos, F. L., Quirit, L. L., Asis, J. L. B., Dy, M. A. K. and Martinez, J. P. G.: Intercomparison between NIOSH, IMPROVE\_A, and EUSAAR\_2 protocols: Finding an optimal thermal–optical protocol for Philippines OC/EC samples, *Atmos. Pollut. Res.*, 6(2), 334–342, doi:10.5094/APR.2015.037, 2015.

Beine, H. J., Argentini, S., Maurizi, A., Mastrantonio, G. and Viola, A.: The local wind field at Ny-Å lesund and the Zeppelin mountain at Svalbard, *Meteorol. Atmos. Phys.*, 78(1), 107–113, doi:10.1007/s007030170009, 2001.

Bereiter, B., Eggleston, S., Schmitt, J., Nehrbass-Ahles, C., Stocker, T. F., Fischer, H., Kipfstuhl, S. and Chappellaz, J.: Revision of the EPICA Dome C CO<sub>2</sub> record from 800 to 600 kyr before present: Analytical bias in the EDC CO<sub>2</sub> record, *Geophys. Res. Lett.*, 42(2), 542–549, doi:10.1002/2014GL061957, 2015.

Bergeron, T.: Über die dreidimensional verknüpfende 397 Wetteranalyse., *Geophys. Norv.*, 1928.

Bernardoni, V., Vecchi, R., Valli, G., Piazzalunga, A. and Fermo, P.: PM<sub>10</sub> source apportionment in Milan (Italy) using time-resolved data, *Sci. Total Environ.*, 409(22), 4788–4795, doi:10.1016/j.scitotenv.2011.07.048, 2011.

Bernardoni, V., Pileci, R. E., Caponi, L. and Massabò, D.: The multi-wavelength absorption analyzer (MWAA) model as a tool for source and component apportionment based on aerosol absorption properties: application to samples collected in different environments, *Atmosphere*, 8(11), 218, doi:10.3390/atmos8110218, 2017.

Bhandari, J., China, S., Chandrakar, K. K., Kinney, G., Cantrell, W., Shaw, R. A., Mazzoleni, L. R., Giroto, G., Sharma, N., Gorkowski, K., Gilardoni, S., Decesari, S., Facchini, M. C., Zanca, N., Pavese, G., Esposito, F., Dubey, M. K., Aiken, A. C., Chakrabarty, R. K., Moosmüller, H., Onasch, T. B., Zaveri, R. A., Scarnato, B. V., Fialho, P. and Mazzoleni, C.: Extensive Soot Compaction by Cloud Processing from Laboratory and Field Observations, *Sci. Rep.*, 9(1), 11824, doi:10.1038/s41598-019-48143-y, 2019.

Bigi, A., Bianchi, F., De Gennaro, G., Di Gilio, A., Fermo, P., Ghermandi, G., Prévôt, A. S. H., Urbani, M., Valli, G., Vecchi, R. and Piazzalunga, A.: Hourly composition of gas and particle phase pollutants at a central urban background site in Milan, Italy, *Atmos. Res.*, 186, 83–94, doi:10.1016/j.atmosres.2016.10.025, 2017.

Birch, M. E. and Cary, R. A.: Elemental carbon-based method for monitoring occupational exposures to particulate diesel exhaust, *Aerosol Sci. Technol.*, 25(3), 221–241, doi:10.1080/02786829608965393, 1996.

Birch, M., Dahmann, D. and Fricke, H.-H.: Comparison of two carbon analysis methods for monitoring diesel particulate levels in mines, *J. Environ. Monit.*, 1(6), 541–544, doi:10.1039/A905204F, 1999.

Bisiaux, M., Edwards, R., McConnell, J., Curran, M., Van Ommen, T., Smith, A., Neumann, T., Pasteris, D., Penner, J. and Taylor, K.: Large scale changes in 20th century black carbon deposition to Antarctica, *Atmos. Chem. Phys.*, 12, 4107–4115, doi:10.5194/acp-12-4107-2012, 2012.

Blanchet, J.-P.: Toward estimation of climatic effects due to arctic aerosols, *Atmos. Environ.*, 23(11), 2609–2625, doi:10.1016/0004-6981(89)90269-2, 1989.

Bohren, C. F. and Huffman, D. R.: *Absorption and scattering of light by small particles*, Wiley., 1983.



Bonazza, A., De Nuntiiis, P., Mandrioli, P. and Sabbioni, C.: Aerosol Impact on Cultural Heritage: Deterioration Processes and Strategies for Preventive Conservation, in *Atmospheric Aerosols*, edited by C. Tomasi, S. Fuzzi, and A. Kokhanovsky, pp. 645–670, Wiley-VCH Verlag GmbH & Co. KGaA, Weinheim, Germany., 2016.

Bond, T. C., Anderson, T. L. and Campbell, D.: Calibration and Intercomparison of Filter-Based Measurements of Visible Light Absorption by Aerosols, *Aerosol Sci. Technol.*, 30(6), 582–600, doi:10.1080/027868299304435, 1999.

Bond, T. C. and Bergström, R. W.: Light absorption by carbonaceous particles: An investigative review, *Aerosol Sci. Technol.*, 40(1), 27–67, doi:10.1080/02786820500421521, 2006.

Bond, T. C., Habib, G. and Bergstrom, R. W.: Limitations in the enhancement of visible light absorption due to mixing state, *J. Geophys. Res. Atmos.*, 111(D20), doi:10.1029/2006JD007315, 2006.

Bond, T. C., Doherty, S. J., Fahey, D. W., Forster, P. M., Berntsen, T., DeAngelo, B. J., Flanner, M. G., Ghan, S., Kärcher, B., Koch, D., Kinne, S., Kondo, Y., Quinn, P. K., Sarofim, M. C., Schultz, M. G., Schulz, M., Venkataraman, C., Zhang, H., Zhang, S., Bellouin, N., Guttikunda, S. K., Hopke, P. K., Jacobson, M. Z., Kaiser, J. W., Klimont, Z., Lohmann, U., Schwarz, J. P., Shindell, D., Storelvmo, T., Warren, S. G. and Zender, C. S.: Bounding the role of black carbon in the climate system: A scientific assessment, *J. Geophys. Res. Atmos.*, 118(11), 5380–5552, doi:10.1002/jgrd.50171, 2013.

Briggs, N. L. and Long, C. M.: Critical review of black carbon and elemental carbon source apportionment in Europe and the United States, *Atmos. Environ.*, 144, 409–427, doi:10.1016/j.atmosenv.2016.09.002, 2016.

Bucci, S., Cristofanelli, P., Decesari, S., Marinoni, A., Sandrini, S., Größ, J., Wiedensohler, A., Di Marco, C. F., Nemitz, E., Cairo, F., Di Liberto, L. and Fierli, F.: Vertical distribution of aerosol optical properties in the Po Valley during the 2012 summer campaigns, *Atmos. Chem. Phys.*, 18(8), 5371–5389, doi:10.5194/acp-18-5371-2018, 2018.

Bueno, P. A., Havey, D. K., Mulholland, G. W., Hodges, J. T., Gillis, K. A., Dickerson, R. R. and Zachariah, M. R.: Photoacoustic Measurements of Amplification of the Absorption Cross Section for Coated Soot Aerosols, *Aerosol Sci. Technol.*, 45(10), 1217–1230, doi:10.1080/02786826.2011.587477, 2011.

Bukowiecki, N., Dommen, J., Prévôt, A. S. H., Richter, R., Weingartner, E. and Baltensperger, U.: A mobile pollutant measurement laboratory—measuring gas phase and aerosol ambient concentrations with high spatial and temporal resolution, *Atmos. Environ.*, 36, 5569–5579, doi:10.1016/S1352-2310(02)00694-5, 2002.

Burr, D. W., Daun, K., Thomson, K. A. and Smallwood, G.: Optimization of measurement angles for soot aggregate sizing by elastic light scattering, through design-of-experiment theory, *J. Quant. Spectrosc. Radiat. Transf.*, 113, 355–365, doi:10.1016/j.jqsrt.2011.12.004, 2012.

Burtscher, H., Baltensperger, U., Bukowiecki, N., Cohn, P., Hüglin, C., Mohr, M., Matter, U., Nyeki, S., Schmatloch, V., Streit, N. and Weingartner, E.: Separation of volatile and non-volatile aerosol fractions by thermodesorption: instrumental development and applications, *J. Aerosol Sci.*, 32(4), 427–442, doi:10.1016/S0021-8502(00)00089-6, 2001.

Calvo, A. I., Alves, C., Castro, A., Pont, V., Vicente, A. M. and Fraile, R.: Research on aerosol sources and chemical composition: Past, current and emerging issues, *Atmos. Res.*, 120–121(Supplement C), 1–28, <https://doi.org/10.1016/j.atmosres.2012.09.021>, 2013.

Canonaco, F., Crippa, M., Slowik, J. G., Baltensperger, U. and Prévôt, A. S. H.: SoFi, an IGOR-based interface for the efficient use of the generalized multilinear engine (ME-2) for the source apportionment: ME-2 application to aerosol mass spectrometer data, *Atmos. Meas. Tech.*, 6(12), 3649–3661, doi:10.5194/amt-6-3649-2013, 2013.

Cao, J.: The Importance of Aerosols in the Earth System: Science and Engineering Perspectives, *Aerosol Sci. and Eng.*, 1, 1-6, doi:10.1007/s41810-017-0005-1, 2017.

Cappa, C. D., Zhang, X., Russell, L. M., Collier, S., Lee, A. K. Y., Chen, C.-L., Betha, R., Chen, S., Liu, J., Price, D. J., Sanchez, K. J., McMeeking, G. R., Williams, L. R., Onasch, T. B., Worsnop, D. R., Abbatt, J. and Zhang, Q.: Light absorption by ambient black and brown carbon and its dependence on black carbon coating state for two

California, USA, cities in winter and summer, *J. Geophys. Res. Atmos.*, 124(3), 1550–1577, doi:10.1029/2018JD029501, 2019.

Cavalli, F., Viana, M., Yttri, K. E., Genberg, J. and Putaud, J.-P.: Toward a standardised thermal-optical protocol for measuring atmospheric organic and elemental carbon: the EUSAAR protocol, *Atmos. Meas. Tech.*, 3(1), 79–89, doi:10.5194/amt-3-79-2010, 2010.

Cavalli, F., Alastuey, A., Areskoug, H., Ceburnis, D., Cech, J., Genberg, J., Harrison, R. M., Jaffrezo, J. L., Kiss, G., Laj, P., Mihalopoulos, N., Perez, N., Quincey, P., Schwarz, J., Sellegri, K., Spindler, G., Swietlicki, E., Theodosi, C., Yttri, K. E., Aas, W. and Putaud, J. P.: A European aerosol phenomenology-4: Harmonized concentrations of carbonaceous aerosol at 10 regional background sites across Europe, *Atmos. Environ.*, 144, 133–145, doi:https://doi.org/10.1016/j.atmosenv.2016.07.050, 2016.

Chan, T. W., Huang, L., Leaitch, W. R., Sharma, S., Brook, J. R., Slowik, J. G., Abbatt, J. P. D., Brickell, P. C., Liggio, J., Li, S.-M. and Moosmüller, H.: Observations of OM/OC and specific attenuation coefficients (SAC) in ambient fine PM at a rural site in central Ontario, Canada, *Atmos. Chem. Phys.*, 10(5), 2393–2411, doi:10.5194/acp-10-2393-2010, 2010.

Chen, B., Bai, Z., Cui, X., Chen, J., Andersson, A. and Gustafsson, Ö.: Light absorption enhancement of black carbon from urban haze in Northern China winter, *Environ. Pollut.*, 221, 418–426, doi:10.1016/j.envpol.2016.12.004, 2017.

Chen, L.-W. A., Chow, J. C., Wang, X. L., Robles, J. A., Sunlin, B. J., Lowenthal, D. H., Zimmermann, R. and Watson, J. G.: Multi-wavelength optical measurement to enhance thermal/optical analysis for carbonaceous aerosol, *Atmos. Meas. Tech.*, 8(1), 451–461, doi:10.5194/amt-8-451-2015, 2015.

Cheng, Y., He, K.-B., Duan, F.-K., Du, Z.-Y., Zheng, M. and Ma, Y.-L.: Ambient organic carbon to elemental carbon ratios: Influence of the thermal-optical temperature protocol and implications, *Sci. Total Environ.*, 468–469C, 1103–1111, doi:10.1016/j.scitotenv.2013.08.084, 2013.

Cherian, R., Quaas, J., Salzmänn, M. and Tomassini, L.: Black carbon indirect radiative effects in a climate model, *Tellus B Chem. Phys. Meteorol.*, 69(1), 1369342, doi:10.1080/16000889.2017.1369342, 2017.

Cheung, H. H. Y., Tan, H., Xu, H., Li, F., Wu, C., Yu, J. Z. and Chan, C. K.: Measurements of non-volatile aerosols with a VTDMA and their correlations with carbonaceous aerosols in Guangzhou, China, *Atmos. Chem. Phys.*, 16(13), 8431–8446, doi:10.5194/acp-16-8431-2016, 2016.

Chiappini, L., Verlhac, S., Aujay, R., Maenhaut, W., Putaud, J. P., Sciare, J., Jaffrezo, J. L., Lioussé, C., Galy-Lacaux, C., Alleman, L. Y., Panteliadis, P., Leoz, E. and Favez, O.: Clues for a standardised thermal-optical protocol for the assessment of organic and elemental carbon within ambient air particulate matter, *Atmos. Meas. Tech.*, 7(6), 1649–1661, doi:https://doi.org/10.5194/amt-7-1649-2014, 2014.

Chin, M., Diehl, T., Tan, Q., Prospero, J. M., Kahn, R. A., Remer, L. A., Yu, H., Sayer, A. M., Bian, H., Geogdzhayev, I. V., Holben, B. N., Howell, S. G., Huebert, B. J., Hsu, N. C., Kim, D., Kucsera, T. L., Levy, R. C., Mishchenko, M. I., Pan, X., Quinn, P. K., Schuster, G. L., Streets, D. G., Strode, S. A., Torres, O. and Zhao, X.-P.: Multi-decadal aerosol variations from 1980 to 2009: a perspective from observations and a global model, *Atmos. Chem. Phys.*, 14(7), 3657–3690, doi:10.5194/acp-14-3657-2014, 2014.

Chow, J. C., Watson, J. G., Pritchett, L. C., Pierson, W. R., Frazier, C. A. and Purcell, R. G.: The direct thermal/optical reflectance carbon analysis system: description, evaluation and applications in U.S. Air quality studies, *Atmos. Environ.*, 27(8), 1185–1201, doi:10.1016/0960-1686(93)90245-T, 1993.

Chow, J. C., Watson, J. G., Crow, D., Lowenthal, D. H. and Merrifield, T.: Comparison of IMPROVE and NIOSH carbon measurements, *Aerosol Sci. Technol.*, 34(1), 23–34, doi:10.1080/02786820119073, 2001.

Chow, J. C., Watson, J. G., Chen, L.-W. A., Arnott, W. P., Moosmüller, H. and Fung, K.: Equivalence of elemental carbon by thermal/optical reflectance and transmittance with different temperature protocols, *Environ. Sci. Technol.*, 38(16), 4414–4422, doi:10.1021/es034936u, 2004.

Chow, J. C., Watson, J. G., Chen, L.-W. A., Chang, M. C. O., Robinson, N. F., Trimble, D. and Kohl, S.: The IMPROVE\_A temperature protocol for thermal/optical carbon analysis: maintaining consistency with a long-term database, *J. Air Waste Manag. Assoc.*, 57(9), 1014–1023, doi:10.3155/1047-3289.57.9.1014, 2007.

Chung, Y., Dominici, F., Wang, Y., Coull, B. A. and Bell, M. L.: Associations between long-term exposure to chemical constituents of fine particulate matter (PM<sub>2.5</sub>) and mortality in Medicare enrollees in the eastern United States, *Environ. Health Perspect.*, 123(5), 467–474, doi:10.1289/ehp.1307549, 2015.

Chýlek, P., Lesins, G. B., Videen, G., Wong, J. G. D., Pinnick, R. G., Ngo, D. and Klett, J. D.: Black carbon and absorption of solar radiation by clouds, *J. Geophys. Res. Atmos.*, 101(D18), 23365–23371, doi:10.1029/96JD01901, 1996.

Clarke, A. D., Shinozuka, Y., Kapustin, V. N., Howell, S., Huebert, B., Doherty, S., Anderson, T., Covert, D., Anderson, J., Hua, X., Moore II, K. G., McNaughton, C., Carmichael, G. and Weber, R.: Size distributions and mixtures of dust and black carbon aerosol in Asian outflow: Physiochemistry and optical properties, *J. Geophys. Res. Atmos.*, 109(D15), S1217–S1218, doi:10.1029/2003JD004378, 2004.

Collaud Coen, M., Weingartner, E., Apituley, A., Ceburnis, D., Fierz-Schmidhauser, R., Flentje, H., Henzing, J. S., Jennings, S. G., Moerman, M., Petzold, A., Schmid, O. and Baltensperger, U.: Minimizing light absorption measurement artifacts of the aethalometer: Evaluation of five correction algorithms, *Atmos. Meas. Tech.*, 3(2), 457–474, doi:10.5194/amt-3-457-2010, 2010.

Contini, D., Vecchi, R. and Viana, M.: Carbonaceous Aerosols in the Atmosphere, *Atmosphere*, 9(5), 181, doi:10.3390/atmos9050181, 2018.

Corbin, J. C. and Gysel-Beer, M.: Detection of tar brown carbon with the single particle soot photometer (SP2), *Atmos. Chem. Phys. Discuss.*, 19(24), 15673–15690, doi:10.5194/acp-2019-568, 2019.

Corbin, J. C., Sierau, B., Gysel, M., Laborde, M., Keller, A., Kim, J., Petzold, A., Onasch, T. B., Lohmann, U. and Mensah, A. A.: Mass spectrometry of refractory black carbon particles from six sources: Carbon-cluster and oxygenated ions, *Atmos. Chem. Phys.*, 14(5), 2591–2603, doi:https://doi.org/10.5194/acp-14-2591-2014, 2014.

Corbin, J. C., Lohmann, U., Sierau, B., Keller, A., Burtscher, H. and Mensah, A. A.: Black carbon surface oxidation and organic composition of beech-wood soot aerosols, *Atmos. Chem. Phys.*, 15(20), 11885–11907, doi:https://doi.org/10.5194/acp-15-11885-2015, 2015.

Corbin, J. C., Pieber, S. M., Czech, H., Zanatta, M., Jakobi, G., Massabò, D., Orasche, J., El Haddad, I., Mensah, A. A., Stengel, B., Drinovec, L., Mocnik, G., Zimmermann, R., Prévôt, A. S. H. and Gysel, M.: Brown and black carbon emitted by a marine engine operated on heavy fuel oil and distillate fuels: optical properties, size distributions, and emission factors, *J. Geophys. Res. Atmos.*, 123(11), 6175–6195, doi:10.1029/2017JD027818, 2018.

Corbin, J. C., Czech, H., Massabò, D., de Mongeot, F. B., Jakobi, G., Liu, F., Lobo, P., Mennucci, C., Mensah, A. A., Orasche, J., Pieber, S. M., Prévôt, A. S. H., Stengel, B., Tay, L.-L., Zanatta, M., Zimmermann, R., El Haddad, I. and Gysel, M.: Infrared-absorbing carbonaceous tar can dominate light absorption by marine-engine exhaust, *Npj Clim. Atmos. Sci.*, 2(1), 12, doi:10.1038/s41612-019-0069-5, 2019.

Corbin, J. C., Moallemi, A., Liu, F., Gagné, S., Olfert, J. S., Smallwood, G. J. and Lobo, P.: Closure between particulate matter concentrations measured ex situ by thermal-optical analysis and in situ by the CPMA-electrometer reference mass system, *Aerosol Sci. Technol.*, 54(11), 1293–1309, doi:10.1080/02786826.2020.1788710, 2020.

COST Action CA16109 COLOSSAL Chemical On-Line cOmposition and Source and Apportionment of fine aerosols, Working Group 1: Guidelines for comparison of ACSM measurement with co-located external data, doi:https://www.costcolossal.eu/, 2019.

Crippa, M., DeCarlo, P. F., Slowik, J. G., Mohr, C., Heringa, M. F., Chirico, R., Poulain, L., Freutel, F., Sciare, J., Cozic, J., Di Marco, C. F., Elsasser, M., Nicolas, J. B., Marchand, N., Abidi, E., Wiedensohler, A., Drewnick, F., Schneider, J., Borrmann, S., Nemitz, E., Zimmermann, R., Jaffrezo, J.-L., Prévôt, A. S. H. and Baltensperger,

U.: Wintertime aerosol chemical composition and source apportionment of the organic fraction in the metropolitan area of Paris, *Atmos. Chem. Phys.*, 13(2), 961–981, doi:10.5194/acp-13-961-2013, 2013.

Crippa, M., Canonaco, F., Lanz, V. A., Äijälä, M., Allan, J. D., Carbone, S., Capes, G., Ceburnis, D., Dall'Osto, M., Day, D. A., DeCarlo, P. F., Ehn, M., Eriksson, A., Freney, E., Hildebrandt Ruiz, L., Hillamo, R., Jimenez, J. L., Junninen, H., Kiendler-Scharr, A., Kortelainen, A.-M., Kulmala, M., Laaksonen, A., Mensah, A. A., Mohr, C., Nemitz, E., O'Dowd, C., Ovadnevaite, J., Pandis, S. N., Petäjä, T., Poulain, L., Saarikoski, S., Sellegri, K., Swietlicki, E., Tiitta, P., Worsnop, D. R., Baltensperger, U. and Prévôt, A. S. H.: Organic aerosol components derived from 25 AMS data sets across Europe using a consistent ME-2 based source apportionment approach, *Atmos. Chem. Phys.*, 14(12), 6159–6176, doi:https://doi.org/10.5194/acp-14-6159-2014, 2014.

Cross, E. S., Onasch, T. B., Ahern, A., Wrobel, W., Slowik, J. G., Olfert, J., Lack, D. A., Massoli, P., Cappa, C. D., Schwarz, J. P., Spackman, J. R., Fahey, D. W., Sedlacek, A., Trimborn, A., Jayne, J. T., Freedman, A., Williams, L. R., Ng, N. L., Mazzoleni, C., Dubey, M., Brem, B., Kok, G., Subramanian, R., Freitag, S., Clarke, A., Thornhill, D., Marr, L. C., Kolb, C. E., Worsnop, D. R. and Davidovits, P.: Soot particle studies—instrument inter-comparison—project overview, *Aerosol Sci. Technol.*, 44(8), 592–611, doi:10.1080/02786826.2010.482113, 2010.

Cui, X., Wang, X., Yang, L., Chen, B., Chen, J., Andersson, A. and Gustafsson, Ö.: Radiative absorption enhancement from coatings on black carbon aerosols, *Sci. Total Environ.*, 551–552, 51–56, doi:10.1016/j.scitotenv.2016.02.026, 2016.

Dahlkötter, F., Gysel, M., Sauer, D., Minikin, A., Baumann, R., Seifert, P., Ansmann, A., Fromm, M., Voigt, C. and Weinzierl, B.: The Pagami Creek smoke plume after long-range transport to the upper troposphere over Europe – aerosol properties and black carbon mixing state, *Atmos. Chem. Phys.*, 14(12), 6111–6137, doi:10.5194/acp-14-6111-2014, 2014.

Dastanpour, R., Momenimovahed, A., Thomson, K., Olfert, J. and Rogak, S.: Variation of the optical properties of soot as a function of particle mass, *Carbon*, 124, 201–211, doi:10.1016/j.carbon.2017.07.005, 2017.

Davidson, C., Phalen, R. and Solomon, P.: Airborne Particulate Matter and Human Health: A Review, *Aerosol Sci. Technol.*, 39, 737–749, doi:10.1080/02786820500191348, 2005.

DeCarlo, P. F., Kimmel, J. R., Trimborn, A., Northway, M. J., Jayne, J. T., Aiken, A. C., Gonin, M., Fuhrer, K., Horvath, T., Docherty, K. S., Worsnop, D. R. and Jimenez, J. L.: Field-deployable, high-resolution, time-of-flight aerosol mass spectrometer, *Anal. Chem.*, 78(24), 8281–8289, doi:10.1021/ac061249n, 2006.

Dines, W. H.: The heat balance of the atmosphere, *Q. J. R. Meteorol. Soc.*, 43(182), 151–158, doi:10.1002/qj.49704318203, 1917.

Ding, S., Zhao, D., He, C., Huang, M., He, H., Tian, P., Liu, Q., Bi, K., Yu, C., Pitt, J., Chen, Y., Ma, X., Chen, Y., Jia, X., Kong, S., Wu, J., Hu, D., Hu, K., Ding, D. and Liu, D.: Observed Interactions Between Black Carbon and Hydrometeor During Wet Scavenging in Mixed-Phase Clouds, *Geophys. Res. Lett.*, 46(14), 8453–8463, doi:10.1029/2019GL083171, 2019.

Dockery, D. W., Pope, C. A., Xu, X., Spengler, J. D., Ware, J. H., Fay, M. E., Ferris, B. G. and Speizer, F. E.: An association between air pollution and mortality in six U.S. cities, *N. Engl. J. Med.*, 329(24), 1753–1759, doi:10.1056/NEJM199312093292401, 1993.

Dou, T.-F. and Xiao, C.-D.: An overview of black carbon deposition and its radiative forcing over the Arctic, *Adv. Clim. Change Res.*, 7(3), 115–122, doi:10.1016/j.accre.2016.10.003, 2016.

Draxler, R. R. and Hess, G. D.: NOAA Technical Memorandum ERL ARL-224, NOAA Tech. Memo. ERL ARL-224, 24, 1997.

Drew Shindell, Kuylenstierna, J., Vignati, E., Van Dingenen, R., Amann, M., Klimont, Z., Anenberg, S., Muller, N., Janssens-Maenhout, G., Raes, F., Schwartz, J., Faluvegi, G., Pozzoli, L., Kupiainen, K., Höglund-Isaksson, L., Emberson, L., Streets, D., Ramanathan, V., Hicks, K. and Fowler, D.: Simultaneously Mitigating Near-Term Climate Change and Improving Human Health and Food Security, *Science*, 335, 183–9, doi:10.1126/science.1210026, 2012.

Drinovec, L., Močnik, G., Zotter, P., Prévôt, A. S. H., Ruckstuhl, C., Coz, E., Rupakheti, M., Sciare, J., Müller, T., Wiedensohler, A. and Hansen, A. D. A.: The “dual-spot” aethalometer: an improved measurement of aerosol black carbon with real-time loading compensation, *Atmos. Meas. Tech.*, 8(5), 1965–1979, doi:10.5194/amt-8-1965-2015, 2015.

Drinovec, L., Gregorič, A., Zotter, P., Wolf, R., Bruns, E. A., Prévôt, A. S. H., Petit, J.-E., Favez, O., Sciare, J., Arnold, I. J., Chakrabarty, R. K., Moosmüller, H., Filep, A. and Močnik, G.: The filter-loading effect by ambient aerosols in filter absorption photometers depends on the coating of the sampled particles, *Atmos. Meas. Tech.*, 10(3), 1043–1059, doi:10.5194/amt-10-1043-2017, 2017.

Dunning, W. J.: Nucleation; homogeneous and heterogeneous. Nucleation processes and aerosol formation, *Discuss. Faraday Soc.*, 30, 9–19, doi:10.1039/DF9603000009, 1960.

Durant, A. J., Bonadonna, C. and Horwell, C. J.: Atmospheric and Environmental Impacts of Volcanic Particulates, *Elements*, 6(4), 235–240, doi:10.2113/gselements.6.4.235, 2010.

Durdina, L., Brem, B. T., Setyan, A., Siegerist, F., Rindlisbacher, T. and Wang, J.: Assessment of particle pollution from jetliners: From smoke visibility to nanoparticle counting, *Environ. Sci. Technol.*, 51(6), 3534–3541, doi:10.1021/acs.est.6b05801, 2017.

Durdina, L., Brem, B. T., Schönenberger, D., Siegerist, F., Anet, J. G. and Rindlisbacher, T.: Nonvolatile particulate matter emissions of a business jet measured at ground level and estimated for cruising altitudes, *Environ. Sci. Technol.*, 53(21), 12865–12872, doi:10.1021/acs.est.9b02513, 2019.

Dutkiewicz, V. A., DeJulio, A. M., Ahmed, T., Laing, J., Hopke, P. K., Skeie, R. B., Viisanen, Y., Paatero, J. and Husain, L.: Forty-seven years of weekly atmospheric black carbon measurements in the Finnish Arctic: Decrease in black carbon with declining emissions, *J. Geophys. Res. Atmos.*, 119(12), 7667–7683, doi:10.1002/2014JD021790, 2014.

Eckhardt, S., Quennehen, B., Olivié, D. J. L., Berntsen, T. K., Cherian, R., Christensen, J. H., Collins, W., Crepinsek, S., Daskalakis, N., Flanner, M., Herber, A., Heyes, C., Hodnebrog, Ø., Huang, L., Kanakidou, M., Klimont, Z., Langner, J., Law, K. S., Lund, M. T., Mahmood, R., Massling, A., Myriokefalitakis, S., Nielsen, I. E., Nøjgaard, J. K., Quaas, J., Quinn, P. K., Raut, J.-C., Rumbold, S. T., Schulz, M., Sharma, S., Skeie, R. B., Skov, H., Uttal, T., von Salzen, K. and Stohl, A.: Current model capabilities for simulating black carbon and sulfate concentrations in the Arctic atmosphere: A multi-model evaluation using a comprehensive measurement data set, *Atmos. Chem. Phys.*, 15(16), 9413–9433, doi:10.5194/acp-15-9413-2015, 2015.

Eleftheriadis, K., Vratolis, S. and Nyeki, S.: Aerosol black carbon in the European Arctic: Measurements at Zeppelin station, Ny-Ålesund, Svalbard from 1998–2007, *Geophys. Res. Lett.*, 36(2), doi:10.1029/2008GL035741, 2009.

Elser, M., El-Haddad, I., Maasikmets, M., Bozzetti, C., Wolf, R., Ciarelli, G., Slowik, J. G., Richter, R., Teinmaa, E., Hüglin, C., Baltensperger, U. and Prévôt, A. S. H.: High contributions of vehicular emissions to ammonia in three European cities derived from mobile measurements, *Atmos. Environ.*, 175, 210–220, doi:10.1016/j.atmosenv.2017.11.030, 2018.

Emerson, E. W., Katich, J. M., Schwarz, J. P., McMeeking, G. R. and Farmer, D. K.: Direct Measurements of Dry and Wet Deposition of Black Carbon Over a Grassland, *J. Geophys. Res. Atmos.*, 123(21), 12,277–12,290, doi:10.1029/2018JD028954, 2018.

EPICA community members: Eight glacial cycles from an Antarctic ice core, *Nature*, 429(6992), 623–628, doi:10.1038/nature02599, 2004.

European Committee for Standardisation Ambient air: Ambient air. Measurement of elemental carbon (EC) and organic carbon (OC) collected on filters., 2017.

Feichter, J., Sausen, R., Graßl, H. and Fiebig, M.: Comment on “Control of fossil-fuel particulate black carbon and organic matter, possibly the most effective method of slowing global warming” by M. Z. Jacobson, *J. Geophys. Res. Atmos.*, 108(D24), 4767, doi:10.1029/2002JD003223, 2003.

Ferrero, L., Castelli, M., Ferrini, B. S., Moscatelli, M., Perrone, M. G., Sangiorgi, G., D'Angelo, L., Rovelli, G., Moroni, B., Scardazza, F., Močnik, G., Bolzacchini, E., Petitta, M. and Cappelletti, D.: Impact of black carbon aerosol over Italian basin valleys: High-resolution measurements along vertical profiles, radiative forcing and heating rate, *Atmos. Chem. Phys.*, 14(18), 9641–9664, doi:<https://doi.org/10.5194/acp-14-9641-2014>, 2014.

Fierce, L., Riemer, N. and Bond, T. C.: Explaining variance in black carbon's aging timescale, *Atmos. Chem. Phys.*, 15(6), 3173–3191, doi:<https://doi.org/10.5194/acp-15-3173-2015>, 2015.

Fierce, L., Bond, T. C., Bauer, S. E., Mena, F. and Riemer, N.: Black carbon absorption at the global scale is affected by particle-scale diversity in composition, *Nat. Commun.*, 7(1), doi:[10.1038/ncomms12361](https://doi.org/10.1038/ncomms12361), 2016.

Findeisen, W.: Kolloid-meteorologische 404 Vorgänge bei Niederschlagsbildung., *Meteorol. Z.*, 55, 121–133, 1938.

Fitzgerald, J. W.: Marine aerosols: A review, *Atmos. Environ.*, 25(3–4), 533–545, doi:[10.1016/0960-1686\(91\)90050-H](https://doi.org/10.1016/0960-1686(91)90050-H), 1991.

Flanner, M. G., Zender, C. S., Randerson, J. T. and Rasch, P. J.: Present-day climate forcing and response from black carbon in snow, *J. Geophys. Res.*, 112(D11), doi:[10.1029/2006JD008003](https://doi.org/10.1029/2006JD008003), 2007.

Forello, A. C., Bernardoni, V., Calzolari, G., Lucarelli, F., Massabò, D., Nava, S., Pileci, R. E., Prati, P., Valentini, S., Valli, G. and Vecchi, R.: Exploiting multi-wavelength aerosol absorption coefficients in a multi-time resolution source apportionment study to retrieve source-dependent absorption parameters, *Atmos. Chem. Phys.*, 19(17), 11235–11252, doi:[10.5194/acp-19-11235-2019](https://doi.org/10.5194/acp-19-11235-2019), 2019.

Frenay, E. J., Adachi, K. and Buseck, P. R.: Internally mixed atmospheric aerosol particles: Hygroscopic growth and light scattering, *J. Geophys. Res. Atmos.*, 115(D19), doi:[10.1029/2009JD013558](https://doi.org/10.1029/2009JD013558), 2010.

Fuller, K. A., Malm, W. C. and Kreidenweis, S. M.: Effects of mixing on extinction by carbonaceous particles, *J. Geophys. Res. Atmos.*, 104(D13), 15941–15954, doi:[10.1029/1998JD100069](https://doi.org/10.1029/1998JD100069), 1999.

Fung, K.: Particulate carbon speciation by MnO<sub>2</sub> oxidation, *Aerosol Sci. Technol.*, 12(1), 122–127, doi:[10.1080/02786829008959332](https://doi.org/10.1080/02786829008959332), 1990.

Fuzzi, S., Baltensperger, U., Carslaw, K., Decesari, S., Denier van der Gon, H., Facchini, M. C., Fowler, D., Koren, I., Langford, B., Lohmann, U., Nemitz, E., Pandis, S., Riipinen, I., Rudich, Y., Schaap, M., Slowik, J. G., Spracklen, D. V., Vignati, E., Wild, M., Williams, M. and Gilardoni, S.: Particulate matter, air quality and climate: lessons learned and future needs, *Atmos. Chem. Phys.*, 15(14), 8217–8299, doi:[10.5194/acp-15-8217-2015](https://doi.org/10.5194/acp-15-8217-2015), 2015.

Ganopolski, A., Winkelmann, R. and Schellnhuber, H. J.: Critical insolation–CO<sub>2</sub> relation for diagnosing past and future glacial inception, *Nature*, 529(7585), 200–203, doi:[10.1038/nature16494](https://doi.org/10.1038/nature16494), 2016.

Gao, R. S., Schwarz, J. P., Kelly, K. K., Fahey, D. W., Watts, L. A., Thompson, T. L., Spackman, J. R., Slowik, J. G., Cross, E. S., Han, J.-H., Davidovits, P., Onasch, T. B. and Worsnop, D. R.: A novel method for estimating light-scattering properties of soot aerosols using a modified single-particle soot photometer, *Aerosol Sci. Technol.*, 41(2), 125–135, doi:[10.1080/02786820601118398](https://doi.org/10.1080/02786820601118398), 2007.

Gelencsér, A., May, B., Simpson, D., Sánchez-Ochoa, A., Kasper-Giebl, A., Puxbaum, H., Caseiro, A., Pio, C. and Legrand, M.: Source apportionment of PM<sub>2.5</sub> organic aerosol over Europe: Primary/secondary, natural/anthropogenic, and fossil/biogenic origin, *J. Geophys. Res.*, 112(D23), doi:[10.1029/2006JD008094](https://doi.org/10.1029/2006JD008094), 2007.

Giannoni, M., Calzolari, G., Chiari, M., Cincinelli, A., Lucarelli, F., Martellini, T. and Nava, S.: A comparison between thermal-optical transmittance elemental carbon measured by different protocols in PM<sub>2.5</sub> samples, *Sci. Total Environ.*, 571, 195–205, doi:[10.1016/j.scitotenv.2016.07.128](https://doi.org/10.1016/j.scitotenv.2016.07.128), 2016.

Gilardoni, S., Lupi, A., Mazzola, M., Cappelletti, D. M., Moroni, B., Markuszewski, P., Rozwadowska, A., Krejci, R., Zieger, P., Tunved, P., Vratolis, S., Eleftheriadis, K. and Viola, A. P.: Atmospheric black carbon in Svalbard (ABC Svalbard), SESS Rep. 2019 – State Environ. Sci. Svalbard, 16, 2019.

Gogoi, M. M., Babu, S. S., Moorthy, K. K., Thakur, R. C., Chaubey, J. P. and Nair, V. S.: Aerosol black carbon over Svalbard regions of Arctic, *Polar Sci.*, 10(1), 60–70, doi:10.1016/j.polar.2015.11.001, 2016.

Grahame, T. J., Klemm, R. and Schlesinger, R. B.: Public health and components of particulate matter: The changing assessment of black carbon, *J. Air Waste Manag. Assoc.*, 64(6), 620–660, doi:10.1080/10962247.2014.912692, 2014.

Gysel, M., Crosier, J., Topping, D. O., Whitehead, J. D., Bower, K. N., Cubison, M. J., Williams, P. I., Flynn, M. J., McFiggans, G. B. and Coe, H.: Closure study between chemical composition and hygroscopic growth of aerosol particles during TORCH2, *Atmos. Chem. Phys.*, 7(24), 6131–6144, doi:10.5194/acp-7-6131-2007, 2007.

Gysel, M., Laborde, M., Olfert, J. S., Subramanian, R. and Gröhn, A. J.: Effective density of aquadag and fullerene soot black carbon reference materials used for SP2 calibration, *Atmos. Meas. Tech.*, 4(12), 2851–2858, doi:10.5194/amt-4-2851-2011, 2011.

Gysel, M., Laborde, M., Mensah, A. A., Corbin, J. C., Keller, A., Kim, J., Petzold, A. and Sierau, B.: Technical Note: The single particle soot photometer fails to reliably detect PALAS soot nanoparticles, *Atmos. Meas. Tech.*, 5(12), 3099–3107, doi:10.5194/amt-5-3099-2012, 2012.

Haefelin, M., Barthès, L., Bock, O., Boitel, C., Bony, S., Bouniol, D., Chepfer, H., Chiriaco, M., Cuesta, J., Delanoë, J., Drobinski, P., Dufresne, J.-L., Flamant, C., Grall, M., Hodzic, A., Hourdin, F., Lapouge, F., Lemaître, Y., Mathieu, A., Morille, Y., Naud, C., Noël, V., O'Hirok, W., Pelon, J., Pietras, C., Protat, A., Romand, B., Scialom, G. and Vautard, R.: SARTA, a ground-based atmospheric observatory for cloud and aerosol research, *Ann. Geophys.*, 23(2), 253–275, doi:10.5194/angeo-23-253-2005, 2005.

Han, Y. M., Chen, L.-W. A., Huang, R.-J., Chow, J. C., Watson, J. G., Ni, H. Y., Liu, S. X., Fung, K. K., Shen, Z. X., Wei, C., Wang, Q. Y., Tian, J., Zhao, Z. Z., Prévôt, A. S. H. and Cao, J. J.: Carbonaceous aerosols in megacity Xi'an, China: Implications of thermal/optical protocols comparison, *Atmos. Environ.*, 132, 58–68, doi:10.1016/j.atmosenv.2016.02.023, 2016.

Hänel, G.: Radiation budget of the boundary layer: Part II. Simultaneous measurement of mean solar volume absorption and extinction coefficients of particles, *Beitr. Phys. Atmos.*, 60, 241–247, 1987.

Hansen, A. D. A., Rosen, H. and Novakov, T.: The aethalometer — An instrument for the real-time measurement of optical absorption by aerosol particles, *Sci. Total Environ.*, 36, 191–196, doi:10.1016/0048-9697(84)90265-1, 1984.

Heidam, N. Z., Christensen, J., Wählin, P. and Skov, H.: Arctic atmospheric contaminants in NE Greenland: levels, variations, origins, transport, transformations and trends 1990–2001, *Sci. Total Environ.*, 331(1), 5–28, doi:10.1016/j.scitotenv.2004.03.033, 2004.

Heidenreich, R. D., Hess, W. M. and Ban, L. L.: A test object and criteria for high resolution electron microscopy, *J. Appl. Crystallogr.*, 1(1), 1–19, doi:10.1107/S0021889868004930, 1968.

Heinzerling, A., Hsu, J. and Yip, F.: Respiratory Health Effects of Ultrafine Particles in Children: A Literature Review, *Water. Air. Soil Pollut.*, 227, 32, doi:10.1007/s11270-015-2726-6, 2016.

Hirdman, D., Burkhart, J. F., Sodemann, H., Eckhardt, S., Jefferson, A., Quinn, P. K., Sharma, S., Ström, J. and Stohl, A.: Long-term trends of black carbon and sulphate aerosol in the Arctic: changes in atmospheric transport and source region emissions, *Atmos. Chem. Phys.*, 10(19), 9351–9368, doi:10.5194/acp-10-9351-2010, 2010.

Hitzenberger, R., Petzold, A., Bauer, H., Ctyroky, P., Pouresmaeil, P., Laskus, L. and Puxbaum, H.: Intercomparison of thermal and optical measurement methods for elemental carbon and black carbon at an urban location, *Environ. Sci. Technol.*, 40(20), 6377–6383, doi:10.1021/es051228v, 2006.

Hodnebrog, Ø., Myhre, G. and Samset, B. H.: How shorter black carbon lifetime alters its climate effect, *Nat. Commun.*, 5, 5065, doi:10.1038/ncomms6065, 2014.

Huang, L., Brook, J. R., Zhang, W., Li, S. M., Graham, L., Ernst, D., Chivulescu, A. and Lu, G.: Stable isotope measurements of carbon fractions (OC/EC) in airborne particulate: A new dimension for source characterization and apportionment, *Atmos. Environ.*, 40(15), 2690–2705, doi:10.1016/j.atmosenv.2005.11.062, 2006.

Huang, J., Minnis, P., Yan, H., Yi, Y., Chen, B., Zhang, L. and Ayers, J. K.: Dust aerosol effect on semi-arid climate over Northwest China detected from A-Train satellite measurements, *Atmos. Chem. Phys.*, 10(14), 6863–6872, doi:10.5194/acp-10-6863-2010, 2010.

Huang, K., Fu, J., Prikhodko, V., Storey, J., Romanov, A., Hodson, E., Cresko, J., Morozova, I., Ignatieva, Y. and Cabaniss, J.: Russian anthropogenic black carbon: Emission reconstruction and Arctic black carbon simulation, *J. Geophys. Res. Atmos.*, 120(11), 306–333, doi:10.1002/2015JD023358, 2015.

Huntzicker, J. J., Johnson, R. L., Shah, J. J. and Cary, R. A.: Analysis of organic and elemental carbon in ambient aerosols by a thermal-optical method, in *Particulate Carbon: Atmospheric Life Cycle*, edited by G. T. Wolff and R. L. Klimisch, pp. 79–88, Springer US, Boston, MA., 1982.

IPCC: *Climate Change 2013: The Physical Science Basis. Contribution of Working Group I to the Fifth Assessment Report of the Intergovernmental Panel on Climate Change*, Camb. Univ. Press Camb. U. K. N. Y. NY USA, 1535, 2013.

Jacobson, M. Z.: Strong radiative heating due to the mixing state of black carbon in atmospheric aerosols, *Nature*, 409(6821), 695–697, doi:10.1038/35055518, 2001.

Janssen, N., Hoek, G., Simic-Lawson, M., Fischer, P., van Bree, L., ten Brink, H., Anderson, H. R., Brunekreef, B. and Cassee, F.: Black Carbon as an Additional Indicator of the Adverse Health Effects of Airborne Particles Compared with PM<sub>10</sub> and PM<sub>2.5</sub>, *Environ. Health Perspect.*, 119(12), 1691–1699, doi:10.1289/ehp.1003369, 2011.

Janssen, N., Gerlofs-Nijland, M., Lanki, T., Salonen, R., Cassee, F., Hoek, G., Fischer, P., Brunekreef, B. and Krzyzanowski, M.: *Health Effects of Black Carbon*, Rep. Jt. Task Force Health WHO UNECE Conv. Long-Range Transbound. Air Pollut., 2012.

Jayne, J. T., Leard, D. C., Zhang, X., Davidovits, P., Smith, K. A., Kolb, C. E. and Worsnop, D. R.: Development of an aerosol mass spectrometer for size and composition analysis of submicron particles, *Aerosol Sci. Technol.*, 33(1–2), 49–70, doi:10.1080/027868200410840, 2000.

Jurado, E., Dachs, J., Duarte, C. M. and Simó, R.: Atmospheric deposition of organic and black carbon to the global oceans, *Atmos. Environ.*, 42(34), 7931–7939, doi:10.1016/j.atmosenv.2008.07.029, 2008.

Karanasiou, A., Diapouli, E., Cavalli, F., Eleftheriadis, K., Viana, M., Alastuey, A., Querol, X. and Reche, C.: On the quantification of atmospheric carbonate carbon by thermal/optical analysis protocols, *Atmos. Meas. Tech.*, 4(11), 2409–2419, doi:10.5194/amt-4-2409-2011, 2011.

Karanasiou, A., Minguillón, M. C., Viana, M., Alastuey, A., Putaud, J.-P., Maenhaut, W., Panteliadis, P., Močnik, G., Favez, O. and Kuhlbusch, T. A. J.: Thermal-optical analysis for the measurement of elemental carbon (EC) and organic carbon (OC) in ambient air a literature review, *Atmos. Meas. Tech. Discuss.*, 8(9), 9649–9712, doi:10.5194/amtd-8-9649-2015, 2015.

Karlsson, L., Krejci, R., Koike, M., Ebell, K. and Zieger, P.: The role of nanoparticles in Arctic cloud formation, *Atmos. Chem. Phys. Discuss.*, doi:10.5194/acp-2020-417, 2020.

Khan, B., Hays, M. D., Geron, C. and Jetter, J.: Differences in the OC/EC ratios that characterize ambient and source aerosols due to thermal-optical analysis, *Aerosol Sci. Technol.*, 46(2), 127–137, doi:10.1080/02786826.2011.609194, 2012.

Kirchstetter, Novakov and Hobbs Peter: Evidence that the spectral dependence of light absorption by aerosols is affected by organic carbon, *J. Geophys. Res. Atmos.*, 109(D21), doi:10.1029/2004JD004999, 2004.



Kirchstetter, T. W. and Thatcher, T. L.: Contribution of organic carbon to wood smoke particulate matter absorption of solar radiation, *Atmos. Chem. Phys.*, 12(14), 6067–6072, doi:<https://doi.org/10.5194/acp-12-6067-2012>, 2012.

Knippertz, P. and Todd, M.: Mineral dust aerosol over the Sahara: Processes of emission and transport, and implications for modeling, *Rev. Geophys.*, 50, doi:10.1029/2011RG000362, 2012.

Knox, A., Evans, G. J., Brook, J. R., Yao, X., Jeong, C.-H., Godri, K. J., Sabaliauskas, K. and Slowik, J. G.: Mass absorption cross-section of ambient black carbon aerosol in relation to chemical age, *Aerosol Sci. Technol.*, 43(6), 522–532, doi:10.1080/02786820902777207, 2009.

Koch, D. and Del Genio, A. D.: Black carbon semi-direct effects on cloud cover: Review and synthesis, *Atmos. Chem. Phys.*, 10(16), 7685–7696, doi:10.5194/acp-10-7685-2010, 2010.

Koch, D., Schulz, M., Kinne, S., McNaughton, C., Spackman, J. R., Balkanski, Y., Bauer, S., Bernsten, T., Bond, T. C., Boucher, O., Chin, M., Clarke, A., Luca, N. D., Dentener, F., Diehl, T., Dubovik, O., Easter, R., Fahey, D. W., Feichter, J., Fillmore, D., Freitag, S., Ghan, S., Ginoux, P., Gong, S., Horowitz, L., Iversen, T., Kirkeva, A., Moteki, N., Myhre, G., Penner, J. E., Perlwitz, J., Pitari, G., Reddy, S., Sahu, L., Sakamoto, H., Schuster, G., Schwarz, J. P., Seland, Ø., Stier, P., Takegawa, N., Takemura, T., Textor, C., van Aardenne, J. A. and Zhao, Y.: Evaluation of black carbon estimations in global aerosol models, *Atmos. Chem. Phys.*, 26, <https://doi.org/10.5194/acp-9-9001-2009>, 2009.

Krewski, D., Jerrett, M., Burnett, R. T., Ma, R., Hughes, E., Shi, Y., Turner, M. C., Pope, C. A., Thurston, G., Calle, E. E., Thun, M. J., Beckerman, B., DeLuca, P., Finkelstein, N., Ito, K., Moore, D. K., Newbold, K. B., Ramsay, T., Ross, Z., Shin, H. and Tempalski, B.: Extended follow-up and spatial analysis of the American Cancer Society study linking particulate air pollution and mortality, *Res. Rep. Health Eff. Inst.*, (140), 5–114; discussion 115–136, PMID: 19627030, 2009.

Kupiszewski, P., Zanatta, M., Mertes, S., Vochezer, P., Lloyd, G., Schneider, J., Schenk, L., Schnaiter, M., Baltensperger, U., Weingartner, E. and Gysel, M.: Ice residual properties in mixed-phase clouds at the high-alpine Jungfraujoch site, *J. Geophys. Res. Atmos.*, 121(20), 12343–12362, doi:10.1002/2016JD024894, 2016.

Kvietkus, K.: Organic and elemental carbon in coastal aerosol of the Baltic Sea, *Lith. J. Phys.*, 47(2), 203–210, 2007.

Laborde, M., Mertes, P., Zieger, P., Dommen, J., Baltensperger, U. and Gysel, M.: Sensitivity of the single particle soot photometer to different black carbon types, *Atmos. Meas. Tech.*, 5(5), 1031–1043, doi:<https://doi.org/10.5194/amt-5-1031-2012>, 2012a.

Laborde, M., Schnaiter, M., Linke, C., Saathoff, H., Naumann, K.-H., Möhler, O., Berlenz, S., Wagner, U., Taylor, J. W., Liu, D., Flynn, M., Allan, J. D., Coe, H., Heimerl, K., Dahlkötter, F., Weinzierl, B., Wollny, A. G., Zanatta, M., Cozic, J., Laj, P., Hittenberger, R., Schwarz, J. P. and Gysel, M.: Single particle soot photometer intercomparison at the AIDA chamber, *Atmos. Meas. Tech.*, 5(12), 3077–3097, doi:10.5194/amt-5-3077-2012, 2012b.

Laborde, M., Crippa, M., Tritscher, T., Jurányi, Z., Decarlo, P. F., Temime-Roussel, B., Marchand, N., Eckhardt, S., Stohl, A., Baltensperger, U., Prévôt, A. S. H., Weingartner, E. and Gysel, M.: Black carbon physical properties and mixing state in the European megacity Paris, *Atmospheric Chem. Phys.*, 13(11), 5831–5856, doi:10.5194/acp-13-5831-2013, 2013.

Lack, D. A. and Cappa, C. D.: Impact of brown and clear carbon on light absorption enhancement, single scatter albedo and absorption wavelength dependence of black carbon, *Atmos. Chem. Phys.*, 10(9), 4207–4220, <https://doi.org/10.5194/acp-10-4207-2010>, 2010.

Lanz, V. A., Alfarra, M. R., Baltensperger, U., Buchmann, B., Hueglin, C. and Prévôt, A. S. H.: Source apportionment of submicron organic aerosols at an urban site by factor analytical modelling of aerosol mass spectra, *Atmos. Chem. Phys.*, 7(6), 1503–1522, doi:10.5194/acp-7-1503-2007, 2007.

Lanz, V. A., Prévôt, A. S. H., Alfarra, M. R., Weimer, S., Mohr, C., DeCarlo, P. F., Gianini, M. F. D., Hueglin, C., Schneider, J., Favez, O., D'Anna, B., George, C. and Baltensperger, U.: Characterization of aerosol chemical composition with aerosol mass spectrometry in Central Europe: an overview, *Atmos. Chem. Phys.*, 10(21), 10453–10471, doi:10.5194/acp-10-10453-2010, 2010.

Larson, E. J. L. and Portmann, R. W.: Anthropogenic aerosol drives uncertainty in future climate mitigation efforts, *Sci. Rep.*, 9(1), doi:10.1038/s41598-019-52901-3, 2019.

Lavanchy, V. M. H., Gäggeler, H. W., Schotterer, U., Schwikowski, M. and Baltensperger, U.: Historical record of carbonaceous particle concentrations from a European high-alpine glacier (Colle Gnifetti, Switzerland), *J. Geophys. Res. Atmos.*, 104(D17), 21227–21236, doi:10.1029/1999JD900408, 1999.

Lee, A. K. Y., Willis, M. D., Healy, R. M., Onasch, T. B. and Abbatt, J. P. D.: Mixing state of carbonaceous aerosol in an urban environment: single particle characterization using the soot particle aerosol mass spectrometer (SP-AMS), *Atmos. Chem. Phys.*, 15(4), 1823–1841, doi:10.5194/acp-15-1823-2015, 2015.

Lewis, K. A., Arnott, W. P., Malm, W. C., Laskin, A., Jimenez, J. L., Ulbrich, I. M., Huffman, J. A., Onasch, T. B., Trimborn, A., Liu, L. and Mishchenko, M. I.: Reduction in biomass burning aerosol light absorption upon humidification: roles of inorganically-induced hygroscopicity, particle collapse, and photoacoustic heat and mass transfer, *Atmos. Chem. Phys.*, 9, 8949–8966, doi:https://doi.org/10.5194/acp-9-8949-2009, 2009.

Liggio, J., Gordon, M., Smallwood, G., Li, S.-M., Stroud, C., Staebler, R., Lu, G., Lee, P., Taylor, B. and Brook, J. R.: Are emissions of black carbon from gasoline vehicles underestimated? Insights from near and on-road measurements, *Environ. Sci. Technol.*, 46(9), 4819–4828, doi:10.1021/es2033845, 2012.

Liousse, C., Cachier, H. and Jennings, S. G.: Optical and thermal measurements of black carbon aerosol content in different environments: Variation of the specific attenuation cross-section,  $\sigma$ , *Atmosph. Environ. Part Gen. Top.*, 27(8), 1203–1211, doi:10.1016/0960-1686(93)90246-U, 1993.

Liu, C., Chung, C. E., Yin, Y. and Schnaiter, M.: The absorption Ångström exponent of black carbon: From numerical aspects, *Atmos. Chem. Phys.*, 18(9), 6259–6273, doi:https://doi.org/10.5194/acp-18-6259-2018, 2018.

Liu, D., Allan, J. D., Young, D. E., Coe, H., Beddows, D., Fleming, Z. L., Flynn, M. J., Gallagher, M. W., Harrison, R. M., Lee, J., Prevot, A. S. H., Taylor, J. W., Yin, J., Williams, P. I. and Zotter, P.: Size distribution, mixing state and source apportionment of black carbon aerosol in London during wintertime, *Atmos. Chem. Phys.*, 14(18), 10061–10084, doi:10.5194/acp-14-10061-2014, 2014.

Liu, D., Quennehen, B., Darbyshire, E., Allan, J. D., Williams, P. I., Taylor, J. W., Bauguitte, S. J.-B., Flynn, M. J., Lowe, D., Gallagher, M. W., Bower, K. N., Choularton, T. W. and Coe, H.: The importance of Asia as a source of black carbon to the European Arctic during springtime 2013, *Atmos. Chem. Phys.*, 15(20), 11537–11555, doi:10.5194/acp-15-11537-2015, 2015a.

Liu, S., Aiken, A. C., Gorkowski, K., Dubey, M. K., Cappa, C. D., Williams, L. R., Herndon, S. C., Massoli, P., Fortner, E. C., Chhabra, P. S., Brooks, W. A., Onasch, T. B., Jayne, J. T., Worsnop, D. R., China, S., Sharma, N., Mazzoleni, C., Xu, L., Ng, N. L., Liu, D., Allan, J. D., Lee, J. D., Fleming, Z. L., Mohr, C., Zotter, P., Szidat, S. and Prévôt, A. S. H.: Enhanced light absorption by mixed source black and brown carbon particles in UK winter, *Nat. Commun.*, 6, 8435, doi:10.1038/ncomms9435, 2015b.

Liu, F., Yon, J., Fuentes, A., Lobo, P., Smallwood, G. J. and Corbin, J. C.: Review of recent literature on the light absorption properties of black carbon: Refractive index, mass absorption cross section, and absorption function, *Aerosol Sci. Technol.*, 54(1), 33–51, doi:10.1080/02786826.2019.1676878, 2020.

Lobo, P., Durdina, L., Smallwood, G. J., Rindlisbacher, T., Siegerist, F., Black, E. A., Yu, Z., Mensah, A. A., Hagen, D. E., Miake-Lye, R. C., Thomson, K. A., Brem, B. T., Corbin, J. C., Abegglen, M., Sierau, B., Whitefield, P. D. and Wang, J.: Measurement of aircraft engine non-volatile pm emissions: Results of the aviation-particle regulatory instrumentation demonstration experiment (A-PRIDE) 4 campaign, *Aerosol Sci. Technol.*, 49(7), 472–484, doi:10.1080/02786826.2015.1047012, 2015.

Lund, M. T., Samset, B. H., Skeie, R. B., Watson-Parris, D., Katich, J. M., Schwarz, J. P. and Weinzierl, B.: Short Black Carbon lifetime inferred from a global set of aircraft observations, *Npj Clim. Atmos. Sci.*, 1(1), doi:10.1038/s41612-018-0040-x, 2018.

Lüthi, D., Le Floch, M., Bereiter, B., Blunier, T., Barnola, J.-M., Siegenthaler, U., Raynaud, D., Jouzel, J., Fischer, H., Kawamura, K. and Stocker, T. F.: High-resolution carbon dioxide concentration record 650,000–800,000 years before present, *Nature*, 453(7193), 379–382, doi:10.1038/nature06949, 2008.

MacFarling Meure, C., Etheridge, D., Trudinger, C., Steele, P., Langenfelds, R., van Ommen, T., Smith, A. and Elkins, J.: Law Dome CO<sub>2</sub>, CH<sub>4</sub> and N<sub>2</sub>O ice core records extended to 2000 years BP, *Geophys. Res. Lett.*, 33(14), doi:10.1029/2006GL026152, 2006.

Mackowski, D. W.: Calculation of total cross sections of multiple-sphere clusters, *J. Opt. Soc. Am. A*, 11(11), 2851–2861, doi:10.1364/JOSAA.11.002851, 1994.

Martins, J. V., Artaxo, P., Liousse, C., Reid, J. S., Hobbs, P. V. and Kaufman, Y. J.: Effects of black carbon content, particle size, and mixing on light absorption by aerosols from biomass burning in Brazil, *J. Geophys. Res. Atmos.*, 103(D24), 32041–32050, doi:10.1029/98JD02593, 1998.

Massabò, D., Altomari, A., Vernocchi, V. and Prati, P.: Two-wavelength thermal–optical determination of light-absorbing carbon in atmospheric aerosols, *Atmos. Meas. Tech.*, 12(6), 3173–3182, doi:10.5194/amt-12-3173-2019, 2019.

Matsui, H., Koike, M., Kondo, Y., Moteki, N., Fast, J. D. and Zaveri, R. A.: Development and validation of a black carbon mixing state resolved three-dimensional model: Aging processes and radiative impact, *J. Geophys. Res. Atmos.*, 118(5), 2304–2326, doi:10.1029/2012JD018446, 2013.

Matsui, H., Hamilton, D. S. and Mahowald, N. M.: Black carbon radiative effects highly sensitive to emitted particle size when resolving mixing-state diversity, *Nat. Commun.*, 9(1), doi:10.1038/s41467-018-05635-1, 2018.

Matta, E., Facchini, M. C., Decesari, S., Mircea, M., Cavalli, F., Fuzzi, S., Putaud, J.-P. and Dell’Acqua, A.: Mass closure on the chemical species in size-segregated atmospheric aerosol collected in an urban area of the Po Valley, Italy, *Atmos. Chem. Phys.*, 3(3), 623–637, doi:10.5194/acp-3-623-2003, 2003.

Maynard Dan, Coull Brent A., Gryparis Alexandros and Schwartz Joel: Mortality Risk Associated with Short-Term Exposure to Traffic Particles and Sulfates, *Environ. Health Perspect.*, 115(5), 751–755, doi:10.1289/ehp.9537, 2007.

McFiggans, G., Artaxo, P., Baltensperger, U., Coe, H., Facchini, M. C., Feingold, G., Fuzzi, S., Gysel, M., Laaksonen, A., Lohmann, U., Mentel, T. F., Murphy, D. M., O’Dowd, C. D., Snider, J. R., Weingartner, E. and Institut, P. S.: The effect of physical and chemical aerosol properties on warm cloud droplet activation, *Atmos. Chem. Phys.*, 6, 2593–2649, <https://doi.org/10.5194/acp-6-2593-2006>, 2006.

McMurry, P. H., Shepherd, M. F. and Vickery, J. S.: Particulate Matter Science for Policy Makers: A NARSTO Assessment, Cambridge University Press, Cambridge, United Kingdom., 2004.

Medalia, A. I. and Heckman, F. A.: Morphology of aggregates—II. Size and shape factors of carbon black aggregates from electron microscopy, *Carbon*, 7(5), 567–582, doi:10.1016/0008-6223(69)90029-3, 1969.

Metcalf, A. R., Loza, C. L., Coggon, M. M., Craven, J. S., Jonsson, H. H., Flagan, R. C. and Seinfeld, J. H.: Secondary organic aerosol coating formation and evaporation: Chamber studies using black carbon seed aerosol and the single-particle soot photometer, *Aerosol Sci. Technol.*, 47(3), 326–347, doi:10.1080/02786826.2012.750712, 2013.

Michelsen, H. A., Schulz, C., Smallwood, G. J. and Will, S.: Laser-induced incandescence: Particulate diagnostics for combustion, atmospheric, and industrial applications, *Prog. Energy Combust. Sci.*, 51, 2–48, doi:10.1016/j.peccs.2015.07.001, 2015.

- Middlebrook, A. M., Bahreini, R., Jimenez, J. L. and Canagaratna, M. R.: Evaluation of composition-dependent collection efficiencies for the aerodyne aerosol mass spectrometer using field data, *Aerosol Sci. Technol.*, 46(3), 258–271, doi:10.1080/02786826.2011.620041, 2012.
- Miyakawa, T., Kanaya, Y., Komazaki, Y., Taketani, F., Pan, X., Irwin, M. and Symonds, J.: Intercomparison between a single particle soot photometer and evolved gas analysis in an industrial area in Japan: Implications for the consistency of soot aerosol mass concentration measurements, *Atmos. Environ.*, 127, 14–21, doi:10.1016/j.atmosenv.2015.12.018, 2016.
- Miyazaki, Y., Kondo, Y., Sahu, L. K., Imaru, J., Fukushima, N. and Kano, M.: Performance of a newly designed continuous soot monitoring system (COSMOS), *J. Environ. Monit.*, 10(10), 1195–1201, doi:10.1039/B806957C, 2008.
- Mohr, C., Richter, R., DeCarlo, P. F., Prévôt, A. S. H. and Baltensperger, U.: Spatial variation of chemical composition and sources of submicron aerosol in Zurich during wintertime using mobile aerosol mass spectrometer data, *Atmos. Chem. Phys.*, 11(15), 7465–7482, doi:https://doi.org/10.5194/acp-11-7465-2011, 2011.
- Mohr, C., DeCarlo, P. F., Heringa, M. F., Chirico, R., Slowik, J. G., Richter, R., Reche, C., Alastuey, A., Querol, X., Seco, R., Peñuelas, J., Jiménez, J. L., Crippa, M., Zimmermann, R., Baltensperger, U. and Prévôt, A. S. H.: Identification and quantification of organic aerosol from cooking and other sources in Barcelona using aerosol mass spectrometer data, *Atmos. Chem. Phys.*, 12(4), 1649–1665, doi:https://doi.org/10.5194/acp-12-1649-2012, 2012.
- Momenimovahed, A. and Olfert, J. S.: Effective density and volatility of particles emitted from gasoline direct injection vehicles and implications for particle mass measurement, *Aerosol Sci. Technol.*, 49(11), 1051–1062, doi:10.1080/02786826.2015.1094181, 2015.
- Moosmüller, H., Chakrabarty, R. K. and Arnott, W. P.: Aerosol light absorption and its measurement: A review, *J. Quant. Spectrosc. Radiat. Transf.*, 110(11), 844–878, doi:10.1016/j.jqsrt.2009.02.035, 2009.
- Moteki, N. and Kondo, Y.: Effects of mixing state on black carbon measurements by laser-induced incandescence, *Aerosol Sci. Technol.*, 41(4), 398–417, doi:10.1080/02786820701199728, 2007.
- Moteki, N. and Kondo, Y.: Method to measure time-dependent scattering cross sections of particles evaporating in a laser beam, *J. Aerosol Sci.*, 39(4), 348–364, doi:10.1016/j.jaerosci.2007.12.002, 2008.
- Moteki, N. and Kondo, Y.: Dependence of laser-induced incandescence on physical properties of black carbon aerosols: Measurements and theoretical interpretation, *Aerosol Sci. Technol.*, 44(8), 663–675, doi:10.1080/02786826.2010.484450, 2010.
- Moteki, N., Kondo, Y., Oshima, N., Takegawa, N., Koike, M., Kita, K., Matsui, H. and Kajino, M.: Size dependence of wet removal of black carbon aerosols during transport from the boundary layer to the free troposphere, *Geophys. Res. Lett.*, 39(13), doi:10.1029/2012GL052034, 2012.
- Moteki, N., Kondo, Y. and Adachi, K.: Identification by single-particle soot photometer of black carbon particles attached to other particles: Laboratory experiments and ground observations in Tokyo, *J. Geophys. Res. Atmos.*, 119(2), 2013JD020655, doi:10.1002/2013JD020655, 2014.
- Moteki, N., Adachi, K., Ohata, S., Yoshida, A., Harigaya, T., Koike, M. and Kondo, Y.: Anthropogenic iron oxide aerosols enhance atmospheric heating, *Nat. Commun.*, 8, 15329, doi:10.1038/ncomms15329, 2017.
- Müller, T., Henzing, J. S., de Leeuw, G., Wiedensohler, A., Alastuey, A., Angelov, H., Bizjak, M., Collaud Coen, M., Engström, J. E., Gruening, C., Hillamo, R., Hoffer, A., Imre, K., Ivanow, P., Jennings, G., Sun, J. Y., Kalivitis, N., Karlsson, H., Komppula, M., Laj, P., Li, S.-M., Lunder, C., Marinoni, A., Martins dos Santos, S., Moerman, M., Nowak, A., Ogren, J. A., Petzold, A., Pichon, J. M., Rodriguez, S., Sharma, S., Sheridan, P. J., Teinilä, K., Tuch, T., Viana, M., Virkkula, A., Weingartner, E., Wilhelm, R. and Wang, Y. Q.: Characterization and intercomparison of aerosol absorption photometers: Result of two intercomparison workshops, *Atmos. Meas. Tech.*, 4(2), 245–268, doi:10.5194/amt-4-245-2011, 2011.

Myhre, G., Samset, B. H., Schulz, M., Balkanski, Y., Bauer, S., Bernsten, T. K., Bian, H., Bellouin, N., Chin, M., Diehl, T., Easter, R. C., Feichter, J., Ghan, S. J., Hauglustaine, D., Iversen, T., Kinne, S., Kirkevåg, A., Lamarque, J.-F., Lin, G., Liu, X., Lund, M. T., Luo, G., Ma, X., van Noije, T., Penner, J. E., Rasch, P. J., Ruiz, A., Seland, Ø., Skeie, R. B., Stier, P., Takemura, T., Tsigaridis, K., Wang, P., Wang, Z., Xu, L., Yu, H., Yu, F., Yoon, J.-H., Zhang, K., Zhang, H. and Zhou, C.: Radiative forcing of the direct aerosol effect from AeroCom Phase II simulations, *Atmos. Chem. Phys.*, 13(4), 1853–1877, doi:10.5194/acp-13-1853-2013, 2013.

Nakayama, T., Kondo, Y., Moteki, N., Sahu, L. K., Kinase, T., Kita, K. and Matsumi, Y.: Size-dependent correction factors for absorption measurements using filter-based photometers: PSAP and COSMOS, *J. Aerosol Sci.*, 41(4), 333–343, doi:10.1016/j.jaerosci.2010.01.004, 2010.

Naoe, H., Hasegawa, S., Heintzenberg, J., Okada, K., Uchiyama, A., Zaizen, Y., Kobayashi, E. and Yamazaki, A.: State of mixture of atmospheric submicrometer black carbon particles and its effect on particulate light absorption, *Atmos. Environ.*, 43(6), 1296–1301, doi:10.1016/j.atmosenv.2008.11.031, 2009.

Ng, N. L., Canagaratna, M. R., Jimenez, J. L., Chhabra, P. S., Seinfeld, J. H. and Worsnop, D. R.: Changes in organic aerosol composition with aging inferred from aerosol mass spectra, *Atmos. Chem. Phys.*, 11(13), 6465–6474, doi:10.5194/acp-11-6465-2011, 2011.

Nomura, T., Alonso, M., Kousaka, Y. and Tenjiku, E.: Simple Model of Aerosol Particle Formation by the Evaporation–Condensation Method, *J. Colloid Interface Sci.*, 231(1), 107–113, doi:10.1006/jcis.2000.7127, 2000.

Noone, K. J., Ogren, J. A., Heintzenberg, J., Charlson, R. J. and Covert, D. S.: Design and Calibration of a Counterflow Virtual Impactor for Sampling of Atmospheric Fog and Cloud Droplets, *Aerosol Sci. Technol.*, 8(3), 235–244, doi:10.1080/02786828808959186, 1988.

Ogren, J. A.: Comment on “Calibration and Intercomparison of Filter-Based Measurements of Visible Light Absorption by Aerosols,” *Aerosol Sci. Technol.*, 44(8), 589–591, doi:10.1080/02786826.2010.482111, 2010.

Onasch, T. B., Massoli, P., Keegan, P. L., Hills, F. B., Bacon, F. W. and Freedman, A.: Single Scattering Albedo Monitor for Airborne Particulates, *Aerosol Sci. Technol.*, 49(4), 267–279, doi:10.1080/02786826.2015.1022248, 2015.

Ostro, B., Feng, W.-Y., Broadwin, R., Green, S. and Lipsett, M.: The effects of components of fine particulate air pollution on mortality in California: results from CALFINE, *Environ. Health Perspect.*, 115(1), 13–19, doi:10.1289/ehp.9281, 2007.

Paatero, P. and Tapper, U.: Positive matrix factorization: A non-negative factor model with optimal utilization of error estimates of data values, *Environmetrics*, 5(2), 111–126, doi:10.1002/env.3170050203, 1994.

Pandolfi, M., Alados-Arboledas, L., Alastuey, A., Andrade, M., Angelov, C., Artiñano, B., Backman, J., Baltensperger, U., Bonasoni, P., Bukowiecki, N., Collaud Coen, M., Conil, S., Coz, E., Crenn, V., Dudoitis, V., Ealo, M., Eleftheriadis, K., Favez, O., Fetfatzis, P., Fiebig, M., Flentje, H., Ginot, P., Gysel, M., Henzing, B., Hoffer, A., Holubova Smejkalova, A., Kalapov, I., Kalivitis, N., Kouvarakis, G., Kristensson, A., Kulmala, M., Lihavainen, H., Lunder, C., Luoma, K., Lyamani, H., Marinoni, A., Mihalopoulos, N., Moerman, M., Nicolas, J., O’Dowd, C., Petäjä, T., Petit, J.-E., Pichon, J. M., Prokopiuk, N., Putaud, J.-P., Rodríguez, S., Sciare, J., Sellegri, K., Swietlicki, E., Titos, G., Tuch, T., Tunved, P., Ulevicius, V., Vaishya, A., Vana, M., Virkkula, A., Vratolis, S., Weingartner, E., Wiedensohler, A. and Laj, P.: A European aerosol phenomenology – 6: scattering properties of atmospheric aerosol particles from 28 ACTRIS sites, *Atmos. Chem. Phys.*, 18(11), 7877–7911, doi:10.5194/acp-18-7877-2018, 2018.

Parrenin, F., Masson-Delmotte, V., Kohler, P., Raynaud, D., Paillard, D., Schwander, J., Barbante, C., Landais, A., Wegner, A. and Jouzel, J.: Synchronous Change of Atmospheric CO<sub>2</sub> and Antarctic Temperature During the Last Deglacial Warming, *Science*, 339(6123), 1060–1063, doi:10.1126/science.1226368, 2013.

Peng, J., Hu, M., Guo, S., Du, Z., Zheng, J., Shang, D., Levy Zamora, M., Zeng, L., Shao, M., Wu, Y.-S., Zheng, J., Wang, Y., Glen, C. R., Collins, D. R., Molina, M. J. and Zhang, R.: Markedly enhanced absorption and direct radiative forcing of black carbon under polluted urban environments, *Proc. Natl. Acad. Sci.*, 113(16), 4266, doi:10.1073/pnas.1602310113, 2016.

Petit, J.-E., Favez, O., Sciare, J., Crehn, V., Sarda-Estève, R., Bonnaire, N., Močnik, G., Dupont, J.-C., Haeffelin, M. and Leoz-Garziandia, E.: Two years of near real-time chemical composition of submicron aerosols in the region of Paris using an aerosol chemical speciation monitor (ACSM) and a multi-wavelength aethalometer, *Atmos. Chem. Phys.*, 15(6), 2985–3005, doi:<https://doi.org/10.5194/acp-15-2985-2015>, 2015.

Petit, J.-E., Favez, O., Albinet, A. and Canonaco, F.: A user-friendly tool for comprehensive evaluation of the geographical origins of atmospheric pollution: Wind and trajectory analyses, *Environ. Model. Softw.*, 88, 183–187, doi:[10.1016/j.envsoft.2016.11.022](https://doi.org/10.1016/j.envsoft.2016.11.022), 2017.

Petzold, A., Kopp, C. and Niessner, R.: The dependence of the specific attenuation cross-section on black carbon mass fraction and particle size, *Atmos. Environ.*, 31(5), 661–672, doi:[10.1016/S1352-2310\(96\)00245-2](https://doi.org/10.1016/S1352-2310(96)00245-2), 1997.

Petzold, A. and Schönlinner, M.: Multi-angle absorption photometry—a new method for the measurement of aerosol light absorption and atmospheric black carbon, *J. Aerosol Sci.*, 35(4), 421–441, doi:[10.1016/j.jaerosci.2003.09.005](https://doi.org/10.1016/j.jaerosci.2003.09.005), 2004.

Petzold, A., Schloesser, H., Sheridan, P. J., Arnott, W. P., Ogren, J. A. and Virkkula, A.: Evaluation of Multiangle Absorption Photometry for Measuring Aerosol Light Absorption, *Aerosol Sci. Technol.*, 39(1), 40–51, doi:[10.1080/027868290901945](https://doi.org/10.1080/027868290901945), 2005.

Petzold, A., Ogren, J. A., Fiebig, M., Laj, P., Li, S.-M., Baltensperger, U., Holzer-Popp, T., Kinne, S., Pappalardo, G., Sugimoto, N., Wehli, C., Wiedensohler, A. and Zhang, X.-Y.: Recommendations for reporting “black carbon” measurements, *Atmos. Chem. Phys.*, 13(16), 8365–8379, doi:<https://doi.org/10.5194/acp-13-8365-2013>, 2013.

Piazzalunga, A., Bernardoni, V., Fermo, P., Valli, G. and Vecchi, R.: Technical Note: On the effect of water-soluble compounds removal on EC quantification by TOT analysis in urban aerosol samples, *Atmos. Chem. Phys.*, 11(19), 10193–10203, doi:[10.5194/acp-11-10193-2011](https://doi.org/10.5194/acp-11-10193-2011), 2011.

Pileci, R. E., Modini, R. L., Bertò, M., Yuan, J., Corbin, J. C., Marinoni, A., Henzing, B. J., Moerman, M. M., Putaud, J. P., Spindler, G., Wehner, B., Tuch, T., Trentini, A., Zanatta, M., Baltensperger, U. and Gysel-Beer, M.: Comparison of co-located rBC and EC mass concentration measurements during field campaigns at several European sites, *Atmos. Meas. Tech.*, 14, 1379–1403, <https://doi.org/10.5194/amt-14-1379-2021>, 2021.

van Pinxteren, D., Mothes, F., Spindler, G., Fomba, K. W. and Herrmann, H.: Trans-boundary PM<sub>10</sub>: Quantifying impact and sources during winter 2016/17 in eastern Germany, *Atmos. Environ.*, 200, 119–130, doi:[10.1016/j.atmosenv.2018.11.061](https://doi.org/10.1016/j.atmosenv.2018.11.061), 2019.

Polissar, A. V., Hopke, P. K., Paatero, P., Kaufmann, Y. J., Hall, D. K., Bodhaine, B. A., Dutton, E. G. and Harris, J. M.: The aerosol at Barrow, Alaska: long-term trends and source locations, *Atmos. Environ.*, 33(16), 2441–2458, doi:[10.1016/S1352-2310\(98\)00423-3](https://doi.org/10.1016/S1352-2310(98)00423-3), 1999.

Pope, C. A., Burnett, R. T., Thun, M. J., Calle, E. E., Krewski, D., Ito, K. and Thurston, G. D.: Lung cancer, cardiopulmonary mortality, and long-term exposure to fine particulate air pollution, *JAMA J. Am. Med. Assoc.*, 287(9), 1132–1141, 2002.

Pósfai, M., Gelencsér, A., Simonics, R., Arató, K., Li, J., Hobbs, P. V. and Buseck, P. R.: Atmospheric tar balls: Particles from biomass and biofuel burning, *J. Geophys. Res. Atmos.*, 109(D6), doi:[10.1029/2003JD004169](https://doi.org/10.1029/2003JD004169), 2004.

Pratt, K. A., Heymsfield, A. J., Twohy, C. H., Murphy, S. M., DeMott, P. J., Hudson, J. G., Subramanian, R., Wang, Z., Seinfeld, J. H. and Prather, K. A.: In Situ Chemical Characterization of Aged Biomass-Burning Aerosols Impacting Cold Wave Clouds, *J. Atmos. Sci.*, 67(8), 2451–2468, doi:[10.1175/2010JAS3330.1](https://doi.org/10.1175/2010JAS3330.1), 2010.

Pueschel, R. F., Livingston, J. M., Ferry, G. V. and DeFelice, T. E.: Aerosol abundances and optical characteristics in the pacific basin free troposphere, *Atmos. Environ.*, 28(5), 951–960, doi:[10.1016/1352-2310\(94\)90253-4](https://doi.org/10.1016/1352-2310(94)90253-4), 1994.

Putaud, J.-P., Van Dingenen, R., Alastuey, A., Bauer, H., Birmili, W., Cyrys, J., Flentje, H., Fuzzi, S., Gehrig, R., Hansson, H. C., Harrison, R. M., Herrmann, H., Hitznerberger, R., Hüglin, C., Jones, A. M., Kasper-Giebl, A., Kiss, G., Kousa, A., Kuhlbusch, T. A. J., Löschau, G., Maenhaut, W., Molnar, A., Moreno, T., Pekkanen, J.,

Perrino, C., Pitz, M., Puxbaum, H., Querol, X., Rodriguez, S., Salma, I., Schwarz, J., Smolik, J., Schneider, J., Spindler, G., ten Brink, H., Tursic, J., Viana, M., Wiedensohler, A. and Raes, F.: A European aerosol phenomenology – 3: Physical and chemical characteristics of particulate matter from 60 rural, urban, and kerbside sites across Europe, *Atmos. Environ.*, 44(10), 1308–1320, doi:10.1016/j.atmosenv.2009.12.011, 2010.

Qi, L., Li, Q., He, C., Wang, X. and Huang, J.: Effects of the Wegener–Bergeron–Findeisen process on global black carbon distribution, *Atmos. Chem. Phys.*, 17(12), 7459–7479, doi:10.5194/acp-17-7459-2017, 2017.

Querol, X., Moreno, T., Karanasiou, A., Reche, C., Alastuey, A., Viana, M., Font, O., Gil, J., de Miguel, E. and Capdevila, M.: Variability of levels and composition of PM<sub>10</sub> and PM<sub>2.5</sub> in the Barcelona metro system, *Atmos. Chem. Phys.*, 12(11), 5055–5076, doi:10.5194/acp-12-5055-2012, 2012.

Raatikainen, T., Brus, D., Hyvärinen, A.-P., Svensson, J., Asmi, E. and Lihavainen, H.: Black carbon concentrations and mixing state in the Finnish Arctic, *Atmos. Chem. Phys.*, 15, 10057–10070, <https://doi.org/10.5194/acp-15-10057-2015>, 2015.

Ram, K. and Sarin, M. M.: Absorption coefficient and site-specific mass absorption efficiency of elemental carbon in aerosols over urban, rural, and high-altitude sites in India, *Environ. Sci. Technol.*, 43(21), 8233–8239, doi:10.1021/es9011542, 2009.

Ram, K., Sarin, M. M. and Tripathi, S. N.: Inter-comparison of thermal and optical methods for determination of atmospheric black carbon and attenuation coefficient from an urban location in northern India, *Atmos. Res.*, 97(3), 335–342, doi:10.1016/j.atmosres.2010.04.006, 2010.

Ramabhadran, T. E., Peterson, T. W. and Seinfeld, J. H.: Dynamics of aerosol coagulation and condensation, *AIChE J.*, 22(5), 840–851, doi:10.1002/aic.690220505, 1976.

Reddington, C. L., McMeeking, G., Mann, G. W., Coe, H., Frontoso, M. G., Liu, D., Flynn, M., Spracklen, D. V. and Carslaw, K. S.: The mass and number size distributions of black carbon aerosol over Europe, *Atmos. Chem. Phys.*, 13(9), 4917–4939, doi:10.5194/acp-13-4917-2013, 2013.

Reisinger, P., Wonaschütz, A., Hitzenberger, R., Petzold, A., Bauer, H., Jankowski, N., Puxbaum, H., Chi, X. and Maenhaut, W.: Intercomparison of measurement techniques for black or elemental carbon under urban background conditions in wintertime: Influence of biomass combustion, *Environ. Sci. Technol.*, 42(3), 884–889, doi:10.1021/es0715041, 2008.

Renzi, L., Levizzani, V., Marinoni, A. and Lupi, A.: Characterization of atmospheric aerosol absorption properties at different sites in the Po Valley during ACTRIS-2 experiment, M.S. thesis, Università di Bologna, Italy., 2019.

Ricciardelli, I., Bacco, D., Rinaldi, M., Bonafè, G., Scotto, F., Trentini, A., Bertacci, G., Ugolini, P., Zigola, C., Rovere, F., Maccone, C., Pironi, C. and Poluzzi, V.: A three-year investigation of daily PM<sub>2.5</sub> main chemical components in four sites: The routine measurement program of the Supersito Project (Po Valley, Italy), *Atmos. Environ.*, 152, 418–430, doi:10.1016/j.atmosenv.2016.12.052, 2017.

Rich, D. Q., Schwartz, J., Mittleman, M. A., Link, M., Luttmann-Gibson, H., Catalano, P. J., Speizer, F. E. and Dockery, D. W.: Association of Short-term Ambient Air Pollution Concentrations and Ventricular Arrhythmias, *Am. J. Epidemiol.*, 161(12), 1123–1132, doi:10.1093/aje/kwi143, 2005.

Riemer, N., Vogel, H. and Vogel, B.: Soot aging time scales in polluted regions during day and night, *Atmos. Chem. Phys.*, 4(7), 1885–1893, doi:10.5194/acp-4-1885-2004, 2004.

Riemer, N., West, M., Zaveri, R. and Easter, R.: Estimating black carbon aging time-scales with a particle-resolved aerosol model, *J. Aerosol Sci.*, 41, 143–158, doi:10.1016/j.jaerosci.2009.08.009, 2009.

Rinaldi, M., Gilardoni, S., Paglione, M., Sandrini, S., Fuzzi, S., Massoli, P., Bonasoni, P., Cristofanelli, P., Marinoni, A., Poluzzi, V. and Decesari, S.: Organic aerosol evolution and transport observed at Mt. Cimone (2165 m a.s.l.), Italy, during the PEGASOS campaign, *Atmos. Chem. Phys.*, 15(19), 11327–11340, doi:10.5194/acp-15-11327-2015, 2015.

Ritter, C., Angeles Burgos, M., Böckmann, C., Mateos, D., Lisok, J., Markowicz, K. M., Moroni, B., Cappelletti, D., Udisti, R., Maturilli, M. and Neuber, R.: Microphysical properties and radiative impact of an intense biomass burning aerosol event measured over Ny-Ålesund, Spitsbergen in July 2015, *Tellus B Chem. Phys. Meteorol.*, 70(1), 1–23, doi:10.1080/16000889.2018.1539618, 2018.

Rosen, H., Hansen, A. D. A., Gündel, L. and Novakov, T.: Identification of the optically absorbing component in urban aerosols, *Appl. Opt.*, 17(24), 3859–3861, doi:10.1364/AO.17.003859, 1978.

Rosenfeld, D.: TRMM observed first direct evidence of smoke from forest fires inhibiting rainfall, *Geophys. Res. Lett.*, 26(20), 3105–3108, doi:10.1029/1999GL006066, 1999.

Saarikoski, S., Carbone, S., Decesari, S., Giulianelli, L., Angelini, F., Canagaratna, M., Ng, N. L., Trimborn, A., Facchini, M. C., Fuzzi, S., Hillamo, R. and Worsnop, D.: Chemical characterization of springtime submicrometer aerosol in Po Valley, Italy, *Atmos. Chem. Phys.*, 12(18), 8401–8421, doi:https://doi.org/10.5194/acp-12-8401-2012, 2012.

Saleh, R., Cheng, Z. and Atwi, K.: The Brown–Black Continuum of Light-Absorbing Combustion Aerosols, *Environ. Sci. Technol. Lett.*, 5(8), 508–513, doi:10.1021/acs.estlett.8b00305, 2018.

Samoli, E., Peng, R., Ramsay, T., Pipikou, M., Touloumi, G., Dominici, F., Burnett, R., Cohen, A., Krewski, D., Samet, J. and Katsouyanni, K.: Acute effects of ambient particulate matter on mortality in Europe and North America: results from the APHENA study, *Environ. Health Perspect.*, 116(11), 1480–1486, doi:10.1289/ehp.11345, 2008.

Samset, B. H., Myhre, G., Herber, A., Kondo, Y., Li, S.-M., Moteki, N., Koike, M., Oshima, N., Schwarz, J. P., Balkanski, Y., Bauer, S. E., Bellouin, N., Berntsen, T. K., Bian, H., Chin, M., Diehl, T., Easter, R. C., Ghan, S. J., Iversen, T., Kirkevåg, A., Lamarque, J.-F., Lin, G., Liu, X., Penner, J. E., Schulz, M., Seland, Ø., Skeie, R. B., Stier, P., Takemura, T., Tsigaridis, K. and Zhang, K.: Modelled black carbon radiative forcing and atmospheric lifetime in AeroCom Phase II constrained by aircraft observations, *Atmos. Chem. Phys.*, 14(22), 12465–12477, doi:10.5194/acp-14-12465-2014, 2014.

Samset, B. H., Stjern, C. W., Andrews, E., Kahn, R. A., Myhre, G., Schulz, M. and Schuster, G. L.: Aerosol absorption: Progress towards global and regional constraints, *Curr. Clim. Change Rep.*, 4(2), 65–83, doi:10.1007/s40641-018-0091-4, 2018.

Sandradewi, J., Prévôt, A. S. H., Weingartner, E., Schmidhauser, R., Gysel, M. and Baltensperger, U.: A study of wood burning and traffic aerosols in an alpine valley using a multi-wavelength aethalometer, *Atmos. Environ.*, 42(1), 101–112, doi:https://doi.org/10.1016/j.atmosenv.2007.09.034, 2008.

Saturno, J., Pöhlker, C., Massabò, D., Brito, J., Carbone, S., Cheng, Y., Chi, X., Ditas, F., Hrabě de Angelis, I., Morán-Zuloaga, D., Pöhlker, M. L., Rizzo, L. V., Walter, D., Wang, Q., Artaxo, P., Prati, P. and Andreae, M. O.: Comparison of different Aethalometer correction schemes and a reference multi-wavelength absorption technique for ambient aerosol data, *Atmos. Meas. Tech.*, 10(8), 2837–2850, doi:10.5194/amt-10-2837-2017, 2017.

Schnaiter M., Linke C., Möhler O., Naumann K.-H., Saathoff H., Wagner R., Schurath U. and Wehner B.: Absorption amplification of black carbon internally mixed with secondary organic aerosol, *J. Geophys. Res. Atmos.*, 110(D19), doi:10.1029/2005JD006046, 2005.

Schraml, S., Heimgärtner, C., Will, S., Leipertz, A. and Hemm, A.: Application of a New Soot Sensor for Exhaust Emission Control Based on Time Resolved Laser Induced Incandescence (TIRE-LII), SAE International., 2000.

Schulz, M., Textor, C., Kinne, S., Balkanski, Y., Bauer, S., Berntsen, T., Berglen, T., Boucher, O., Dentener, F., Guibert, S., Isaksen, I. S. A., Iversen, T., Koch, D., Kirkeva, A., Penner, J. E., Pitari, G., Reddy, S., Seland, Ø., Stier, P. and Takemura, T.: Radiative forcing by aerosols as derived from the AeroCom present-day and pre-industrial simulations, *Atmos. Chem. Phys.*, (6), 5225–5246, https://doi.org/10.5194/acp-6-5225-2006, 2006.

Schwartz, J., Litonjua, A., Suh, H., Verrier, M., Zanobetti, A., Syring, M., Nearing, B., Verrier, R., Stone, P., MacCallum, G., Speizer, F. and Gold, D.: Traffic related pollution and heart rate variability in a panel of elderly subjects, *Thorax*, 60(6), 455–461, doi:10.1136/thx.2004.024836, 2005.



Schwarz, Gao R. S., Fahey D. W., Thomson D. S., Watts L. A., Wilson J. C., Reeves J. M., Darbeheshti M., Baumgardner D. G., Kok G. L., Chung S. H., Schulz M., Hendricks J., Lauer A., Kärcher B., Slowik J. G., Rosenlof K. H., Thompson T. L., Langford A. O., Loewenstein M. and Aikin K. C.: Single-particle measurements of midlatitude black carbon and light-scattering aerosols from the boundary layer to the lower stratosphere, *J. Geophys. Res. Atmos.*, 111(D16), doi:10.1029/2006JD007076, 2006.

Schwarz, J. P., Gao, R. S., Spackman, J. R., Watts, L. A., Thomson, D. S., Fahey, D. W., Ryerson, T. B., Peischl, J., Holloway, J. S., Trainer, M., Frost, G. J., Baynard, T., Lack, D. A., de Gouw, J. A., Warneke, C. and Del Negro, L. A.: Measurement of the mixing state, mass, and optical size of individual black carbon particles in urban and biomass burning emissions, *Geophys. Res. Lett.*, 35(13), doi:10.1029/2008GL033968, 2008.

Schwarz, J. P., Spackman, J. R., Gao, R. S., Perring, A. E., Cross, E., Onasch, T. B., Ahern, A., Wrobel, W., Davidovits, P., Olfert, J., Dubey, M. K., Mazzoleni, C. and Fahey, D. W.: The detection efficiency of the single particle soot photometer, *Aerosol Sci. Technol.*, 44(8), 612–628, doi:10.1080/02786826.2010.481298, 2010.

Schwarz, J. P., Gao, R. S., Perring, A. E., Spackman, J. R. and Fahey, D. W.: Black carbon aerosol size in snow, *Sci. Rep.*, 3(1), doi:10.1038/srep01356, 2013.

Schwarz, J. P.: Extrapolation of single particle soot photometer incandescent signal data, *Aerosol Sci. Technol.*, 53(8), 911–920, doi:10.1080/02786826.2019.1610154, 2019.

Sedlacek, A. J., Lewis, E. R., Kleinman, L., Xu, J. and Zhang, Q.: Determination of and evidence for non-core-shell structure of particles containing black carbon using the Single-Particle Soot Photometer (SP2), *Geophys. Res. Lett.*, 39(6), L06802, doi:10.1029/2012GL050905, 2012.

Sedlacek, A. J., Onasch, T. B., Nichman, L., Lewis, E. R., Davidovits, P., Freedman, A. and Williams, L.: Formation of refractory black carbon by SP2-induced charring of organic aerosol, *Aerosol Sci. Technol.*, 52(12), 1521–7388, doi:10.1080/02786826.2018.1531107, 2018.

Seinfeld, J. H. and Pandis, S. N.: *Atmospheric chemistry and physics: From air pollution to climate change*, 2nd ed., J. Wiley, Hoboken, N.J., ISBN: 978-1-118-94740-1, 2006.

Serreze, M. C. and Barry, R. G.: Processes and impacts of Arctic amplification: A research synthesis, *Glob. Planet. Change*, 77(1–2), 85–96, doi:10.1016/j.gloplacha.2011.03.004, 2011.

Severinghaus, J. P.: Abrupt Climate Change at the End of the Last Glacial Period Inferred from Trapped Air in Polar Ice, *Science*, 286(5441), 930–934, doi:10.1126/science.286.5441.930, 1999.

Sharma, S., Lavoué, D., Cachier, H., Barrie, L. and Gong, S.: Long-term trends of the black carbon concentrations in the Canadian Arctic, *J. Geophys. Res.*, 109(D15), doi:10.1029/2003JD004331, 2004.

Sharma, S., Andrews, E., Barrie, L., Ogren, J. and Lavoué, D.: Variations and sources of the equivalent black carbon in the High Arctic revealed by long term observations at Alert and Barrow: 1989–2003, *J. Geophys. Res.*, 111(D14), doi:10.1029/2005JD006581, 2006.

Sharma, S., Leaitch, W. R., Huang, L., Veber, D., Kolonjari, F., Zhang, W., Hanna, S. J., Bertram, A. K. and Ogren, J. A.: An evaluation of three methods for measuring black carbon in Alert, Canada, *Atmos. Chem. Phys.*, 17(24), 15225–15243, doi:https://doi.org/10.5194/acp-17-15225-2017, 2017.

Shaw, G. E.: The Arctic Haze Phenomenon, *Bull. Am. Meteorol. Soc.*, 76(12), 2403–2413, https://doi.org/10.1175/1520-0477(1995)076<2403:TAHP>2.0.CO;2, 1995.

Shaw, G. E. and Stamnes, K.: Arctic haze: perturbation of the polar radiation budget, *Ann. N. Y. Acad. Sci.*, 338(1), 533–539, doi:10.1111/j.1749-6632.1980.tb17145.x, 1980.

Shindell, D. T., Chin, M., Dentener, F., Doherty, R. M., Faluvegi, G., Fiore, A. M., Hess, P., Koch, D. M., MacKenzie, I. A., Sanderson, M. G., Schultz, M. G., Schulz, M., Stevenson, D. S., Teich, H., Textor, C., Wild, O., Bergmann, D. J., Bey, I., Bian, H., Cuvelier, C., Duncan, B. N., Folberth, G., Horowitz, L. W., Jonson, J., Kaminski, J. W., Marmer, E., Park, R., Pringle, K. J., Schroeder, S., Szopa, S., Takemura, T., Zeng, G., Keating,

- T. J. and Zuber, A.: A multi-model assessment of pollution transport to the Arctic, *Atmos. Chem. Phys.*, 8, 5353–5372, doi:https://doi.org/10.5194/acp-8-5353-2008, 2008.
- Shiraiwa, M., Kondo, Y., Moteki, N., Takegawa, N., Sahu, L. K., Takami, A., Hatakeyama, S., Yonemura, S. and Blake, D. R.: Radiative impact of mixing state of black carbon aerosol in Asian outflow, *J. Geophys. Res.*, 113(D24), doi:10.1029/2008JD010546, 2008.
- Shiraiwa, M., Kondo, Y., Iwamoto, T. and Kita, K.: Amplification of light absorption of black carbon by organic coating, *Aerosol Sci. Technol.*, 44(1), 46–54, doi:10.1080/02786820903357686, 2010.
- Shrestha, G., Traina, S. and Swanston, C.: Black Carbon's Properties and Role in the Environment: A Comprehensive Review, *Sustainability*, 2, 294–320, doi:10.3390/su2010294, 2010.
- Slowik, J. G., Cross, E. S., Han, J.-H., Davidovits, P., Onasch, T. B., Jayne, J. T., Williams, L. R., Canagaratna, M. R., Worsnop, D. R., Chakrabarty, R. K., Moosmüller, H., Arnott, W. P., Schwarz, J. P., Gao, R.-S., Fahey, D. W., Kok, G. L. and Petzold, A.: An inter-comparison of instruments measuring black carbon content of soot particles, *Aerosol Sci. Technol.*, 41(3), 295–314, doi:10.1080/02786820701197078, 2007.
- Snyder, C. W.: Evolution of global temperature over the past two million years, *Nature*, 538(7624), 226–228, doi:10.1038/nature19798, 2016.
- Sokolik, I. N. and Toon, O. B.: Incorporation of mineralogical composition into models of the radiative properties of mineral aerosol from UV to IR wavelengths, *J. Geophys. Res. Atmos.*, 104(D8), 9423–9444, doi:10.1029/1998JD200048, 1999.
- Sørensen, M., Hurley, M. ., Wallington, T. ., Dibble, T. . and Nielsen, O. .: Do aerosols act as catalysts in the OH radical initiated atmospheric oxidation of volatile organic compounds?, *Atmos. Environ.*, 36(39–40), 5947–5952, doi:10.1016/S1352-2310(02)00766-5, 2002.
- Soto, K. F., Garza, K. M., Shi, Y. and Murr, L. E.: Direct contact cytotoxicity assays for filter-collected, carbonaceous (soot) nanoparticulate material and observations of lung cell response, *Atmos. Environ.*, 42(9), 1970–1982, doi:10.1016/j.atmosenv.2007.12.027, 2008.
- Spindler, G., Brüggemann, E., Gnauk, T., Grüner, A., Müller, K. and Herrmann, H.: A four-year size-segregated characterization study of particles PM<sub>10</sub>, PM<sub>2.5</sub> and PM<sub>1</sub> depending on air mass origin at Melpitz, *Atmos. Environ.*, 44(2), 164–173, doi:10.1016/j.atmosenv.2009.10.015, 2010.
- Spindler, G., Gnauk, T., Gruener, A., Inuma, Y., Mueller, K., Scheinhardt, S. and Herrmann, H.: Size-segregated characterization of PM<sub>10</sub> at the EMEP site Melpitz (Germany) using a five-stage impactor: A six year study, *J. Atmos. Chem.*, 69, 127–157, doi:10.1007/s10874-012-9233-6, 2012.
- Spindler, G., Grüner, A., Mueller, K., Schlimper, S. and Herrmann, H.: Long-term size-segregated particle (PM<sub>10</sub>, PM<sub>2.5</sub>, PM<sub>1</sub>) characterization study at Melpitz - Influence of air mass inflow, weather conditions and season, *J. Atmos. Chem.*, 70, 165–195, doi:10.1007/s10874-013-9263-8, 2013.
- Stanek, L., Sacks, J., Dutton, S. and Dubois, J.-J.: Attributing health effects to apportioned components and sources of particulate matter: An evaluation of collective results, *Atmos. Environ.*, 45, 5655–5663, doi:10.1016/j.atmosenv.2011.07.023, 2011.
- Stephens, M., Turner, N. and Sandberg, J.: Particle identification by laser-induced incandescence in a solid-state laser cavity, *Appl. Opt.*, 42(19), 3726–3736, doi:10.1364/AO.42.003726, 2003.
- Stephens, G. L., Li, J., Wild, M., Clayson, C. A., Loeb, N., Kato, S., L'Ecuyer, T., Stackhouse, P. W., Lebsock, M. and Andrews, T.: An update on Earth's energy balance in light of the latest global observations, *Nat. Geosci.*, 5(10), 691–696, doi:10.1038/ngeo1580, 2012.
- Stier, P., Seinfeld, J. H., Kinne, S., Feichter, J. and Boucher, O.: Impact of nonabsorbing anthropogenic aerosols on clear-sky atmospheric absorption, *J. Geophys. Res. Atmos.*, 111, D18201, doi:10.1029/2006JD007147, 2006.

Stohl, A.: Characteristics of atmospheric transport into the Arctic troposphere, *J. Geophys. Res.*, 111(D11306), doi:10.1029/2005JD006888, 2006.

Ström, J., Umegård, J., Tørseth, K., Tunved, P., Hansson, H.-C., Holmén, K., Wismann, V., Herber, A. and König-Langlo, G.: One year of particle size distribution and aerosol chemical composition measurements at the Zeppelin Station, Svalbard, March 2000–March 2001, *Phys. Chem. Earth Parts ABC*, 28(28–32), 1181–1190, doi:10.1016/j.pce.2003.08.058, 2003.

Subramanian, R., Khlystov, A. Y. and Robinson, A. L.: Effect of peak inert-mode temperature on elemental carbon measured using thermal-optical analysis, *Aerosol Sci. Technol.*, 40(10), 763–780, doi:10.1080/02786820600714403, 2006.

Takemura, T. and Suzuki, K.: Weak global warming mitigation by reducing black carbon emissions, *Sci. Rep.*, 9(1), 4419, doi:10.1038/s41598-019-41181-6, 2019.

Taketani, F., Miyakawa, T., Takashima, H., Komazaki, Y., Pan, X., Kanaya, Y. and Inoue, J.: Shipborne observations of atmospheric black carbon aerosol particles over the Arctic Ocean, Bering Sea, and North Pacific Ocean during September 2014, *J. Geophys. Res. Atmos.*, 121(4), 1914–1921, doi:10.1002/2015JD023648, 2016.

Tirpitz, J.-L., Frieß, U., Hendrick, F., Alberti, C., Allaart, M., Apituley, A., Bais, A., Beirle, S., Berkhout, S., Bogner, K., Bösch, T., Bruchkouski, I., Cede, A., Chan, K. L., den Hoed, M., Donner, S., Drosoglou, T., Fayt, C., Friedrich, M. M., Frumau, A., Gast, L., Gielen, C., Gomez-Martín, L., Hao, N., Hensen, A., Henzing, B., Hermans, C., Jin, J., Kreher, K., Kuhn, J., Lampel, J., Li, A., Liu, C., Liu, H., Ma, J., Merlaud, A., Peters, E., Pinardi, G., Pitters, A., Platt, U., Puenteadura, O., Richter, A., Schmitt, S., Spinei, E., Stein Zweers, D., Strong, K., Swart, D., Tack, F., Tiefengraber, M., van der Hoff, R., van Roozendaal, M., Vlemmix, T., Vonk, J., Wagner, T., Wang, Y., Wang, Z., Wenig, M., Wiegner, M., Wittrock, F., Xie, P., Xing, C., Xu, J., Yela, M., Zhang, C., and Zhao, X.: Intercomparison of MAX-DOAS vertical profile retrieval algorithms: studies on field data from the CINDI-2 campaign, *Atmos. Meas. Tech.*, 14, 1–35, doi:10.5194/amt-14-1-2021, 2021.

Tsai, F. C., Apte, M. G. and Daisey, J. M.: An Exploratory Analysis of the Relationship Between Mortality and the Chemical Composition of Airborne Particulate Matter, *Inhal. Toxicol.*, 12(sup2), 121–135, doi:10.1080/08958378.2000.11463204, 2000.

Tunved, P., Ström, J. and Krejci, R.: Arctic aerosol life cycle: linking aerosol size distributions observed between 2000 and 2010 with air mass transport and precipitation at Zeppelin station, Ny-Ålesund, Svalbard, *Atmos. Chem. Phys.*, 13(7), 3643–3660, doi:10.5194/acp-13-3643-2013, 2013.

Twomey, S.: Pollution and the planetary albedo, *Atmos. Environ.*, 8(12), 1251–1256, doi:10.1016/0004-6981(74)90004-3, 1974.

Ulbrich, I. M., Canagaratna, M. R., Zhang, Q., Worsnop, D. R. and Jimenez, J. L.: Interpretation of organic components from positive matrix factorization of aerosol mass spectrometric data, *Atmos. Chem. Phys.*, 9, 2891–2918, <https://doi.org/10.5194/acp-9-2891-2009>, 2009.

Van de Hulst: Multiple light scattering, Academic Press, New York., ISBN: 9780323155571, 1980.

Vecchi, R., Marcazzan, G. and Valli, G.: A study on nighttime–daytime PM10 concentration and elemental composition in relation to atmospheric dispersion in the urban area of Milan (Italy), *Atmos. Environ.*, 41(10), 2136–2144, doi:10.1016/j.atmosenv.2006.10.069, 2007.

Vecchi, R., Bernardoni, V., Fermo, P., Lucarelli, F., Mazzei, F., Nava, S., Prati, P., Piazzalunga, A. and Valli, G.: 4-hours resolution data to study PM10 in a “hot spot” area in Europe, *Environ. Monit. Assess.*, 154(1–4), 283–300, doi:10.1007/s10661-008-0396-1, 2009.

Viana, M., Pey, J., Querol, X., Alastuey, A., de Leeuw, F. and Lükewille, A.: Natural sources of atmospheric aerosols influencing air quality across Europe, *Sci. Total Environ.*, 472, 825–833, doi:10.1016/j.scitotenv.2013.11.140, 2014.

Vignati, E., Karl, M., Krol, M., Wilson, J., Stier, P. and Cavalli, F.: Sources of uncertainties in modelling black carbon at the global scale, *Atmos. Chem. Phys.*, 10(6), 2595–2611, doi:10.5194/acpd-9-24317-2009, 2010.

Virkkula, A., Mäkelä, T., Hillamo, R., Yli-Tuomi, T., Hirsikko, A., Hämeri, K. and Koponen, I. K.: A simple procedure for correcting loading effects of aethalometer data, *J. Air Waste Manag. Assoc.*, 57(10), 1214–1222, doi:10.3155/1047-3289.57.10.1214, 2007.

Wagner, P. E.: Aerosol Growth by Condensation, in *Aerosol Microphysics II: Chemical Physics of Microparticles*, edited by W. H. Marlow, pp. 129–178, Springer Berlin Heidelberg, Berlin, Heidelberg., ISBN: 978-3-642-81805-9, 1982.

Wang, Y., Chung, A. and Paulson, S. E.: The effect of metal salts on quantification of elemental and organic carbon in diesel exhaust particles using thermal-optical evolved gas analysis, *Atmos. Chem. Phys.*, 10(23), 11447–11457, doi:10.5194/acp-10-11447-2010, 2010.

Warneke, C., Froyd, K. D., Brioude, J., Bahreini, R., Brock, C. A., Cozic, J., de Gouw, J. A., Fahey, D. W., Ferrare, R., Holloway, J. S., Middlebrook, A. M., Miller, L., Montzka, S., Schwarz, J. P., Sodemann, H., Spackman, J. R. and Stohl, A.: An important contribution to springtime Arctic aerosol from biomass burning in Russia, *Geophys. Res. Lett.*, 37(1), doi:10.1029/2009GL041816, 2010.

Watson, J. G., Chow, J. C. and Chen, L.-W. A.: Summary of organic and elemental carbon/black carbon analysis methods and intercomparisons, *Aerosol Air Qual. Res.*, 5(1), 65–102, doi:10.4209/aaqr.2005.06.0006, 2005.

Wegener, A.: *Thermodynamik der Atmosphäre.*, Leipzig, 506 Germany: Barth., 1911.

Wehner, B., Philippin, S., Wiedensohler, A., Scheer, V. and Vogt, R.: Variability of non-volatile fractions of atmospheric aerosol particles with traffic influence, *Atmos. Environ.*, 38(36), 6081–6090, doi:10.1016/j.atmosenv.2004.08.015, 2004.

Weimer, S., Mohr, C., Richter, R., Keller, J., Mohr, M., Prévôt, A. S. H. and Baltensperger, U.: Mobile measurements of aerosol number and volume size distributions in an Alpine valley: Influence of traffic versus wood burning, *Atmos. Environ.*, 43(3), 624–630, doi:10.1016/j.atmosenv.2008.10.034, 2009.

Weingartner, E., Burtscher, H. and Baltensperger, U.: Hygroscopic properties of carbon and diesel soot particles, *Atmos. Environ.*, 31(15), 2311–2327, doi:10.1016/S1352-2310(97)00023-X, 1997.

Weingartner, E., Saathoff, H., Schnaiter, M., Streit, N., Bitnar, B. and Baltensperger, U.: Absorption of light by soot particles: determination of the absorption coefficient by means of aethalometers, *J. Aerosol Sci.*, 34(10), 1445–1463, doi:10.1016/S0021-8502(03)00359-8, 2003.

WHO: *Ambient air pollution: A global assessment of exposure and burden of disease*, World Health Organization, ISBN: 9789241511353, 2016.

Wiedensohler, A., Birmili, W., Nowak, A., Sonntag, A., Weinhold, K., Merkel, M., Wehner, B., Tuch, T., Pfeifer, S., Fiebig, M., Fjåraa, A. M., Asmi, E., Sellegri, K., Depuy, R., Venzac, H., Villani, P., Laj, P., Aalto, P., Ogren, J. A., Swietlicki, E., Williams, P., Roldin, P., Quincey, P., Hüglin, C., Fierz-Schmidhauser, R., Gysel, M., Weingartner, E., Riccobono, F., Santos, S., Grüning, C., Faloon, K., Beddows, D., Harrison, R., Monahan, C., Jennings, S. G., O'Dowd, C. D., Marinoni, A., Horn, H.-G., Keck, L., Jiang, J., Scheckman, J., McMurry, P. H., Deng, Z., Zhao, C. S., Moerman, M., Henzing, B., de Leeuw, G., Löschau, G. and Bastian, S.: Mobility particle size spectrometers: harmonization of technical standards and data structure to facilitate high quality long-term observations of atmospheric particle number size distributions, *Atmos. Meas. Tech.*, 5(3), 657–685, doi:10.5194/amt-5-657-2012, 2012.

Winiger, P., Andersson, A., Eckhardt, S., Stohl, A., Semiletov, I. P., Dudarev, O. V., Charkin, A., Shakhova, N., Klimont, Z., Heyes, C. and Gustafsson, Ö.: Siberian Arctic black carbon sources constrained by model and observation, *Proc. Natl. Acad. Sci.*, 114(7), E1054–E1061, doi:10.1073/pnas.1613401114, 2017.

Wolf, R., El Haddad, I., Crippa, M., Decesari, S., Slowik, J. G., Poulain, L., Gilardoni, S., Rinaldi, M., Carbone, S., Canonaco, F., Huang, R.-J., Baltensperger, U. and Prévôt, A. S. H.: Marine and urban influences on summertime PM<sub>2.5</sub> aerosol in the Po basin using mobile measurements, *Atmos. Environ.*, 120, 447–454, doi:10.1016/j.atmosenv.2015.09.007, 2015.

Yan, J., Wang, X., Gong, P., Wang, C. and Cong, Z.: Review of brown carbon aerosols: Recent progress and perspectives, *Sci. Total Environ.*, 634, 1475–1485, doi:10.1016/j.scitotenv.2018.04.083, 2018.

Yang, H. and Yu, J. Z.: Uncertainties in charring correction in the analysis of elemental and organic carbon in atmospheric particles by thermal/optical methods, *Environ. Sci. Technol.*, 36(23), 5199–5204, doi:10.1021/es025672z, 2002.

Yu, J. Z., Xu, J. and Yang, H.: Charring characteristics of atmospheric organic particulate matter in thermal analysis, *Environ. Sci. Technol.*, 36(4), 754–761, doi:10.1021/es015540q, 2002.

Yuan, J., Modini, R. L., Zanatta, M., Herber, A. B., Müller, T., Wehner, B., Poulain, L., Tuch, T., Baltensperger, U. and Gysel-Beer, M.: Variability in the mass absorption cross-section of black carbon (BC) aerosols is driven by BC internal mixing state at a central European background site (Melpitz, Germany) in winter, *Atmos. Chem. Phys.*, <https://doi.org/10.5194/acp-21-635-2021>, 2021.

Zanatta, M., Gysel, M., Bukowiecki, N., Müller, T., Weingartner, E., Areskou, H., Fiebig, M., Yttri, K. E., Mihalopoulos, N., Kouvarakis, G., Beddows, D., Harrison, R. M., Cavalli, F., Putaud, J. P., Spindler, G., Wiedensohler, A., Alastuey, A., Pandolfi, M., Sellegri, K., Swietlicki, E., Jaffrezo, J. L., Baltensperger, U. and Laj, P.: A European aerosol phenomenology-5: Climatology of black carbon optical properties at 9 regional background sites across Europe, *Atmos. Environ.*, 145, 346–364, doi:10.1016/j.atmosenv.2016.09.035, 2016.

Zanatta, M., Laj, P., Gysel, M., Baltensperger, U., Vratolis, S., Eleftheriadis, K., Kondo, Y., Dubuisson, P., Winiarek, V., Kazadzis, S., Tunved, P. and Jacobi, H.-W.: Effects of mixing state on optical and radiative properties of black carbon in the European Arctic, *Atmos. Chem. Phys.*, 18(19), 14037–14057, doi:10.5194/acp-18-14037-2018, 2018.

Zhang, Q., Jimenez, J. L., Canagaratna, M. R., Ulbrich, I. M., Ng, N. L., Worsnop, D. R. and Sun, Y.: Understanding atmospheric organic aerosols via factor analysis of aerosol mass spectrometry: A review, *Anal. Bioanal. Chem.*, 401(10), 3045–3067, doi:10.1007/s00216-011-5355-y, 2011.

Zhang, X., Kim, H., Parworth, C. L., Young, D. E., Zhang, Q., Metcalf, A. R. and Cappa, C. D.: Optical properties of wintertime aerosols from residential wood burning in Fresno, CA: results from DISCOVER-AQ 2013, *Environ. Sci. Technol.*, 50(4), 1681–1690, doi:10.1021/acs.est.5b04134, 2016.

Zhang, X., Mao, M., Yin, Y. and Wang, B.: Numerical Investigation on Absorption Enhancement of Black Carbon Aerosols Partially Coated With Nonabsorbing Organics, *J. Geophys. Res. Atmos.*, 123(2), 1297–1308, doi:10.1002/2017JD027833, 2018a.

Zhang, Y., Favez, O., Canonaco, F., Liu, D., Močnik, G., Amodeo, T., Sciare, J., Prévôt, A. S. H., Gros, V. and Albinet, A.: Evidence of major secondary organic aerosol contribution to lensing effect black carbon absorption enhancement, *Npj Clim. Atmos. Sci.*, 1(1), 47, doi:10.1038/s41612-018-0056-2, 2018b.

Zhang, Y. L., Perron, N., Ciobanu, V. G., Zotter, P., Minguillón, M. C., Wacker, L., Prévôt, A. S. H., Baltensperger, U. and Szidat, S.: On the isolation of OC and EC and the optimal strategy of radiocarbon-based source apportionment of carbonaceous aerosols, *Atmos. Chem. Phys.*, 12(22), 10841–10856, doi:10.5194/acp-12-10841-2012, 2012.

Zhao, D., Huang, M., Liu, D., Ding, D., Tian, P., Liu, Q., Zhou, W., Sheng, J., Wang, F., Bi, K., Yang, Y., Li, X., Hu, Y., Guo, X., Gao, Y., He, H., Chen, Y., Kong, S. and Huang, J.: Aircraft measurements of black carbon in the boundary layer over the North China Plain, *Atmos. Chem. Phys. Discuss.*, 1–25, doi:https://doi.org/10.5194/acp-2017-1118, 2018.

Zhu, Y., Kuhn, T., Mayo, P. and Hinds, W. C.: Comparison of daytime and nighttime concentration profiles and size distributions of ultrafine particles near a major highway, *Environ. Sci. Technol.*, 40(8), 2531–2536, doi:10.1021/es0516514, 2006.

Zielinski, T., Bolzacchini, E., Cataldi, M., Ferrero, L., Graßl, S., Hansen, G., Mateos, D., Mazzola, M., Neuber, R., Pakszys, P., Posyniak, M., Ritter, C., Severi, M., Sobolewski, P., Traversi, R. and Velasco-Merino, C.: Study of Chemical and Optical Properties of Biomass Burning Aerosols during Long-Range Transport Events toward the Arctic in Summer 2017, *Atmosphere*, 11(1), 84, doi:10.3390/atmos11010084, 2020.

Zotter, P., Herich, H., Gysel, M., El-Haddad, I., Zhang, Y., Močnik, G., Hüglin, C., Baltensperger, U., Szidat, S. and Prévôt, A. S. H.: Evaluation of the absorption ångström exponents for traffic and wood burning in the aethalometer-based source apportionment using radiocarbon measurements of ambient aerosol, *Atmos. Chem. Phys.*, 17(6), 4229–4249, doi:<https://doi.org/10.5194/acp-17-4229-2017>, 2017.

# Curriculum Vitae

## Personal information



Name: Rosaria Erika  
Family name: Pileci  
Address: Milan, Italy  
Mobile number: +39 3409196701  
e-mail: rosariaerika.pileci@gmail.com  
rosariaerika.pileci@u-earth.eu  
Gender: Female  
Date of birth: Jan 11 1991  
Nationality: Italian

## Work Experience

Nov 2020 – Present      Role: Senior Project Manager  
Company: U-Earth Biotech Ltd  
Tasks: Coordination, organization, and management of the research and development activities of the company.

## Education and training

2017 – 2020      PhD: Atmospheric Chemistry at the Laboratory of Atmospheric Chemistry (LAC) – Aerosol Physics Group  
Institute: Paul Scherrer Institute (PSI)  
University: Eidgenössische Technische Hochschule of Zürich (ETH)  
Date of graduation: 7 September 2020  
Thesis title: From the Po Valley to the Arctic: field experiments to characterize the variability in physical and optical properties of atmospheric black carbon particles from polluted to clean environments  
Advisors: Martin Gysel and Urs Baltensperger  
Co-advisor: Robin Modini  
Activities: Tutor of Aerosol 1 (Oct 2017, Oct 2018)  
Activities: Tutor of Aerosol 2 (May 2019)

2014 – 2017      Master degree in Physics (2nd cycle degree)  
University of Milan – Sciences and Technology  
Date of graduation: 7 April 2017  
Graduation mark: 110/110 cum Laude  
Thesis title: Study of the effects of sampling artifacts in multi-lambda measurements of the absorption coefficient of atmospheric aerosol  
Advisor: Roberta Vecchi  
Co-advisors: Vera Bernardoni and Gianluigi Valli  
Activities: student representative

2010 – 2014      Bachelor degree in Physics (1st level degree)  
University of Milan – Sciences and Technology  
Thesis title: Climatology of extreme daily precipitation in Lombardy from 1951 to 2013

Keywords: extreme events, climatology, precipitation  
Tutor: Maurizio Maugeri  
Activities: student representative

2005 – 2010 Italian secondary school diploma  
Scientific Lyceum PNI (National Plan of Computer Studies)

### **Personal competences**

Programming languages known:

- Basic knowledge of: Octave, Matlab and G (LabVIEW);
- Good knowledge of: C++, R, Igor, Python;

Language spoken: Italian (native), English (C1), French (A1), German (A1)

Driving license: B

### **Experience**

March 2020 Polar week March 2020  
Period: Nov 2019 – March 2020  
Description: Organization of online events for the Polar Week as Council Member of APECS.

Nov 2019 Field campaign  
Location: Ny Ålesund, Svalbard  
Description: calibration of the Single Particle Soot Photometer Extended Range (SP2-XR)

March 2019 Field campaign  
Location: Ny Ålesund, Svalbard  
Description: set up and calibration of the Single Particle Soot Photometer Extended Range (SP2-XR)

May 2018 Title: European Youth Event 2018 (EYE2018)  
Location: Strasbourg, European Parliament  
Description: Oral presentation during a Science Slam on the topic “Man vs Nature” with the title: “Aerosols: tiny particles, huge effect”; presence in the group: “Youth for Climate Ambition Delegation”.

March 2018 Title: Winter School on Advanced Analysis of Atmosphere-Surface Interactions and Feedbacks  
Location: Hyytiälä, Finland  
Mark: 5/5 credit points (ECTS)

July 2017 Field campaign  
Location: Po Valley, Italy  
Description: study of the variability of physical and optical properties of freshly emitted and aged black carbon particles determined from stationary and mobile measurements in the Po Valley (Italy), during summertime.



## **Publications**

Yan, C., Yin, R., Lu, Y., Dada, L., Yang, D., Fu, Y., Kontkanen, J., Deng, C., Garmash, O., Ruan, J., Baalbaki, R., Schervis, M., Cai, R., Bloss, M., Chan, T., Chen, T., Chen, W., Chen, X., Chen, Y., Chu, B., Dällenbach, K., Foreback, B., He, X., Heikkinen, L., Jokinen, T., Junninen, H., Kangasluoma, J., Kokkonen, T., Kruppa, M., Lehtipalo, K., Li, Haiyan, Li, Hui, Li, X., Liu, Y., Ma, Q., Paasonen, P., Rantala, P., [Pileci, R.E.](#), Rusanen, A., Sarnela, N., Simonen, P., Wang, S., Wang, W., Wang, Y., Xue, M., Yang, G., Yao, L., Zhou, Y., Kujansuu, J., Petäjä, T., Nie, W., Ma, Y., Ge, M., He, H., Donahue, N., Worsnop, D.R., Kerminen, V.M., Wang, L., Liu, Y., Zheng, J., Kulmala, M., Jiang, J., and Bianchi F., The synergistic role of sulfuric acid, bases, and oxidized organics governing new-particle formation in Beijing, accepted for publication in *Geophysical Research Letters*, <https://doi.org/10.1029/2020GL091944>, 2021.

Modini, R. L., Corbin, J. C., Brem, B.T., Irwin, M., Bertò, M., [Pileci, R.E.](#), Fetfatizis, P., Eleftheriadis, K., Henzing, B., Moerman, M.M., Liu, F., Müller, T., and Gysel-Beer, M., Detailed characterization of the CAPS single scattering albedo monitor (CAPS PMssa) as a field-deployable instrument for measuring aerosol light absorption with the extinction-minus-scattering method, *Atmospheric Measurements Techniques*, 14, 819–851, <https://doi.org/10.5194/amt-14-819-2021>, 2021.

[Pileci, R.E.](#), Modini R.L., Bertò, M., Yuan, J., Corbin, J.C., Marinoni, A., Henzing, B.J., Moerman, M.M., Putaud, J. P., Spindler, G., Wehner, B., Müller, T., Tuch, T., Trentini, A., Zanatta, M., Baltensperger, U., and Gysel-Beer, M., Comparison of co-located rBC and EC mass concentration measurements during field campaigns at several European sites, *Atmospheric Measurements Techniques*, 14, 1379–1403, <https://doi.org/10.5194/amt-14-1379-2021>, 2021.

Forello, A.C., Bernardoni, V., Calzolari, G., Lucarelli, F., Massabò, D., Nava, S., [Pileci, R.E.](#), Prati, P., Valentini, S., Valli, G., and Vecchi, R., Exploiting multi-wavelength aerosol absorption coefficients in a multi-time resolution source apportionment study to retrieve source-dependent absorption parameters., *Atmospheric Chemistry and Physics*, 19(17), 11235–11252, <https://doi.org/10.5194/acp-19-11235-2019>, 2019.

Bernardoni, V., [Pileci, R.E.](#), Caponi, L., & Massabò, D., The multi-wavelength absorption analyzer (MWA) model as a tool for source and component apportionment based on aerosol absorption properties: Application to samples collected in different environments, *Atmosphere*, 8(11), 218. <https://doi.org/10.3390/atmos8110218>, 2017.

Alimonti, G., Brambilla, R., [Pileci, R.E.](#), Romano, R., Rosa, F. & Spinicci, L., Edible energy: balancing inputs and waste in food supply chain and biofuels from algae., *European Physical Journal Plus*, 132(14), <https://doi.org/10.1140/epjp/i2017-11301-8>, 2017.

## **Conferences**

- |            |   |
|------------|---|
| May 2019   | Title: Asian Aerosol Conference (AAC 2019)<br>Location: Hong Kong, China<br>Description: Oral presentation on the topic: “Variability of physical and optical properties of freshly emitted and aged black carbon particles determined from stationary and mobile measurements in the Po Valley (Italy), during summertime” |
| April 2019 | Title: 12 <sup>th</sup> International Conference on Carbonaceous Particle in the Atmosphere 2019 (ICCPA 2019)<br>Location: Vienna, Austria<br>Description: Oral presentation on the topic: “Comparison of collocated rBC and EC mass concentration measurements during field campaigns at several European sites”           |

November 2018	<p>Title: Swiss Aerosol Group Meeting 2018  Location: Bern, Switzerland  Description: Oral presentation on the topic: "Variability of physical and optical properties of freshly emitted and aged black carbon particles determined from stationary and mobile measurements in the Po Valley (Italy), during summertime"</p>
October 2018	<p>Title: Ny Ålesund Atmospheric flagship workshop  Location: Postdam, Germany</p>
July 2018	<p>Title: Organized the visit at Joint Research Centre (JRC)  Description: Oral presentation of the Aerosol Physics Group Activities</p>
June 2018	<p>Title: 22<sup>nd</sup> ETH-Conference on Combustion Generated Nanoparticles  Location: ETH, Zürich, Switzerland  Description: Staff member</p>
May 2018	<p>Title: Particulate Matter Conference 2018 (PM2018)  Location: Matera, Italy  Description: Oral presentation: "Physical, chemical and optical properties of freshly emitted exhaust particles determined from mobile measurements on different road types in the Po Valley, Italy".</p>
August 2017	<p>Title: European Aerosol Conference 2017 (EAC2017)  Location: Zürich  Description: Staff member, Poster: "Study of the effects of sampling artifacts in multi-lambda measurements of the absorption coefficient of atmospheric aerosol"</p>
November 2016	<p>Title: Nano symposium  Company: XEarPro (Earth protection)  Location: Milano</p>
October 2016	<p>Title: 23rd World Energy Congress 2016  Company: World Energy Council (WEC)  Location: Istanbul, Turkey  Description: Oral presentation: "From Food to Energy: A Bridge from Milano EXPO 2015 to the Astana EXPO 2017".</p>
October 2016	<p>Title: 55° National Congress of Physics Teaching  Company: Association for the teaching of Physics (AIF)  Location: Gran Sasso National Laboratories (LNGS)  Description: Oral presentation</p>
May 2016	<p>Title: VII National Conference on Atmospheric Particulate  Company: Italian Aerosol Society (IAS)  Location: Rome</p>
October 2015	<p>Title: EXPO Milano 2015: "Feed the planet, energy for life".  Company: EnergyLab  Location: Milano, EXPO  Description: Oral presentation: "Feed the planet, energy for life: a link between Expo Milano 2015 and Astana 2017".</p>

September 2015                      Title: European Aerosol Conference 2015 (EAC)  
Company: Italian Aerosol Society (IAS)  
Location: Milano, University Bicocca  
Description: Staff member

**Memberships**

Italian Aerosol Society (IAS)  
Italian Climate Network (ICN)  
Association of Polar Early Career Scientists (APECS) – APECS Council 2019-2020

# Acknowledgments

Only 3+ years ago, I changed my life. I decided to leave my comfortable and loving life, to get out of my comfort zone and chase the desire to grow and discover. Now, the finish line is over there. In these years I have been running trying to reach it as quickly as possible, I was hungry of experiences, opportunities and knowledge and this group met my match perfectly. However, “Happiness is not about the trophy or the finish line. It is the journey. If you can enjoy your journey, you can enjoy your life”, Pharrell Williams said... and today, slowing down, and looking back I realize how exciting, emotional and formative these 3+ years were for me.

The stay in the LAC has been professionally amazing thanks to the outstanding scientific level, expertise and passion of all the members. Getting to know all these wonderful people has been incredible: a mixture of cultures, different ways of thinking, living and cooking (someone told me that if I do not mention the cooking part somewhere, I am not a real Italian, so...). All the people I met gave me something I will bring with me forever. For this reason, I feel very grateful to all of the persons that walked (and most of the time ran) next to me during this PhD experience.

The first person I want to thank sincerely is **Urs**. Urs is not only our doctoral father but also a real “father-in-law”. Thank you for your support, advices, for listening to me and for inspiring me. You are the true definition of a perfect leader. “A leader is one who knows the way, goes the way, and shows the way”, John Maxwell said. Thank you for showing me the way.

Thank you **Denise** for being such an inspirational example of how a woman can perfectly handle a family and a successful career. I really admire you.

Thank you **Paola** and **Jing** for being my co-referees and reviewing my thesis.

I would like to thank the person that was at the top of my thoughts even more than my girlfriend was: **Martin**. You taught me the meaning of incandescence but also of excellence. You taught me being patient, dedicated, passionate, precise, and wait the success to come consequently. Thanks for satisfying my hunger of experiences. Thanks also for sending me to the Arctic after I said that I hated the Swiss cold winters... actually, now I love them.

Thank you **Rob**, for the wonderful experiences we enjoyed together (I would mention some of them but it is not appropriate in a thesis acknowledgments). Thank you for the endless chats about life and science. Thank you for your positive, exaggerated positive, mood that tricked me into believing PSI was a good place (\*kidding\*). Thank you for your precious advices and for the time you dedicated to me. It was the best gift you could make me.

Thank you **Günther**, for your precious unavoidable help and for the adventures we shared from the Po Valley to the Arctic. Thank you also for taking absurd pictures of me in the most unexpected places and situations. Thank you for listening my never-ending Italian complaints. As you said: “One little Italian, many big problems”.

Thank you **Michele** because the PhD is less tough if shared with a compatriot. Thank you **Jinfeng** for your friendship and your limitless smile! Thank you **Simon** for our caffè and affection. Thank you **Reza** for our shared frustration. Thank you **Ian** for your support and enthusiasm. Thank you in advance **Varun** for inviting me to my first Indian wedding, I am looking forward. Thank you **Pragati** and **Anna** for supporting me and answering my 1000 questions on the thesis submission process. Thank you to all the other excellent mates, **Andrea, Roberto, Ping, Rubi, Kristty, Yandong, Vaivos, Mihnea, Liwei**, I shared PhD crises and joys with. Thank you to all the other senior LAC members: you taught me that I really do not know anything about aerosols, you are all incredibly good.

Thank you to my flat mate, **Davide**, for letting me experience the first cohabitation of my life. Thank you **Max** for the great time we had together and for being so close even now that you are far away. Thank you **Frenk** for our passionate Brugg-Turgi walks (and for many other common passions).

Thank you to my best friend **Eliana**, for being always there, for knowing me better than I know myself and for being my spiritual guide, always. Thank you to my friends, **Riccardo, Orazio, Pietro, Giulia, Klaudia** and **Ra** for recharging my batteries during weekends. A special thanks to **Gio**, we both know the reason.

Thank you **Roberta** for being a constant presence during these years and for teaching me that if you follow your heart and passions you are never wrong. Thank you for introducing me to this fortifying, formative and incredible experience here at PSI.

Now the biggest thank goes to my family members.

Thank you sister **Stella** for all the support I have always received from your side in all these years. Thank you **Matty (Marinä)** because sometimes you need to get lost to find yourself again... and I am so happy that we found each other, stronger and closer than ever. Thank you **Marina** for your precious encouragements and support. Thank you to my favorite family **Albi, Lisa** and my wonderful three nephews: **Edo, Aliciotta and Anna** for releasing my weekly stress watching Dragon Ball, playing and cuddling together.

Thank you to my mum, **Maria** and my dad **Mimmo**. I really love you and I will always take care of you. All this to make you proud of me.

Thank you to my girlfriend **Giulia** for the magnificent journey we went through together. It is amazing to see how much we have grown during these ten years. Distance is nothing if there is true love (included that for public transportation) and I am looking forward to spending my entire life with you. Get ready!

